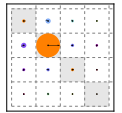


# Demonstrating Quantum Speed-Up with a Two-Transmon Quantum Processor.

Andreas Dewes

July 2012





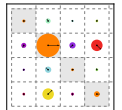
# Contents

<b>1</b>	<b>Introduction &amp; Summary</b>	<b>17</b>
1.1	Quantum Computing with Superconducting Circuits . . . . .	17
1.1.1	Context of this thesis work: 25 years of superconducting quantum circuits . . . . .	18
1.1.2	This Thesis Work . . . . .	19
1.2	Realizing a Two-Qubit Quantum Processor . . . . .	20
1.3	Demonstrating Simultaneous Single-Shot Readout . . . . .	21
1.4	Generating and Characterizing Entanglement . . . . .	23
1.5	Realizing a Universal Two-Qubit Quantum Gate . . . . .	25
1.6	Running a Quantum Search Algorithm . . . . .	26
1.7	Demonstrating Quantum Speed-Up . . . . .	28
1.8	Towards a Scalable Multi-Qubit Architecture . . . . .	29
<b>2</b>	<b>Theoretical Foundations</b>	<b>31</b>
2.1	Classical & Quantum Information Processing . . . . .	31
2.2	Principles of "Conventional" Quantum Computing . . . . .	32
2.2.1	Quantum Bits and registers . . . . .	33
2.2.2	Quantum Gates . . . . .	34
2.2.3	Quantum Algorithms . . . . .	35
2.2.4	Quantum Simulation . . . . .	36
2.2.5	Realization of a Quantum Computer . . . . .	36
2.3	Superconducting Quantum Circuits . . . . .	37
2.3.1	The Josephson junction . . . . .	37
2.3.2	Quantization of Electrical Circuits . . . . .	38
2.3.3	The LCR Resonator . . . . .	41
Coplanar Waveguide Resonators . . . . .	42	
Quantization of the Resonator . . . . .	44	
2.3.4	The Cooper Pair Box . . . . .	45
The Transmon Qubit . . . . .	49	
Decoherence of the Transmon . . . . .	49	

## *CONTENTS*

---

Relaxation through the Charge Channel . . . . .	51
Relaxation through the Flux Channel . . . . .	51
Dephasing through the Charge Channel . . . . .	51
Dephasing through the Flux Channel . . . . .	52
<b>2.4 Circuit Quantum Electrodynamics . . . . .</b>	<b>52</b>
2.4.1 Qubit Driving . . . . .	54
2.4.2 Dispersive Limit & Qubit Readout . . . . .	55
2.4.3 The Josephson Bifurcation Amplifier . . . . .	55
Operation Principle . . . . .	57
2.4.4 Qubit-Qubit Interaction . . . . .	58
Direct Capacitive Coupling . . . . .	59
Coupling Bus . . . . .	59
2.4.5 Qubit Decoherence in CQED . . . . .	60
Relaxation . . . . .	60
Dephasing . . . . .	60
<b>2.5 Master Equation Formalism . . . . .</b>	<b>62</b>
2.5.1 Simulation of our Two-Qubit Processor . . . . .	63
<b>3 Realizing a Two-Qubit Processor . . . . .</b>	<b>65</b>
3.1 Introduction & Motivation . . . . .	65
3.1.1 Processor Operation . . . . .	66
3.2 Qubit Design . . . . .	68
3.2.1 Qubit Frequency & Junction Asymmetry . . . . .	68
3.2.2 Single-Qubit Gates . . . . .	69
Charge Driving . . . . .	69
Flux Driving . . . . .	71
3.2.3 Qubit-Qubit Coupling . . . . .	71
3.2.4 Relaxation and Dephasing . . . . .	73
Qubit Relaxation . . . . .	74
Relaxation through the Gate Charge Channel . . . . .	74
Relaxation through the Flux Channel . . . . .	75
Qubit Dephasing . . . . .	75
Dephasing through the Flux Channel . . . . .	75
Dephasing through the Charge Channel . . . . .	75
3.3 Readout Design . . . . .	76
3.4 Summary: Qubit and Readout Parameters . . . . .	78
3.5 Processor Layout & Fabrication . . . . .	78
3.6 Electromagnetic Simulation of the Qubit-Chip . . . . .	81
3.7 Fabrication . . . . .	81

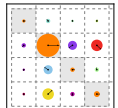


<b>4 Measurement Setup &amp; Techniques</b>	<b>85</b>
4.1 Sample Holder & PCB . . . . .	85
4.2 Signal Generation & Acquisition . . . . .	86
4.2.1 Driving and Measurement of the Qubit . . . . .	86
4.2.2 Microwave Sideband Mixing . . . . .	88
4.2.3 Fast Magnetic Flux Pulses . . . . .	90
4.2.4 Pulse Synchronization . . . . .	92
4.3 Measurement Techniques . . . . .	92
4.4 Qubit Readout . . . . .	93
4.5 Qubit Manipulation . . . . .	95
4.5.1 Spectroscopic Measurements of the Qubit State . . . . .	96
4.5.2 Rabi Oscillations . . . . .	97
4.6 Dephasing Time Measurement . . . . .	98
4.7 Relaxation Time Measurement . . . . .	99
<b>5 Characterizing the Two-Qubit Processor</b>	<b>101</b>
5.1 Qubit & Readout Characterization . . . . .	101
Qubit Frequency, Anharmonicity and Asymmetry . . . . .	102
Readout Parameters . . . . .	102
Qubit/Readout Coupling . . . . .	103
Qubit Parameter Survey . . . . .	103
5.2 Choice of Processor Working Points . . . . .	105
5.3 Qubit Readout Characterization . . . . .	105
5.4 Single-Qubit Operations . . . . .	106
5.5 Two Qubit Operations . . . . .	107
5.5.1 Creation of Entanglement . . . . .	108
5.5.2 Quantum State Tomography . . . . .	110
Maximum Likelihood Estimation of Quantum States . . . . .	111
Including Experimental Tomography Errors . . . . .	112
5.5.3 Characterizing Two-Qubit States using QST . . . . .	112
5.5.4 Creation of Bell states . . . . .	115
5.5.5 Violation of the Bell Inequality . . . . .	115
Errors . . . . .	118
5.6 Realizing a Two-Qubit Gate . . . . .	120
5.6.1 Principle . . . . .	120
5.6.2 Experimental Implementation . . . . .	120
5.6.3 Quantum Process Tomography of the Gate . . . . .	121
Theoretical Description of a Quantum Process . . . . .	121
Implementation . . . . .	122

## **CONTENTS**

---

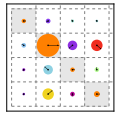
From the $\chi$ matrix to the Kraus representation . . . . .	123
Experimental Results: Input/Output Matrices And $\chi$ -Matrix . . . . .	123
5.6.4 Gate Fidelity . . . . .	127
5.6.5 Gate Error Analysis . . . . .	127
Tomographic Errors . . . . .	127
Unitary and Non-Unitary Gate Errors . . . . .	128
<b>6 Running the Grover Search Algorithm</b>	<b>131</b>
6.1 Introduction & Motivation . . . . .	131
6.1.1 Deriving the Grover Algorithm from Schrödinger's Equation . . . . .	134
Efficiency of Quantum Searching . . . . .	136
6.1.2 Implementation & Comparability to Classical Algorithms . . . . .	137
6.1.3 Ancilla-based Implementation of the Algorithm . . . . .	138
6.2 Comparision to a Classical Algorithm . . . . .	139
6.3 Experimental Implementation . . . . .	140
6.3.1 Pulse Sequence . . . . .	141
6.4 Results . . . . .	142
6.4.1 State Tomography of the Quantum Register . . . . .	142
6.4.2 Single Run Results . . . . .	142
6.5 Algorithm Fidelity . . . . .	143
6.6 Comparision to a Classical Search Algorithm . . . . .	144
6.7 Error Analysis . . . . .	146
6.7.1 Gate Errors & Decoherence . . . . .	146
Modeling Decoherence . . . . .	146
Fidelity of the Oracle and diffusion operators . . . . .	149
6.7.2 Readout Errors . . . . .	150
6.8 Conclusions . . . . .	150
<b>7 Conclusions &amp; Perspective</b>	<b>153</b>
7.1 Designing a Scalable Architecture for Quantum Bits . . . . .	153
7.1.1 Requirements . . . . .	153
7.1.2 Qubit-Qubit Coupling . . . . .	153
7.1.3 Realizing A Four-Qubit Architecture . . . . .	153
7.1.4 Scaling Up . . . . .	153
7.2 Future Directions in Superconducting QC . . . . .	153
7.2.1 3D Circuit Quantum Electrodynamics . . . . .	153
7.2.2 Hybrid Quantum Systems . . . . .	153
7.2.3 Quantum Error Correction & Feedback . . . . .	153



<b>A Modeling of Multi-Qubit Systems</b>	<b>155</b>
A.1 Analytical Approach . . . . .	155
A.1.1 Multi-Qubit Hamiltonian . . . . .	155
A.1.2 Energies and Eigenstates . . . . .	155
A.2 Master Equation Approach . . . . .	155
Relaxation and Dephasing . . . . .	156
A.2.1 Direct Integration . . . . .	157
A.2.2 Monte Carlo Simulation . . . . .	158
A.2.3 Speeding Up Simulations . . . . .	158
<b>B Data Acquisition &amp; Management</b>	<b>159</b>
B.1 Data Acquisition Infrastructure . . . . .	159
B.2 Data Management Requirements . . . . .	159
B.3 PyView . . . . .	159
B.3.1 Overview . . . . .	159
B.3.2 Instrument Management . . . . .	160
B.3.3 Data Acquisition . . . . .	160
B.3.4 Data Management . . . . .	160
B.3.5 Data Analysis . . . . .	160
<b>C Design &amp; Fabrication</b>	<b>161</b>
C.1 Mask Design . . . . .	161
C.2 Optical Lithography . . . . .	161
C.3 Electron Beam Lithography . . . . .	161
<b>D Bibliography</b>	<b>161</b>
<b>E Publications</b>	<b>172</b>

## *CONTENTS*

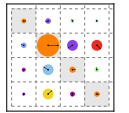
---



# List of Figures

1.1 Blueprint of a “canonical” two-qubit quantum processor . . . . .	17
1.3 Circuit schematic of the realized two-qubit processor . . . . .	21
1.4 Switching probabilities of the two qubit readouts as a function of the read-out excitation power . . . . .	22
1.5 Generating entangled two-qubit states by swapping interaction . . . . .	24
1.6 Measurement of the CHSH operator of an entangled two-qubit state . . . . .	25
1.7 Measured $\chi$ -matrix of the $\sqrt{i\text{SWAP}}$ gate . . . . .	26
1.8 Schematic of the Grover search algorithm and measured density matrices when running it . . . . .	27
1.9 Single-run results of the Grover search algorithm . . . . .	28
1.10 Schematic of the four-qubit chip realized in this work . . . . .	29
1.11 Measured $ S_{12} $ transmission coefficient for the input transmission line of our four-qubit chip . . . . .	30
2.1 The Bloch sphere representation of a qubit state $ \psi\rangle = \cos \frac{\theta}{2}  0\rangle + e^{i\phi} \sin \frac{\theta}{2}  1\rangle$ . The state $ \psi\rangle$ is fully characterized by specifying its “latitude” and “azimuth” angles $\theta$ and $\phi$ . Pure quantum states will always lie on the surface of the Bloch sphere, whereas mixed quantum states can also lie anywhere inside the sphere. . . . .	32

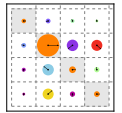
2.3	a) The electric field $E$ and current $I$ inside a $\lambda/2$ resonator. b) The circuit model of an open $\lambda/2$ resonator capacitively coupled to a drive circuit. The (lossless) resonator can be modeled as a series of infinitesimal sections of $LC$ elements, as shown in the inset. c) The schematic of a coplanar waveguide (CPW) resonator, showing the electric field $E$ , magnetic field $B$ and the current $I$ in the resonator. d) The reflected phase $\arg(S_{11})$ and absolute value of the input impedance $ Z_{in} $ and resonator impedance $ Z_{res} $ of an LCR resonator with $\omega_r = Z_r = Z_0 = 1$ , $R \rightarrow \infty$ and $C_{in} = 0.1$ (dotted lines) as well a $\lambda/2$ resonator with the same effective $\omega_r$ and $Z_r$ (solid lines), plotted as a function of the reduced frequency. As can be seen, the resonance frequency of the loaded resonator shifts in respect to that of the uncoupled one. In this case, $\omega_r^{\text{loaded}} \approx 0.969$ . . . . .	43
2.4	a) The circuit schematic of a Cooper Pair Box (CPB). The device consists of a Josephson junction capacitively coupled to a voltage source. The extra capacitance of the Josephson junction is modeled by a capacitor $C_J$ . Charges can accumulate on the island between the voltage source and the Josephson junction. b) A <i>split Cooper pair box</i> , where instead of one junction two of them are arranged in a loop. With this geometry it is possible to tune the effective Josephson energy of the circuit by changing the magnetic flux inside the junction loop. c) The schematic of a split CPB capacitively coupled to ground. This schematic corresponds most closely to the experimental CPB circuit that we use in this work. . . . .	45
2.5	Energies of the first four energy levels of the Cooper pair box for different ratios $E_J/E_C$ , plotted as a function of the gate charge $n_g$ . As can be seen, for $E_J \gg E_C$ , the charge-dispersion curve becomes almost completely flat.	48
2.6	a) Schematic of a typical CQED circuit, consisting of a Transmon qubit capacitively coupled to a transmission line resonator. c) The equivalent circuit using a lumped-element model of the $\lambda/2$ resonator. . . . .	53
2.7	a) Circuit schematic of the CJBA, consisting of two parts of transmission line joined by a Josephson junction, forming a non-linear $\lambda/2$ resonator. b) Equivalent lumped elements circuit model of the CJBA. . . . .	55
2.8	a) Current in the driven non-linear resonator as a function of the drive detuning $\Omega$ , plotted for various drive powers $P_p$ . For drive detunings $\Omega > \Omega_c$ , the resonator becomes bistable above a certain power threshold $P_p > P_c$ . b) Phase diagram of the non-linear resonator, showing the regions of bistability as a function of the drive power $P_p$ and the drive detuning $\Omega$ . For $\Omega > \Omega_c$ , a bistable region exists that permits to operate the resonator as a CJBA. . . . .	57



## LIST OF FIGURES

3.1	Circuit schematic of the two-qubit processor . . . . .	65
3.2	.....	66
3.3	Single-qubit $\pi$ -pulse gate time, gate fidelity and AC stark detuning as a function of drive strength . . . . .	70
3.10	Optical and electron microscope photos of the two-qubit processor realized in this work. a) shows an optical image of the full processor with the two coupled qubits, fluxlines and readout resonator. b) shows an SEM image of an enlarged part of the central region of the chip with the two qubits and the coupling capacitor. c) Shows an SEM image of a single qubit junction loop. . . . .	82
4.2	The measurement setup used for the two-qubit experiments . . . . .	87
4.3	.....	89
4.5	a) Microwave pulse envelope used for exciting the CJBA during readout. The pulse consists of a measurement part with amplitude $h_m$ and a latching part with amplitude $h_l < h_m$ . To determine the state of the resonator during the latching interval, the phase of the reflected signal is measured in the time window $t_m$ . b) Distribution of the measured average $(I, Q)$ values in the IQ plane. The line $P$ that intersects the average quadratures $(I_0, Q_0)$ provides optimal separation between the two clusters corresponding to the state L and H of the resonator. c) Switching probability histograms corresponding to the distribution of the measured $(I, Q)$ values projected along the axis $\perp P$ . . . . .	93
4.6	Exemplary s-curve measurement for one of the qubits on the chip. Shown is the switching probability $p$ of the CJBA as a function of the readout signal power, plotted for different qubit states $ 0\rangle,  1\rangle$ and $ 2\rangle$ . The readout contrast between different states is given as the probability difference between the associated switching probability curves. Light and dark red arrows indicate the optimal working points for the $c_{01}$ and $c_{02}$ readout contrasts, respectively. . . . .	94
5.1	Spectroscopy of the Two-Qubit Processor . . . . .	102
5.2	Spectroscopic measurement of the avoided level crossing between the two qubits and their corresponding readout resonator . . . . .	103
5.3	A qubit parameter survey showing $T_1$ , readout contrast and Rabi frequency of the two qubits over a range of qubit frequencies . . . . .	104

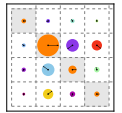
5.4 The measured readout matrix of our two-qubit processor. Shown are the conditional measurement probabilities $p_m(x y)$ where $x, y \in \{00, 01, 10, 11\}$ . The diagonal elements correspond to the readout fidelities of the four basis states. The single qubit readout fidelities as obtained from the matrix are $p_m^I(0 *  00) = 0.88$ , $p_m^I(1 *  10) = 0.85$ , $p_m^{II}(*0 00) = 0.9$ and $p_m^{II}(*1 01) = 0.85$ , the readout crosstalks are $p_m(0 *  00) - p_m(0 *  01) = -0.01$ , $p_m(1 *  10) - p_m(1 *  11) = -0.02$ , $p_m(*0 00) - p_m(*0 10) = 0$ and $p_m(*1 01) - p_m(*1 11) = -0.01$ . . . . .	105
5.5 Demonstration of single-qubit XY control . . . . .	106
5.6 Spectroscopic measurement of the avoided level crossing between the two qubits of our processor . . . . .	107
5.7 Pulse sequence used to create an entangled two-qubit state . . . . .	108
5.12 Reconstructed density matrices of experimentally created Bell states. Shown are the states $ \Psi_{\pm}\rangle = 1/\sqrt{2}( 01\rangle \pm  10\rangle)$ and $ \Phi_{\pm}\rangle = 1/\sqrt{2}( 00\rangle \pm  11\rangle)$ . The trace fidelities of the density matrices, $F_{tr} = \langle\psi \rho \psi\rangle$ range between 83 % and 87 %. . . . .	116
5.16 Experimental pulse sequence used for implementing the two-qubit $\sqrt{i\text{SWAP}}$ gate. The sequence shown for an exemplary input state $ 10\rangle$ consists in exciting the first qubit to the state $ 1\rangle$ , bringing the qubits in resonance for a time $t = 1/8g$ , separating them and compensating the acquired dynamical phases by using two single-qubit $Z$ -pulses. Finally, optional tomographic pulses are applied before reading out the qubit state at the optimal readout frequencies of the qubits. . . . .	121
5.17 The experimental input-output density matrices of the quantum process tomography of the $\sqrt{i\text{SWAP}}$ gate. Shown are the measured density matrices of 16 different input states and the corresponding output matrices with their state fidelities. The ideal matrices are overlaid in black. (part I/II) . . . . .	124
5.18 The experimental input-output density matrices of the quantum process tomography of the $\sqrt{i\text{SWAP}}$ gate. Shown are the measured density matrices of 16 different input states and the corresponding output matrices with their state fidelities. The ideal matrices are overlaid in black. (part II/II) . . . . .	125
5.19 The reconstructed $\chi$ matrix of our implementation of the $\sqrt{i\text{SWAP}}$ quantum gate. a) shows the lower half of the Hermitian matrix is shown. b) shows the product $\tilde{\chi} = \chi \cdot \chi_{id}^{-1}$ of the measured $\chi$ matrix and the ideal process matrix $\chi_{id}$ . The colored arrows connecting different elements of $\tilde{\chi}$ indicate unitary and non-unitary error processes to which the corresponding matrix elements can be associated. . . . .	126
5.20 Drive waveform $ \epsilon $ and qubit-qubit detuning $\Delta_q q$ used when simulating the iSWAP gate using a coupled three-level qubit master equation model. . . . .	128



5.21 Simulated state occupation probabilities for two different input states. a) corresponds to the input state $ 01\rangle$ to the $\sqrt{i\text{SWAP}}$ gate, b) to the input state $ 11\rangle$ . In both cases, a small excitation of the higher Transmon level $ 2\rangle$ can be observed in the simulation. For the $ 11\rangle$ input state, an oscillation between the states $ 11\rangle$ and $ 02\rangle/ 20\rangle$ can be observed, which is an unwanted effect. . . . .	129
6.1 A wavefunction $\psi(x)$ and potential $V(x)$ defined on a grid of points $x_1, \dots, x_N$ . . . . .	134
6.3 Full version of an ancilla-based implementation of the two-qubit Grover search algorithm . . . . .	139
6.4 Classical reversible implementation of a search algorithm on a two-bit input register. An exemplary Oracle function can be implemented using two single-bit NOT operations and a Toffoli gate. R designates the generation of a random binary value at the beginning of the algorithm. If the Oracle does not yield the correct answer, the test state is incremented. The average success probability of the algorithm is 50 %. . . . .	139
6.5 Schematic of our implementation of the Grover search algorithm . . . . .	140
6.6 Pulse sequence used for implementing Grovers search algorithm . . . . .	141
6.7 Quantum state tomographies at different steps during the Grover search algorithm and single-run outcome probabilities . . . . .	143
6.8 Single-run success probabilities of the Grover search algorithm . . . . .	144
6.10 Error model used for analyzing gate and decoherence errors for the Grover search algorithm . . . . .	147
6.11 . . . . .	150
A.1 . . . . .	157
A.2 . . . . .	158

*LIST OF FIGURES*

---

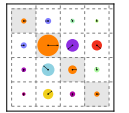


# List of Tables

6.1	Conditional probabilities $p_{ab}/ uv\rangle$ and user fidelities $f_{ab}$ for all possible outcomes $ab$ for our implementation of Grover's algorithm. . . . .	144
6.2	Fitted gate error parameters of the Grover algorithm . . . . .	149
6.3	Measured fidelities of the quantum Oracle and diffusion operators used in the Grover search algorithm . . . . .	149

*LIST OF TABLES*

---



# Chapter 1

## Introduction & Summary

### 1.1 Quantum Computing with Superconducting Circuits

This thesis presents experiments performed with a superconducting two-qubit quantum processor. The main goal of this work was to demonstrate a possible quantum computing architecture based on superconducting qubits that follows the canonical blueprint of a quantum processor as sketched in fig. 1.1, in accordance with the five criteria formulated by DiVincenzo [32]. By this definition, a universal quantum computer is a register of well-defined quantum bits (1) with long coherence times (2), on which one can implement any unitary evolution using a universal set of quantum gates (3), fitted with individual high fidelity readout of the qubits (4) and with the possibility to reset them to their ground state (5). Implementing this allegedly simple list of requirements in a system of superconducting qubits has been a major research challenge during the last decade, and is part of more general line of research on superconducting quantum circuits briefly summarized below.

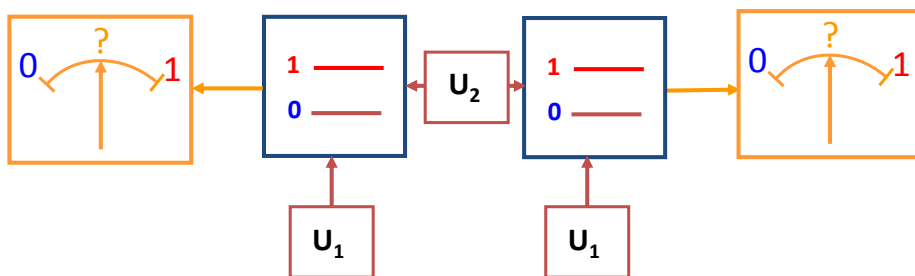


Figure 1.1: The blueprint of a “canonical” two-qubit quantum processor. The two qubits can be individually manipulated ( $U_1$ ) and a universal two-qubit gate  $U_2$  can be applied to them. Each of the qubits can be read out individually.

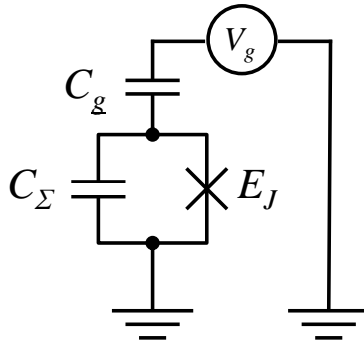
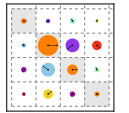


Figure 1.2: The schematic of the simple Cooper pair box (CPB) circuit, consisting of a capacitor in parallel with a Josephson junction capacitively coupled to a voltage source.

### 1.1.1 Context of this thesis work: 25 years of superconducting quantum circuits

The observation of quantum tunneling in a current-biased Josephson junction switching out of its zero-voltage state by Devoret *et. al.* [29, 66], first demonstrated that a collective electrical variable such as the superconducting phase difference across a Josephson junction (or the conjugated variable, i.e. the number of Cooper pairs that crossed it) can exhibit quantum properties. Then, the observation of microwave induced transitions between the quantum states of the junction by Martinis *et. al.* [66] further confirmed the quantum nature of this degree of freedom (See also [66, 67, 20]). A somewhat simpler quantum electrical circuit called the single Cooper Pair Box (CPB), made of a Josephson junction in series with a gate capacitor and a voltage source as shown in fig. 1.2, was later developed in the Quantronics group during the 1990s [13], and its ground state was characterized. With this electrical circuit, Nakamura *et. al.* [73] performed the first superconducting qubit experiment, demonstrating coherent oscillations between its ground and first excited eigenstates. Although the achieved coherence time was quite short, in the 5-10 ns range, this result attracted a huge interest and triggered the active development of research on superconducting quantum bits.

In the years after, several types of superconducting qubits were proposed using Josephson junctions in different configurations. Different regimes, in which the quantum state of the junctions ranges from almost Cooper pair number states to phase states, were realized. Let us cite here the flux qubit [71, 16] and the phase qubit [68], which were very successful qubits in many aspects. On the side of Cooper Pair Boxes, the Quantronics group contributed to the progress by operating a new circuit called the *Quantronium* (Vion *et. al.* [99]), fitted with a strategy for fighting dephasing due to the noise of the electrical control parameters, and with a single-shot readout (although with limited fidelity). The robustness of the quantronium arises from its operation at a so-called *sweet spot* where the qubit frequency is stationary in respect to variations in charge and phase control parameters. The improved coherence of the quantronium allowed to perform all the basic manipulations possible on spins and more generally on



two level systems [22]. Shortly after, another CPB design, inspired from cavity-QED, was developed at Yale by Wallraff *et. al.* [100]. In this so-called circuit-QED (CQED) design, the CPB, embedded in a microwave resonator, can be thought of as an artificial atom in a resonant cavity. The qubit readout is performed dispersively, i.e. through the cavity pull of the resonator frequency controlled by the qubit state. This small frequency change results in a small phase change of a resonant microwave pulse, which yields –after sufficient repetition– the probability of the two qubit states [12].

Another great bonus of CQED is that the electromagnetic environment in which the qubit relaxes its energy consists of a microwave resonator with a well-controlled impedance. The modern version of the Cooper Pair Box called *Transmon*, follows this design with an extra feature that makes it insensitive to the charge noise, that has always plagued single electron and single Cooper Pair devices. This feature consists in placing the Cooper Pair Box in the phase regime by adding an extra capacitance in parallel with the junction: the qubit frequency is then totally insensitive to the gate charge, and hence to the charge noise to all orders in charge, thus transforming the sweet spot into a “sweet line” in the charge-phase parameter space. This new design, that still leaves sufficient anharmonicity to operate the device as a qubit and allows to drive it, yielded a sizable improvement in coherence times, qubit robustness and usability. The CQED concept was thus rapidly extended to flux and phase qubits [47].

In 2010, a new type of CQED architecture has been developed by Paik *et. al.* [78] that combines Transmon qubits with 3D cavities instead of CPW resonators, resulting again in an impressive increase of qubit coherence times by a large factor, with reported qubit relaxation times approaching  $100\ \mu\text{s}$  and dephasing times of the same order. Very recently, these drastically improved coherence times have made possible the realization of elemental quantum feedback and error correction schemes with these systems [98].

The progress achieved during the last decade on the Cooper Pair Box and on the phase qubits has benefited to quantum processors. So far, superconducting CQED processors with up to three qubits have been realized and two- and three-qubit quantum gates [37], multi-qubit entanglement [31, 2] and simple quantum algorithms [30, 64] as well as quantum error correction [84] have recently been demonstrated.

### 1.1.2 This Thesis Work

At the beginning of this thesis work, CQED processors having demonstrated quantum algorithms did not comply with the rules established by DiVincenzo [32]. In other words, they did not follow the canonical blueprint able to demonstrate quantum speed-up: they were all fitted with a joint readout, which allows to measure the average value of a collective variable of the qubit register, but not each qubit individually. By repeating a given

sequence of gates a large number of times, one can nevertheless determine the quantum state of the qubit register at different steps of the algorithm being run. Since the whole interest of quantum computing is precisely to perform computational tasks more efficiently than with a classical processor, it was essential, in our mind, to demonstrate the quantum speed-up expected from quantum algorithms with a CQED quantum processor fitted with an individual single shot and non-demolishing (QND) readout for each qubit. Such a high fidelity single-shot readout had been developed for a single transmon during a previous thesis in the Quantronics group [63, 79], and it was natural to use it in the present work.

This thesis discusses therefore the realization of a superconducting two-qubit processor based on Transmon qubits, fitted with individual single-shot readouts. In chapter 2, we present the theoretical building blocks of this work. Chapter 3 outlines the design of the two-qubit processor, whereas chapter 4 presents the most relevant measurement techniques used here. With the two-qubit processor, we implement elementary one- and two-qubit quantum operations, as detailed in chapter 5. We use it to run a simple quantum algorithm that demonstrates probabilistic quantum speed-up: the Grover search algorithm, as explained in chapter 6. Finally, we discuss in chapter ?? the design of a four-qubit quantum processor using a more scalable approach that could possibly be extended to an even larger number of qubits.

Note that during this thesis work, quantum speed-up was also demonstrated for the Deutsch-Josza algorithm with a phase qubit processor using individual single-shot and destructive readouts [103].

## 1.2 Realizing a Two-Qubit Quantum Processor

The quantum processor implemented in this work is shown in fig. 1.3. It consists of two superconducting quantum bits of the Transmon type, each equipped with its own drive and readout circuit. In order to obtain a high fidelity single-shot readout of the qubit register, we use the Cavity Josephson Bifurcation Amplifier (CJBA) readout method, which is based on the Josephson Bifurcation Amplifier (JBA) readout first developed in the team of Michel Devoret at Yale for the quantronium qubit [91, 97, 90]. This method had indeed already been successfully adapted to the transmon, and yielded a 93 % readout fidelity [63].

Each qubit can be manipulated by driving it with microwave pulses through its readout resonator, allowing robust and fast single-qubit operations. The qubit frequencies can be tuned individually using fast flux lines, allowing us to change the frequency of each qubit over a range of several GHz. The coupling between the two qubits is realized through a fixed capacitance that connects the two top-electrodes of the Transmons

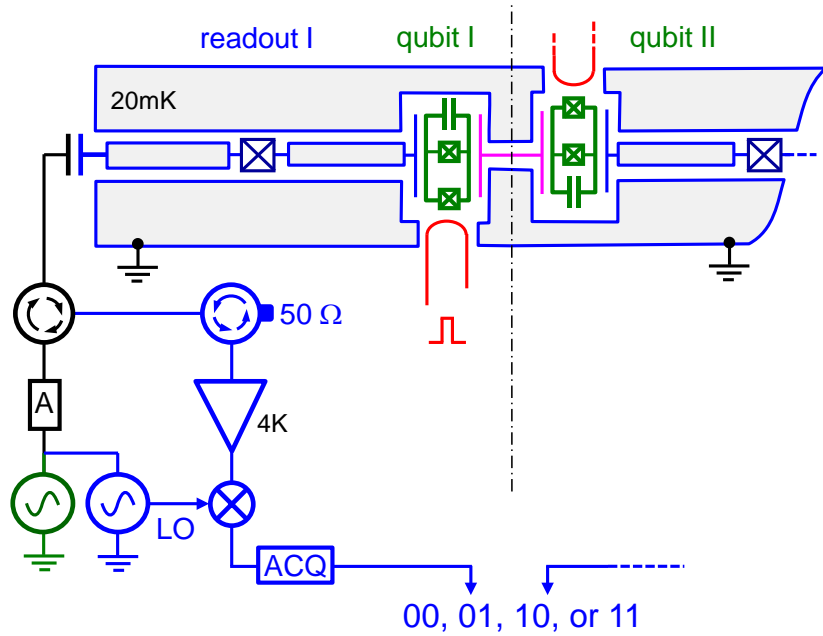
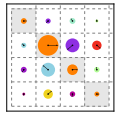


Figure 1.3: Circuit schematic of the two-qubit processor realized in this thesis work, showing the two qubits (in green) coupled by a fixed capacitor (in purple), as well as the fast flux lines (in red) used to tune the qubit frequencies and the qubit readouts (in blue). Each qubit is embedded in its own nonlinear readout resonator and can be driven and read out by microwave reflectometry through an individual microwave line.

and implements a fixed  $\sigma_{xx}$ -type qubit-qubit coupling. This coupling allows us to generate entangled two-qubit states and to implement a two-qubit gate. We use this simple processor to generate entangled two-qubit states, test the Bell inequality, implement a universal two-qubit gate and perform a simple quantum algorithm that demonstrates quantum speed-up, as discussed in the following sections.

### 1.3 Demonstrating Simultaneous Single-Shot Readout

For readout, each qubit is capacitively coupled to a coplanar waveguide resonator made nonlinear by placing a Josephson junction in its central conductor. We exploit the frequency pull of the bifurcation transition that occurs in this resonator when driven at a suitable frequency and power to map the qubit states on the bifurcated and non bifurcated cavity states, which are then discriminated by reflectometry. Here, the hysteretic character of the bifurcation transition allows to reduce the measuring power, to latch the cavity state, and to measure it without being affected by subsequent qubit relaxation. The state of the resonator can thus be determined reliably without being limited by qubit relaxation, thereby providing a high-fidelity single-shot qubit readout. Contrary to previous CQED processors, our processor is fitted with individual readouts, and a

### 1.3. DEMONSTRATING SIMULTANEOUS SINGLE-SHOT READOUT

---

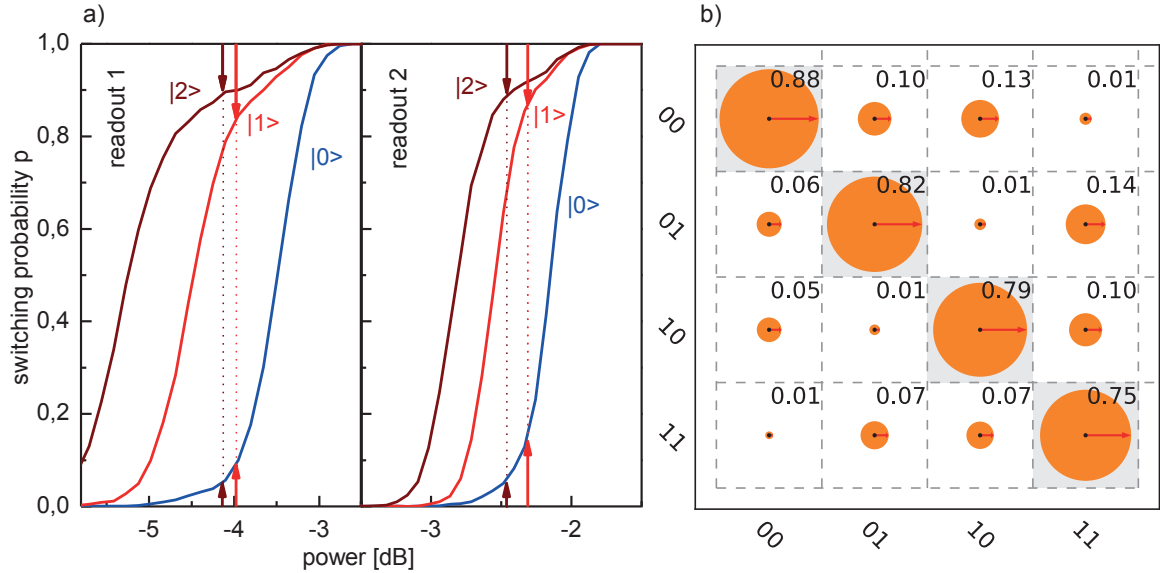
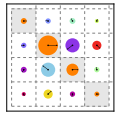


Figure 1.4: a) Switching probabilities of the two readout resonators as a function of the readout drive power at a fixed driving frequency. The measurement is performed after preparing the qubits in the states  $|0\rangle$ ,  $|1\rangle$  and  $|2\rangle$ . The readout contrast is given as the difference in probability between the curves corresponding to the states  $|0\rangle$  and  $|1\rangle$  or  $|2\rangle$ , respectively. The highest contrasts of 88 and 89 % are achieved when the qubit is shelved from state  $|1\rangle$  to  $|2\rangle$ . b) Readout matrix of the two-qubit system, giving the probabilities to obtain the different outcomes  $ij$  after having prepared the register in the different computational basis states  $|kl\rangle$ .

simultaneous readout of the full two-qubit register is possible, as requested by the Di-Vincenzo criteria. For a single-qubit CJBA readout, fidelities up to 93 % have been achieved [63] by shelving the first excited state of the transmon  $|1\rangle$  to the higher excited state  $|2\rangle$ . However, due to the higher complexity and design constraints of our system, only 83-89 % fidelity has been achieved for the processor presented here. The full characterization of the readout of our processor is shown in fig. 1.4. Panel a shows the switching probabilities of each individual readout as a function of the drive amplitude, measured at a fixed drive frequency. Individual curves correspond to the qubit being prepared (or shelved) in different states  $|0\rangle$ ,  $|1\rangle$  or  $|2\rangle$ , the difference between either two curves giving the readout contrast between those qubit states. Shelving the qubit from state  $|1\rangle$  to state  $|2\rangle$  before readout can increase the readout fidelity by more than 10 % and is therefore often used in the experiments presented in this thesis. Panel b shows the full readout matrix of the two-qubit register that relates measured readout switching probabilities with real qubit state occupation probabilities and allows us to correct readout errors when performing quantum state tomography. In chapter 5 we discuss all relevant readout fidelities and errors in detail and analyze different error sources limiting the readout performance in our experiments.



## 1.4 Generating and Characterizing Entanglement

The capacitive coupling between the two qubits provides a  $\sigma_{xx}$ -type interaction that can be used to generate entangled two-qubit states. Conveniently, this coupling is only effective when the qubit frequencies are near-resonant and can therefore be effectively switched on and off by tuning the qubit frequencies in and out of resonance. For the processor realized in this work, the effective coupling constant  $g$  of the two qubits has been measured as  $2g/2\pi = 8.2$  MHz. When the two qubits are in resonance, the effective evolution operator of the two-qubit system is:

$$U(t) = \begin{pmatrix} 1 & 0 & 0 & 0 \\ 0 & \cos 2\pi t g & i \sin 2\pi t g & 0 \\ 0 & i \sin 2\pi t g & \cos 2\pi t g & 0 \\ 0 & 0 & 0 & 1 \end{pmatrix}_{\{|00\rangle, |01\rangle, |10\rangle, |11\rangle\}} \quad (1.1)$$

in the two-qubit basis  $\{|00\rangle, |01\rangle, |10\rangle, |11\rangle\}$ . By using fast flux pulses to non-adiabatically tune the qubits in and out of resonance, we can switch on this interaction for a well-defined time. We first characterize the effect of the coupling on the qubit register by preparing the state  $|10\rangle$ , tuning the qubits in resonance for a given time and measuring the qubit state afterward. The resulting curve is shown in fig. 1.5a and shows swapping oscillations between the two qubits. Analyzing this curve allows us to extract the effective coupling strength between them. Leaving the interaction between the qubits on for a well-defined time allows us to generate entangled Bell states that we characterize by performing quantum state tomography. The experimental reconstruction of the density matrix of such a Bell-state of the type  $|\psi\rangle = (|01\rangle + i|10\rangle)/\sqrt{2}$  is shown in fig. 1.5b. The measured fidelity of the prepared state of 91 % and the concurrence of 85 % confirm that entanglement is present in the system. We also characterize the entanglement between the two qubits by measuring the average value of the so-called *Clauser-Horne-Shimony-Holt* operator (CHSH) [21], which combines measurements of the state of the two qubits along different axes on the Bloch sphere and provides a test that can distinguish between classical correlations and quantum entanglement in a two-qubit system.

For classical states, the maximum value of the CHSH operator is bound by 2 but for entangled states it can reach a maximum of  $2\sqrt{2}$ . Figure 1.6 shows the result of such a CHSH-type measurement performed on a state created by the method described above, showing the value of  $\langle \text{CHSH} \rangle$  as a function of the angle  $\phi$  of the measurement basis. We observe a violation of the classical boundary 2 of the operator by 22 standard deviations when correcting the readout errors that are present in our system. The raw, uncorrected data fails to exceed the classical threshold because of readout errors mainly caused by qubit relaxation during the readout. Nevertheless, the observed violation in

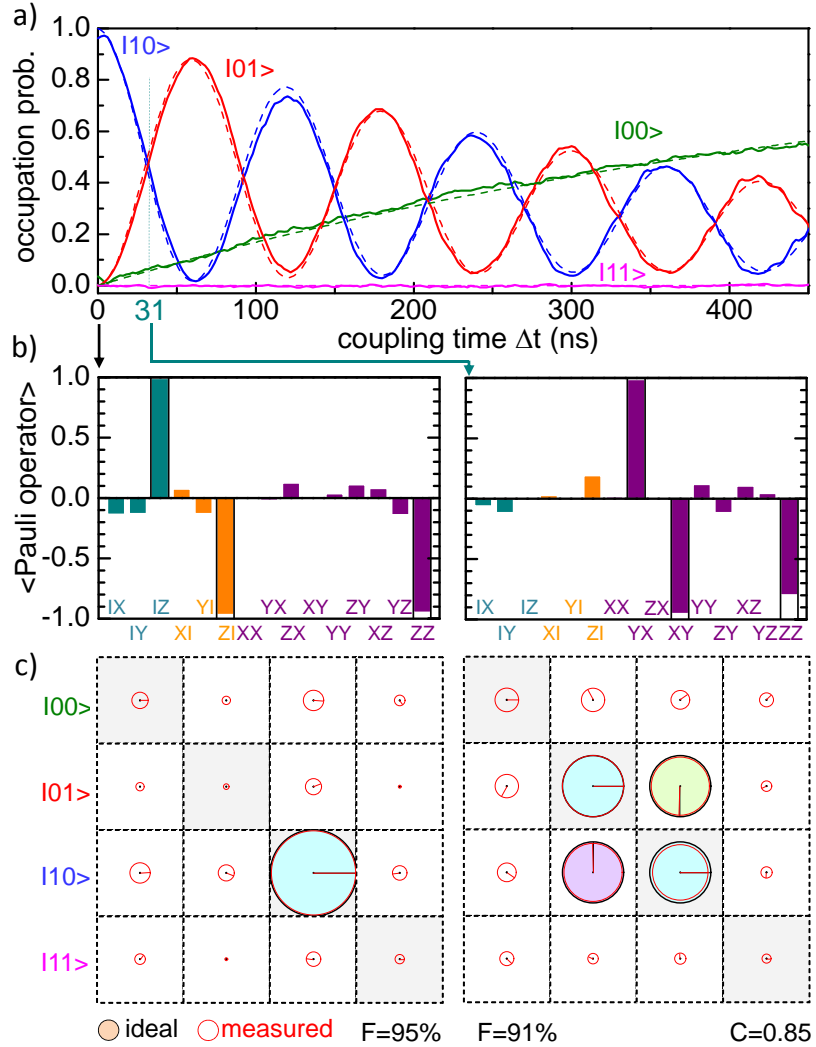


Figure 1.5: Coherent exchange of a single quantum of excitation (swapping oscillations) between the two qubits initially prepared the register state  $|10\rangle$ , obtained from the resonant interaction between them. a) Register state probabilities as a function of the swapping time  $\Delta t$ . The frequency of the oscillations corresponds to  $2g/2\pi = 8.7$  MHz. b) Measured average values of the Pauli operators products  $\{I, \sigma_x, \sigma_y, \sigma_z\} \otimes \{I, \sigma_x, \sigma_y, \sigma_z\}$  (Pauli set) for the register states obtained at times 0 ns and 31 ns. c) Corresponding reconstructed density matrices. The area of each circle corresponds to the absolute value of each matrix element and the color and direction of the arrow to the phase of the element. The black circles correspond to the density matrices of the ideal states  $|10\rangle$  and  $(|10\rangle + i|01\rangle)/\sqrt{2}$ , respectively.

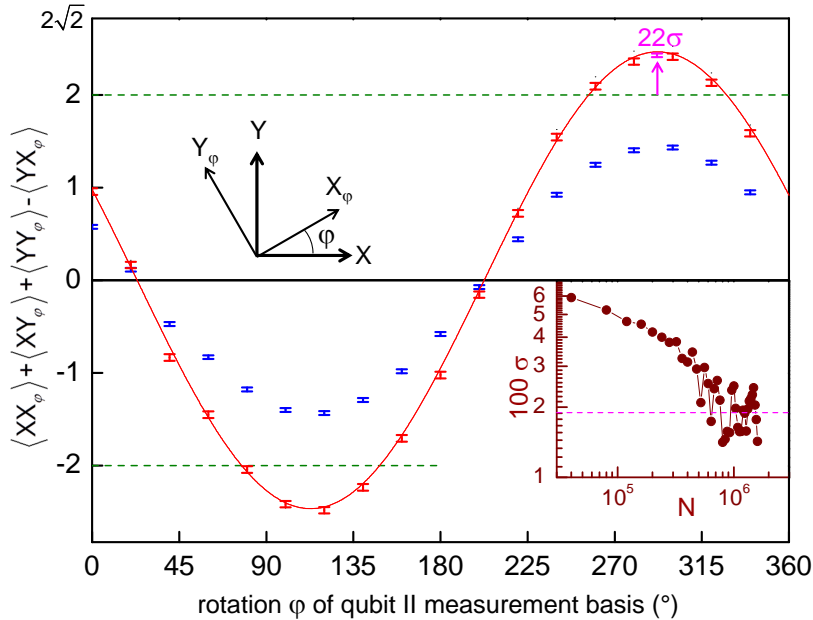
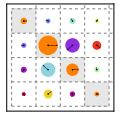


Figure 1.6: Measured average value of CHSH operator for a prepared Bell state. After readout error corrections, the CHSH expectation value (red points) exceeds the classical boundary of 2. The raw measurement data (blue points) lies below this critical threshold. The inset shows the standard deviation  $\sigma$  at the highest point of the curve as a function of the measurement sample size. For the highest sample count, the classical boundary is exceeded by 22 standard deviations.

the calibrated data is a strong indication of entanglement in the system. A more detailed overview of this experiment can be found in chapter 5.

## 1.5 Realizing a Universal Two-Qubit Quantum Gate

The swapping evolution given by eq. (1.1) allows not only to prepare entangled two-qubit states but also to implement a universal two-qubit gate: When switching on the interaction for a time  $t_{\pi/2} = 1/8g$  one realizes the so-called  $\sqrt{i\text{SWAP}}$  gate, represented by the evolution operator

$$U(t) = \begin{pmatrix} 1 & 0 & 0 & 0 \\ 0 & 1/\sqrt{2} & i/\sqrt{2} & 0 \\ 0 & i/\sqrt{2} & 1/\sqrt{2} & 0 \\ 0 & 0 & 0 & 1 \end{pmatrix}_{\{|00\rangle, |01\rangle, |10\rangle, |11\rangle\}} \quad (1.2)$$

which forms together with single qubit gates a universal set of gates, on which any algorithm can be decomposed. We characterize the operation and errors of our implementation of this gate by performing quantum process tomography, obtaining a gate fidelity of 90 %. The 10 % error in gate fidelity is caused mainly by qubit relaxation and

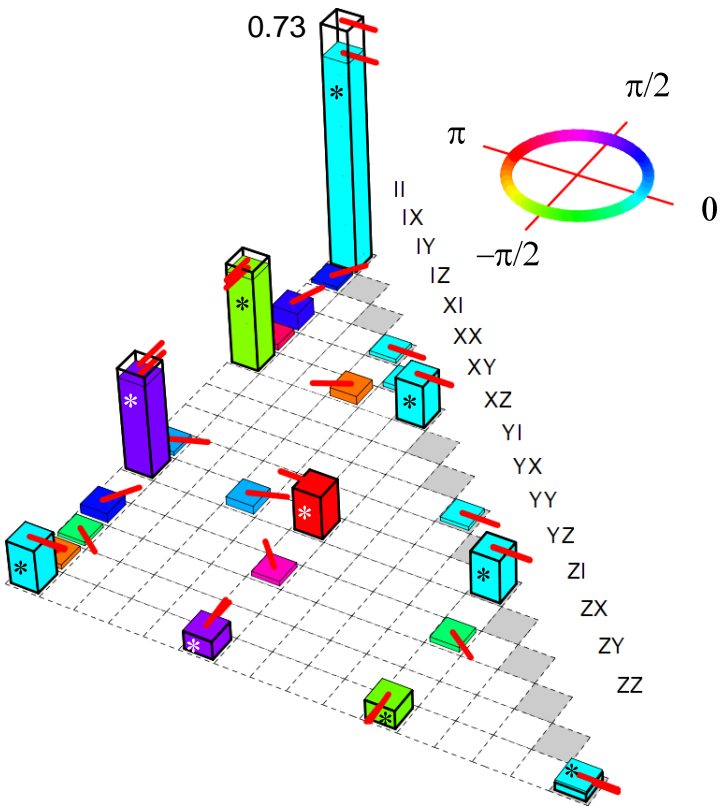
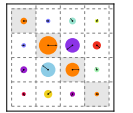


Figure 1.7: Measured  $\chi$ -matrix of the implemented  $\sqrt{i}$ SWAP gate. The row labels correspond to the indices of the  $E_i$  Pauli operators, the height of each bar to the absolute value of the corresponding matrix element, and the color and red arrow direction to the argument of the element. The ideal  $\chi$ -matrix of the  $i\sqrt{2}$ SWAP gate is given by the outlined bars. The upper half of the positive-hermitian matrix is not shown.

dephasing during the gate operation and only marginally by deterministic preparation errors, as will be discussed in chapter 5. Figure 1.7 shows the measured  $\chi$  matrix of the gate, that describes its effect in the Pauli basis of two-qubit operators. The  $\chi$  matrix provides the full information on the unitary and non-unitary action of the gate. The achieved fidelity of the gate operation is sufficient to allow the implementation of simple quantum algorithms with our processor.

## 1.6 Running a Quantum Search Algorithm

Using a two-qubit quantum gate related to the one described above, we run a simple quantum algorithm on our processor, the so called *Grover search algorithm* [44]. The version of this algorithm that we implement operates on the two-qubit basis  $x_i \in \{|00\rangle, |01\rangle, |10\rangle, |11\rangle\}$  and can distinguish between four different *Oracle functions*  $C_j(x)$  with  $x \in x_i$  that give  $C_j(x = x_j) = 1$  and  $C_j(x \neq x_j) = 0$ . In the two-qubit case, this algorithm requires only one evaluation of the Oracle function  $C_j(x)$ , implemented as a unitary operator, to determine which state among the four possible ones it tags. This case thus provides a simple benchmark of the operation of the quantum processor, and a simple and illustrative example of quantum speed-up in comparison with classical algorithms, as discussed in chapter 6. The diagram of the Grover search algorithm implemented



in our processor is shown in fig. 1.8a and involves two *iSWAP* gate operations and six single-qubit operations along with a single-shot qubit readout at the end of the algorithm. We measure the success probability of the algorithm from the obtained outcomes, and complete the analysis of its operation by performing the tomography of the quantum state at different steps of the algorithm. We first discuss this evolution that sheds light on how quantum speed-up is achieved.

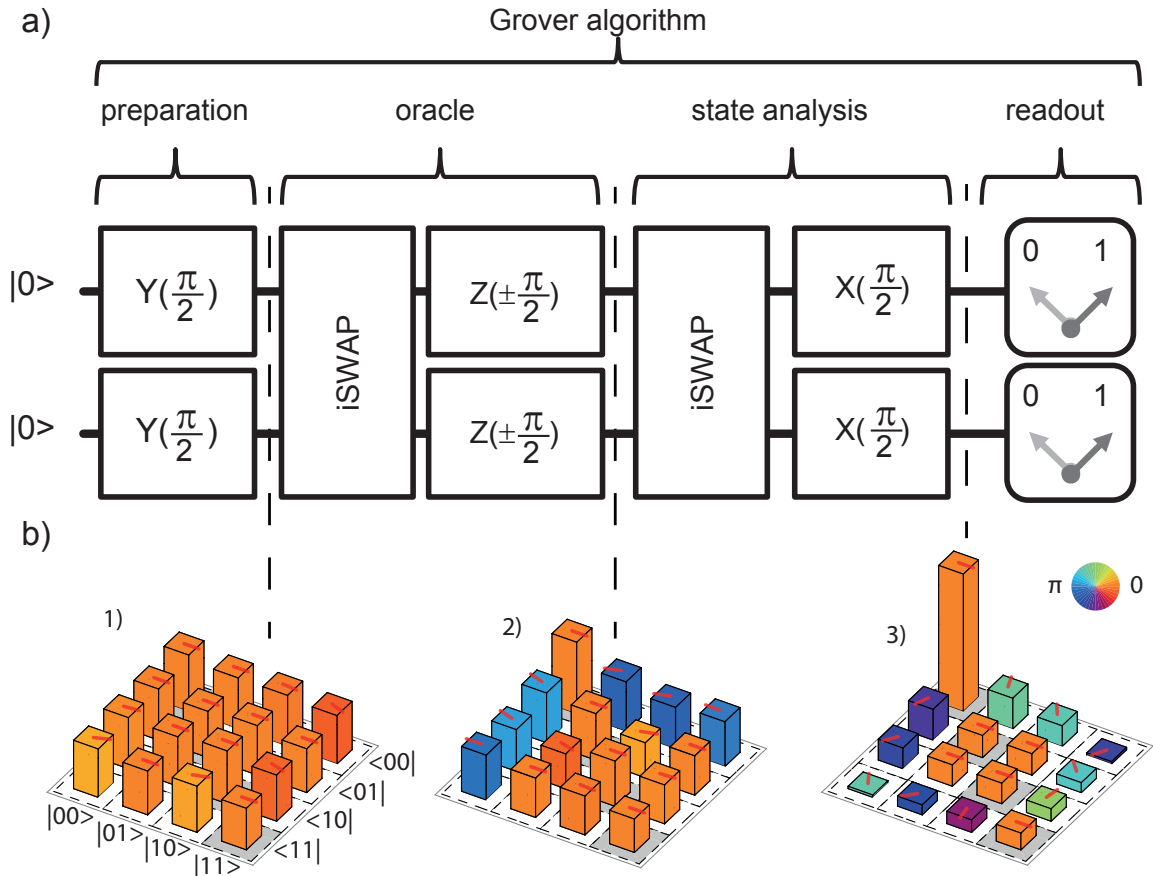


Figure 1.8: a) A two-qubit version of the Grover search algorithm that we implemented on our quantum processor. The algorithm consists in preparing a fully superposed state, applying a given Oracle operator to it only once, and analyzing the resulting output to determine the quantum state tagged by this Oracle operator. b) Measured density matrices when running the Grover search algorithm with a search oracle marking the state  $|00\rangle$ . 1) shows the state after the generalized Hadamard transform, 2) after applying the quantum oracle and 3) after the final step of the algorithm.

Fig. 1.8b shows the density matrices determined experimentally when running the Grover search algorithm with the Oracle operator tagging the state  $|00\rangle$ . State tomography is first shown after preparation with a generalized Hadamard transform applied to the initial state  $|00\rangle$ . It clearly corresponds to a superposition of all the computational basis states. The quantum state after having applied the quantum Oracle is  $-|00\rangle + |01\rangle + |10\rangle + |11\rangle$  and the information on the tagged state is encoded in the

phase of the state  $|00\rangle$ . After extracting this phase information, the tomography displays a large peak on state  $|00\rangle$  at the end of the algorithm, just as expected. The fidelity of the final quantum state of the algorithm is 68%, 61%, 64% and 65% for the four different Oracle operators, respectively. These fidelities, corrected for readout errors, do not quantify the quantum speed-up achieved when running the algorithm. For this, it is necessary to analyze the results obtained after a single run, which does not allow for any corrections of the readout outcomes.

## 1.7 Demonstrating Quantum Speed-Up

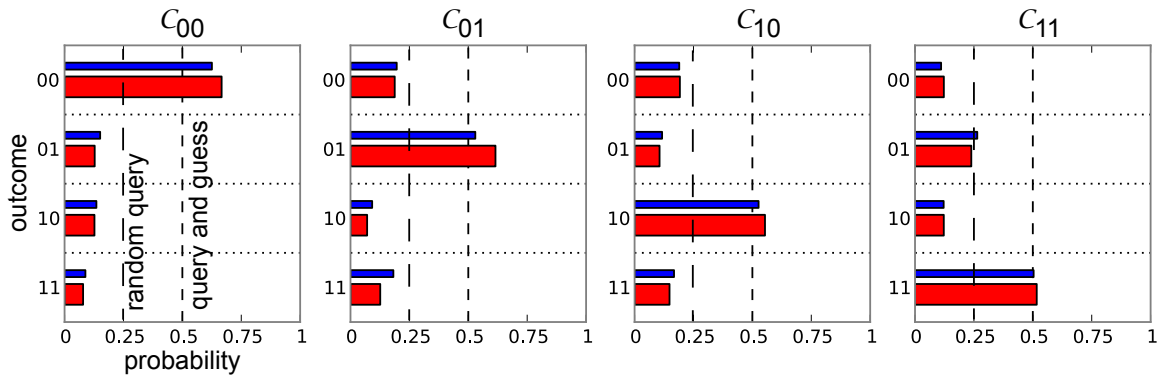
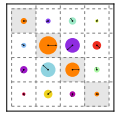


Figure 1.9: Single-run results when running the Grover search algorithm on our two-qubit quantum processor. Shown are the probabilities of measuring the qubit register in state  $|i\rangle$  for an Oracle function  $\mathcal{C}_j$  marking the state  $|j\rangle$  provided to the algorithm. In all four cases, the success probability of the algorithm is  $> 50\%$ , thus outperforming any classical “random query” or “query and guess” algorithm using a single Oracle call.

The main interest of running a quantum algorithm is to obtain an advantage in the run-time in comparison to a classical algorithm, the so-called *quantum speed-up*. To characterize this speed-up as obtained with our processor, we run the Grover algorithm for all four possible Oracle functions and directly read out the state of the qubit register after the last step of the algorithm instead of performing quantum state tomography, thus not correcting any readout errors. By averaging the outcomes of many such individual runs with different Oracle functions we obtain the so-called *single-run fidelities*, which – for the four different Oracle functions – have been measured as 66%, 55%, 61% and 52%. The full probability distributions for the four possible cases are shown in fig. 1.9. The achieved success probability is always lower than the theoretically possible value of 100 %, mainly because of relaxation and decoherence of the qubit state during the run time of the algorithm and –to a small degree– errors in the pulse sequence. The measured success probabilities are however larger than the 50% success probability of a classical query-and-guess algorithm using the outcome of a single query. The algorithm thus



demonstrates quantum speed-up, as explained in greater detail in chapter 6.

## 1.8 Towards a Scalable Multi-Qubit Architecture

The approach to superconducting quantum computing outlined in the previous sections is well suited for the implementation of simple quantum processors with a few qubits. However, due to several design limitations it is not suitable for implementing a large scale quantum computer. As an example, the direct qubit-qubit coupling employed in this thesis work is not suitable for coupling a large number of qubits since it becomes increasingly difficult to deterministically switch on and off the coupling between individual qubits as the number of qubits increases, a problem sometimes referred to as “frequency crowding”. Also, fitting each qubit of the processor with individual drive and readout circuitry –as done in this work– is usually not extensible to a large number of qubits due to topological and space constraints on the chip, as well as financial and practical constraints for a cryogenic experimental setup.

Recently, several research groups have started to address these issues by devising new architectures for superconducting quantum processors that can –in theory– be scaled to a larger number of qubits. Here we will mention only the so-called “Rez-Qu” architecture [41] and the surface-code approach [33] pursued e.g. by IBM. In this thesis work we discuss our own approach towards more scalable superconducting quantum processors, where we have developed a revised version of our qubit chip that provides a way to implement a system with a larger –albeit still small– number of qubits. Key elements of this architecture are a quantum bus in form of a high-Q microwave resonator that is used for coupling the qubits and a multiplexed drive and readout circuit that allows us to measure and manipulate all qubits through one single microwave transmission line.

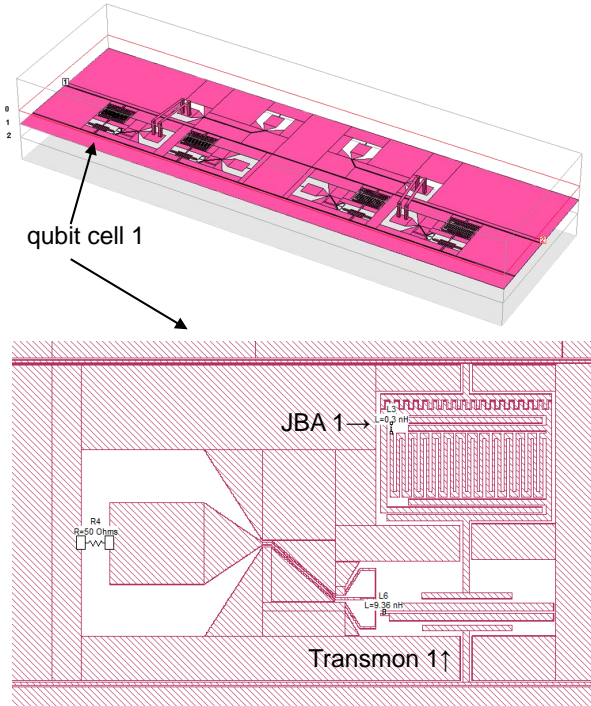


Figure 1.10: Schematic of the four-qubit chip realized in this thesis work. Shown on top is the whole chip with connectors for the drive and readout transmission line and for the four fast flux lines. Below we show a single qubit cell with a Transmon qubit coupled to the quantum bus, a flux line and a JBA readout.

Figure 1.10 shows the schematic of the first version of this architecture. Our chip contains four Transmon qubits which are capacitively coupled to a distributed high-Q resonator acting as a quantum bus. In addition, each qubit is coupled to a low-Q non-linear lumped element resonator acting as a CJBA, which is used for reading out the qubit state. Each of these resonators is in turn coupled capacitively to the input transmission line. The resonance frequencies of the readout resonators are arranged in ascending order with a frequency spacing of  $\approx 50$  MHz between adjacent resonators. This frequency spacing allows us to address each resonator individually and to read out the state of the full qubit register in parallel using only one single transmission line. Figure 1.11 shows the measured  $|S_{12}|$  matrix element of such a chip with four CJBA resonators at frequencies between 6.78 GHz and 6.95 GHz, plotted as a function of the incident microwave power.

The “knee” in each of the four resonance curves appearing between -45 and -40 dBm corresponds to the bifurcation point of the resonators. Still, this approach suffers from a relatively bad ON/OFF ratio in the qubit-qubit coupling. To alleviate this problem, the Transmon qubit used in the current version of this architecture can be replaced by a qubit with a tunable coupling [94]. Alternatively, it is possible to use a fixed-frequency coupling scheme for the qubits, thereby altogether eliminating the need for frequency tuning of individual qubits and also reducing the number of input transmission lines from  $n + 1$  to 1, with  $n$  the number of qubits.

A more detailed discussion of the scalable architecture and the first preliminary measurements performed with a four-qubit chip are presented in chapter 7 of this thesis.

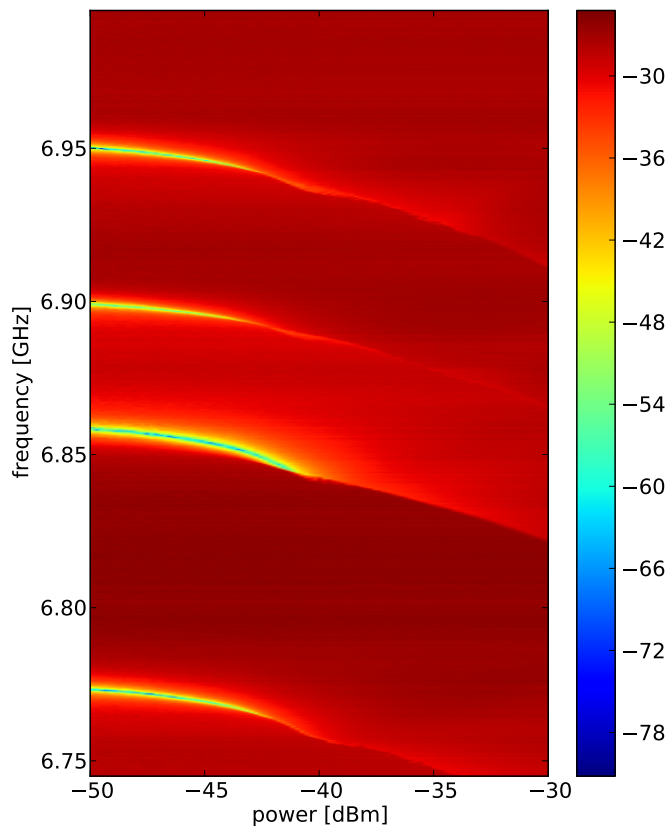
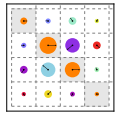


Figure 1.11: The measured  $|S_{12}|$  transmission coefficient for the input transmission line of our four-qubit chip. Clearly visible are four resonances of the CJBA resonators and the bifurcation of each resonator at high input power.



# Chapter 2

## Theoretical Foundations

In this chapter we provide the reader with the minimal conceptual background and theoretical building blocks necessary to understand our thesis work. We begin our discussion with a general overview of classical and quantum information processing with a Turing machine, followed by an introduction to superconducting quantum circuits. We summarize the method to quantize electrical circuits and apply it to Cooper pair box devices, and in particular to the Transmon that will be used to implement the qubit register of our quantum processor. We then present coplanar waveguide resonators, and introduce circuit quantum electrodynamics on the example of a transmon coupled to a such a resonator. Finally, we consider the case of a nonlinear resonator used as a Josephson bifurcation amplifier since we use such a readout device in our processor architecture.

### 2.1 Classical & Quantum Information Processing

By definition, computing designates the activity of using computer hardware and software to process information, or *data*. Classical information processing can be divided in so-called *analog and digital information processing*, the former being based on continuous physical variables whereas the latter is based on discrete variables. The fundamental unit of digital information processing is the so-called *bit*, which represents a Boolean (true/false) information. The discipline of theoretical computer science has been created to investigate the fundamental limits and properties of classical information processing. One of the main foundational theorems of theoretical computer science is the so-called *Church-Turing thesis* which provides a universal computing model by saying (basically) that everything which is computable can be efficiently computed using a *Turing machine*. Such a Turing machine, in turn, is a simple theoretical device which is able to run programs that operate on a discrete set of data using a well-specified set of operations. The Turing machine is universal in the sense that any other classical computing device can be efficiently emulated using a Turing machine with the appropriate

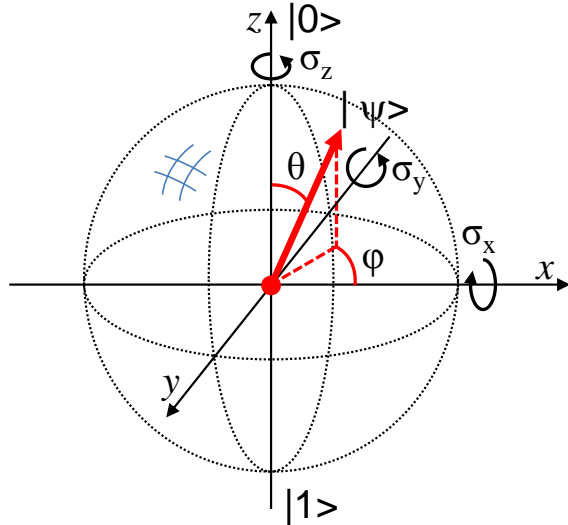


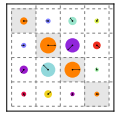
Figure 2.1: The Bloch sphere representation of a qubit state  $|\psi\rangle = \cos \frac{\theta}{2} |0\rangle + e^{i\phi} \sin \frac{\theta}{2} |1\rangle$ . The state  $|\psi\rangle$  is fully characterized by specifying its “latitude” and “azimuth” angles  $\theta$  and  $\phi$ . Pure quantum states will always lie on the surface of the Bloch sphere, whereas mixed quantum states can also lie anywhere inside the sphere.

program and data.

In the early 1980s, Richard Feynman showed that a classical Turing machine as described above would be unable to efficiently simulate a quantum-mechanical system [38]. He introduced the concept of a *quantum Turing machine* that would be able to simulate quantum-mechanical systems in an efficient manner. A few years later, David Deutsch took up Feynman’s idea and developed an information processing framework based on quantum mechanics [27], coining the terms *quantum computing* and *quantum information processing*. He showed that by making use of different properties of quantum mechanics, namely, the superposition principle and entanglement, one could solve certain mathematical problems faster than possible with any classical computer [27]. The work by Deutsch created a large interest in the physics community and led to a huge theoretical and experimental effort aimed at realizing an operational quantum computer and developing quantum algorithms for relevant real-world problems.

## 2.2 Principles of "Conventional" Quantum Computing

The first scheme imagined for quantum information processing is directly inspired from the classical digital Turing machine: information is stored in a set of quantum two level systems, the *quantum bits* or *qubits*, forming a quantum register, which is manipulated by sequentially applying unitary (and possibly non-unitary) operators to subsets of qubits in the register, typically one or two. As for a classical Turing machine, any arbitrary operation of this quantum processor can be decomposed as a sequence of gate operations chosen from a surprisingly small set of gates, said universal. The power of such a machine comes from the gates operating on superposed states, which provides an intrinsic parallelism in the processing. This *quantum gate* approach is the method relevant to



the present thesis work, and we ignore other approaches introduced more recently such as *one-way quantum computing* [83], *adiabatic quantum computing* [36] or *topological quantum computing* [52]. In this section we introduce very briefly quantum bits and quantum gates, as well as some examples of quantum algorithms that are relevant to this work.

### 2.2.1 Quantum Bits and registers

As in classical computing, one can define in quantum computing a fundamental unit of information: the qubit. Such a qubit is a quantum-mechanical two-level system that can be put in any superposition

$$|\psi\rangle = \cos \frac{\theta}{2} |0\rangle + e^{i\phi} \sin \frac{\theta}{2} |1\rangle \quad (2.1)$$

of its two states  $|0\rangle$  and  $|1\rangle$ . As can be seen, any state can be described by a pair of real numbers  $\theta$  and  $\phi$  that characterize the amplitude of each of the two basis states and the phase between them. A useful and intuitive representation of such a single-qubit state is the so-called *Bloch sphere representation*, shown in fig. 2.1. The north and south poles of this sphere correspond by convention to the qubit states  $|0\rangle$  and  $|1\rangle$  (or vice versa). All states lying on the sphere between those two correspond to pure superposition states, which are characterized by their “latitude” and “azimuth” angles  $\theta$  and  $\phi$ .

Often it is necessary to describe the qubit not as being in one well-defined pure state but rather being in one of several such states  $|\psi_i\rangle$ . Usually, we can then associate a classical probability  $p_i$  with finding the qubit in either of these states. In this case, we can then describe the qubit by a density matrix  $\rho = \sum_i p_i \rho_i$ , where  $\rho_i = |\psi_i\rangle \langle \psi_i|$  is the density matrix of the pure state  $|\psi_i\rangle$ . All single-qubit density matrices  $\rho$  are Hermitian  $2 \times 2$  matrices with non-negative eigenvalues and can thus be written as

$$\rho = \begin{pmatrix} \rho_{00} & \rho_{01} \\ \rho_{01}^* & \rho_{11} \end{pmatrix} \quad (2.2)$$

in the  $|0\rangle, |1\rangle$  basis, with  $\rho_{00}$  and  $\rho_{11}$  being real numbers and  $\rho_{01}$  a complex number. For any state, the matrix has a unity trace  $\text{Tr}(\rho) = 1$ , for pure states,  $\rho = \rho^2$  in addition. The expectation value  $\langle A \rangle$  of any operator  $A$  acting on the density matrix  $\rho$  is given as  $\text{Tr}(\rho A)$ .

A mixed single-qubit state  $\rho$  can also be represented as a 3D vector lying in the so-called *Bloch sphere*. For this, we decompose the density matrix of the state as  $\rho = c_i \sigma_I + c_x \sigma_x + c_y \sigma_y + c_z \sigma_z$ , where  $c_{i,x,y,z}$  are real coefficients and the identity matrix

$\sigma_I$  and Pauli matrices  $\sigma_x, \sigma_y, \sigma_z$  are given as

$$\sigma_I = \begin{pmatrix} 1 & 0 \\ 0 & 1 \end{pmatrix} \quad \sigma_x = \begin{pmatrix} 0 & 1 \\ 1 & 0 \end{pmatrix} \quad \sigma_y = \begin{pmatrix} 0 & -i \\ i & 0 \end{pmatrix} \quad \sigma_z = \begin{pmatrix} 1 & 0 \\ 0 & -1 \end{pmatrix}. \quad (2.3)$$

We can then plot the vector  $(c_x, c_y, c_z)$  in a 3D space. The length of it decreases from 1 for a pure state down to 0 for a completely mixed state, hence it will always lie inside a unity sphere.

Quantum states of  $n > 1$  qubits cannot be described graphically in an easy way but can be characterized by a density matrix of dimension  $2^n \otimes 2^n$  in the computational basis  $|q_1 \dots q_n\rangle = |q_1\rangle \otimes |q_2\rangle \dots \otimes |q_n\rangle$ , where  $|q_i\rangle$  is the state vector of the  $i$ -th qubit. For example, a two-qubit Bell state of the form  $|\psi_+\rangle = (|01\rangle + |10\rangle)/\sqrt{2}$  can be written as

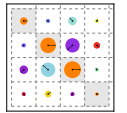
$$\rho_{\psi_+} = \frac{1}{2} \begin{pmatrix} 0 & 0 & 0 & 0 \\ 0 & 1 & 1 & 0 \\ 0 & 1 & 1 & 0 \\ 0 & 0 & 0 & 0 \end{pmatrix}_{(|00\rangle, |01\rangle, |10\rangle, |11\rangle)} \quad (2.4)$$

whereas a completely mixed state of 50 %  $|01\rangle$  and 50 %  $|10\rangle$  is represented by the matrix

$$\rho = \frac{1}{2} \begin{pmatrix} 0 & 0 & 0 & 0 \\ 0 & 1 & 0 & 0 \\ 0 & 0 & 1 & 0 \\ 0 & 0 & 0 & 0 \end{pmatrix}_{(|00\rangle, |01\rangle, |10\rangle, |11\rangle)} \quad (2.5)$$

## 2.2.2 Quantum Gates

Analogously to classical information processing, in quantum computing one defines *quantum gates* that act on individual or multiple qubits and allow us to process information. Such a quantum gate can be described as a unitary operator acting on the state of one or several qubits. Theoretically there is an infinite number of possible quantum gates, however in order to describe all possible quantum operations that can be performed on a qubit register of arbitrary length, it is sufficient to define a so-called *universal set of quantum gates*. Such a set contains a small number of quantum gates that can, by concatenation, produce any arbitrary unitary quantum operator, as shown by the so-called *Solovay-Kitaev theorem* [75, 26]. A universal gate set that will be especially



relevant to this work consists of the three single-qubit rotation operators

$$R_x(\theta) = e^{-i\sigma_x \frac{\theta}{2}} \quad (2.6)$$

$$R_y(\theta) = e^{-i\sigma_y \frac{\theta}{2}} \quad (2.7)$$

$$R_z(\theta) = e^{-i\sigma_z \frac{\theta}{2}} \quad (2.8)$$

that describe rotations of an angle  $\theta$  around the  $X$ ,  $Y$  and  $Z$  axes of the Bloch sphere, together with the so-called  $\sqrt{i\text{SWAP}}$  gate

$$\sqrt{i\text{SWAP}} = \begin{pmatrix} 1 & 0 & 0 & 0 \\ 0 & 1/\sqrt{2} & i/\sqrt{2} & 0 \\ 0 & i/\sqrt{2} & 1/\sqrt{2} & 0 \\ 0 & 0 & 0 & 1 \end{pmatrix}_{(|00\rangle, |01\rangle, |10\rangle, |11\rangle)} \quad (2.9)$$

By applying the  $\sqrt{i\text{SWAP}}$  operation twice we obtain the  $i\text{SWAP}$  quantum gate, which is, by itself, **not** a universal quantum gate but which is nevertheless used in some practical quantum algorithms:

$$i\text{SWAP} = \begin{pmatrix} 1 & 0 & 0 & 0 \\ 0 & 0 & i & 0 \\ 0 & i & 0 & 0 \\ 0 & 0 & 0 & 1 \end{pmatrix}_{(|00\rangle, |01\rangle, |10\rangle, |11\rangle)} \quad (2.10)$$

This universal set is not minimal, since in principle two single-qubit gates with a fixed rotation angle (e.g.  $R_x(\pi/4)$  and  $R_y(\pi/4)$ ) together with a universal two-qubit gate would be sufficient to form a universal set of gates [26]. However, it is often advantageous if one can use single-qubit rotations with arbitrary rotation angles around all three axes of the Bloch sphere since it can significantly reduce the number of gates required to implement a given unitary operation.

### 2.2.3 Quantum Algorithms

The interest in quantum computing is mainly due to the fact that certain problems can be solved faster on a quantum computer than on a classical one. By faster we mean here that the order  $\mathcal{O}$  of the run time of the algorithm increases faster on a classical computer than on a quantum computer as a function of the problem size, i.e. the number of bits needed to encode the problem. Up to this day it has not been demonstrated that a quantum computer can perform all tasks faster than a classical computer. However, a small number of real-world problems have been found that can be solved exponentially to polynomially faster on a quantum computer. Here we cite only the two most “famous”

ones:

**1. The Shor Factorization Algorithm** Developed by Peter Shor in 1994 [88, 89].

This algorithm can factorize a binary number of length  $N$  into its prime factors in  $\mathcal{O}(\log N)^3$  steps, therefore exponentially outperforming any known classical factorization algorithm. There is large interest in this algorithm since the security of many asymmetrical cryptographic key exchange protocols rely on the assumption that it is difficult to factorize large numbers into their prime components. Hence, realizing a polynomial-time method for number factorization would undermine the security of these algorithms.

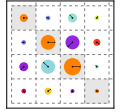
**2. The Grover Search Algorithm:** Discovered by Lov Grover in 1996 [43], this search algorithm can find a single well-defined state in an unsorted database of size  $N$  in  $\mathcal{O}(\sqrt{N})$  steps, being hence  $\sqrt{N}$  faster than a classical search algorithm. Recently, similar algorithms using quantum random walks on graphs have been found that provide similar speed-up [87].

#### 2.2.4 Quantum Simulation

Another domain of interest for quantum computers is the so called *quantum simulation* [59]. Here the goal is to simulate the behavior of an arbitrary quantum system using a quantum computer by either engineering the quantum computer in direct analogy with the system being modeled (so called *analog quantum simulation*) or by numerically simulating the Hamiltonian of the quantum system on a general-purpose quantum computer (so-called *digital quantum simulation*). Since no classical computer can simulate a quantum system efficiently, there is a large interest in quantum simulation, especially in the fields of biology & chemistry [6], quantum field theory [42, 39] and many-body physics [93].

#### 2.2.5 Realization of a Quantum Computer

To realize a working quantum computer, it is necessary to implement highly coherent qubits that can be manipulated, read out and coupled with high fidelity. So far, no fully working quantum computer has been experimentally demonstrated. However, larger progress towards its realization has been achieved in the last decade. Promising approaches for its realization include, among others, ions trapped in magnetic and electric fields [70, 18], nuclear magnetic resonance of organic molecules [49, 96], cold atomic gases [14], photonic circuits [53], semiconductor circuits [60] and, last but not least, superconducting circuits, on which we focus our attention.



## 2.3 Superconducting Quantum Circuits

In this section we discuss several types of superconducting circuit elements that are most relevant to this work. First, we introduce the reader to the Josephson junction, which is the device we use to realize superconducting qubits and amplifiers. Then, we present a general method for the quantization of arbitrary electrical circuits that we use afterwards to perform canonical quantization of our circuits. We use this method to derive the Hamiltonian of the Cooper pair box and treat the Transmon qubit as a special case. Afterwards, we discuss the properties of transmission lines and transmission line resonators that we use extensively for implementing readout and coupling elements in our qubit design. Then we give a short overview of the field of circuit quantum electrodynamics, which describes the interaction of a superconducting qubit capacitively coupled to a resonator. Finally, we introduce the reader to the Josephson and cavity bifurcation amplifiers that we use for our qubit readout.

### 2.3.1 The Josephson junction

The core element used to construct superconducting quantum circuits is the *Josephson junction*. A Josephson junction is based on the so-called Josephson effect [50], which states that between two superconductors connected through an insulating barrier, a supercurrent

$$I_{12} = I_c \sin \varphi \quad (2.11)$$

will flow, depending on the difference  $\varphi = \varphi_1 - \varphi_2$  between the gauge-invariant superconducting phases  $\varphi_1$  and  $\varphi_2$  on each side of the link.  $I_c$ , the *critical current* of the Josephson junction, is the maximum super-current that it can support.  $\varphi$  is related to the instantaneous voltage between the electrodes of the junction as

$$V = \varphi_0 \frac{\partial \varphi}{\partial t}, \quad (2.12)$$

where  $\varphi_0 = \hbar/2e \approx 2.05/2\pi \times 10^{-15}$  Wb. These two simple equations yield a system exhibiting a wealth of interesting physical phenomena which are used today in various applications such as the detection of weak magnetic fields [19], voltage standards [58], generation of Terahertz radiation [77] and quantum limited amplifiers [97]. The energy associated with the phase difference across the Josephson junction is

$$E = E_J \cdot (1 - \cos \varphi) \quad (2.13)$$

where  $E_J = I_c \varphi_0$  is the *Josephson energy*. In addition, the junction usually has an electrostatic energy associated to the capacitance formed by its two electrodes given as

$E_C = Q^2/2C$ , with  $\pm|Q|$  being the charge accumulated on each of the electrodes of the junction.

For currents  $I \ll I_c$ , the Josephson junction behaves approximately like a nonlinear inductance

$$L_J(\varphi) = \frac{\varphi_0}{I_c \cos \varphi} \approx L_{J0} \left[ 1 + \frac{\varphi^2}{2} + \mathcal{O}(\varphi^4) \right], \quad (2.14)$$

where  $L_{J0} = \varphi_0/I_c$  is the so-called *Josephson inductance*.

Using the potential and capacitive energies of the Josephson junction alone, we can formulate the quantum Hamiltonian of the junction, which is

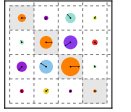
$$\hat{H} = \frac{1}{2C} \hat{Q}_{tr}^2 + E_J(1 - \cos \hat{\varphi}), \quad (2.15)$$

where  $\hat{Q}_{tr}$  is the charge transferred between the two electrodes of the junction and  $\hat{\varphi}$  and  $\hat{Q}_{tr}$  are conjugate quantum operators that, in analogy to a classical pendulum, play the role of position and momentum for the Josephson junction. In the limit of small angles  $\varphi$ , the Hamiltonian becomes that of a harmonic LC oscillator. The nonlinearity present in the system is a key ingredient for realizing a Josephson qubit since it makes it possible to drive transitions between the first two quantum states of the device without also exciting higher quantum states, as would be the case when driving a harmonic oscillator.

#### 2.3.2 Quantization of Electrical Circuits

In this section we outline a general method to treat arbitrary electrical circuits as the ones discussed before within the framework of quantum-mechanics, hence *quantizing* them. This introduction on circuit quantization is based on a seminal article by B. Yurke [104] and an article by M. Devoret [28]. A more specific example of circuit quantization can be found in [15].

An electrical circuit is fully characterized by the parameters of its elements and its topology. The latter can be described as a set of nodes  $j$  connected by a number of branches  $i$  that are formed by dipolar circuit elements. In classical circuit theory, each branch is described by a voltage  $V_i$  between its ends and a current  $I_i$  flowing through it. The Kirchhoff laws demand that the sum of the branch voltages  $V_i$  along any closed path in the circuit must be zero and that the sum of currents flowing in and out of each node must be zero. For quantization it is usually more convenient to replace voltages



and currents with branch charges and fluxes that are defined as

$$\Phi_i(t) = \int_{t_{ref}}^t V_i(t') dt', \quad (2.16)$$

$$Q_i(t) = \int_{t_{ref}}^t I_i(t') dt', \quad (2.17)$$

where  $t_{ref}$  is an arbitrarily chosen reference time. The Kirchhoff laws now write

$$\sum_i Q_i = Q_c, \quad \sum_i \Phi_i = \Phi_c \quad (2.18)$$

with  $Q_c$  and  $\Phi_c$  constants, where the first sum is over charges  $Q_i$  of all elements connected to a certain node  $c$  and the second one is over all branches forming a closed loop in the circuit. We can obtain a complete set of node and branch equations for any given circuit by constructing a so-called *spanning tree* of the circuit, which is a tree in which all nodes are connected to an arbitrarily chosen *ground node* by one unique path [28]. From the spanning tree we obtain a complete set of branches and the corresponding Kirchoff equations for the fluxes  $\Phi_i$  around them. Together with the set of Kirchhoff equations for the charges at each node, we can use this system of equations to eliminate unnecessary circuit variables and obtain a description of the circuit using a minimal set of degrees of freedom. Now, to quantize a circuit made up of non-dissipative elements we can follow the method given in [104], writing the Lagrangian (using the reduced set of variables) as

$$\mathcal{L}(\Phi_1, \dots, \Phi_n, \dot{\Phi}_1, \dots, \dot{\Phi}_n) = \sum_i \mathcal{V}_i - \sum_i \mathcal{T}_i, \quad (2.19)$$

where the sum  $i$  runs over all circuit elements and  $\mathcal{V}_i$  and  $\mathcal{T}_i$  are the potential and kinetic energies associated to the  $i$ -th element. Here, linear inductances contribute only to the potential energy as  $\mathcal{V}_{L_i} = \Phi_i^2 / 2L_i$ , whereas linear capacitances contribute only to the kinetic energy as  $\mathcal{T}_{C_i} = C_i \dot{\Phi}_i^2 / 2$ . Resistors can be described within the Lagrangian formalism by modeling them as semi-infinite transmission lines with a characteristic impedance matching their resistance [104]. We can also include general nonlinear capacitances and inductances that obey the relations  $\dot{\Phi} = f_C(Q)$  and  $\dot{Q} = g_L(\Phi)$  between their node flux and charge, and whose energies are given as

$$E_C = \int_0^Q f_C(Q) dQ, \quad (2.20)$$

$$E_L = \int_0^\Phi g_L(\Phi) d\Phi. \quad (2.21)$$

A Josephson junction, for example, can be described as a nonlinear inductance with  $g_L^{JJ}(\Phi) = I_c \sin(\Phi/\varphi_0)$ , having an associated energy

$$E_L^{JJ} = \int_0^\Phi I_c \sin(\Phi/\varphi_0) d\Phi = E_J(1 - \cos\left[\frac{\Phi}{\varphi_0}\right]). \quad (2.22)$$

Transmission lines can be quantized by a similar approach, as shown e.g. in [104]. Externally imposed charges and fluxes can be modeled as “pre-charged” capacitors and inductors with infinite charge or flux and infinite capacitance or inductance that get renormalized at the end of the quantization process [28]. Externally imposed voltages and currents can be treated like this as well by converting them to corresponding fluxes or charges. From the Lagrangian as given by eq. (2.19) we can obtain the classical equations of motion of the system by variation of the action

$$\frac{\partial}{\partial t} \left( \frac{\partial \mathcal{L}}{\partial \dot{\Phi}_i} \right) - \frac{\partial \mathcal{L}}{\partial \Phi_i} = 0. \quad (2.23)$$

For each flux  $\Phi_i$  we obtain its canonically conjugate momentum  $Q_i$  by the equation

$$Q_i = \frac{\partial \mathcal{L}}{\partial (\dot{\Phi}_i)}, \quad (2.24)$$

where  $\dot{\Phi}_i = d\Phi_i/dt$ . Having obtained  $\Phi_i$  and  $Q_i$ , we can calculate the Hamiltonian  $\mathcal{H}$  of the system by applying the transformation

$$\mathcal{H}(\Phi_1, \dots, \Phi_n, Q_1, \dots, Q_n) = \sum_j \dot{\Phi}_i Q_i - \mathcal{L}(\Phi_1, \dots, \Phi_n, \dot{\Phi}_1, \dots, \dot{\Phi}_n). \quad (2.25)$$

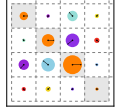
This Hamiltonian, written in generalized coordinates, yields the full set of equations of motion of the electrical circuit and depends only on the canonically conjugate variables  $\Phi_1, \dots, \Phi_n$  and  $Q_1, \dots, Q_n$ . First quantization of the circuit can then be done by simply replacing the classical variables by quantum observables such that  $\Phi_i \rightarrow \hat{\Phi}_i$  and  $Q_i \rightarrow \hat{Q}_i$  and imposing commutation relations between them:

$$[\hat{Q}_i, \hat{Q}_j] = 0, \quad (2.26)$$

$$[\hat{\Phi}_i, \hat{\Phi}_j] = 0, \quad (2.27)$$

$$[\hat{\Phi}_i, \hat{Q}_j] = i\hbar\delta_{ij}. \quad (2.28)$$

In the following sections we apply this quantization method to the Cooper pair box circuit that we use to implement a superconducting qubit and to the simple LCR resonator circuit that we use as a qubit readout and coupling bus.



### 2.3.3 The LCR Resonator

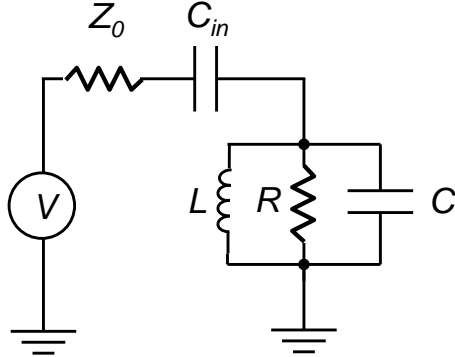


Figure 2.2: An *LCR* resonator coupled to a voltage source through an input capacitance  $C_{in}$ .

The *LCR* resonator is the circuit element that forms the basis of our qubit readout. The schematic of a *LCR* resonator coupled to a voltage source through an input capacitance  $C_{in}$  is shown in fig. 2.2. The impedance of the resonator alone is

$$Z_{LCR} = \frac{1}{\frac{1}{R} + i\omega C - \frac{i}{\omega L}}, \quad (2.29)$$

yielding a resonance frequency  $\omega_r = 1/\sqrt{LC}$  and an *internal quality factor*  $Q_{int} = R/Z_r$  with  $Z_r = \sqrt{L/C}$  the characteristic impedance of the resonator. To probe the resonator we couple it through a gate capacitance  $C_{in}$  to an input transmission line with characteristic impedance  $Z_0$ . We can model the resulting circuit as a modified LCR resonator with a frequency-dependent, effective resistance  $R'$  such that

$$\frac{1}{R'(\omega)} = \frac{1}{R} + \frac{1}{R_{ext}(\omega)}, \quad (2.30)$$

with

$$\frac{R_{ext}(\omega)}{Z_0} = \frac{1}{C_{in}^2 Z_0^2 \omega^2} + 1, \quad (2.31)$$

and a new capacitance

$$C'(\omega) = C + \frac{C_{in}}{1 + (C_{in}\omega_r Z_0)^2}, \quad (2.32)$$

yielding a shifted resonance frequency  $\omega'_r = 1/\sqrt{LC'}$  and a modified quality factor

$$Q_r^{-1} = Q_{int}^{-1} + Q_{ext}^{-1}, \quad (2.33)$$

where  $Q_{ext} = R_{ext}/Z_r$ . As can be seen, the external quality factor increases  $\propto 1/C_{in}^2$ . We can define a coupling or decay rate  $\kappa = \omega_r/Q_r$ , which corresponds to the rate at which energy leaks out of the resonator. For frequencies close to the resonance

frequency of the resonator, we can write its impedance as

$$Z_{LCR}(\Delta) = \frac{\omega_r Z_r}{\kappa + 2i\Delta} \quad (2.34)$$

where  $\Delta = \omega_r - \omega$  and  $Z_r = \sqrt{L/C}$  is the characteristic impedance of the resonator. This approximation is useful when e.g. experimentally fitting resonance data to obtain the quality factor of the resonator.

Before quantizing the LCR resonator, we will first show how we can map a transmission line resonator to the LCR model presented here.

#### Coplanar Waveguide Resonators

Due to practical reasons we use so-called *coplanar waveguide resonators* instead of lumped elements LCR resonators in our experiments. We will therefore briefly discuss them and show how we can map them to the simple LCR resonator model. A coplanar waveguide is a flat structure with a central conductor that is separated by a gap from a ground plane on either side, as shown in fig. 2.3c. In general, it can be treated as a so-called *transmission line*. A detailed treatment of the physics of transmission lines can be found e.g. in [81]. If we regard a transmission line of finite length  $l$ , the voltages and currents at both ends are related through [81]

$$\begin{pmatrix} V_1 \\ I_1 \end{pmatrix} = \begin{pmatrix} \cos \gamma l & iZ_r \cos \gamma l \\ iY_r \sin \gamma l & \cos \gamma l \end{pmatrix} \cdot \begin{pmatrix} V_2 \\ I_2 \end{pmatrix}, \quad (2.35)$$

where  $\gamma = \alpha + i\beta = \sqrt{(R + i\omega L)(G + i\omega C)}$  is the *propagation constant* which describes the dispersion and damping of electromagnetic waves along the waveguide,  $\omega$  is the angular frequency of the electromagnetic wave,  $L$ ,  $C$ ,  $R$  and  $G$  are the characteristic inductance, capacitance, resistance and conductance of the transmission line per unit length (for a superconducting, lossless line  $G = R = 0$ ),  $Z_r = \sqrt{L/C}$  is the characteristic impedance of the waveguide and  $Y_r = 1/Z_r$  the corresponding admittance.

Let us now consider the open-ended  $\lambda/2$  CPW resonator that we use in our experiments to realize the qubit readout resonator, as shown in fig. 2.3b-c. To realize the resonator, we terminate the transmission line at one end by an open gap and connect the other end to a drive line through an input capacitance  $C_{in}$ . We can then make use of eq. (2.35) to calculate the end voltages and currents of the resonator, demanding that  $I_2 = 0$  (since the resonator is open-ended). We obtain for the voltage  $V_1$  and current  $I_2$

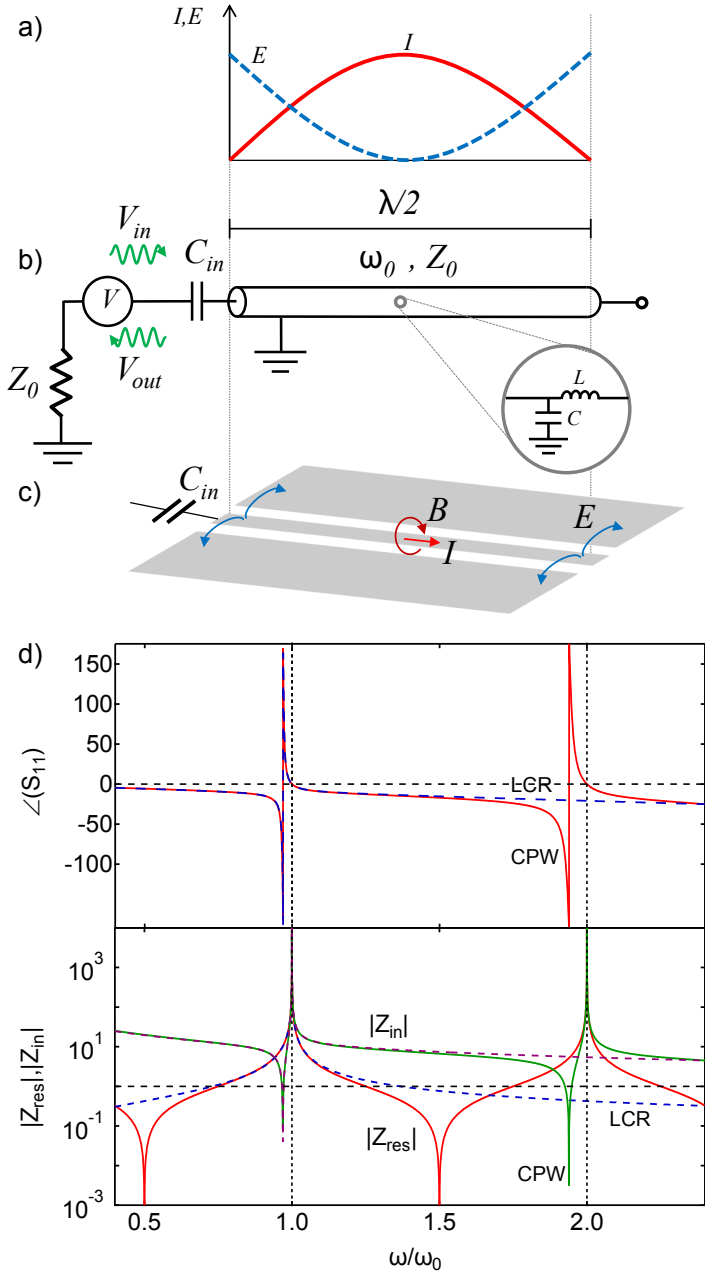
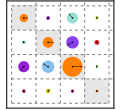


Figure 2.3: a) The electric field  $E$  and current  $I$  inside a  $\lambda/2$  resonator. b) The circuit model of an open  $\lambda/2$  resonator capacitively coupled to a drive circuit. The (lossless) resonator can be modeled as a series of infinitesimal sections of  $LC$  elements, as shown in the inset. c) The schematic of a coplanar waveguide (CPW) resonator, showing the electric field  $E$ , magnetic field  $B$  and the current  $I$  in the resonator. d) The reflected phase  $\arg(S_{11})$  and absolute value of the input impedance  $|Z_{in}|$  and resonator impedance  $|Z_{res}|$  of an LCR resonator with  $\omega_r = Z_r = Z_0 = 1$ ,  $R \rightarrow \infty$  and  $C_{in} = 0.1$  (dotted lines) as well as a  $\lambda/2$  resonator with the same effective  $\omega_r$  and  $Z_r$  (solid lines), plotted as a function of the reduced frequency. As can be seen, the resonance frequency of the loaded resonator shifts in respect to that of the uncoupled one. In this case,  $\omega_r^{\text{loaded}} \approx 0.969$ .

the relation

$$V_1 = \cos \gamma l V_2, \quad (2.36)$$

$$I_1 = i Y_r \sin \gamma l V_2. \quad (2.37)$$

The impedance of the resonator is thus given as  $V_1/I_1 = -i Z_r \cot \gamma l$ . We can approximately model this distributed CPW resonator as a lumped element parallel LCR resonator by equating their impedances close to their resonance frequency  $\omega_r$ . This

yields an effective inductance, capacitance and resistance for the CPW resonator of

$$L_r = \frac{2Z_r}{\omega_r \pi} \quad (2.38)$$

$$C_r = \frac{\pi}{2\omega_r Z_r} \quad (2.39)$$

$$R_r = \frac{2Z_r Q}{\pi} \quad (2.40)$$

Using this mapping, we can calculate all relevant resonator properties using the theory of the lumped element LCR resonator, disregarding however the internal multi-mode structure of the resonator.

### Quantization of the Resonator

We can quantize the LCR resonator by following the procedure outlined in the last section. The circuit in fig. 2.2 contains two active nodes. If we disregard for now the input voltage source  $V$ , the input capacitance  $C_{in}$  and the resistance  $R$ , we can directly obtain the Hamiltonian of the non-dissipative part of the LCR resonator as

$$H = \frac{1}{2C}Q^2 + \frac{1}{2L}\Phi^2, \quad (2.41)$$

where  $Q$  is the charge accumulated on the capacitor and  $\Phi$  the flux in the inductance of the resonator. This Hamiltonian corresponds to that of a harmonic oscillator given in second quantization as

$$\hat{H} = \omega_r \hbar \left( \hat{a}^\dagger \hat{a} + \frac{1}{2} \right), \quad (2.42)$$

with the *creation and annihilation operators*

$$\hat{a}^\dagger = \sqrt{\frac{1}{2\hbar Z_r}} (\hat{\Phi} + iZ_r \hat{Q}), \quad (2.43)$$

$$\hat{a} = \sqrt{\frac{1}{2\hbar Z_r}} (\hat{\Phi} - iZ_r \hat{Q}). \quad (2.44)$$

By inverting these relations we obtain the flux and charge operators  $\hat{\Phi}$  and  $\hat{Q}$ . Calculating their time derivatives gives us the voltage and current operators  $\hat{V} = i[\hat{H}, \hat{\Phi}]/\hbar$  and

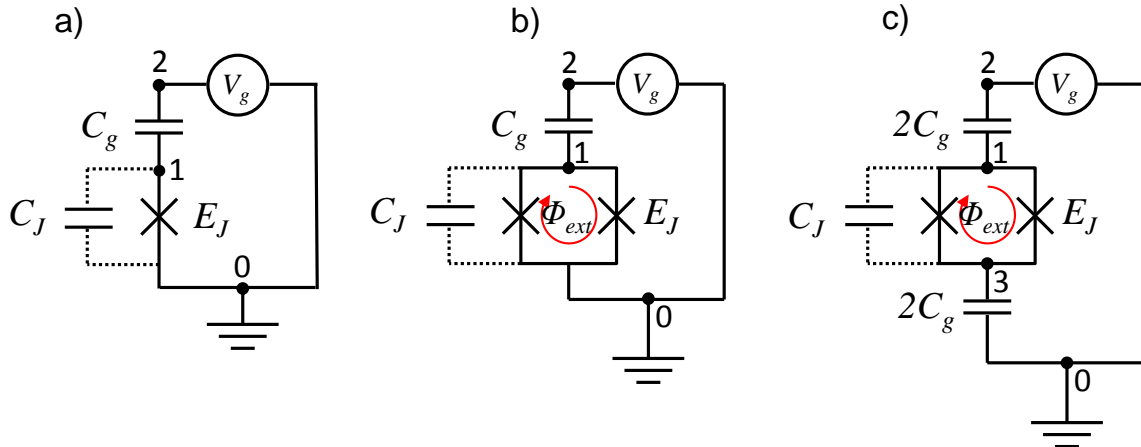
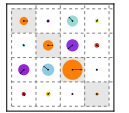


Figure 2.4: a) The circuit schematic of a Cooper Pair Box (CPB). The device consists of a Josephson junction capacitively coupled to a voltage source. The extra capacitance of the Josephson junction is modeled by a capacitor  $C_J$ . Charges can accumulate on the island between the voltage source and the Josephson junction. b) A *split Cooper pair box*, where instead of one junction two of them are arranged in a loop. With this geometry it is possible to tune the effective Josephson energy of the circuit by changing the magnetic flux inside the junction loop. c) The schematic of a split CPB capacitively coupled to ground. This schematic corresponds most closely to the experimental CPB circuit that we use in this work.

$$\hat{I} = i[\hat{H}, \hat{Q}]/\hbar:$$

$$\hat{V} = V_{rms} (\hat{a}^\dagger + \hat{a}), \quad (2.45)$$

$$\hat{\Phi} = \frac{V_{rms}}{\omega_r} (\hat{a}^\dagger + \hat{a}), \quad (2.46)$$

$$\hat{I} = i\omega_r C V_{rms} (\hat{a}^\dagger - \hat{a}), \quad (2.47)$$

$$\hat{Q} = iC V_{rms} (\hat{a}^\dagger - \hat{a}), \quad (2.48)$$

where  $V_{rms} = \sqrt{\hbar\omega_r/2C}$  is the root-mean-square voltage corresponding to one photon in the resonator.

### 2.3.4 The Cooper Pair Box

The LC resonator discussed in the last section is one of the key elements for building quantum circuits. However, it is not possible to implement a superconducting qubit using such a linear resonator since the transition frequencies between all adjacent energy levels are equal, which makes it impossible to drive e.g. the  $|0\rangle \rightarrow |1\rangle$  transition of the system without also exciting higher energy states. Therefore, to realize a qubit we need to introduce a non-linear element in the circuit. One way of doing this is to replace the linear inductance of the LC resonator by a non-linear one. A Josephson junction con-

veniently provides such a non-linear inductance. The resulting circuit, called a *Cooper pair box (CPB)* contains thus a Josephson junction in parallel with a capacitance and is coupled to an input voltage source through a gate capacitance  $C_g$ , as shown in fig. 2.4a. Often one also uses two junctions in a loop instead of a single one, as shown in fig. 2.4b, which allows one to tune the effective Josephson energy of the system by changing the flux inside the junction loop. Finally, in our experimental setup, we can separate the bottom electrode of the CPB capacitively from the ground, as shown in fig. 2.4c. In this section we discuss only the circuit a), since b) can be mapped to the simpler version a) and the topology of c) is mathematically equivalent to that of b). The simple CPB circuit 2.4a consists of three nodes (including ground) and two branches. The flux  $\Phi_2$  is not independent since it is set by the voltage source  $V_g$ , so we can directly eliminate it from the equations. This leaves us with only one remaining active node  $\Phi_1$ . Using these specifications, the Lagrangian of the circuit is given as

$$\mathcal{L} = \frac{1}{2}C_J\dot{\Phi}_1^2 + \frac{1}{2}C_g(\dot{\Phi}_1 + V_g)^2 - E_J(1 - \cos\phi_1), \quad (2.49)$$

where  $\phi_1 = \Phi_1/\varphi_0$ . The canonical momentum  $Q_1$  associated to the flux  $\Phi_1$  is given as

$$Q_1 = \frac{\partial \mathcal{L}}{\partial \dot{\Phi}_1} = C_J\dot{\Phi}_1 + C_g(V_g + \dot{\Phi}_1). \quad (2.50)$$

From this, we can directly calculate the Hamiltonian by using eq. (2.25) and substituting  $Q_1$  as given by eq. (2.50) for  $\dot{\Phi}_1$ , which yields

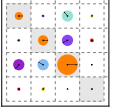
$$\mathcal{H} = E_J(1 - \cos\phi_1) + \frac{(Q_1 - C_gV_g)^2}{2(C_J + C_g)} - \frac{1}{2}C_gV_g^2. \quad (2.51)$$

Quantization of the Hamiltonian is completed by replacing  $Q_i \rightarrow \hat{Q}_i$  and  $\phi_1 \rightarrow \hat{\phi}_1$  and imposing the commutation relations given by eqs. (2.28). If, in addition we introduce reduced operators for the charge  $\hat{n} = \hat{Q}/2e$  and discard the energy stored in the voltage source (which is irrelevant), we obtain the Hamiltonian of the Cooper pair box, as formulated e.g. in the thesis of V. Bouchiat [13],

$$\hat{H} = E_C(\hat{n} - n_g)^2 - E_J \cos \hat{\theta}, \quad (2.52)$$

with  $\hat{\theta} = \hat{\phi}_1$ ,  $E_C = (2e)^2/(C_J + C_g)$  the charging energy of the Cooper pair box and  $n_g = C_gV_g/2e$  the reduced gate charge.

For the split Cooper pair box as shown in fig. 2.4b, the treatment is slightly modified [23]. First of all, we write the Josephson energies of the two junctions as  $E_{J1} = (1 + d)E_J/2$  and  $E_{J2} = (1 - d)E_J/2$ , where  $d \in [0, 1]$  is the energy asymmetry between the junctions. When imposing an external phase  $\phi_{ext} = \Phi_{ext}/\varphi_0$  in the loop, the potential



energy of the two junctions can be written as

$$\mathcal{V}_J = -\frac{E_J}{2} [(1+d) \cos(\phi_1 - \phi_{ext}/2) + (1-d) \cos(\phi_2 + \phi_{ext}/2)] \quad (2.53)$$

$$= -E_J \left[ \cos \phi_1 \cos \frac{\phi_{ext}}{2} + d \sin \phi_1 \sin \frac{\phi_{ext}}{2} \right]. \quad (2.54)$$

The remaining part of the quantization process proceeds as above, yielding a Hamiltonian of the split Cooper pair box of the form

$$\hat{H}_{split} = E_C(\hat{n} - n_g)^2 - E_J \left[ \cos \hat{\phi}_1 \cos \frac{\phi_{ext}}{2} + d \sin \hat{\phi}_1 \sin \frac{\phi_{ext}}{2} \right]. \quad (2.55)$$

This Hamiltonian can be recast in the form [23]

$$\hat{H}_{split} = E_C(\hat{n} - n_g)^2 - E'_J(d, \phi_{ext}) \cos [\hat{\phi}_1 + \gamma(\phi_{ext})], \quad (2.56)$$

with

$$E'_J(d, \phi_{ext}) = E_J \sqrt{\frac{1 + d^2 + (1 - d^2) \cos \phi_{ext}}{2}}, \quad (2.57)$$

$$\tan \gamma(\phi_{ext}) = -d \tan \frac{\phi_{ext}}{2}. \quad (2.58)$$

It is therefore possible to map the Hamiltonian of the split CPB to that of the single-junction one by defining  $\hat{\theta} \rightarrow \hat{\phi}_1 + \gamma(\phi_{ext})$  and  $E_J \rightarrow E'_J(d, \phi_{ext})$ .

Using the Hamiltonian (2.52), we can calculate the eigen wave functions of the simple Cooper pair box. The variables  $\hat{n}$  and  $\hat{\theta}$  are conjugate such that  $[\hat{\theta}, \hat{n}] = i\hbar$ , the corresponding wave function  $\Psi_k(\theta) = \langle \theta, k \rangle$  will therefore satisfy a Schrödinger equation of the form

$$E_k \Psi_k(\theta) = E_C \left( \frac{1}{i} \frac{\partial}{\partial \theta} - n_g \right)^2 \Psi_k(\theta) - E_J \cos(\theta) \Psi_k(\theta). \quad (2.59)$$

Since the potential  $-E_J \cos(\theta)$  is  $2\pi$  periodic, the solution will be of the form

$$\Psi_k(\theta) = \Psi_k(\theta + 2\pi), \quad (2.60)$$

which allows us to map eq. (2.59) to the so-called *Mathieu equation*

$$\frac{d^2 y}{dx^2} + [a - 2q \cos(2x)] y = 0. \quad (2.61)$$

### 2.3. SUPERCONDUCTING QUANTUM CIRCUITS

---

The *Floquet theorem* states that all solutions to this equation can be written in the form

$$F(a, q, x) = \exp(i\mu x)P(a, q, x), \quad (2.62)$$

and the most general solutions are [23]

$$\Psi_k(r, q, \theta) = \mathcal{C}_1 \exp(in_g \theta) \mathcal{M}_C \left( \frac{4E_k}{E_C}, -\frac{2E_J}{E_C}, \frac{\theta}{2} \right) + \mathcal{C}_2 \exp(in_g \theta) \mathcal{M}_S \left( \frac{4E_k}{E_C}, -\frac{2E_J}{E_C}, \frac{\theta}{2} \right), \quad (2.63)$$

with

$$E_k = \frac{E_C}{4} \mathcal{M}_A \left( r_k, -\frac{2E_J}{E_C} \right). \quad (2.64)$$

Here,  $\mathcal{M}_C$ ,  $\mathcal{M}_S$  are the cosine and sine *Mathieu functions* and  $\mathcal{M}_A$  corresponds to the Mathieu characteristic value of each solution. Following the convention in [23] we order the  $E_k$  such that the energy increases with increasing  $k$ , yielding [54]

$$\begin{aligned} r_k(n_g) &= \sum_{l \pm 1} [\text{int}(n_g + l/2) \bmod 2] \\ &\times \left\{ \text{int}(n_g/2) + l(-1)^k[(k+1)\text{div } 2] \right\}, \end{aligned} \quad (2.65)$$

where  $x\text{div}y$  denotes the integer part of  $x/y$ .

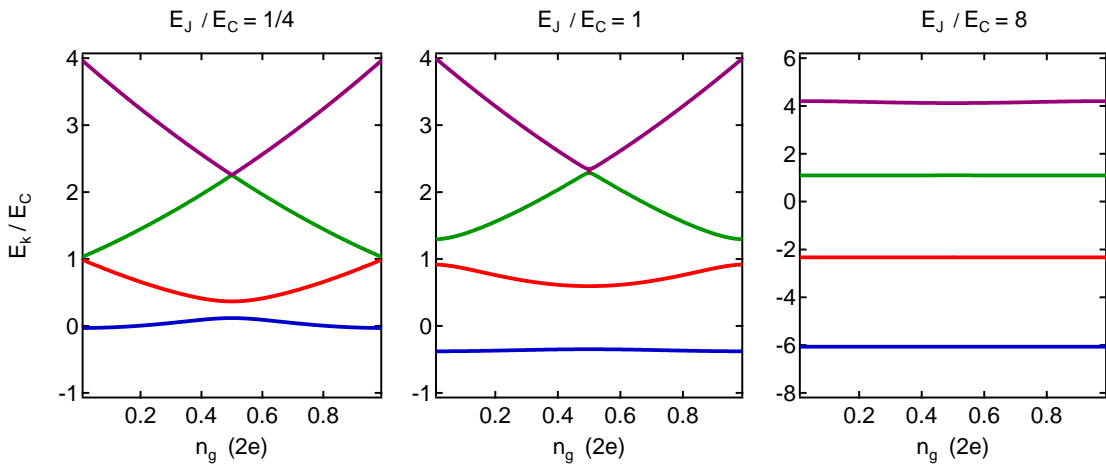
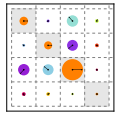


Figure 2.5: Energies of the first four energy levels of the Cooper pair box for different ratios  $E_J/E_C$ , plotted as a function of the gate charge  $n_g$ . As can be seen, for  $E_J \gg E_C$ , the charge-dispersion curve becomes almost completely flat.

We denote the energy differences between individual energy levels  $i, j$  by  $E_{ij} = E_j - E_i$ . We also define the absolute and relative anharmonicities of the first two energy levels as  $\alpha \equiv E_{12} - E_{01}$  and  $\alpha_r \equiv \alpha/E_{01}$ . An in-depth treatment of the Cooper pair box can be found in [23]. Using the basis states  $|i\rangle$  of the CPB, we can rewrite its Hamiltonian



in the form

$$\hat{H} = \hbar \sum_{i=0} \omega_i |i\rangle \langle i|, \quad (2.66)$$

where  $\hbar\omega_i$  is the energy associated to the  $i$ -th CPB state. Disregarding CPB levels  $i \geq 2$ , we can also formulate an approximate qubit Hamiltonian of the CPB of the form

$$\hat{H} = -\frac{\hbar\omega_{01}}{2} \hat{\sigma}_z, \quad (2.67)$$

where  $\omega_{01} = \omega_1 - \omega_0$  is the frequency of the transition  $|0\rangle \rightarrow |1\rangle$ .

### The Transmon Qubit

The Transmon qubit as developed in R. Schoelkopf's lab [54, 100] is a Cooper pair box whose charging energy is strongly reduced by putting a large capacitance in parallel to the Josephson junction, such that the device is in the regime  $E_J \gg E_C$ . As shown in fig. 2.5, in this regime the charge dispersion of the energy levels of the Cooper pair box becomes extremely weak, thus rendering the transition frequency  $E_{01}$  practically insensitive to the value of the gate charge  $n_g$ . This reduced sensitivity to charge noise is highly advantageous in experiments since it increases the coherence time of the qubit. However, when increasing the ratio  $E_J/E_C$ , we also reduce the anharmonicity  $\alpha_r$  of the qubit, therefore limiting the speed of gate operations that can be realized with this system (driving errors related to weak anharmonicity will be discussed more thoroughly chapter 5). In the limit  $E_J \gg E_C$  the qubit anharmonicity is well approximated by  $\alpha \simeq -E_C/4$ ,  $\alpha_r \simeq -(2E_J/E_C)^{-1/2}$ . In this limit we can also approximate the transition frequency of the Transmon as  $\hbar\omega_{01} \approx \sqrt{2E_J E_C}$ .  $\alpha_r$  decreases only geometrically with  $E_J/E_C$ , whereas the sensitivity of the qubit to charge noise decreases exponentially with the ratio of Josephson and charging energy.

### Decoherence of the Transmon

An in-depth derivation of the decoherence of the CPB and the Transmon can be found e.g. in [23, 54]. Here, we give the relevant expressions that we use to estimate the coherence of the qubits in our quantum processor. Fundamentally, *relaxation* and *dephasing* are the relevant decoherence mechanisms of the qubit, each one characterized by relaxation and dephasing rates  $\Gamma_1$  and  $\Gamma_\phi$  and corresponding coherence times  $T_1 = \Gamma_1^{-1}$  and  $T_\phi = \Gamma_\phi^{-1}$ . Following the treatment by Cottet et. al. [23], a perturbation of the CPB Hamiltonian can be written as  $\delta\hat{H}_\lambda = -\hbar/2(\hat{\mathbf{D}}_\lambda \cdot \boldsymbol{\sigma})\delta\lambda$ , where  $\hat{\mathbf{D}}_\lambda = 1/\hbar \cdot \partial\hat{H}/\partial\lambda$  describes the sensitivity of the Hamiltonian to a noise source  $\lambda$ . In the operator  $\hat{\mathbf{D}}_\lambda = \vec{D}_\lambda \cdot \vec{\sigma} = D_{\lambda,x} \cdot \hat{\sigma}_x + D_{\lambda,y} \cdot \hat{\sigma}_y + D_{\lambda,z} \cdot \hat{\sigma}_z$  we can distinguish between transversal parts  $\vec{D}_{\lambda,\perp}$  (in the XY plane) that describe relaxation processes and longi-

tudinal parts  $\vec{D}_{\lambda,z}$  that describe dephasing processes. For the relaxation processes, we can calculate the relaxation rate from the sensitivity  $D_{\lambda,\perp}$  and spectral density of the noise channel  $S_\lambda(\omega_{01})$  using Fermi's golden rule:

$$\Gamma_{S,\lambda}^{rel} = \frac{\pi}{2} D_{\lambda,\perp}^2 S_\lambda(\omega_{01}) \quad (2.68)$$

Similarly, for the dephasing processes  $\hat{D}_{\lambda,z}$  we can calculate the dephasing rates using the corresponding sensitivities and spectral densities as

$$\Gamma_{S,\lambda}^\phi = \pi D_{\lambda,z}^2 S_\lambda(\omega = 0). \quad (2.69)$$

Here, the spectral density of the noise is to be evaluated at  $\omega = 0$  or at a natural cutoff frequency defined by the experimental protocol if  $S_\lambda(\omega = 0)$  diverges [23], as for example for the case of  $1/f$  noise. In that particular case, the dephasing will be described not by an exponential decay  $\propto \exp(-\Gamma_\phi t)$  but rather by a Gaussian one  $\propto \exp(-\Gamma_\phi^2 t^2)$  with a corresponding rate

$$\Gamma_\phi = 3.7A \left| \frac{\partial \omega_{01}}{\partial \lambda} \right|. \quad (2.70)$$

The most relevant couplings for relaxation and dephasing through the charge and current/phase channels of the CPB are

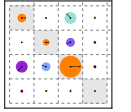
$$D_{n_g,z} = 2 \frac{E_C}{\hbar} (\langle 0 | \hat{n} | 0 \rangle - \langle 1 | \hat{n} | 1 \rangle), \quad (2.71)$$

$$D_{\phi_{ext},z} = \frac{2E_J}{\hbar} \left| (\langle 0 | \cos \hat{\theta} | 0 \rangle - \langle 1 | \cos \hat{\theta} | 1 \rangle) \sin \frac{\phi_{ext}}{2} \right|, \quad (2.72)$$

$$D_{n_g,\perp} = 4 \frac{E_C}{\hbar} |\langle 0 | \hat{n} | 1 \rangle|, \quad (2.73)$$

$$D_{\phi_{ext},\perp} = \frac{E_J}{2\hbar} d \left| \langle 0 | \sin \hat{\theta} | 1 \rangle \cos \frac{\phi_{ext}}{2} \right|, \quad (2.74)$$

where we have neglected matrix elements that nearly vanish due to wave-function parity reasons. Using these sensitivities and the spectral density of the corresponding noise parameter, we can calculate the relevant dephasing or relaxation rate. In general, relaxation and dephasing through the charge and flux channel can occur due to microscopic and macroscopic noise sources. In the following paragraph we discuss decoherence through the most relevant channels and present the corresponding spectral noise densities and relaxation or dephasing rates.



**Relaxation through the Charge Channel** Relaxation through the charge channel can occur due to microscopic charge noise and macroscopic charge noise in the gate circuit. Here, we focus on the latter since it is usually the most relevant charge relaxation channel in our experiments. The spectral density of the charge noise seen by the qubit through its gate circuit is

$$S_{V_g}(\omega) = \frac{\hbar\omega}{2\pi} \left[ \coth\left(\frac{\hbar\omega}{2k_B T}\right) + 1 \right] \operatorname{Re}[Z_g(\omega)]. \quad (2.75)$$

At low temperatures  $k_B T \ll \hbar\omega$ ,  $\coth(\hbar\omega/2k_B T) \approx 1$ , so the resulting relaxation rate as given by eq. (2.68) simply becomes

$$\Gamma_1^{n_g} = 16\pi\beta^2\omega_{01} \frac{\operatorname{Re}[Z_g(\omega_{01})]}{R_K} |\langle 0 | \hat{n} | 1 \rangle|^2, \quad (2.76)$$

where  $R_K = h/e^2$  and  $\beta = C_g/C_\Sigma$  and  $C_\Sigma = C_g + C_J$ .

**Relaxation through the Flux Channel** As before, we discuss relaxation of the qubit through the flux line circuit, which is the most relevant flux relaxation channel in our experiments. The spectral density of magnetic flux fluctuations, as induced by current fluctuations in the flux line coupled to the qubit by a mutual inductance  $M$  is given as

$$S_{\phi_{ext}}(\omega) = \left(\frac{M}{\Phi_0}\right)^2 S_I(\omega) = \left(\frac{M}{\Phi_0}\right)^2 \frac{\hbar\omega}{2\pi} \operatorname{Re}\left(\frac{1}{Z_{fl}(\omega)}\right) \left[ \coth\left(\frac{\hbar\omega}{2k_B T}\right) + 1 \right], \quad (2.77)$$

where  $Z_{fl}(\omega)$  is the impedance of the flux line coupled to the qubit. As before, the resulting relaxation rate is thus given as

$$\Gamma_1^{\phi_{ext}} = \frac{\hbar\omega_{01}}{4} \left(\frac{E_J dM}{\Phi_0}\right)^2 \operatorname{Re}\left(\frac{1}{Z_{fl}(\omega_{01})}\right) \left| \langle 0 | \sin \hat{\theta} | 1 \rangle \cos\left(\frac{\phi_{ext}}{2}\right) \right|^2 \quad (2.78)$$

**Dephasing through the Charge Channel** Noise in the gate charge  $n_g$  randomly changes the transition frequency of the CPB and induces dephasing. Again, both microscopic and macroscopic noise sources contribute to dephasing. Here, we look at microscopic charge noise, which is most relevant to our experiments. The corresponding dephasing rate in the case of a  $1/f$  gate charge noise can be written as [23, 95]

$$\Gamma_\phi^{\delta n_g} \simeq 3.7A \left| \frac{\partial\omega_{01}}{\partial n_g} \right|, \quad (2.79)$$

where  $A \approx 10^{-5}$  is a measured parameter that describes the amplitude of the microscopic gate charge fluctuations. In the limit  $E_J \gg E_C$  this rate can be written analytically

as

$$\Gamma_{\phi}^{\delta N_g} \simeq 3.7 \frac{A\pi}{\hbar} |(\epsilon_1 - \epsilon_0) \sin(2\pi N_g)| \leq 3.7 \frac{A\pi}{\hbar} |\epsilon_1|, \quad (2.80)$$

where  $\epsilon_i$  is the energy modulation amplitude of the  $i$ -th CPB level, given as [54]

$$\epsilon_m \simeq (-1)^m E_C \frac{2^{4m+3}}{m!} \sqrt{\frac{2}{\pi}} \left(\frac{2E_J}{E_C}\right)^{\frac{m}{2} + \frac{3}{4}} \exp\left(-\sqrt{\frac{32E_J}{E_C}}\right). \quad (2.81)$$

As can be seen, the sensitivity of the CPB to charge noise decreases exponentially with the ratio  $E_J/E_C$  for  $E_J \gg E_C$ .

**Dephasing through the Flux Channel** Analogously to charge-induced dephasing, one can consider dephasing due to microscopic  $1/f$ -type flux noise seen by the CPB, which has an associated dephasing rate

$$\Gamma_{\phi}^{\delta\phi_{ext}} \simeq 3.7 A \left| \frac{\partial\omega_{01}}{\partial\phi_{ext}} \right| \quad (2.82)$$

where again  $A = 10^{-5}$  is a measured noise amplitude [54]. For the general, asymmetric CPB in the limit  $E_J \gg E_C$  we obtain a dephasing rate

$$\Gamma_{\phi}^{\delta\phi_{ext}} \approx \frac{1}{2} A \omega_{01}^{\max} \left| \sin(\phi_{ext})(1-d^2) \left( \frac{1+d^2+(1-d^2)\cos(\phi_{ext})}{2} \right)^{-3/4} \right| \quad (2.83)$$

where  $\omega_{01}^{\max} = \sqrt{2E_C E_J}/\hbar$  is the maximum transition frequency of the qubit.

## 2.4 Circuit Quantum Electrodynamics

All experiments reported in this thesis rely on the coupling between a superconducting qubit and a resonator, where the latter serves either for reading out the qubit state and/or for coupling several qubits. In this section, we will therefore discuss the physics of such a coupled qubit-resonator system. The corresponding research field is today referred to as *circuit quantum electrodynamics* (CQED), a term coined in reference to *cavity quantum electrodynamics*, a field that investigates the physics of Rydberg atoms interacting with a microwave cavity (see e.g. [62, 101] for a review of cavity QED). In circuit QED, qubits that act as “artificial atoms” interact with coplanar or lumped elements resonators on a chip, where the qubit-resonator system can be represented as in fig. 2.6. There, a Transmon qubit is capacitively coupled to a  $\lambda/2$  resonator which itself is capacitively coupled to an input transmission line. The Hamiltonian of the resonator and the qubit are given by eqs. (2.42) and (2.67). Due to the capacitance between the qubit and the resonator, a coupling energy between the two arises. The full Hamiltonian of the

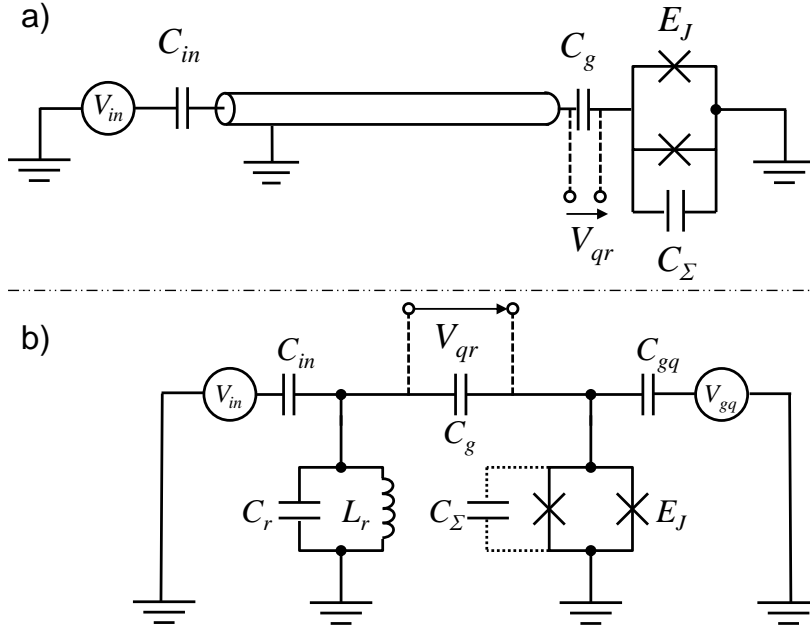
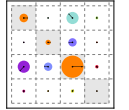


Figure 2.6: a) Schematic of a typical CQED circuit, consisting of a Transmon qubit capacitively coupled to a transmission line resonator. b) The equivalent circuit using a lumped-element model of the  $\lambda/2$  resonator.

qubit-resonator system can therefore be written as

$$\hat{H}_{cqed} = \hat{H}_r + \hat{H}_q + \hat{H}_{qr}, \quad (2.84)$$

where  $\hat{H}_r$  and  $\hat{H}_q$  are the Hamiltonians of the resonator and the qubit as given by eqs. (2.42) and (2.52), respectively, and  $\hat{H}_{qr}$  is the interaction Hamiltonian between them. For small couplings  $C_g \ll C_{in}, C_r, C_\Sigma$ , we can estimate the coupling energy between the qubit and the resonator simply as

$$\hat{H}_{qr} = \frac{1}{2} C_g \hat{V}_{qr}^2 = \frac{1}{2} C_g \left( V_{rms}^0 (a^\dagger + a) - \hat{V} \right)^2, \quad (2.85)$$

where  $\hat{V}_{qr}$  is the voltage across the coupling capacitance  $C_g$  and  $\hat{V} = 2e/C_\Sigma \cdot (n_g - \hat{n})$  is the voltage across the Transmon electrodes. A rigorous treatment of the coupling energy, which is necessary for large coupling capacitances  $C_{qr} \simeq C_r, C_\Sigma$ , would require a full quantization of the coupled qubit-resonator circuit, as performed e.g. in [74]. The coupling energy in eq. (2.86) can be rewritten as

$$\begin{aligned} \hat{H}_{qr} &= \frac{1}{2} C_g \left[ V_{rms}^0 (a^\dagger + a) - \frac{2e}{C_\Sigma} (n_g - \hat{n}) \right]^2 \\ &= 2e\beta V_{rms}^0 \hat{n} (a^\dagger + a) + \dots \end{aligned} \quad (2.86)$$

in the limit  $\beta = C_g/C_\Sigma \ll C_\Sigma$ . The terms omitted in eq. (2.86) correspond to energy shifts of the qubit and the resonator which are not directly relevant for the coupling between them. In the limit where the resonator capacitance  $C_r \gg C_\Sigma$ , we can write the effective Hamiltonian of the qubit-resonator system using the uncoupled basis states  $|i\rangle$

of the Transmon as

$$\hat{H} = \hbar \sum_{j=0} \omega_j |j\rangle \langle j| + \hbar \omega_r \hat{a}^\dagger \hat{a} + \hbar \sum_{i \neq j} g_{ij} |i\rangle \langle j| (\hat{a} + \hat{a}^\dagger), \quad (2.87)$$

where the coupling energies  $g_{ij}$  are given as

$$\hbar g_{ij} = 2\beta e V_{rms}^0 \langle i | \hat{n} | j \rangle. \quad (2.88)$$

When the coupling between the resonator and the Transmon is such that  $g_{ij} \ll \omega_r, E_{01}/\hbar$ , we can ignore the terms in eq. (2.87) that describe simultaneous excitation or de-excitation of the Transmon and the resonator and obtain the so-called *rotating wave approximation*, yielding the Hamiltonian

$$\hat{H} = \hbar \sum_{j=0} \omega_j |j\rangle \langle j| + \hbar \omega_r \hat{a}^\dagger \hat{a} + \hbar \sum_{i=0} g_{i,i+1} (|i\rangle \langle i+1| \hat{a}^\dagger + |i+1\rangle \langle i| \hat{a}) \quad (2.89)$$

The term  $|i\rangle \langle i+1| \hat{a}^\dagger$  describes the creation of a photon in the resonator accompanied by the de-excitation of the n-level system by one energy level and the term  $|i+1\rangle \langle i| \hat{a}$  describes the opposite process.

## 2.4.1 Qubit Driving

When driving the qubit with a classical signal we can model the drive as a voltage  $V_d(t)$  coupled to the qubit gate charge. The coupling Hamiltonian in this case is given as

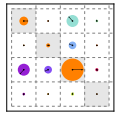
$$\hat{H}_d = 2\beta e V_d(t) \hat{n} \quad (2.90)$$

In the reduced  $\{|0\rangle, |1\rangle\}$  basis, this Hamiltonian can be written as

$$\hat{H}_d = 2\beta e V_d(t) \begin{pmatrix} 0 & n_{01}^* \\ n_{01} & 0 \end{pmatrix}, \quad (2.91)$$

where  $n_{01} = \langle 0 | \hat{n} | 1 \rangle$ . Usually, we apply the drive voltage through the resonator coupled to the qubit. That resonator acts then as a band-pass filter which filters the voltage seen by the qubit. For an input drive signal at a fixed frequency  $\omega$ ,  $V_{in}(t) = V_{in} \cdot \cos \omega t$ , the voltage  $V_d(t) = V_d \cdot \cos \omega t$  seen by the qubit at its gate capacitance is given as

$$V_d(t) = V_{in}(t) 2\sqrt{2} \frac{\sqrt{Z_r}}{\sqrt{Z_0}} \frac{Q_r / \sqrt{Q_{ext}}}{\sqrt{1 + 4Q_r^2(\omega_r - 1)^2}} \quad (2.92)$$



## 2.4.2 Dispersive Limit & Qubit Readout

When the qubit frequency is far detuned from the resonator frequency such that  $\Delta_{ij} = |\omega_{ij} - \omega_r| \gg g_{ij}$ , direct energy exchange between the qubit and the resonator is completely suppressed and only a dispersive shift of the transition frequency of both systems remains as an effect of the coupling between them. This effect has been discussed e.g. in [12, 54] and yields the effective Hamiltonian

$$\hat{H}_{eff} = \frac{\hbar\omega'_{01}}{2}\hat{\sigma}_z + (\hbar\omega'_r + \hbar\chi\hat{\sigma}_z)\hat{a}^\dagger\hat{a}, \quad (2.93)$$

where we have used the two-level qubit Hamiltonian as given by eq. (2.67). Here, the resonance frequencies of the qubit and the resonator are shifted as  $\omega'_{01} = \omega_{01} + \chi_{01}$  and  $\omega'_r = \omega_r - \chi_{12}/2$  and the dispersive shift is given as  $\chi = \chi_{01} - \chi_{12}/2$  [54], where  $\chi_{ij} = g_{ij}^2/(\omega_{ij} - \omega_r)$ . As can be seen, for a state with  $n$  photons the qubit transition frequency  $\omega_{01}$  is given as

$$\omega_{01}^n = \omega'_{01} + 2\chi n. \quad (2.94)$$

Thus, there is a dispersive shift of the qubit transition frequency that is proportional to the number of photons in the resonator. Likewise, the resonance frequency of the resonator gets also shifted by  $\pm\chi$  depending on the state of the qubit. This *cavity pull* is very useful since it allows us to read out the state of the qubit by measuring the state-dependent frequency displacement of the resonator, as will be explained now.

## 2.4.3 The Josephson Bifurcation Amplifier

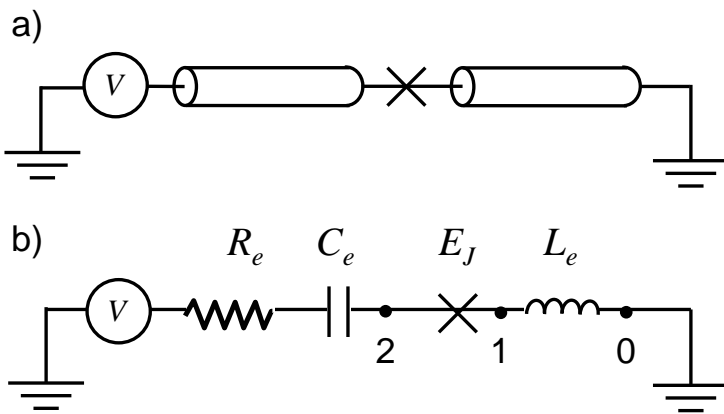


Figure 2.7: a) Circuit schematic of the CJBA, consisting of two parts of transmission line joined by a Josephson junction, forming a non-linear  $\lambda/2$  resonator. b) Equivalent lumped elements circuit model of the CJBA.

In this section we discuss the physics of superconducting nonlinear bifurcation amplifiers, which we use to realize a single-shot readout scheme for our qubits. Most notably, we discuss the so-called *cavity Josephson bifurcation amplifier (CJBA)*, as shown in fig. 2.7a. A detailed discussion of the CJBA can be found e.g. in [79]. The device consists

of a transmission line resonator with a Josephson junction embedded in its central conductor. We can model the whole circuit as a lumped elements resonator, as shown in fig. 2.7b. The Hamiltonian of the resonator, disregarding the resistor and the voltage source, is

$$H = \frac{\Phi_1^2}{2L_e} - E_J \cos\left(\frac{\Phi_2 - \Phi_1}{\varphi_0}\right) + \frac{Q_2^2}{2C_e}. \quad (2.95)$$

By using the current-phase relation of the Josephson junction we obtain the current

$$I = \frac{\Phi_1}{L_e} = I_0 \sin\left(\frac{\Phi_2 - \Phi_1}{\varphi_0}\right). \quad (2.96)$$

We can hence write  $\Phi_1 = g(\Phi_2)$ . When we develop this equation to second order in  $\Phi_2$  and insert in eq. (2.95), we obtain

$$H = \frac{\phi_2^2}{2L_t} + \frac{Q_2^2}{2C_e} - \frac{1}{24} p^3 \frac{\Phi_2^4}{L_t \varphi_0^2}, \quad (2.97)$$

where  $L_t = L_J + L_e$  and  $p = L_J/L_t$  is the so-called *participation ratio*. Quantizing this Hamiltonian and writing  $\Phi_2$  and  $Q_2$  in terms of creation and annihilation operators yields, up to second order, the Hamiltonian

$$H_{N_L} = \hbar \omega_r \left( \hat{a}^\dagger \hat{a} + \frac{K}{2} \hat{a}^{\dagger 2} \hat{a}^2 \right), \quad (2.98)$$

where  $\omega_r = 1/\sqrt{L_t C_e}$ ,  $R_K = h/e^2$  and  $K = -\pi p^3 Z_e / R_K$  is the so-called *reduced Kerr constant*. When subjecting the resonator to a classical drive signal

$$H_p/\hbar = \epsilon_p e^{-i\omega_p t} \hat{a}^\dagger + \text{h.c.}, \quad (2.99)$$

the complex amplitude of the intra-resonator field  $\alpha$  will satisfy the equation

$$i \left( \Omega \frac{\kappa}{2} \alpha + K |\alpha|^2 \alpha \right) + \frac{\kappa}{2} \alpha = -i \epsilon_p, \quad (2.100)$$

where  $\Omega = 2Q(1 - \omega_p/\omega_r)$ . For certain drive parameters, this equation has one or two stable solutions for  $\alpha$ . Fig. 2.8a shows the current in the resonator as a function of  $\Omega$ , plotted for several values of the drive power  $P_p \propto |\epsilon_p|^2$ . Fig. 2.8b shows the different regimes of the resonator as a function of the input power and the detuning  $\Omega$ . For drive frequencies with  $\Omega > \Omega_c = \sqrt{3}$ , a bistable region exists in the phase diagram, in which we typically operate the resonator when using it as a CJBA readout of our qubit. For this, we make use of the dispersive shift of the resonance frequency  $\omega_r$  caused by the qubit, which allows us to map the qubit state to one of the bistable resonator states.

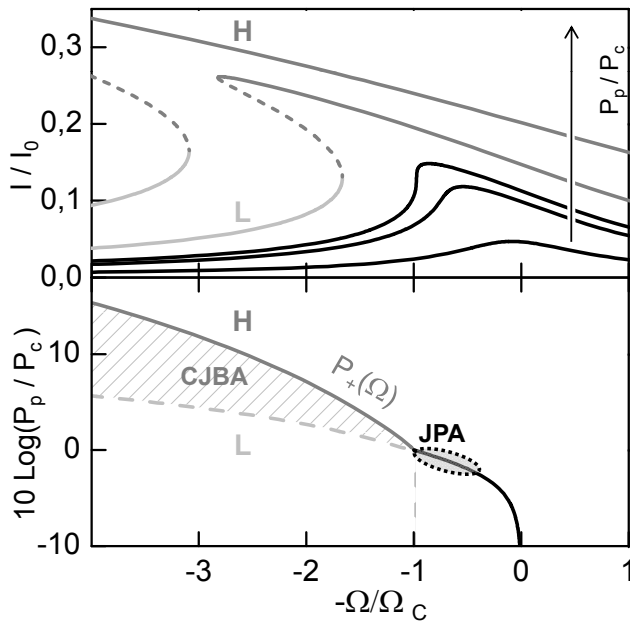
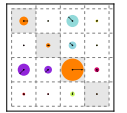


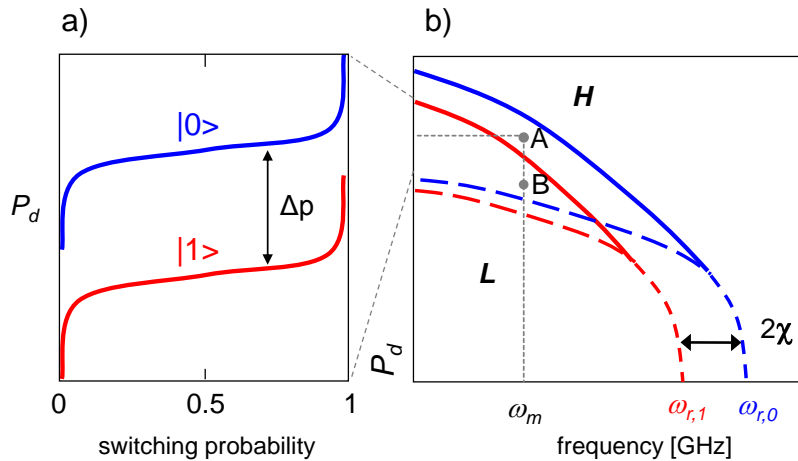
Figure 2.8: a) Current in the driven non-linear resonator as a function of the drive detuning  $\Omega$ , plotted for various drive powers  $P_p$ . For drive detunings  $\Omega > \Omega_c$ , the resonator becomes bistable above a certain power threshold  $P_p > P_c$ . b) Phase diagram of the non-linear resonator, showing the regions of bistability as a function of the drive power  $P_p$  and the drive detuning  $\Omega$ . For  $\Omega > \Omega_c$ , a bistable region exists that permits to operate the resonator as a CJBA.

### Operation Principle

We can use the CJBA to read out the qubit state using the dispersive interaction between the qubit and the resonator as given by eq. (2.93). Due to this interaction, the frequency of the resonator gets shifted depending on the qubit state by  $\pm\chi \simeq g_{01}^2/\Delta$  (neglecting the effect of higher Transmon levels), where  $\Delta = \omega_r - \omega_{01}$  is the frequency difference between qubit and resonator. Fig. 2.9b shows again the phase diagram of the CJBA, indicating the stability regions of the different solutions  $L$  (low-amplitude) and  $H$  (high-amplitude) of the driven system for two different qubit states. If we drive the resonator at a frequency  $\omega_m$  and ramp the drive power up to point  $A$  as indicated in the diagram, the resonator will remain in the low-amplitude state  $L$  if the qubit is in state  $|0\rangle$ , whereas it will switch to the high-amplitude state  $H$  if it is in  $|1\rangle$ . We can thus map the state of the qubit to one of the two states of the resonator, and since these two states can be easily distinguished by measuring the phase of the reflected resonator drive signal, we can obtain a single-shot readout of the qubit state. The measurement of the phase of the reflected drive signal has to be carried out during a long time interval (typically  $1 - 2 \mu\text{s}$ ) to distinguish between the two oscillator states with certainty. To avoid further switching processes during the measurement of the phase, we reduce the drive power of the resonator down to point  $B$  in fig. 2.9b. There, the switching probability of the resonator regardless of the qubit state is very small, thus virtually no switching events will occur and we can hence measure the phase of the reflected drive signal for an arbitrarily long time without being limited by spurious switching events. This phase of the readout is usually referred to as *latching*.

In theory, the CJBA readout method is able to achieve perfect readout fidelity. However, in reality several factors can degrade its performance:

Figure 2.9: a) The switching probability of the CJBA as a function of the input drive power, shown for the qubit in the states  $|0\rangle$  and  $|1\rangle$ . b) The bifurcation diagram of the CJBA, shown for the qubit in the states  $|0\rangle$  and  $|1\rangle$ . L and H indicate solutions with low and high amplitude, respectively.

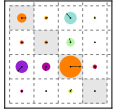


- Since the switching of the resonator is a stochastic process, the associated switching probability will exhibit a s-shaped dependence on the drive power, as shown in fig. 2.9. Now, if the shift of this distribution along the power axis which is induced by the shift of the resonator frequency that depends itself on the state of the qubit is less than the width of the distribution, there cannot be perfect mapping between the qubit and resonator states.
- If the qubit state changes during the measurement step at point A, e.g. due to qubit relaxation or excitation, the resonator state will, with high probability, also fall to the state corresponding to the new qubit state, thereby producing a wrong readout signal.
- The resonator state can switch back from  $H$  to  $L$  during the latching phase of the readout (so-called *retrapping*), producing a wrong readout value.

With the CJBA, a single-shot readout contrast of 93 % has been achieved in past experiments [63].

#### 2.4.4 Qubit-Qubit Interaction

In this section we discuss possible qubit-qubit coupling schemes. We regard a direct coupling scheme involving a capacitive coupling between two qubits and an indirect scheme involving the coupling of multiple qubits to a resonator which acts as a *quantum bus*.



## Direct Capacitive Coupling

A direct capacitive coupling  $C_{qq}$  between two qubits yields a coupling Hamiltonian of the form

$$\hat{H}_{qq} = \frac{1}{2}C_{qq}\hat{V}_{qq}^2 = \frac{1}{2}C_{qq}\left[\frac{2e}{C_{\Sigma 1}}(n_{g1} - \hat{n}_1) - \frac{2e}{C_{\Sigma 2}}(n_{g2} - \hat{n}_2)\right]^2 \quad (2.101)$$

$$= \frac{4e^2C_{qq}}{C_{\Sigma 1}C_{\Sigma 2}}\hat{n}_1\hat{n}_2 + \dots \quad (2.102)$$

Again, this equation is valid in the limit where  $C_{qq} \ll C_{\Sigma 1}, C_{\Sigma 2}$ . For larger capacitances  $C_{qq}$  the coupling gets renormalized by a factor  $\alpha = 1/(1 - C_{qq}^2/[C_{\Sigma 1}C_{\Sigma 2}])$  [74]. Rewriting this coupling in the basis of uncoupled qubit states yields the effective Hamiltonian

$$\hat{H}_{qq} = \hbar g_{qq}(\sigma_1^+ \sigma_2^- + \sigma_1^- \sigma_2^+), \quad (2.103)$$

where  $\sigma^+ = |1\rangle\langle 0|$  and  $\sigma^- = |0\rangle\langle 1|$  and  $\sigma_1^\pm = \sigma^\pm \otimes I$ ,  $\sigma_2^\pm = I \otimes \sigma^\pm$  and where we have defined the effective qubit-qubit coupling as  $\hbar g_{qq} = 4e^2C_{qq}/C_{\Sigma 1}C_{\Sigma 2}$ . Full energy exchange between the qubits is achieved when the qubit frequencies are on resonance. For the more general case of two coupled n-level Transmons, the coupling Hamiltonian takes a slightly more complicated form, as discussed in the Appendix. The time evolution operator of the Hamiltonian in eq. (2.103) yields a swapping interaction of the form

$$i\text{SWAP}(t, \Delta) = \begin{pmatrix} 1 & 0 & 0 & 0 \\ 0 & \cos tg_e - i\frac{\Delta}{g_e} \sin tg_e & i\frac{g_{qq}}{g_e} \sin tg_e & 0 \\ 0 & i\frac{g_{qq}}{g_e} \sin tg_e & \cos tg_e + i\frac{\Delta}{g_e} \sin tg_e & 0 \\ 0 & 0 & 0 & 1 \end{pmatrix}, \quad (2.104)$$

where  $\Delta = \omega_{01}^2 - \omega_{01}^1$  is the detuning between the qubits and  $g_e = \sqrt{4g_{qq}^2 + \Delta^2}$  is the effective swapping frequency. Using this interaction, it is straightforward to implement e.g. an  $\sqrt{i\text{SWAP}}$  or  $i\text{SWAP}$  quantum gate by tuning the qubits non-adiabatically from an off-resonant condition  $\Delta \gg g_{qq}$  to a resonance-condition  $\Delta = 0$  and letting them interact there for a well-defined time before re-establishing the large detuning, after  $t = \pi/4g_e$  for the  $\sqrt{i\text{SWAP}}$  gate and  $t = \pi/2g_e$  for the  $i\text{SWAP}$  gate.

## Coupling Bus

For this particular coupling scheme, which was first proposed by Zheng *et. al.* [106, 105, 76], we consider two (or more) Transmon qubits coupled to the same resonator. Blais *et. al.* [11] showed that extending the single-qubit rotating-wave Hamiltonian as given in eq. (2.89) to the case of two qubits coupled to a resonator yields an effective qubit-qubit

coupling Hamiltonian of the form

$$\hat{H}_{2q} = \hbar \frac{g_1 g_2 (\Delta_1 + \Delta_2)}{2\Delta_1 \Delta_2} (\sigma_1^+ \sigma_2^- + \sigma_1^- \sigma_2^+) \quad (2.105)$$

This approximation is valid in the limit of large qubit-resonator detuning where  $\Delta_1 \gg g_1, \Delta_2 \gg g_2$  with  $\Delta_{1,2} = \omega_{01}^{1,2} - \omega_r$  the detuning of the  $|0\rangle \rightarrow |1\rangle$  transition frequency of each qubit to the bus resonator. Full energy-exchange between the qubits is achieved when the qubit frequencies are on resonance. By detuning the qubits from the resonator, the effective coupling constant can be varied, which is often advantageous. The time evolution operator resulting from eq. (2.105) is identical to eq. (6.20) when taking into account the modified coupling constant  $g_{qq,r} = g_1 g_2 (\Delta_1 + \Delta_2) / 2\Delta_1 \Delta_2$ .

### 2.4.5 Qubit Decoherence in CQED

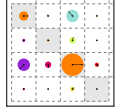
In this section we discuss new relaxation and dephasing mechanisms specific to the CQED architecture.

**Relaxation** In CQED, the qubit is coupled capacitively to a resonator, which itself is coupled to a low-Q input transmission line. The qubit can relax into this transmission line through the gate circuit. The resulting relaxation rate is given by eq. (2.76). If we assume that the Transmon sees only the impedance of the readout resonator through its gate capacitance, as given by eq. (2.34), we can insert the impedance of the resonator in the equation and obtain the resulting relaxation rate:

$$\begin{aligned} \Gamma_1^{Purcell} &= 2\pi \frac{\omega_{01}}{Z_0 \omega_r^2} g_{01}^2 \operatorname{Re}[Z(\omega_{01})] \\ &= \kappa \cdot \frac{g_{01}^2}{\Delta^2 + \kappa^2/4} \end{aligned} \quad (2.106)$$

As can be seen, the rate is proportional to  $(\Delta^2 + \kappa^2/4)^{-1}$  ( $\approx \Delta^{-2}$  for  $\Delta \gg \kappa$ ). The relaxation (or emission) rate of the Transmon compared to the relaxation rate of a qubit get thus modified by the presence of the resonator, which is the so-called *Purcell effect* [82]. For our processor, this effect is advantageous since it shields the qubit from the low impedance environment presented by the input transmission line and increases thus its relaxation time compared to a direct gate coupling to the input line. For a real-world qubit chip, we have to take into account further capacitive couplings of the qubit to e.g. the fast flux line, which will also contribute to the relaxation rate.

**Dephasing** Besides the usual mechanisms discussed above, dephasing can also occur due to photon-number fluctuations that can occur when the resonator is not in state



$|0\rangle$ , e.g. due to thermal noise or during readout. These fluctuations affect the qubit frequency through the induced AC-Stark shift (2.94) [9, 10, 85].

The sensitivity of the qubit to fluctuations of the photon number  $n$  can be derived in the dispersive limit from the Hamiltonian (2.93) as

$$\delta\hat{H}_{\bar{n}} = \hbar\delta\bar{n}\chi\hat{\sigma}_z = -\frac{\hbar}{2}(\hat{D}_{\bar{n}} \cdot \hat{\sigma}_z) \cdot \delta\bar{n}, \quad (2.107)$$

where  $\hat{D}_{\bar{n}} = -2\chi$ . When driving the resonator, shot-noise induced photon number fluctuations  $\delta n$  will randomly change the transition frequency of the qubit through the AC Stark effect and cause the qubit phase  $\phi(t)$  to diffuse. In the limit where  $\kappa \gg \gamma$ , we can model the dephasing according to the equation

$$\delta\phi(t) = 2\chi \int_0^t d\tau \delta n(\tau) \quad (2.108)$$

The dephasing rate of the qubit induced by this noise can be calculated from the correlator

$$\langle \hat{\sigma}_-(t)\hat{\sigma}_+(0) \rangle = \langle e^{-i\delta\phi(t)} \rangle. \quad (2.109)$$

Here, for a linear resonator with a loss rate  $\kappa$ , the correlator of the photon-number noise  $\delta n(t)$  is given as

$$\langle \delta n(t_1)\delta n(t_2) \rangle = \bar{n}e^{-\frac{\kappa}{2}|t_1-t_2|} \quad (2.110)$$

Inserting this in eq. (2.109) yields a dephasing rate in the limit  $t \gg \kappa$  of

$$\Gamma_{\phi}^{\bar{n}} = \frac{8\chi^2}{\kappa}\bar{n} \quad (2.111)$$

As expected, the dephasing rate depends on the dispersive shift  $\chi$  and the resonator photon loss-rate  $\kappa$ . For thermal photon noise, the correlator given above in eq. (2.110) is slightly modified to

$$\langle \delta n(t_1)\delta n(t_2) \rangle = \bar{n}_{th}(\bar{n}_{th} + 1)e^{-\frac{\kappa}{2}|t_1-t_2|}, \quad (2.112)$$

yielding a modified dephasing rate

$$\Gamma_{\phi}^{\bar{n}_{th}} = \frac{8\chi^2}{\kappa}\bar{n}_{th}(\bar{n}_{th} + 1) \quad (2.113)$$

The dephasing induced through photon number shot-noise during the readout is relevant when performing measurements of the qubit state. Thermal photon-noise induced dephasing can be relevant when the thermal photon distribution in the resonator is not negligible. We will take both dephasing mechanisms into account in the design of our

processor, as discussed in chapter 3.

## 2.5 Master Equation Formalism

As already explained, the qubits that we use in this work are subjected to decoherence. This means that their quantum state will at least partially evolve in a non-unitary way, making it impossible to model their evolution using a Schrödinger equation approach alone. In this work we will therefore employ the *master equation approach*, which is a more powerful formalism that can treat the qubit register as an *open quantum system* which interacts with its environment.

A detailed introduction to the master equation formalism can be found e.g. in [46]. Here we give only a brief overview of the most relevant concepts and results. A quantum system  $A$ , described by its density matrix  $\rho_A$  defined in a Hilbert space  $\mathcal{H}_A$ , interacts with an environment  $E$  that induces a non-unitary evolution of the density operator  $\rho_A$ .

In general, any evolution of the quantum system  $\rho_A$  between two points in time can be described by a so-called *quantum map*. Such a quantum map transforms  $\rho_A$  into a new matrix  $\mathcal{L}_A(\rho_A)$  and can be described as a linear *super-operator* acting in the space of operators defined in  $\mathcal{H}_A$ . To be a valid quantum operator,  $\mathcal{L}_A$  must fulfill the following conditions:

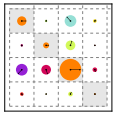
- **Linearity:** The operator  $\mathcal{L}_A$  must be linear, i.e.  $\mathcal{L}_A(p\rho_A + q\rho'_A) = p\mathcal{L}_A(\rho_A) + q\mathcal{L}_A(\rho'_A)$  with  $p + q = 1$ .
- **Preservation of  $\text{Tr}(\rho_A)$ :** The operator  $\mathcal{L}_A$  must preserve the unity trace of  $\rho_A$ , i.e.  $\text{Tr}(\mathcal{L}_A(\rho_A)) = 1$ .
- **Complete Positivity:**  $\mathcal{L}_A(\rho_A)$  must be positive, i.e.  $\langle \phi^{(A)} | \mathcal{L}_A(\rho_A) | \phi^{(A)} \rangle \geq 0$  for all  $|\phi^{(A)}\rangle$  in  $\mathcal{H}_A$ . In addition, for any composite quantum system  $A \otimes B$ , the quantum map  $\mathcal{L}_A \otimes 1_B$  (where  $1_B$  is the identity super-operator acting in  $\mathcal{H}_B$ ) must be positive, i.e.

$$\langle \phi^{(AB)} | \mathcal{L}_A \otimes 1_B(\rho_{AB}) | \phi^{(AB)} \rangle \geq 0$$

for all  $|\phi^{(AB)}\rangle$  in  $\mathcal{H}_{AB}$ .

Under these conditions it can be shown that any quantum map  $\mathcal{L}_A$  can be expressed as a sum of operators [55]

$$\mathcal{L}_A(\rho_A) = \sum_{\mu}^{N_k} M_{\mu} \rho_A M_{\mu}^{\dagger} \quad (2.114)$$



where  $N_k \leq N_A^2$  and  $N_A$  is the dimension of the Hilbert space  $\mathcal{H}_A$  and  $M_\mu$  are the *Kraus operators* of the quantum map. These operators satisfy the normalization condition

$$\sum_{\mu=0} M_\mu^\dagger M_\mu = 1. \quad (2.115)$$

Now, we can also use a quantum map  $\mathcal{L}_\tau$  to describe the evolution of a density matrix  $\rho_A(t)$  during an infinitesimal time  $\tau$ . In this case, we approximate the time derivative of  $\rho(t)$  as

$$\frac{d\rho_A(t)}{dt} = \frac{\mathcal{L}_\tau[\rho_A(t)] - \rho_A(t)}{\tau}. \quad (2.116)$$

In order for this approximation to be valid,  $\tau$  needs to be longer than the “memory time” of correlations between the system  $A$  and its environment and smaller than the characteristic evolution time of system A [46]. In general, since  $\mathcal{L}_\tau \rightarrow \mathbb{1}$  for  $\tau \rightarrow 0$ , the Kraus operators  $M_\mu$  of the process  $\mathcal{L}_\tau$  will depend on  $\tau$  and can be usually written as  $M_\mu = \sqrt{\tau} L_\mu$ , where the  $L_\mu$  are the time-independent *Lindblad operators*. By developing eq. (2.116) up to first order in  $\tau$ , we obtain the so-called *Lindblad master equation*

$$\frac{d\rho_A}{dt} = -\frac{i}{\hbar}[H_A, \rho] + \sum_{\mu=1} \left( L_\mu \rho_a L_\mu^\dagger - \frac{1}{2} L_\mu^\dagger L_\mu \rho_A - \frac{1}{2} \rho_A L_\mu^\dagger L_\mu \right), \quad (2.117)$$

This equation describes the evolution of quantum system under a Hamiltonian  $H_A$  and coupled to an environment that is simulated by the non-unitary action of the operators  $L_\mu$ . Often these operators can be guessed or derived from the relevant decoherence mechanism present in the quantum system. We will make extensive use of eq. (2.117) in this work to simulate the dynamics of the qubit register of our quantum processor and fit experimental data to a master equation model of our system.

### 2.5.1 Simulation of our Two-Qubit Processor

To simulate our two qubit processor using the master equation formalism, we will normally use a model that takes into account only the levels  $|0\rangle$  and  $|1\rangle$  of each qubit. However, in order to e.g. quantify the effect of the finite qubit anharmonicity, we are forced to take into account the state  $|2\rangle$  of the Transmon as well, which leads to a slightly more complicated Hamiltonian that we discuss in section A.2. For the simple two-level variant, the Hamiltonian of the two-qubit system can be written as

$$\hat{H} = \hat{H}_1^d \otimes \mathbb{I} + \mathbb{I} \otimes \hat{H}_2^d + \hat{H}_{qq} \quad (2.118)$$

where  $\hat{H}_1^d$  and  $\hat{H}_2^d$  are the drive Hamiltonians of the first and second qubit, respectively, and are given as

$$\hat{H}_{1,2}^d = \alpha_{1,2}(t)\hat{\sigma}_x + \beta_{1,2}(t)\hat{\sigma}_y + \gamma_{1,2}(t)\hat{\sigma}_z, \quad (2.119)$$

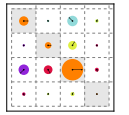
where  $\alpha_{1,2}(t)$  and  $\beta_{1,2}(t)$  are complex functions and  $\gamma_{1,2}(t)$  are real-valued functions. The interaction Hamiltonian in the frame rotating at the average qubit-frequency  $(\omega_{01}^1 + \omega_{01}^2)/2$  is given as

$$\hat{H}_{qq} = \begin{pmatrix} 0 & 0 & 0 & 0 \\ 0 & -\frac{\Delta(t)}{2} & g & 0 \\ 0 & g & +\frac{\Delta(t)}{2} & 0 \\ 0 & 0 & 0 & 0 \end{pmatrix}, \quad (2.120)$$

where  $\Delta(t) = \omega_{01}^2(t) - \omega_{01}^1(t)$  is the time-dependent frequency detuning between the two qubits. Inserting the Hamiltonian in eq. (2.118) into eq. (2.117) we can simulate the operation of the two qubit Hamiltonian. To model qubit relaxation and decoherence, we use for each qubit two Lindblad operators of the form  $L_{01}^{r,i} = \sqrt{\Gamma_{01}^{r,i}}\hat{\sigma}_{01}^-$  and  $L_{01}^{\phi,i} = \sqrt{\Gamma_{01}^{\phi,i}/2}\hat{\sigma}_{01}^z$ , where  $i \in \{1, 2\}$  and  $\Gamma_{01}^{r,i}$  and  $\Gamma_{01}^{\phi,i}$  are the effective relaxation and dephasing rates of each qubit, respectively, and where  $\hat{\sigma}_{01}^-$  and  $\hat{\sigma}_{01}^z$  are matrices

$$\hat{\sigma}_{01}^- = \begin{pmatrix} 0 & 1 \\ 0 & 0 \end{pmatrix} \quad \hat{\sigma}_{01}^z = \begin{pmatrix} 1 & 0 \\ 0 & -1 \end{pmatrix} \quad (2.121)$$

that describe a relaxation or dephasing process, respectively. The relaxation and dephasing rates depend on the qubit frequency and can be adapted in the simulation according to the chosen qubit frequency working point. Single-qubit gate sequences are fully described by the three functions  $\alpha_{1,2}(t)$ ,  $\beta_{1,2}(t)$  and  $\gamma_{1,2}(t)$ , a two-qubit swap gate can be modeled by changing the parameter  $\Delta(t)$ .



# Chapter 3

## Realizing a Two-Qubit Processor

This chapter discusses the design and fabrication processes of the two-qubit processor used in this thesis work. We start by introducing the general constraints faced when designing our two-qubit processor, followed by a component-wise discussion of its individual parts and the associated parameters we need to choose for them.

### 3.1 Introduction & Motivation

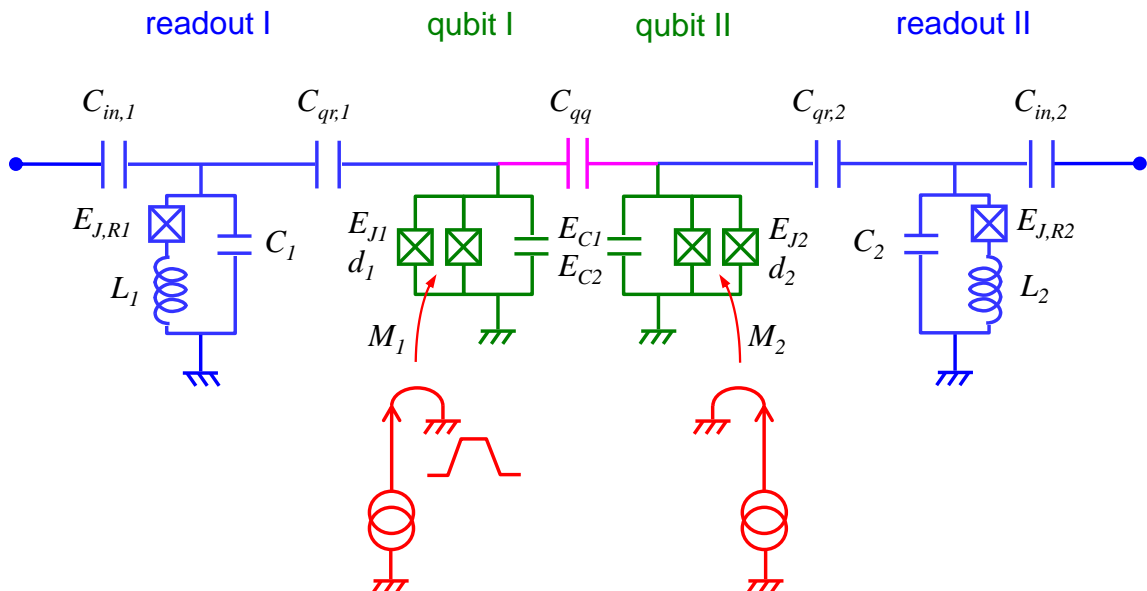


Figure 3.1: The circuit schematic of the two-qubit processor used in this work, together with all parameters that have to be chosen. Shown are the two Transmon qubits in green, the drive and readout circuit in blue, the fast flux lines in red and the coupling capacitance in magenta.

As discussed in the introduction, the most simple imaginable quantum processor consists of two qubits that can be manipulated and read out individually, and between

### 3.1. INTRODUCTION & MOTIVATION

which one can realize a universal two-qubit gate. We implement such a two-qubit processor using two Transmon qubits that are coupled by a fixed capacitor and that can be read out individually by a pair of cavity Josephson bifurcation amplifiers (CJBAs). Figure 3.1 shows the circuit diagram of our processor with all relevant design parameters. Shown are the two qubits in green, the drive and readout circuit in red, the coupling capacitance between them in magenta, and in red fast flux lines required to tune the qubit frequencies (as we show below).

#### 3.1.1 Processor Operation

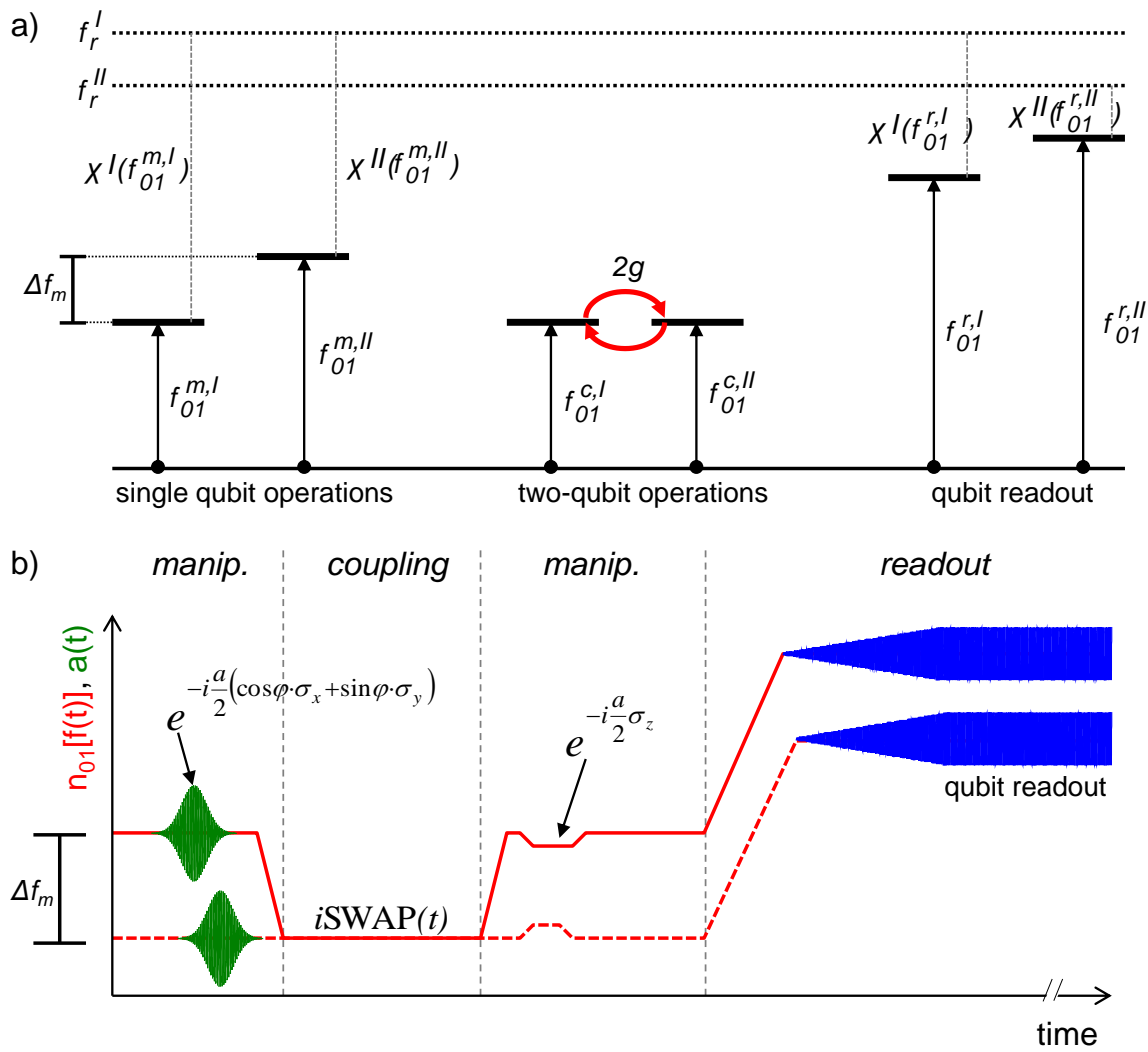
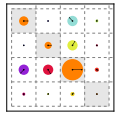


Figure 3.2: Operation principle of the two-qubit processor. a) The qubit frequencies for different operations. I: Single-qubit manipulation and parking. II: Two-qubit coupling. III: Qubit readout. For each operation, different qubit frequencies are chosen, resulting in different qubit-qubit coupling and qubit-readout couplings  $\chi_r^{I,II}(f_{01}^{I,II})$ . b) Typical gate sequence illustrating the different operations. The sequence consists of two single-qubit XY-gates, a two-qubit  $i\text{SWAP}(t)$  gate, two single-qubit Z-gates and ends with the qubit readout.



We want to perform three basic operations with the quantum processor:

- **Single-qubit gates:** Manipulating a single qubit by rotating its Bloch vector around the  $X$ ,  $Y$  or  $Z$  axis of the Bloch sphere.
- **Two-qubit gate:** Performing a (universal) two-qubit gate, in this work in particular the  $\sqrt{i\text{SWAP}}$  and  $i\text{SWAP}$  gates.
- **Qubit readout:** Performing single-shot readout of the state of each qubit, possibly simultaneously for both of them.

The parameter requirements for each of these operations are usually conflicting: For single-qubit manipulation, no interaction between the qubits must be present, hence the qubit frequencies need to be strongly detuned. However, to implement the two-qubit gates, strong resonant interaction between the qubits is required, hence the two qubit frequencies should be resonant. Furthermore, during qubit manipulation the relaxation of the qubit state through the readout resonator should be negligible, hence the frequency detuning  $\Delta$  between each qubit and its readout resonator should be large, as shown by eq. (2.106). On the other hand, to obtain a high state fidelity during the readout of the qubit state, the interaction between the qubit and its readout resonator should be large, which requires a small frequency detuning  $\Delta$  between the two.

We solve these conflicting requirements by dynamically changing the qubit frequencies during the operation of the processor using fast on-chip flux lines. Fig. 3.2 illustrates this basic operating principle of the two-qubit processor: For each of the three basic operations (single-qubit manipulation, two-qubit gate and readout), we choose a different set of qubit frequencies  $f_{01}^{I,II}$ . For the single-qubit gates, the two frequencies  $f_{01}^{m,I}$  and  $f_{01}^{m,II}$  are detuned by  $\Delta f_m = f_{01}^{m,II} - f_{01}^{m,I}$ . This tuning is chosen such that only negligible qubit-qubit interaction is present when performing single-qubit manipulations or no operation. Furthermore, at this working point the detuning between each qubit and its readout resonator is such that the qubit lifetime is not limited by relaxation through the gate circuit. To realize a two qubit gate, the two qubits get tuned in resonance such that  $f_{01}^{c,I} = f_{01}^{c,II}$ . At this point, the qubits experience a swapping interaction as given by eq. (2.103) with an effective swapping frequency  $2g$ . For the readout, we change the qubit frequencies to  $f_{01}^{r,I}$ ,  $f_{01}^{r,II}$ , reducing the qubit-resonator detuning such that the corresponding dispersive shift  $\chi^I(f_{01}^{r,I})$  and  $\chi^{II}(f_{01}^{r,II})$  of the resonator during readout assures an optimal readout fidelity. The displacement of the qubit frequency between the different working points has to be performed on a time scale faster than all relevant qubit manipulation and coupling frequencies but not as a fast as to induce transitions of the qubit state.

We discuss now the parameters of each component of the processor in greater detail, explaining each time the relevant design goals and possible conflicts and presenting the parameter choice or compromise we arrive at.

## 3.2 Qubit Design

The main design goals for the qubits are large coherence times, good frequency tunability and the possibility of fast single-qubit driving. Good frequency tunability is important since we need to move the qubits to different frequency working points for single-qubit and two-qubit manipulation as well as qubit readout. The maximum qubit drive frequency should be large compared to the decoherence times of the qubit, so that we are able to perform a large number of gate operations on the qubit before its coherence is destroyed, which is crucial when running quantum algorithms.

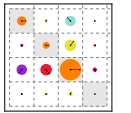
### 3.2.1 Qubit Frequency & Junction Asymmetry

The choice of the maximum qubit frequency is influenced by several requirements:

- The density of thermal photons at the qubit frequency should be sufficiently low at the operating temperature of the circuit (typically 20-100 mK) such that the thermal excitation of the qubit into higher energy levels is negligible.
- Robust equipment for signal generation and measurement in the frequency range of the qubit should be available. This includes microwave sources needed to generate the charge drive pulses as well as room-temperate and cryogenic microwave components such as mixers, splitters, circulators and amplifiers.
- The design of microwave circuits is all the more easy, the lower the required frequency range.

In addition, the choice of the qubit frequency also influences the choice of the readout resonator frequency. For our qubits, we choose a minimum transition frequency of  $\omega_{01}^{1,2}/2\pi = 4$  GHz, which ideally yields a negligible excited state occupation probability of  $p(|1\rangle) = 1/[1 + \exp(\hbar\omega/k_B T)] = 2.1\%$  at  $T = 50$  mK. In addition, in the frequency range 2 – 18 GHz, commercial microwave equipment and components are available for both room-temperature as well as cryogenic applications. A qubit frequency tunability bandwidth of 3 GHz being sufficient for the operation of the processor, we choose a maximum qubit frequency  $\omega_{01}^{max}/2\pi = 7$  GHz.

As described in chapter 2, we use a split Josephson junction geometry as shown in fig. 2.4b to make the Josephson energy of the qubit tunable by an external flux  $\Phi_{ext}$ . The



modulation depth of  $E_J(\Phi_{ext})$  is given by eq. (2.58): The higher the junction asymmetry  $d$ , the smaller the modulation depth of the Josephson energy  $\simeq 1 - d$ . In general, it can be advantageous to operate the qubit at a working point where  $\partial E_J(\Phi)/\partial\Phi = 0$  since at that point the qubit will be insensitive to flux noise at first order. Hence we chose an asymmetry  $d \approx 0.35$  so that the minimum qubit frequency coincides with our lower boundary frequency of 4 GHz.

### 3.2.2 Single-Qubit Gates

We distinguish between single-qubit rotations around the  $X$  and  $Y$  axes and around the  $Z$  axis of the Bloch sphere. The latter are implemented by changing the qubit frequency using a fast on-chip flux line, whereas the former are implemented by driving the qubit with an oscillatory electrical drive signal at its resonance frequency. For the  $X/Y$  gates, it is necessary to capacitively couple the qubit to an external charge driving circuit.

**Charge Driving** The maximum drive frequency of the qubit is limited by its anharmonicity: Since the Transmon qubit is only weakly anharmonic, when driving the qubit at a frequency comparable to the qubit anharmonicity, transitions to higher Transmon levels will be induced, therefore producing a leakage of the qubit state out of the computational basis and hence unitary drive errors. This effect can be partially alleviated by increasing the anharmonicity of the qubit. However, by increasing the anharmonicity, one also increases the sensitivity of the qubit to charge noise. Hence it is necessary to find a compromise for the value of the qubit anharmonicity which allows sufficiently fast qubit driving but which does not incur too much dephasing.

To estimate the drive error arising due to the finite anharmonicity of a Transmon, we model its driving using a simple three-level Hamiltonian in the rotating-frame, as used e.g. in [72]:

$$\hat{H} = \alpha \begin{pmatrix} 0 & \epsilon^*(t)/\alpha & 0 \\ \epsilon(t)/\alpha & \delta/\alpha & \sqrt{2}\epsilon^*(t)/\alpha \\ 0 & \sqrt{2}\epsilon(t)/\alpha & 2\delta/\alpha + 1 \end{pmatrix} \quad (3.1)$$

Here,  $\epsilon(t) = \epsilon_x(t) + i\epsilon_y(t)$  is the complex drive IQ amplitude in the rotating qubit frame,  $\delta$  is the detuning of the microwave drive from the Transmon  $\omega_{01}$  transition frequency and  $\alpha$  is the Transmon anharmonicity. Due to the presence of the third energy level, the effective  $|0\rangle \rightarrow |1\rangle$  transition frequency will get shifted with respect to the bare frequency  $\omega_{01}$  when driving the qubit. For  $\delta = \alpha = 0$ , the characteristic polynomial of  $\hat{H}$  is given as  $E(E^2 - 3|\epsilon|^2/4) = 0$  with the two eigenvalues  $E = \pm|\epsilon|\sqrt{3}/2$ . Thus, for weak anharmonicities this frequency shift is given approximately as  $\Delta_{ac} = \sqrt{3}|\epsilon|/2$ . To estimate the leakage to the Transmon level  $|2\rangle$  when driving the system, we calcu-

### 3.2. QUBIT DESIGN

---

late the eigenvalues and eigenvectors of the Hamiltonian (3.1). We then decompose an initial state  $|0\rangle$  in the basis of eigenstates of  $\hat{H}$  and calculate its evolution operator  $U_d(t, \delta, \epsilon_0)$  under a constant drive amplitude  $\epsilon_0$ . By numerically maximizing the occupation probability of the state  $|1\rangle$  as a function of the evolution time  $t$  and the drive detuning  $\delta$  we obtain the ideal gate time, gate error and frequency shift for a  $\pi$ -pulse at a given drive frequency/anharmonicity ratio. In fig. 3.3 we show these quantities as a function of  $\epsilon/\alpha$ . As can be seen, the gate error due to leakage into the level  $|2\rangle$  increases with the drive frequency. For very large drive frequencies, the gate fidelity saturates at a value of  $F \approx 0.86$  (the numerically obtained maximum  $\pi$ -pulse fidelity for ultra-strong driving of the three-level system is  $F_{max} \approx 0.895$ ). We can make use of fig. 3.3 to estimate the minimum required qubit anharmonicity given the desired gate fidelity and gate time. If we demand a maximum Rabi frequency  $\epsilon/2 = \Omega_{Rabi}^{max} = 2\pi \cdot 100$  MHz, which corresponds to a gate time for a single-qubit  $\pi$ -pulse of  $T_\pi = 5$  ns small compared to the targeted relaxation and dephasing times of the qubit of  $T_1, T_\phi \simeq 1 \mu$ s, and a maximum  $\pi$ -gate error of  $1 - F_\pi = 0.04$ , we need an absolute anharmonicity  $\alpha > 250$  MHz.

It is possible to correct leakage errors using optimized DRAG drive pulses [61, 17], thereby eliminating leakage to the third qubit level. In this work, we did not use such techniques but we will include possible errors arising due to this leakage to higher Transmon levels in our error models when discussing experimental data.

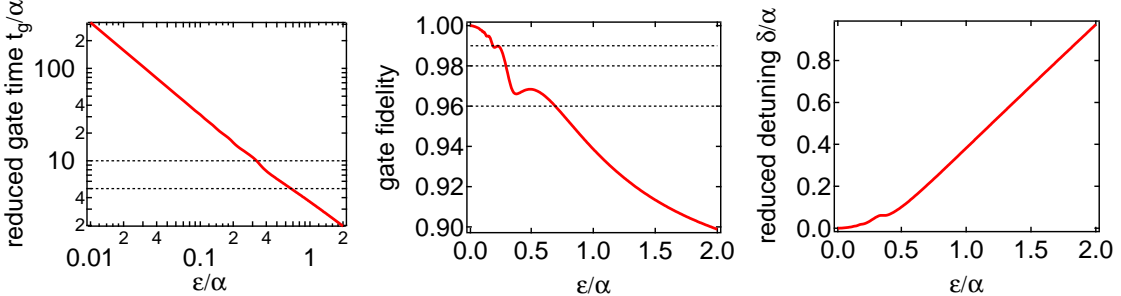
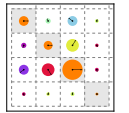


Figure 3.3: The single-qubit  $\pi$ -pulse gate time, gate fidelity and AC Stark detuning, plotted as a function of the reduced drive strength  $\epsilon/\alpha$  applied to the three-level Transmon. As the drive strength increases, the gate time decreases as  $\alpha/\epsilon$  whereas the gate fidelity decreases non-monotonously.

Furthermore, charge driving of the qubit is done through the readout resonator on the chip, as shown in fig. 3.1. The Rabi frequency of the qubit in eq. (2.91) is given as  $\Omega_{Rabi} = 2\beta e V_d \langle 0 | \hat{n} | 1 \rangle$ , where the drive voltage  $V_d$  seen at the qubit gate capacitance depends on the input voltage  $V_{in}$  at the input capacitance of the resonator as given by eq. (2.92). Since the resonator acts as a band-pass filter for the input drive signal, the more the drive frequency  $\omega_d$  is detuned from the resonator frequency  $\omega_r$ , the smaller the gate voltage seen by the qubit is. A Rabi frequency of  $\Omega_{Rabi}^{max}/2\pi = 100$  MHz at  $\omega_{01}/2\pi = 4$  GHz corresponds to  $V_{in} = 0.4$  mV for the resonator parameters that we



will choose below,  $\omega_r/2\pi = 6.7$  GHz,  $g_{01}/2\pi = 50$  MHz and  $Q = 800$ . With 70 dB attenuation inside the cryostat this corresponds to an input power of  $P \approx 15$  dBm at room temperature, which is compatible with our microwave setup.

**Flux Driving** To rapidly change the flux in the qubit loop, we couple each qubit inductively to a fast flux line. The flux induced in the qubit loop by this line is given as  $\Phi_{ext} = MI_{fl}$ , where  $I_{fl}$  is the current in the line and  $M$  is the mutual inductance between the flux line and the qubit loop, which can be estimated as  $M = \mu_0 l \ln [(d_f + w)/d]/2\pi$ , where  $l$  is the length of the qubit loop parallel to the flux line,  $d_f$  the distance of the loop to the line and  $w$  the width of the qubit loop perpendicular to the flux line. In order to avoid sample heating through the flux line, we demand a maximum current for inducing one flux quantum  $\Phi_0$  in the loop not in excess of  $I_{\Phi_0}^{max} = 10$  mA, corresponding to an electrical input power of  $P_{in}^{max} = 50$  mW on a  $50 \Omega$  transmission line with 20 dB attenuation and  $P_{out}^{max} = 500 \mu\text{W}$  on the output transmission line, which can be easily dissipated on the 1 K stage of the cryostat. This yields a minimal value of the mutual inductance  $M \geq 0.23$  pH, which can easily be achieved with a qubit loop of  $l = w = 4 \mu\text{m}$  at a distance  $d_f = 12 \mu\text{m}$  to the flux line. The coupling of the qubit to the flux line also induces decoherence that we will take into account later when confirming our choice of  $M$ .

In general, when passing a low-frequency or DC current through the flux line, superconducting shielding currents will build up in the ground plane around the line. Therefore, we usually remove the ground plane between the center pin of the flux line and the qubit loop, since otherwise the induced shielding currents will modify the effective flux seen by the qubit and lead to unwanted distortions in the shape of the applied flux signal. However, removing this ground plane also leads to stronger capacitive coupling of the qubit to the flux line, thereby increasing qubit relaxation, which we also have to take into account.

### 3.2.3 Qubit-Qubit Coupling

We use a direct capacitive coupling between our qubits to create an interaction between them suitable to implement a two-qubit gate. The full interaction Hamiltonian is given by eq. (6.20), and the coupling strength  $g_{qq}$  between the two qubits can be calculated with eq. (2.102). This coupling strength must be chosen such that the interaction between the qubits is sufficiently fast to realize two-qubit gate operations with adequate fidelity, but not too strong in order to still allow to sufficiently suppress the coupling by detuning the qubit frequencies, as needed. By diagonalizing the Hamiltonian (2.103) we find for the eigen-energies  $E_{qq}^\pm$ , the swapping frequency  $f_{qq}$  and the swap amplitude  $a_{qq}$  of the

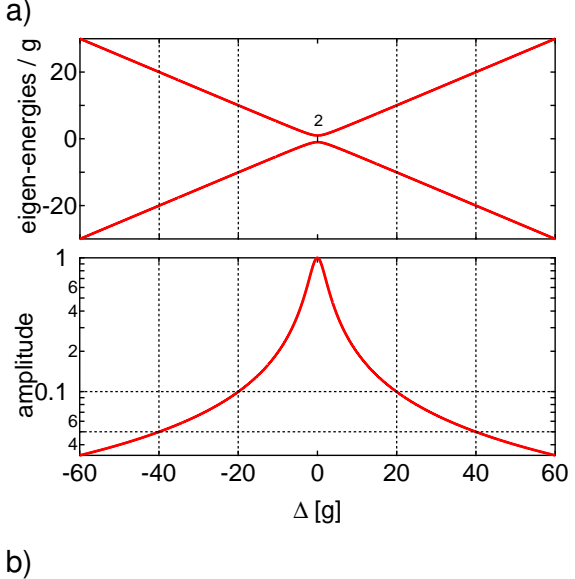
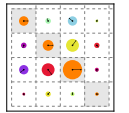


Figure 3.4: a) The two-qubit eigen-energies  $E_{\pm}$  and swapping amplitude  $a_{qq}$  as given by eqs. (3.2). For  $\Delta \gg g$ , the amplitude of the swap decreases  $\propto 1/\Delta$  and the frequency increases  $\propto \Delta$ . To effectively switch off the swapping interaction to  $a_{qq} = 0.1$ , a detuning of  $\Delta = 20g$  is required. b) Illustration of the swapping amplitude and frequency on the  $|01\rangle, |10\rangle$  Bloch sphere: The rotation axis depends on the ratio  $\Delta/g$ , for  $\Delta = 0$  it coincides with the  $x$  axis whereas for  $\Delta \gg g$  it asymptotically approaches the  $z$  axis. At the same time, the frequency of rotation around this axis increases  $\propto \Delta$ .

two coupled qubits as a function of the qubit-qubit detuning  $\Delta/2\pi = f_{01}^I - f_{01}^{II}$  the values

$$\begin{aligned} E_{qq}^{\pm} &= \pm \frac{1}{2} \sqrt{4g_{qq}^2 + \Delta^2}, \\ f_{qq} &= \sqrt{4g_{qq}^2 + \Delta^2}, \\ a_{qq} &= \frac{2g_{qq}}{\sqrt{4g_{qq}^2 + \Delta^2}}. \end{aligned} \quad (3.2)$$

Figure 3.4 shows the eigen energies and qubit-qubit swapping amplitude as a function of the normalized qubit-qubit detuning  $\Delta/g$ . As can be seen, for  $\Delta \gg g$  the swap amplitude decreases  $\propto 1/\Delta$  whereas the swap frequency increases  $\propto \Delta$ . For our processor, we demand that the residual swapping amplitude  $a \leq 0.1$  when the qubits are “parked” for single-qubit gates and readout, hence it is necessary to de-



tune the qubits by  $\Delta \approx 20g$ . At this detuning, the swapping frequency is given as  $f_{qq}(20g) \approx 20g$ . For our processor, we choose  $2g/2\pi = 10$  MHz, corresponding to a qubit-qubit detuning of 200 MHz at  $a_{qq} = 0.1$  and an associated swapping frequency  $f_{qq} = 100$  MHz =  $(10\text{ ns})^{-1}$ . The required frequency displacement is easily achievable with the on-chip fast flux lines. On resonance, the swap frequency of 10 MHz allows us to realize an  $\sqrt{i\text{SWAP}}$  gate in 25 ns and an  $i\text{SWAP}$  gate in 50 ns, which is sufficiently fast compared to the estimated relaxation and dephasing times of the qubits. The residual swapping between the qubits at their parking position is usually small enough to be irrelevant for most experiments performed in this work. However, when executing long gate sequences, as required for certain algorithms, the induced error may be too large, hence a larger detuning should be chosen for these cases.

To estimate the error due to finite rise times for the flux pulse before the  $i\text{SWAP}$  gate, we numerically solve the Schrödinger equation of the 2-qubit system in the  $|01\rangle, |10\rangle$  basis, which is given as

$$i\hbar \begin{pmatrix} \dot{\psi}_{01} \\ \dot{\psi}_{10} \end{pmatrix} = \begin{pmatrix} -\frac{\Delta(t)}{2} & g \\ g & \frac{\Delta(t)}{2} \end{pmatrix} \cdot \begin{pmatrix} \psi_{01} \\ \psi_{10} \end{pmatrix} \quad (3.3)$$

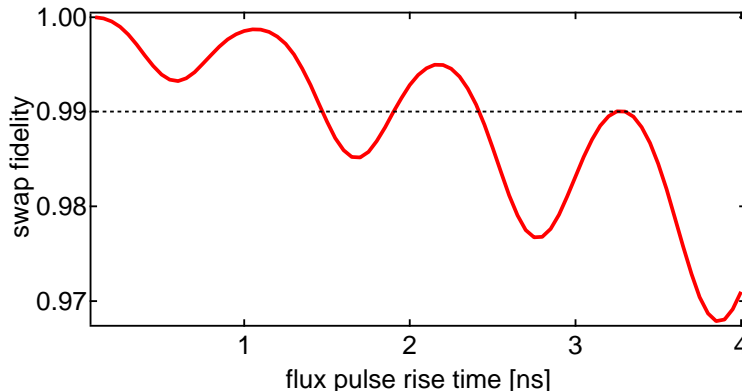


Figure 3.5: Numerically obtained maximum fidelity of a two-qubit  $i\text{SWAP}$  gate realized by changing the detuning  $\Delta$  in eq. (3.3) from  $\Delta = 20g$  to  $\Delta = 0$  using a Gaussian pulse of width  $\delta t$ .

To estimate the error, we go from a detuning  $\Delta = 20g$  at  $t = 0$  to a detuning  $\Delta = 0$  using a Gaussian waveform with a rise time  $\delta t$ . We then numerically determine the maximum SWAP amplitude between the qubits and plot the resulting value against  $\delta t$ . The result of this simulation is shown in fig. 3.5. As can be seen, the fidelity of the gate decreases in a non-monotonous way as a function of the flux pulse rise time. In order to obtain  $F > 0.99$ , a flux pulse rise time of  $\delta t \leq 1.5$  ns is required.

### 3.2.4 Relaxation and Dephasing

In this section we discuss the relaxation and dephasing channels of the Transmon qubit which are most relevant to our experiment. We analyze the relaxation and dephas-

ing rates as a function of the Transmon parameters and optimize these parameters to achieve maximum qubit coherence times.

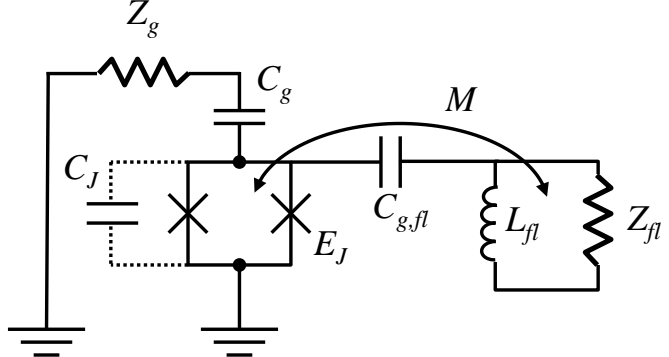
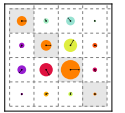


Figure 3.6: A schematic model showing the coupling of the qubit to its environment, modeled by impedances  $Z_g$  and  $Z_{fl}$ , through capacitive and inductive couplings  $C_g$  and  $M$ .

### Qubit Relaxation

Relaxation of the qubit can occur either through the charge channel or the flux channel. The qubit has a capacitive coupling to both the flux line and the readout resonator, hence charge relaxation through both of them is possible. On the other hand, the only relevant relaxation channel through the flux channel is through the inductive coupling to the external flux line.

**Relaxation through the Gate Charge Channel** Since the CPB is coupled to an external impedance (in this case the readout resonator that is coupled to a lossy input transmission line) through a gate capacitance  $C_g$ , as shown in fig. 3.6, relaxation into modes of the input impedance seen by the qubit can occur. The relaxation time of the Transmon qubits used in previous experiments was found to be limited to  $T_1^{int} = 1 - 4 \mu\text{s}$  independent of the circuit [92, 65]. Consequently, we require the relaxation time associated to charge relaxation through the gate circuit to be significantly longer than this intrinsic relaxation time, i.e.  $\Gamma_1^{Purcell} \ll 1 \text{ MHz}$ . This requirement influences the choice of the coupling of the qubit to the readout resonator  $g_{01}$ , the quality factor and associated loss rate  $\kappa$  of this resonator and the qubit-resonator detuning  $\Delta$  for the different processor operations. The relaxation rate due to the coupling of the qubit to the input resonator is given by eq. (2.106). For the qubit parameters chosen above, a resonator quality factor  $Q = 800$  and a resonator-qubit coupling of  $g_{01}/2\pi = 50 \text{ MHz}$  chosen below, the relaxation rate is  $\Gamma_1^{Purcell} \approx 0.25 \text{ MHz}$  at  $\Delta/2\pi = 2 \text{ GHz}$  (for qubit manipulation) and  $\Gamma_1^{Purcell} \approx 1 \text{ MHz}$  at  $\Delta/2\pi = 1 \text{ GHz}$  (for qubit readout). This rate is comparable or larger than the typical intrinsic relaxation rate of the qubit and thus compatible with our design goals.



In addition to the capacitive coupling to the input impedance  $Z_g$ , the qubit is also coupled to its flux line by  $C_{g,fl}$ , which can lead to relaxation through the charge channel of the flux line [48]. Assuming that the flux line is terminated by a  $50 \Omega$  load and that  $C_{g,fl} \leq 10 \text{ fF}$ , yields a relaxation rate  $\Gamma_1^{\text{fl},n_g} \leq 260 \text{ kHz}$  for the qubit parameters discussed above, which is lower than the maximum demanded relaxation rate and thus compatible with our design requirements.

**Relaxation through the Flux Channel** On the two-qubit chip, each Transmon is equipped with a fast magnetic flux line that is used to perform flux biasing and fast frequency displacements. The flux lines are coupled to the qubits through a mutual inductance  $M$ , as shown in fig. 3.6. The sensitivity of the qubit to relaxation through the flux channel via the mutual inductance  $M$  is given by eq. (2.74). For the mutual inductance discussed above,  $M \approx 0.23 \text{ pH}$ , a characteristic impedance of the flux line of  $Z_{fl} = 50 \Omega$ , a qubit frequency  $\omega_{01}/2\pi = 7 \text{ GHz}$  and anharmonicity  $\alpha = -250 \text{ MHz}$  and an asymmetry  $d = 0.35$ , we obtain a maximum relaxation rate of  $\Gamma_1^{fl} = xxx \text{ Hz}$  (0.5 matrix element), which is absolutely negligible compared to all other relevant relaxation channels. We confirm therefore our choice of the mutual inductance  $M = 0.25 \text{ pH}$  for the flux coupling of the qubit.

## Qubit Dephasing

Dephasing of the qubit can occur due to coupling to external charge or flux noise. Here we will calculate the associated rates for both cases for our designed qubit parameters.

**Dephasing through the Flux Channel** For the qubit parameters discussed in the last paragraph, using eq. (2.82) we obtain a maximum dephasing rate  $\Gamma_\phi^{\delta\phi_{ext}} = 0.3 \text{ MHz}$  in the relevant frequency interval  $\omega_{01}/2\pi = 4 - 7 \text{ GHz}$ . This rate is thus smaller than the relaxation-limited dephasing rate of the qubit at all relevant working frequencies of our processor. Our choice of qubit parameters is thus compatible with the demanded dephasing time.

**Dephasing through the Charge Channel** We can use eq. (2.81) to calculate the charge-induced dephasing rate of our Transmon qubit. This rate depends exponentially on the ratio  $E_J/E_C$ . The highest dephasing rate occurs thus at the smallest qubit frequency that we operate our qubit at, in our case  $\omega_{01}/2\pi = 4 \text{ GHz}$ . The chosen maximum tolerable dephasing rate of  $(\Gamma_\phi^{\delta N_g})^{-1} \approx 1 \mu\text{s}$  at  $\omega_{01}/2\pi = 4 \text{ GHz}$  is obtained for a qubit anharmonicity of  $\alpha \approx -500 \text{ MHz}$ , which is thus the upper bound for the anharmonicity. However, for this work we choose  $\alpha = -250 \text{ MHz}$ , since it allows already for sufficiently

fast driving of the qubit, as discussed in section 3.2.2. For this parameter choice, we obtain a negligible maximum dephasing rate  $(\Gamma_\phi^{\delta N_g})^{-1} \approx 1 \text{ ms}$  at  $\omega_{01}/2\pi = 4 \text{ GHz}$ .

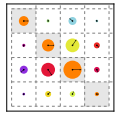
As mentioned in section 2.4.5, the coupling of the qubit to the readout resonator can induce dephasing through the AC-Stark shift of the qubit induced by photon-number fluctuations in the resonator. The resulting relaxation rate is given by eq. (2.113). For the qubit parameters discussed above and a qubit-resonator coupling  $g_{01}/2\pi = 50 \text{ MHz}$ , the dephasing rate is  $\Gamma_\phi^{\bar{n}} = 0.95 \cdot \bar{n} \text{ MHz}$  at the minimum chosen qubit-resonator detuning  $\Delta = 1 \text{ GHz}$ . The average number of photons in a resonator with  $\omega_r/2\pi = 6.7 \text{ GHz}$  at  $T = 100 \text{ mK}$  is given as  $\bar{n} = [\exp(\hbar\omega_r/k_B T) - 1]^{-1} \approx 0.05$ , yielding an effective dephasing rate  $\Gamma_\phi^{\bar{n}} \approx 38 \text{ kHz}$ , which is small compared to the flux-induced dephasing rate at all working points of the qubit.

## 3.3 Readout Design

As explained in section 2.4.3 of chapter 2, the readout fidelity is influenced by three sources of error: Finite overlap between the switching probability distributions for different qubit states, relaxation of the qubit during the measurement phase of the readout and retrapping of the resonator state during the latching phase of the readout. In order to minimize these errors, the following constraints should be met for the readout resonator:

1. The state-dependent dispersive shift of the resonator frequency should be large enough such that the switching probability distributions of the resonator corresponding to the qubit states  $|0\rangle$  and  $|1\rangle$  do not overlap.
2. The measurement phase of the readout should be completed in a time  $T_{meas}$  which is short compared to the relaxation time of the qubit, i.e.  $T_{meas} \ll T_1$ .
3. There should be no retrapping of the resonator state during the latching period of the readout.

In order to maximize the dispersive shift, we can either increase the coupling  $g_{01}$  between the resonator and the qubit or reduce the frequency detuning  $\Delta$  between them. However, increasing  $g_{01}$  or decreasing  $\Delta$  will also increase the relaxation rate of the qubit through the Purcell effect, thereby reducing the readout fidelity. There is thus an optimum choice for  $g_{01}$  and  $\Delta$  [63]. To counteract the qubit relaxation through the cavity, we can simply increase the quality factor of the resonator. However, usually the maximum relaxation time of the Transmon qubit used in this work is limited to  $T_1 \approx 1 - 4 \mu\text{s}$  due to intrinsic relaxation processes. Therefore, increasing the quality factor of the resonator does not necessarily increase the readout fidelity because a higher quality factor also increases the time required to excite the readout resonator by the drive pulse



and hence the measurement time of the qubit state. Therefore, if the qubit relaxation time is intrinsically limited, a longer measurement time at a constant relaxation rate implies a higher probability for the qubit to relax during the measurement, hence actually reducing the readout fidelity. We therefore need to find a compromise for the values of  $g_{01}$ ,  $\chi$  and  $\Delta$  that will maximize the readout fidelity under the given constraints.

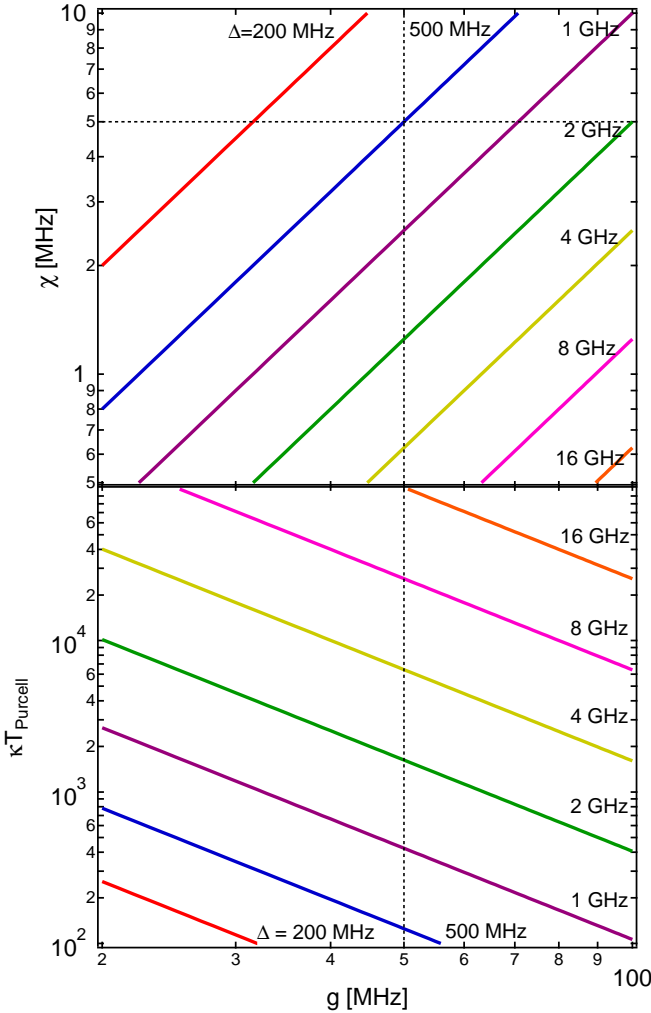


Figure 3.7: The dispersive shift  $\chi$  of the resonator and the relaxation time  $\kappa \cdot T_{Purcell}$  (normalized to the decay rate  $\kappa = \omega_r/Q$  of the resonator) of the qubit for a qubit dispersively coupled to a resonator, plotted as a function of the coupling strength  $g_{01}$  and shown for different values of the qubit-resonator detuning  $\Delta = \omega_r - \omega_{01}$ .

To illustrate the effect of  $g_{01}$  and  $\Delta$  on the relaxation time  $T_1$  and the dispersive shift  $\chi$ , fig. 3.7 shows both quantities as a function of  $g_{01}$ , plotted for several choices of  $\Delta$ . Now, criterion 1 above demands that the dispersive shift be large enough to completely separate the switching probability distributions for different qubit states. The width of these probability curves can be calculated theoretically, however for this discussion we rely on experimentally measured values and assume that a dispersive shift of  $\Delta\chi \approx 5$  MHz suffices to fully separate the two distributions. This assumption limits the range of possible values for  $g_{01}$  and  $\Delta$  to the region above the horizontal line in fig. 3.7a. On the other hand, criterion 2 demands that the time required to map the qubit state to the oscillator state should be small compared to the relaxation time of the qubit. For the

### 3.4. SUMMARY: QUBIT AND READOUT PARAMETERS

---

CJBA parameters relevant to this work, this time is given as  $T_{meas} \approx 50 - 100$  ns. In order to have negligible qubit relaxation during the readout, we therefore demand that  $T_1 \geq 1 \mu\text{s}$ , which corresponds to a 5 % relaxation probability during the measurement interval. This again limits the choice of possible values of  $g_{01}$  and  $\Delta$ .

Another important design parameter of the CJBA is the Kerr constant  $K$ . This constant defines the non-linearity of the resonator and determines the power at which the resonator becomes bistable. Also, the number of photons in the low- and high-amplitude solution of the resonator increases with increasing  $K$ . Since the dispersive shift of the qubit frequency caused by the resonator is proportional to the number of these photons, choosing a too high  $K$  should be avoided since it can induce large displacements of the qubit frequency, thereby recoupling the two qubits of the processor during the readout operation.

Taking these constraints into account, for the final choice of parameter values we rely on a set of optimized CJBA parameters that have been obtained in an earlier experiment by Mallet *et. al.* [63]. For our processor we choose readout resonator frequencies  $\omega_r^1/2\pi = 6.7$  GHz and  $\omega_r^2/2\pi = 6.85$  GHz, quality factors  $Q^{1,2} = 800$ , Kerr constants  $2\pi K^{1,2}/\omega_r^{1,2} = -2.5 \times 10^{-5}$  and qubit-resonator couplings  $g_{01}^{1,2}/2\pi = 50$  MHz. In addition, we choose a detuning  $\Delta/2\pi = 500$  MHz for reading out the qubits, yielding a relaxation rate  $\Gamma_1^{Purcell} \approx 0.5$  MHz during readout.

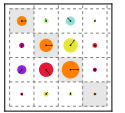
## 3.4 Summary: Qubit and Readout Parameters

Having discussed the relevant properties of all building blocks of our processor and their dependence on the sample parameters, we choose a full set of these parameters, summarized in table 3.1. The left column contains the processor parameters, the right column the related sample parameters.

## 3.5 Processor Layout & Fabrication

After having chosen a set of sample parameters, it remains to find a physical implementation of the design that we can realize. In this section we discuss therefore the layout design of the qubit processor. From the beginning, we will restrict our discussion to lithographically fabricated circuits on a chip, disregarding recent approaches to the realization of superconducting qubits and resonators using 3D microwave cavities [78].

The readout resonator can be realized as a lumped-elements LC resonator or as a transmission line resonator. In the original approach to CQED [100], a coplanar waveguide (CPW) resonator was used. Distributed microwave resonators such as CPW res-



Parameter	Value	Related Parameters
$E_J$	$h \cdot 28.4$ GHz	$f_{01} = 7$ GHz, $\alpha = -250$ MHz
$E_C$	$h \cdot 0.92$ GHz	$C_q = 83.8$ fF, $I_c = 57.4$ nA
$d$	0.35	
$M_{1,2}$	0.25 pH	
$g_{qq}/2\pi$	10 MHz	$C_{qq} = 0.45$ fF
$g_{01}/2\pi$	50 MHz	$C_{qr} \approx 62.8$ fF
$\omega_r^1/2\pi$	6.7 GHz	$L_r^1 = 756$ pH, $C_r^1 = 497$ fF
$\omega_r^2/2\pi$	6.85 GHz	$L_r^2 = 739$ pH, $C_r^2 = 486$ pF
$Q_r^{1,2}$	800	$C_{in}^{1,2} \approx 17$ fF
$K_r^{1,2}$	$-2.5 \times 10^{-5}$	$I_{J,r} \approx 2.3$ $\mu$ A

Table 3.1: The sample parameters chosen for the two-qubit processor. The table contains all independent parameters of the processor as well as the dependent parameters derived from them.

onators are often advantageous since they can be fabricated with a high intrinsic quality factors [69, 24, 102, 5], although recently large progress has been made concerning the quality factors of discrete LC resonators as well [51]. Also, the isolation between the input port of the distributed resonator and the qubit electrode to which the open end of the resonator is coupled is high, whereas for a discrete LC resonator a significant capacitive coupling between the input port of the resonator and the qubit can exist, which is unwanted since it will cause additional relaxation. For this work, we therefore chose a distributed design using a  $\lambda/2$  CPW resonator. The open port of the resonator is capacitively coupled to one of the qubit electrodes to achieve the desired coupling factor  $g_{01}$ .

The flux lines can be realized in several ways. For our processor, we choose a simple  $50 \Omega$  CPW transmission line that is passing nearby the qubit SQUID at a distance of  $d \approx 12 \mu\text{m}$ . Since we use the flux line for DC biasing of the qubits as well, shielding currents will flow in the ground planes on either side of the line when a DC current gets applied. These currents can create an unwanted flux bias in the qubit loop and should therefore be eliminated. We achieve this by removing the ground plane between the qubit and the central conductor of the flux line. By doing this, we also increase the capacitive coupling between the line and the qubit electrodes, thereby increasing the charge relaxation rate through the flux line. However, as discussed in section 3.2.4, for our sample parameters this effect is usually negligible. The flux line can be terminated

### 3.5. PROCESSOR LAYOUT & FABRICATION

---

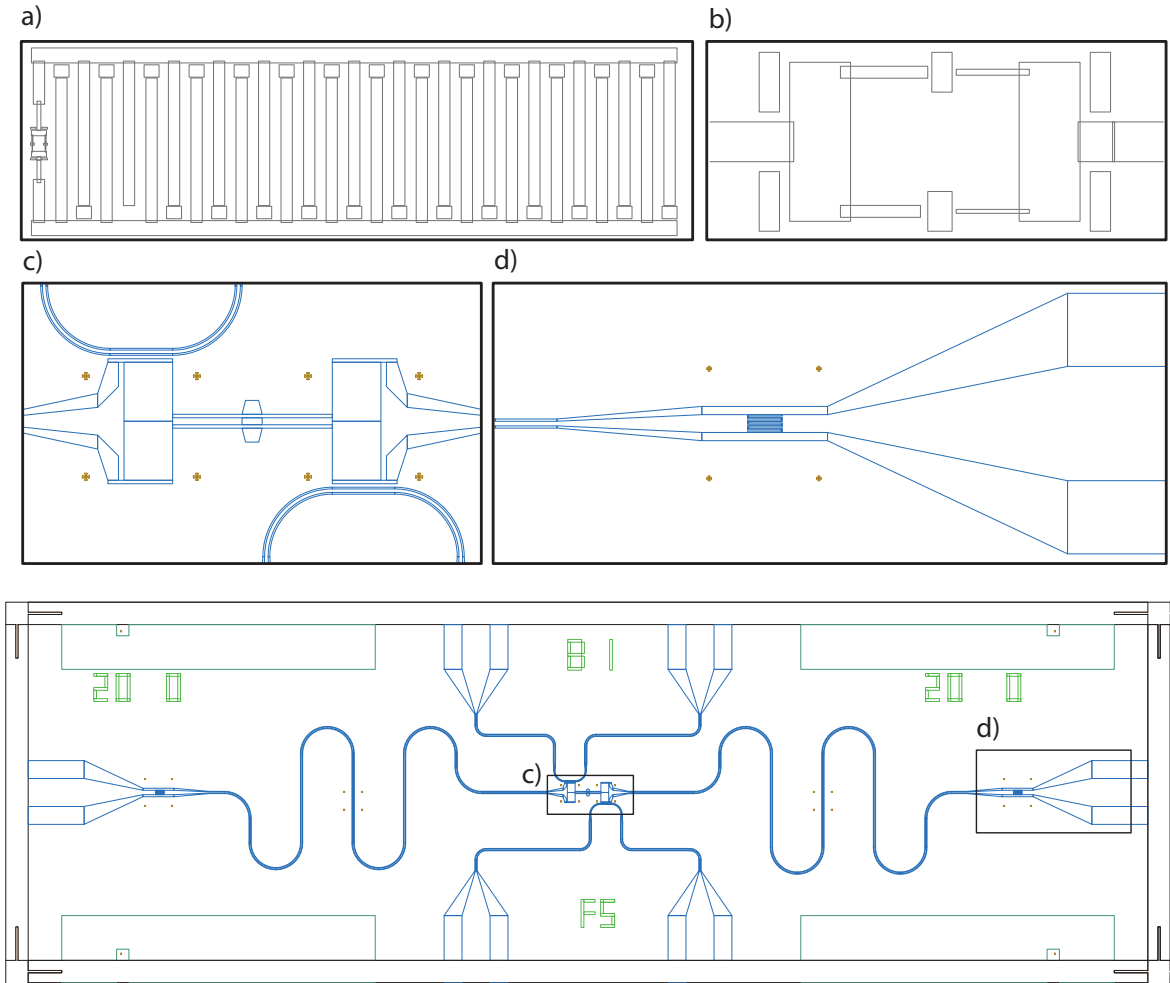
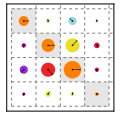


Figure 3.8: CAD layout schematic of the two-qubit processor, showing the two CPW readout resonators and the two qubits with their adjacent fast flux lines. Subfigure a) gives a magnified view of the two qubits and their capacitive coupling element, subfigure b) shows the input coupling capacitance of the CPW resonator to the input transmission line.

either directly at the 20 mK stage by wire-bonding it to the ground plane of the chip, or by connecting it to a matched impedance at the 1 K stage of the cryostat. Alternatively, we can also feed back the flux signal to room temperature, which is useful for e.g. measuring the response function of the line.

For the Transmon qubit itself, we need to fabricate a large shunt capacitance  $C_J$  in order to achieve the desired charging energy. We implement this capacitance as an interdigitated planar capacitor that we pattern together with the qubit junctions using electron-beam lithography. The Josephson junctions of the qubit are realized in a SQUID geometry with a loop area of  $A \approx 16 \mu\text{m}^2$  and are fabricated using double-angle shadow-evaporation of Aluminium.



### 3.6 Electromagnetic Simulation of the Qubit-Chip

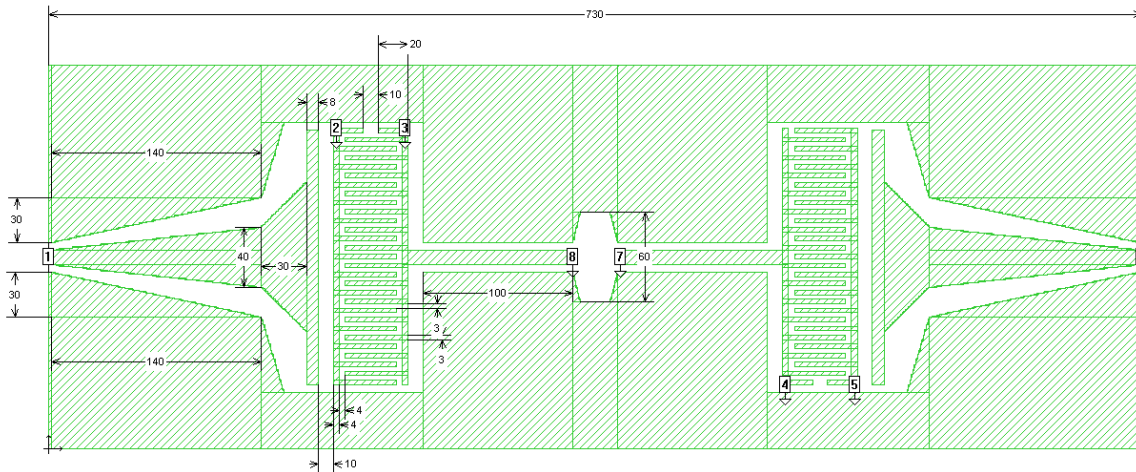


Figure 3.9: 2D Electromagnetic model of the processor chip, generated using Sonnet microwave simulator (SONNET). Shown are the two Transmon qubit capacitances that are capacitively coupled to each other and to their readout resonator (not shown). Numerical simulation of the circuit yields the capacitances and inductances between all ports of the circuit (1-8).

We use a software package for electromagnetic simulation (SONNET) to simulate individual parts of the chip and obtain the transmission coefficients between all relevant circuit components and an equivalent lumped-element model of the circuit. Using this equivalent model we calculate all relevant capacitances and inductances. We can then iteratively adapt the geometry of individual elements in order for them to match the designed parameter values.

We can also simulate the Transmon qubits as harmonic oscillators by modeling their Josephson junction as an inductance that matches the Josephson inductance of the junction, as given by eq. (2.14). By simulating the resonance curve of this harmonic resonator and calculating the corresponding quality factor  $Q$ , we can estimate the relaxation rate of the qubit through the gate circuit. We can also obtain an estimate of the coupling strength between the two qubits by simulating them as two coupled, linear resonators. We can obtain the impedance seen by the qubit through the gate circuit by this method as well, thereby being able to calculate the corresponding qubit relaxation rate.

### 3.7 Fabrication

We fabricate the processor on a high-resistivity silicon substrate with a 50 nm thermal oxide layer. First, we deposit 150 nm of Niobium by magnetron sputtering. Af-

### 3.7. FABRICATION

---

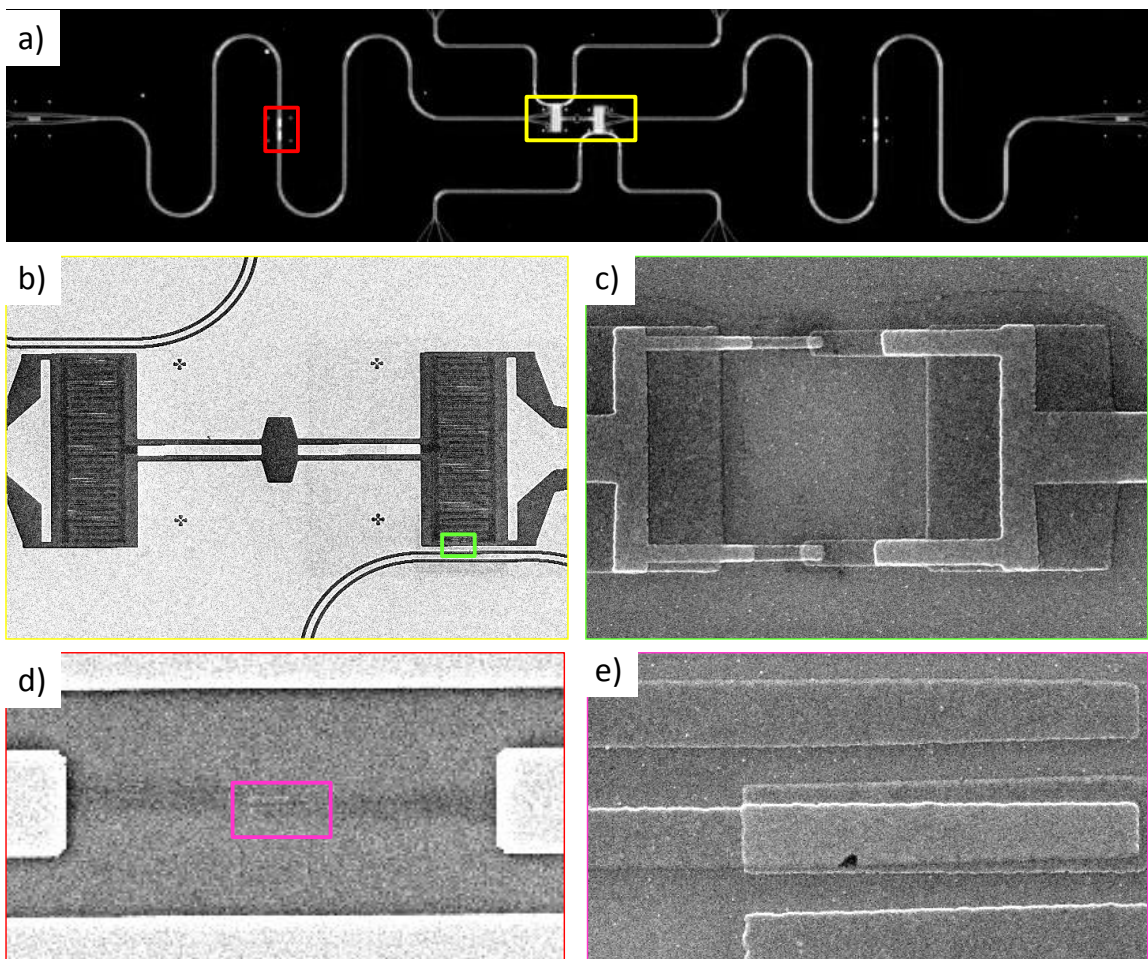
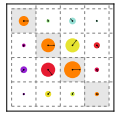


Figure 3.10: Optical and electron microscope photos of the two-qubit processor realized in this work. a) shows an optical image of the full processor with the two coupled qubits, fluxlines and readout resonator. b) shows an SEM image of an enlarged part of the central region of the chip with the two qubits and the coupling capacitor. c) Shows an SEM image of a single qubit junction loop.



terwards, we spin a photo resist and define an etch mask through optical lithography. Then we dry-etch in a  $\text{SF}_6$  plasma, defining the readout resonators, transmission lines and qubit flux lines on the chip. This optical patterning is performed for the wafer as a whole. Afterwards, we spin a bilayer of MAA/PMMA electron beam resist (with typically 1050 nm of MMA and 115 nm of PMMA thickness). Then the wafer gets diced and the qubits and JBA junctions are patterned per chip using electron beam lithography, using a double-angle shadow evaporation technique to define the Josephson junctions and capacitances on the chip. The e-beam resist is then lifted off chemically in an Acetone bath. We characterize the chip optically afterwards. In addition, we place “twin” structures of the Transmon qubits and the JBAs on each chip that we can use to measure their normal state resistance at room temperature in order to obtain an estimate of the corresponding resistance of the real structures. Giving the normal-state resistance of a Josephson junction we can calculate the Josephson energy by using the Ambegaokar-Baratoff relation

$$E_J = \frac{2\pi^2\Delta}{R_n h}, \quad (3.4)$$

where  $E_J = hI_c/4\pi e$ . When measuring  $R_n$  at room temperature, a corrective factor of  $\approx 17\%$  has to be applied to the resulting value of  $E_J$  to account for variations in  $R_n$  with temperature.

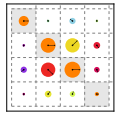
Following we discuss the detailed procedure followed for fabrication of the two-qubit processor chip.

1. **Niobium Sputtering:** Deposit 150 nm Niobium at an argon pressure of 1.25 mbar and a power of  $0.66 \text{ W/cm}^2$  with a 5 minute pre-deposition and  $\approx 2 \text{ min } 20 \text{ sec}$  deposition time.
2. **Spinning of Photo-Resist:** Spin S1813 + Shipley Primer at 6000 RPM for 60 sec, bake at  $115^\circ \text{C}$  for 1 min 15 sec.
3. **Photo Lithography of Resonators:** Expose the wafer through a contact mask at  $5 \text{ mW / cm}^2$  for 30 sec.
4. **Development:** Develop in pure MF 319 for 50 s.
5. **Reactive Ion Etching:** Pump the RIE chamber to  $P \leq 4 \times 10^{-5} \text{ mbar}$ . Etch using 20 cc of  $\text{SF}_6$ , 10 cc Ar and 2 cc  $\text{O}_2$  at a pressure of  $\approx 0.013 \text{ mbar}$  at a power of 50 W and a voltage of 150 V. The total etch time should be  $\approx 60 \text{ sec} + 10 \text{ sec}$  for the finish. Remove the resists in warm acetone ( $40^\circ \text{C}$ ) for at least 10 min, possibly clean further in an ultrasonic bath.
6. **Niobium Surface Regeneration:** Pump the RIE chamber to  $P \leq 4 \times 10^{-5} \text{ mbar}$ , etch using 20 cc of  $\text{SF}_6$ , 10 cc Ar at  $\approx 0.0133 \text{ mbar}$ , 50 W and 150 V for 8 sec.

### *3.7. FABRICATION*

---

7. **Electron Resist Spinning:** Spin twice an MAA EL 10 layer at 2000 RPM for 60 sec, 6000 RPM for 2 sec. Bake after each step at 170 °C for 60 sec. Spin PMMA 950k A3 at 4000 RPM for 60 sec, 6000 RPM for 2 sec. Bake at 170 °C for 20 min. This should yield  $\approx$  1050 nm of MAA and 110 nm of PMMA (verify using interferometer).
8. **Dicing:** Dice the wafer using either a diamond cutter or wafer saw.
9. **Electron Beam Lithography of Transmons and CJBA junctions:** Clean the chip in iso-propanol (possibly in ultrasound) for less than 2 minutes. Perform electron beam lithography at a dose of  $\approx$  250-320  $\mu\text{C}/\text{cm}^2$ . Develop the chip in a 1:3 aceton/iso-propanol solution for 50 sec.
10. **Aluminum Deposition:** Put the sample in the evaporation chamber and pump to  $P < 10^{-6}$  mbar. Ion mill the sample at the two evaporation angles (typically  $\pm 22$  deg) with 500 eV neutralized argon ions at the dose of  $2 \cdot 10^{15}/\text{cm}^2$ . Deposit first aluminum layer at a rate of 1 nm/sec. Oxidize at an adequate oxygen pressure (typically 15 - 25 mbar) for 10 min. Deposit the second aluminum layer at 1 nm/sec.
11. **Lift-Off:** Put the chip in a heated Acetone bath at 65 °C for at least 5 min. Rinse in Iso-Propanol. Thermally stabilizee the chip at 100 °C for 1 min.



# Chapter 4

## Measurement Setup & Techniques

In this chapter we discuss the measurement setup and techniques that we use in this thesis work. We present all individual parts of our signal generation and measurement chain, putting emphasis on the generation and measurement of high-frequency signals. Afterwards we briefly discuss the calibration and compensation techniques that we use to correct signal imperfections when generating qubit drive and flux signals. Finally we introduce the different measurement techniques that we use in this work, including qubit readout and driving as well as more advanced methods used to obtain all relevant qubit parameters such as frequency, anharmonicity as well as relaxation and dephasing times.

Our experimental setup consists of the qubit chip discussed in chapter 3, which is put at the 20 mK stage of a  $\text{He}_3/\text{He}_4$  dilution cryostat and connected to a room temperature signal generation and measurement chain via cryogenic microwave components and  $50 \Omega$  coaxial transmission lines. At room temperature, we generate microwave pulses as well as DC and high-frequency flux bias pulses using heterodyne mixing and/or high-frequency arbitrary signal generators. We use a cryogenic amplifier chain and homodyne demodulation at room temperature to perform reflectometric measurements of the phase of our microwave readout signal.

### 4.1 Sample Holder & PCB

For mounting the qubit chip as shown in fig. 3.10 in the sample holder, the chip is first glued to a custom-designed high-frequency PCB, as shown in fig. 4.1 (bottom). On this PCB, six  $50 \Omega$  CPW waveguides terminated by Mini-SMP connectors are bond-wired to the drive/readout and fast flux lines of the qubit chip. For each qubit, we have one readout/drive line and two flux lines on the chip. In addition, bond wires are used to connect the ground plane of the chip to that of the PCB. On-chip bond wires are used to connect separated parts of the on-chip ground plane which are isolated from each

## 4.2. SIGNAL GENERATION & ACQUISITION

---

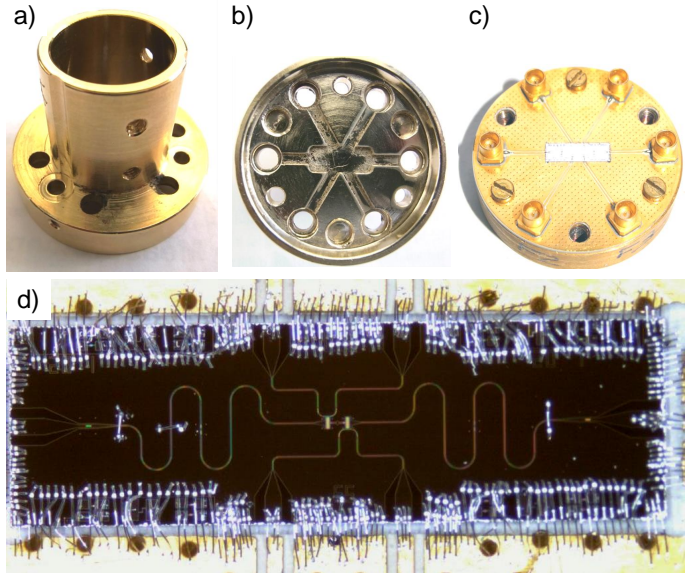


Figure 4.1: The sample holder with the mounted PCB carrying the qubit chip. Bond wires are used to connect the on-chip transmission lines to the PCB, which in turn uses a Mini-SMP connector to connect the bondwire to a set of external coaxial SMP cables. The top part of the sample holder is screwed to the bottom part, forming a closed box with cavities only for the transmission lines and the qubit chip. The whole sample holder is screwed to the 20 mK stage of the dilution cryostat.

other due to the circuit topology. This is important in order to avoid spurious on-chip resonances in the relevant frequency range between 4 – 7 GHz [86]. The PCB with the mounted chip is then screwed to a sample holder machined in copper that fully encloses the PCB, as shown in fig. 4.1 and that consists of a bottom part on which the PCB is screwed and that is itself screwed to the top part of the sample holder. The top part provides holes for the SMP connectors and is pressed against the surface of the PCB. Machined grooves in the top part provide the necessary open space above the qubit chip and the transmission lines on the PCB. The function of the sample holder is to thermally anchor the PCB and the qubit chip to the cryostat and, more importantly, to shield the qubit chip from spurious electromagnetic signals and enclose it in a conducting cavity that is small enough to suppress box resonances at all relevant working frequencies.

## 4.2 Signal Generation & Acquisition

Fig. 4.2 shows the wiring of our experiment from room temperature down to the 20 mK state of the dilution cryostat. Superconducting cables are used where adequate to minimize signal attenuation, in addition lossy cables made from special alloys such as CuNi are used to minimize heat transfer into the cryostat, which is especially critical between the 300 mK and 20 mK stages. Pairs of bifilar cables are used to provide DC biasing of one or several superconducting coils.

### 4.2.1 Driving and Measurement of the Qubit

Each of the qubits together with its corresponding readout resonator on our chip is fitted with an individual drive and readout circuit. At room temperature we generate qubit and

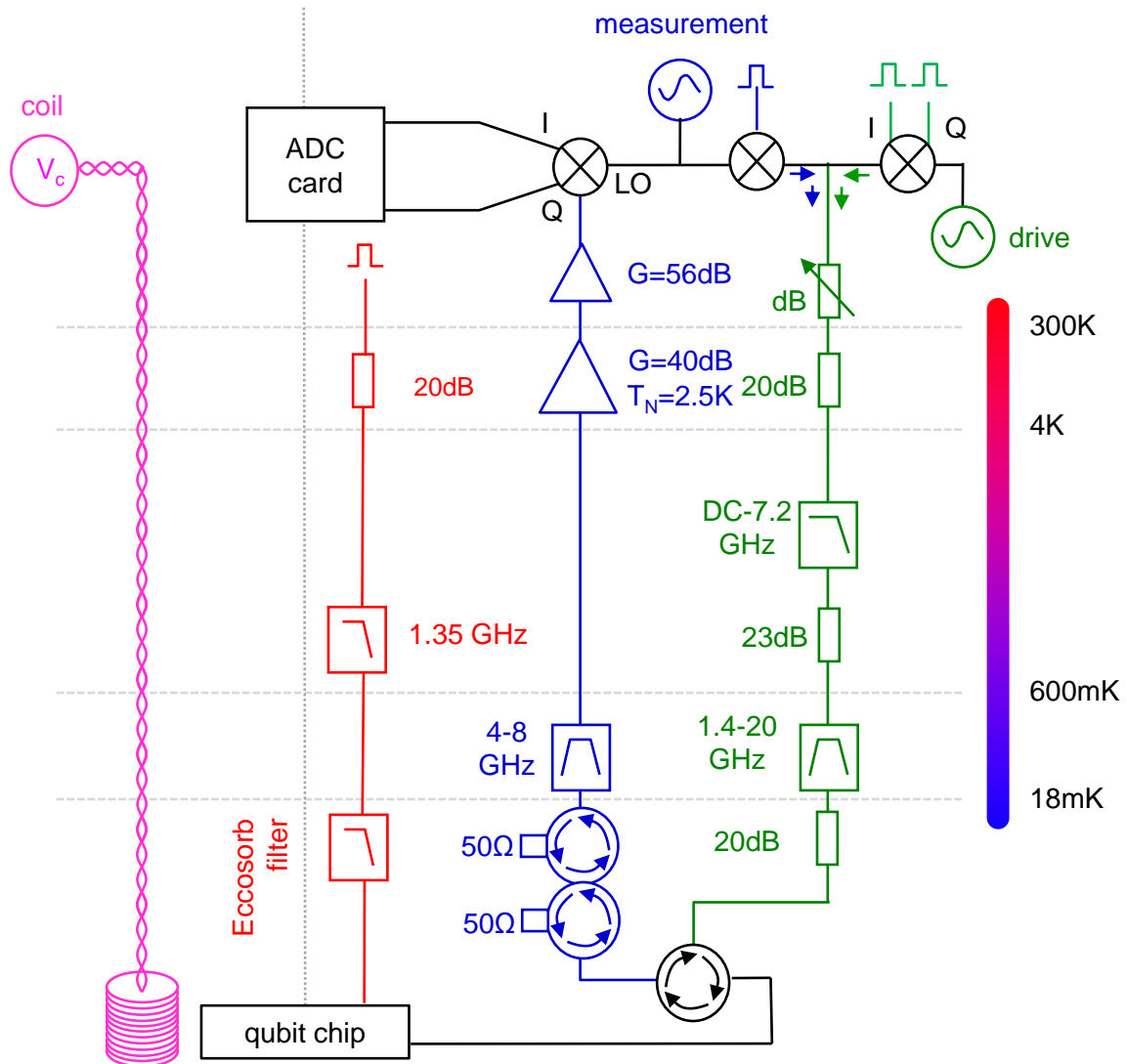
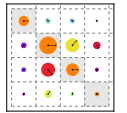


Figure 4.2: The measurement setup used for the two-qubit experiments. Exactly the same drive and readout scheme is used for both qubits with phase-locked microwave sources and arbitrary waveform generators.

resonator drive waveforms using phase-locked single-tone microwave sources whose continuous output is mixed with fast control pulses, that are generated by two arbitrary waveform generators (the details of this microwave mixing will be discussed in the following paragraph). The drive and readout signals are then combined and sent to the qubit chip through a series of (cryogenic) attenuators and filters. A cryogenic circulator at the 20 mK sample stage of the dilution cryostat routes the incoming pulses to the qubit chip, where they are sent to the qubit readout resonator and finally reflected by it. The reflected signal passes again through the input microwave circulator and gets routed through a double isolator and a band-pass filter to a cryogenic HEMT amplifier with a gain of 40 dB. The amplified signal gets then transmitted to the room temperature electronics, where it is filtered and amplified further. Finally, the signal is demodulated

with a continuous microwave reference tone and fed to an ADC board through a pair of low-noise amplifiers.

In addition to this, each qubit is equipped with a pair of fast flux lines. High-frequency and DC flux pulses are generated using an arbitrary waveform generator at room temperature. The flux signal is then sent to the qubit chip through 20 dB of attenuation, a conventional Microtronics low-pass filter as well as a custom-made high-frequency powder filter that uses an absorptive material (Eccosorb) to attenuate high-frequency noise. After passing through the transmission line on the qubit chip, the outgoing flux signal gets routed to room temperature through a transmission line identical to the input line. There, the signal can be measured, which is useful for characterizing possible signal imperfections caused by the non-ideal character of the transmission line.

### 4.2.2 Microwave Sideband Mixing

To generate the qubit drive pulses we use single-sideband mixing techniques. We use a pair of IQ mixers that we drive with a continuous single-frequency microwave tone and two synchronized fast control signals generated by an arbitrary waveform generator (Tektronix AWG5014b). In general, when feeding a signal  $LO(t) = i_0 \cos(\omega_{LO}t)$  to the LO port of an IQ mixer and two signals  $I(t)$ ,  $Q(t)$  to the I and Q ports of the mixer, we obtain a signal

$$RF(t) = I(t) \cos(\omega_{LO}t) + Q(t) \sin(\omega_{LO}t) \quad (4.1)$$

at the RF port of the mixer. Since the IQ mixer that we use is a passive, reciprocal device one can as well feed two input signals to the LO and RF ports and obtain the demodulated signal quadratures at the I and Q ports, a technique that we make use of in our qubit readout scheme. Typically we use heterodyne sideband mixing to generate drive pulses that are displaced in frequency in respect to the original LO (carrier) waveform.

Commercially available IQ mixers often deviate from the ideal behavior as given by eq. (4.1). Typical imperfections include large insertion losses –i.e. loss of signal power between the different ports of the mixer–, RF signal leakage at zero IQ-input and frequency-dependent phase and amplitude errors of the mixed sideband signals. In order to achieve reliable single-qubit operations we need to correct the signal leakage and quadrature-specific amplitude and phase errors. The signal leakage causes a small part of the LO signal to leak through to the RF port even when the IQ inputs are zeroed. This leakage can be compensated by adding LO frequency  $\omega_{LO}$  dependent DC offset voltages to the IQ ports. The appropriate offset voltages can be determined by applying a continuous input signal at a frequency  $\omega_c$  to the LO port of the mixer and minimizing

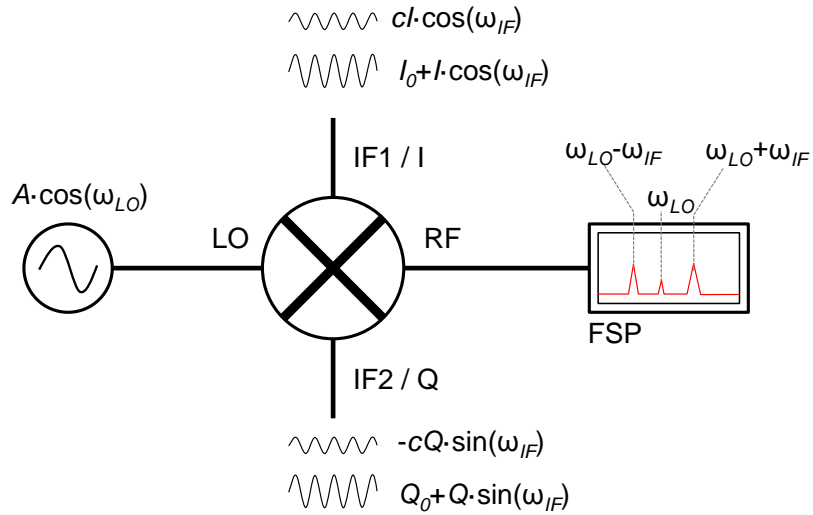
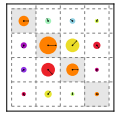


Figure 4.3: Illustration of the method used to measure and correct the imperfect signal behavior of the IQ mixer used in our experiments: To minimize the leakage of the LO signal to the RF port, we apply a continuous input signal at frequency  $\omega_{LO}$  to the LO port and minimize the power at  $\omega_{LO}$  at the RF port, as measured by a fast spectrum analyzer, by tuning the two offset voltages  $I_0$  and  $Q_0$  at the IF1/I and IF2/Q ports. To correct phase and amplitude errors during heterodyne mixing, we apply the same signal as before to the LO port and in addition two sideband signals to the IF ports. We then minimize the measured power at the RF port at  $\omega_{LO} + \omega_{IF}$  by adding a correction waveform at the IF ports.

the measured signal power at the RF port by varying the IQ offset voltages. To correct the sideband amplitude and phase errors we apply another correction procedure that we outline here. First, for the signals at the IQ inputs of the mixer we introduce the notation

$$A(t) = I(t) + iQ(t) = a(t) \exp(-i\phi(t)) \quad (4.2)$$

We consider an IQ signal at a single sideband frequency  $\omega_{IF}$  and at fixed complex amplitude  $a(t) = a = a_0 \exp(i\phi_0)$  such that  $A(t) = a \exp(-i\omega_{IF}t)$ . The effect of the gain and phase imperfections of the IQ mixers can then be modeled by assuming that the mixer adds another IQ signal  $\epsilon(\omega_{IF}, \omega_{LO})A^*(t)$  at the mirrored sideband frequency  $-\omega_{IF}$ . We can correct this unwanted signal by adding a small correction  $c(\omega_{IF}, \omega_{LO})A^*(t)$  to our IQ input signal. The complex-valued correction coefficient  $c(\omega_{IF}, \omega_{LO}) = |c| \exp(i\angle c)$  usually depends both on the LO frequency  $\omega_{LO}$  and the sideband frequency  $\omega_{IF}$ . We determine the correction coefficients by generating a continuous waveform at a given center and sideband frequency, measuring the amplitude of the unwanted sideband signal with a fast spectrum analyzer and minimizing its amplitude by varying the correction coefficient  $c(\omega_{IF}, \omega_{LO})$ .

Both the offset and the sideband-amplitude and -phase corrections have been automated using our data acquisition software. By using the optimization techniques described above we can achieve  $\leq -80$  dBm residual leakage power at the RF port of

the mixer when no input IQ signal is present and a suppression of the unwanted mirror sideband during heterodyne modulation by  $> 70$  dB.

### 4.2.3 Fast Magnetic Flux Pulses

We use a pair of superconducting coaxial cables to realize the qubit flux lines. Each qubit is connected to an on-chip transmission line, whose ends are connected to two fully symmetric transmission lines through the PCB. These two lines lead back to the room-temperature stage and can be used to send signals down the flux line and measure the transmitted signal. Between room temperature and the 20 mK stage of the cryostat, we apply 20 dB attenuation to each line and low-pass filter all signals both at the 4K and 20 mK stages of the cryostat. The low-pass filters at the 20 mK stage consist of custom-built powder filters made from a commercially available, highly absorptive and lossy material (Eccosorb). Appendix ?? contains details on the fabrication and frequency attenuation characteristic of these filters. The heavy filtering of the flux line is necessary since it reduces the high-frequency noise seen by the qubit. On the other hand, it also distorts all deterministic input signals that we send through the flux line, which is an unwanted effect and needs to be corrected. For this, we measure and compensate the frequency response of the flux line by sending a well-defined test signal down the line and measuring the transmitted signal at the other end of the line. This allows us to obtain the response function of the input line. Fig. 4.4a shows the model of the qubit flux line that we use to model the response function of the line. The Fourier transform of the measured signal at the output of the flux line is

$$\chi_{\text{fl}}(\omega) = \chi_{\text{signal}} \cdot \chi_{\text{DAC}} \cdot \chi_{\text{input}} \cdot \chi_{\text{output}} \cdot \chi_{\text{ADC}} \quad (4.3)$$

Here,  $\chi_{\text{signal}}$  is the Fourier transform of the ideal input signal,  $\chi_{\text{ADC}}$  and  $\chi_{\text{DAC}}$  describe the response functions of the DAC and ADC,  $\chi_{\text{input}}$  and  $\chi_{\text{output}}$  corresponds to the response function of the input and output transmission lines. We can assume that  $\chi_{\text{input}} \approx \chi_{\text{output}}$  since the input and output lines are symmetrical. By measuring  $\chi_{\text{fl}}$  and correcting the measured Fourier spectrum for the response function  $\chi_{\text{ADC}}$  of the ADC (which can be measured separately) we obtain the input line response function  $\chi_{\text{DAC}}\chi_{\text{input}}$  which includes the DAC response. To correct the signal distortion seen by the qubit, we can replace the original input signal with a corrected one with the Fourier transform

$$\chi_{\text{signal}}^{\text{corr}} = \chi_{\text{signal}} \cdot (\chi_{\text{DAC}} \cdot \chi_{\text{input}})^{-1} \cdot G(\omega, \omega_{\text{co}}). \quad (4.4)$$

Here,  $G(\omega, \omega_{\text{co}})$  is a Gaussian filter function with a cutoff frequency  $\omega_{\text{co}}$  that we apply to the measured response function to renormalize the signal distortion at high frequencies that is caused by the fact that we are not able to accurately measure the response func-

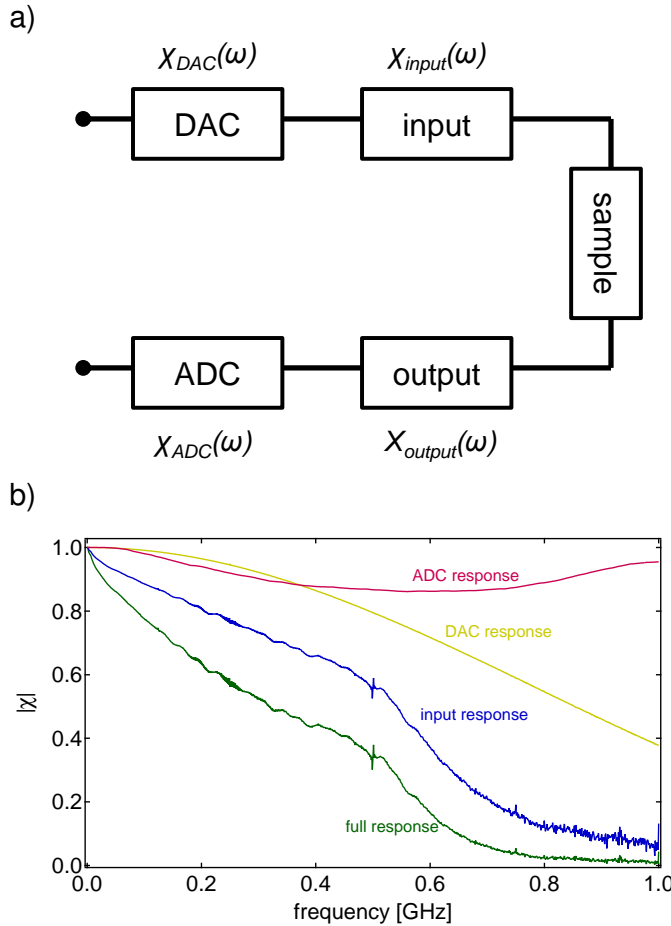
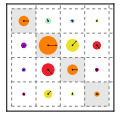


Figure 4.4: a) Schematic of the flux line chain used in our setup. The flux signal is generated by a DAC, fed through the input line to the sample, returned to room temperature through the output line and digitized by an ADC. b) The signal, time derivative and response function of an experimentally generated flux pulse as seen by the qubit, determined through spectroscopic measurements of the qubit transition frequency.

tion of the flux line above a certain frequency threshold due to the limited bandwidth of our measurement equipment. Usually, we set this cutoff frequency to  $\omega_{co}/2\pi = 400$  MHz, which allows us to correct most signal distortion in the frequency band up to  $f = 1$  GHz that is relevant to this work.

After having corrected the response of the flux line by this technique, we can further reduce signal distortion by directly probing the flux seen by the qubit at a given time. For this, we apply a small test flux signal  $\phi_{ext}^{fl}(t)$  to the qubit and reconstruct the flux seen by it. If the qubit frequency is chosen well away from its maximum and minimum frequencies (where  $\partial\omega_{01}/\partial\phi_{ext}^{fl} \neq 0$ ) and the flux signal is comparably small, we can write the time-dependent qubit frequency as  $\omega_{01}(t) = \omega_{01}^0 + \gamma\phi_{ext}^{fl}(t)$ , where  $\gamma$  is a constant. The frequency displacement of the qubit is thus proportional to the applied flux signal. Now, if we drive the qubit with a calibrated  $X_\pi$  Rabi pulse at a given drive frequency  $\omega_d$  at time

### 4.3. MEASUREMENT TECHNIQUES

---

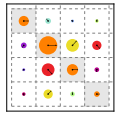
$t_0$ , the probability of finding it in state  $|1\rangle$  afterwards is maximum if  $\omega_d = \omega_{01}(t_0)$ . Thus, by maximizing this qubit readout probability as a function of  $\omega_d$ , we can reconstruct the flux  $\phi_{ext}^{fl}(t_0)$  seen by the qubit at any given moment. Of course, the time resolution that can be achieved with this method is limited to the pulse duration of the  $X_\pi$  pulse, which is typically 3 – 5 ns. After having reconstructed the flux signal  $\phi_{ext}^{fl}(t)$  seen by the qubit, we can then again calculate its Fourier transform and correct imperfections by changing the input signal that we send. Fig. 4.4b shows the measured flux signal seen by the qubit, the corresponding response function and the corrected input waveform for one of our qubits.

#### 4.2.4 Pulse Synchronization

In our experiment, each qubit possesses two microwave sources that generate the drive and readout signals for it. The fast drive pulses for each qubit are generated by a single arbitrary waveform generator (AWG). A second AWG generates the flux pulses for the two qubits. The measurement of the reflected and demodulated readout signal of both qubits is done by a single ADC card. All these different signal generators and measurement devices need to be synchronized in order to maintain the relative phases and time differences between them at individual runs of our experiment. For this, we use a 10 MHz frequency reference chain, whose master clock is generated by the AWG that is responsible for generating the qubit drive pulses. The reference signal is then passed on to all microwave sources and signal generators as well as oscilloscopes, spectrum analyzers and ADC cards in our setup. In addition, to avoid random phase-jitter between the signals of the two microwave sources that generate the drive pulses of the two qubits, their drive frequencies need to be chosen such that they correspond a multiple of the repetition frequency of the master AWG, which is typically 50 kHz. If this condition is met, the relative phases between the two microwave signals is conserved between individual runs of the experiment, which is crucial when performing measurements that are sensitive to this phase such as quantum state tomography of entangled two-qubit states. In addition, a 1 GHz phase synchronization chain is used to phase-lock the two microwave generators and reduce phase drift between them.

## 4.3 Measurement Techniques

In this section, we discuss the techniques used to characterize and manipulate our two-qubit processor. We will cover the qubit readout and manipulation and will describe how we can determine all relevant qubit parameters using microwave reflectometry measurements.



## 4.4 Qubit Readout

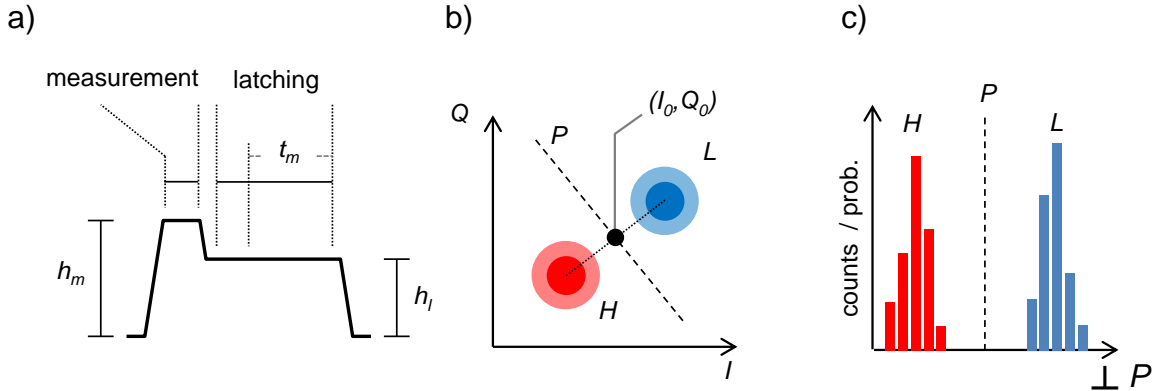


Figure 4.5: a) Microwave pulse envelope used for exciting the CJBA during readout. The pulse consists of a measurement part with amplitude  $h_m$  and a latching part with amplitude  $h_l < h_m$ . To determine the state of the resonator during the latching interval, the phase of the reflected signal is measured in the time window  $t_m$ . b) Distribution of the measured average ( $I, Q$ ) values in the IQ plane. The line  $P$  that intersects the average quadratures  $(I_0, Q_0)$  provides optimal separation between the two clusters corresponding to the state L and H of the resonator. c) Switching probability histograms corresponding to the distribution of the measured ( $I, Q$ ) values projected along the axis  $\perp P$ .

The general readout principle of the CJBA readout that we use in this work is described in section 2.4.3. Here we explain how we choose the frequency and drive amplitude working point for the readout. To bring up the readout, we first determine the resonance frequency  $f_r$  of the CJBA by reflectometry, with the qubit in state  $|0\rangle$  and largely detuned from the resonator. We then choose a relative drive detuning  $\Omega > \sqrt{3}$  at which the bistable regime is accessible. Next, we mix a continuous drive signal with a drive pulse as shown in fig. 4.5a. We then attenuate the resulting drive signal using a tunable attenuator at room temperature and send it to the CJBA. The reflected and amplified signal is then demodulated with the continuous input drive signal using an IQ demodulator. The resulting I/Q quadrature signals are again amplified and get digitized by an ADC card at a sampling rate of 1 GHz during the time window  $t_m$ , as indicated in fig. 4.5a. We then average the digitized I/Q signals over the whole measurement window to obtain a single measurement point in the IQ plane and repeat this sequence a large number of times (typically  $10^4$ ). We then repeat this whole procedure for various values of the input attenuation, each time calculating the estimated variance  $\hat{\sigma}_{IQ}^2 = \sum_i ((I_i - \bar{I}_i)^2 + \sum_i (Q_i - \bar{Q}_i)^2)/n$  of the obtained data sets. When starting with a high attenuation and reducing it, at some point the input power sent to the CJBA will be sufficient to make it switch from the L to the H state, thereby changing the phase and consequently the average position of the I/Q values of the obtained signal. Since the switching is a stochastic process, we will observe two families of points close to the

transition power. At an input power where approximately 50 % of switching occurs, the variance  $\sigma_{IQ}^2$  of the obtained IQ data points will be largest, as shown in fig. 4.5b. At this point, we can subtract the averages ( $I_0 = \sum_i I_i/n, Q_0 = \sum_i Q_i/n$ ) from the data and perform a principal axis transformation, which diagonalizes the covariance matrix

$$\text{var}_{IQ} = \begin{pmatrix} \text{var}(I) & \text{cov}(I, Q) \\ \text{cov}(I, Q) & \text{var}(Q) \end{pmatrix} \quad (4.5)$$

of the data. Using this transformation, we can project the measured (I,Q) data points on the axis  $\perp P$ , as shown in fig. 4.5, and obtain a one-dimensional switching probability distribution. The obtained offsets  $I_0, Q_0$  and principal axis rotation angle  $\alpha_{IQ}$  gives us then the discrimination criterion  $Q_L < Q_0 + \tan \alpha_{IQ}(I - I_0)$  that we can use to classify new data points as belonging to the L or H state at the chosen working point. Normally, if the measurement window  $t_m$  is large enough and no retrapping occurs during the measurement, the distributions corresponding to the L and H states will not overlap, yielding perfect discrimination between them.

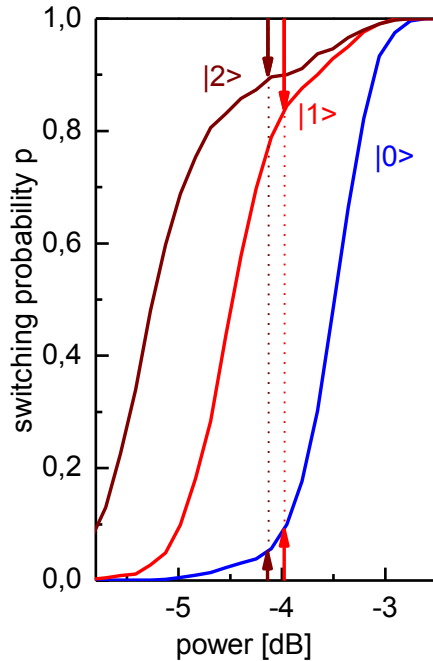
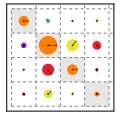


Figure 4.6: Exemplary s-curve measurement for one of the qubits on the chip. Shown is the switching probability  $p$  of the CJBA as a function of the readout signal power, plotted for different qubit states  $|0\rangle, |1\rangle$  and  $|2\rangle$ . The readout contrast between different states is given as the probability difference between the associated switching probability curves. Light and dark red arrows indicate the optimal working points for the  $c_{01}$  and  $c_{02}$  readout contrasts, respectively.

After having determined the  $I_0, Q_0$  and  $\alpha_{IQ}$ , we slightly tune the attenuation such that we obtain  $\approx 20\%$  of switching. At this working point, the readout contrast of the CJBA is usually already sufficient to perform a simple qubit spectroscopy, as described in section 4.5.1 and calibrate a  $X_\pi$  Rabi pulse, as described in section 4.5.2. After having done this, we can measure the switching probability of the CJBA readout as a function of the input power while either leaving the qubit in state  $|0\rangle$  or exciting it to the state  $|1\rangle$ . Fig. 4.6 shows an example of such a measurement. Here, the difference  $c_{01}$



between the two curves corresponding to the  $|1\rangle$  and  $|0\rangle$  states corresponds to the input-power dependent readout contrast and allows us to choose the optimum input power for the qubit readout. If desired, we can also perform a  $X_{\pi}^{10} \cdot X_{\pi}^{12}$  pulse sequence on the qubit to bring it into the state  $|2\rangle$  before the readout. In this state, the dispersive shift of the resonator frequency is larger than in the state  $|1\rangle$ , therefore resulting in a maximum readout contrast  $\max(c_{02}) > \max(c_{01})$ , as shown in fig. 4.6, which is advantageous when performing e.g. single-run quantum algorithms on the processor, as described in chapter 6.

## 4.5 Qubit Manipulation

To drive the qubits, we need to generate fast microwave pulses with a well defined frequency and phase. As described in one of the previous paragraphs we can use IQ sideband mixing to shape arbitrary drive pulses of the form

$$u(t) = I(t) \cos \omega_{LOT} t + Q(t) \sin \omega_{LOT} t \quad (4.6)$$

We can rewrite this as a product of two complex quantities

$$u(t) = \Re [A(t) \cdot \exp(-i\omega_{LOT}t)]. \quad (4.7)$$

The X axis of each qubits Bloch sphere is defined by the reference phase of the microwave pulse and can be chosen arbitrarily but must be conserved during one single experimental run. In addition, when performing experiments on multiple qubits, the phase differences between the reference phases of individual qubit drive signals must be conserved between individual runs of the experiment. Thus, to realize a rotation of the qubit state in the XY-plane of the Bloch sphere around an axis  $\cos \phi \vec{X} + \sin \phi \vec{Y}$ , we can use a Gaussian-shaped pulse of the form

$$A(t) = A_0 \cdot \exp\left(-\frac{(t-t_0)^2}{2\sigma_t^2}\right) \cdot \exp(-i\phi) \quad (4.8)$$

Here, we typically use a pulse rise time  $\sigma_t = 3$  ns. The advantage of using Gaussian pulses is that the Fourier transform of the pulse is again a Gaussian and, in contrast to a rectangular pulse, does not exhibit side lobes in the frequency domain [7]. Whenever possible, we just change the height of this pulse to tune the Rabi angle of a given drive pulse. However, for large Rabi angles this is not possible, hence in that case we simply add a flat plateau to the top of the Gaussian pulse. In the following sections we explain how we use such microwave drive pulses to perform qubit spectroscopy, Rabi oscillations and decoherence time measurements.

### 4.5.1 Spectroscopic Measurements of the Qubit State

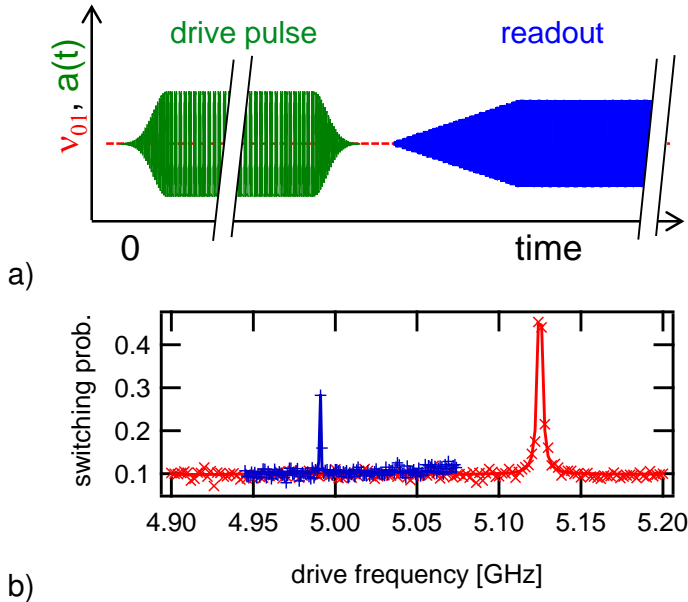
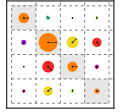


Figure 4.7: a) Qubit drive and readout pulse sequence used for performing qubit spectroscopy. b) Example of a measured qubit spectroscopy. Shown is the switching probability of the qubit readout when driving the qubit with a very long drive pulse (typically  $1 \mu\text{s}$ ) at a given drive frequency. The resonance to the right (red data points) corresponds to the  $|0\rangle \rightarrow |1\rangle$  transition of the qubit at frequency  $f_{01}$ , the resonance on the left (blue data points) to the 2-photon  $|0\rangle \rightarrow |2\rangle$  transition at frequency  $f_{02}/2$ . We fit of the two resonances with a Lorentzian to obtain an estimate of the transition frequencies.

In order to characterize the transition frequency and anharmonicity of the qubit we perform spectroscopic measurements of the qubit state. For this we drive the qubit with a very long Rabi pulse (usually  $> 500 \text{ ns}$ ) at a frequency  $\omega_d$ . When the drive frequency  $\omega_d$  is close to the  $\omega_{01}$  frequency of the qubit, the drive pulse will induce a Rabi oscillation of the quantum state of the qubit. The induced rotation amplitude will be largest at  $\omega_d = \omega_{01}$ . Due to decoherence of the qubit during the driven evolution, the maximum probability for measuring the qubit in the state  $|1\rangle$  after the pulse is limited to 50 %. Furthermore, if the drive frequency is sufficiently far detuned from the qubit transition frequency such that  $|\omega_d - \omega_{01}| \gg \Gamma^\phi$ , no oscillation will be induced and hence the qubit will remain in the state  $|0\rangle$ . By repeating the pulse sequence shown in fig. 4.7a for a range of drive frequencies  $\omega_d$ , a full spectroscopy of the qubit can be obtained. Fig. 4.7b shows an example of this, where we show the probability of measuring the qubit in state  $|1\rangle$  after applying a  $1 \mu\text{s}$  Rabi pulse, plotted as a function of  $\omega_d$  and shown for two different drive amplitudes. Here, the blue curve has been measured at 10 dB higher power than the red curve and shows the two-photon  $|0\rangle \rightarrow |2\rangle$  transition of the qubit, which can be excited at sufficiently high drive power. By fitting the two resonance



curves with a Lorentzian model we obtain the qubit frequencies  $f_{01}$  and  $f_{02}/2$  and thus the charging and Josephson energies of the qubit at the given working point.

### 4.5.2 Rabi Oscillations

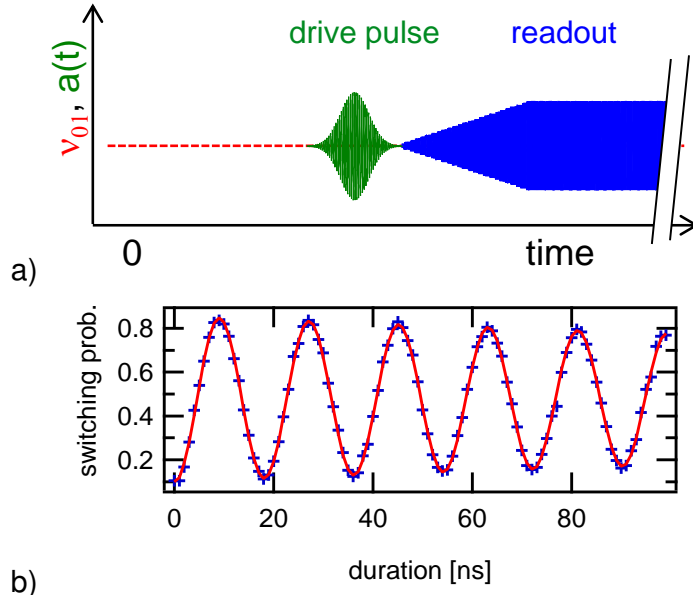


Figure 4.8: Example of a measured qubit Rabi experiment. Shown is the switching probability of the qubit readout when driving the qubit at  $f_{01}$  with a Gaussian drive pulse of varying duration. The measurement results are not corrected for readout errors.

After having obtained the proper qubit transition frequency  $f_{01}$  using the technique described above, we can perform a Rabi oscillation experiment by driving the qubit for a well-defined time with a drive pulse at the  $f_{01}$  transition frequency and measuring the state of the qubit directly afterwards. Figure 4.8a shows the pulse sequence that we use for a Rabi experiment and fig. 4.8b shows the resulting measurement data, plotting the readout switching probability as a function of the Rabi drive time. The blue points correspond to measured data whereas the continuous red line corresponds to a fit of a model of the form  $p(t) = p_0 + a \cos(\Omega t) \exp(-\Gamma_1 t)$  to the experimental data. As can be seen, the amplitude of the Rabi oscillations gets damped the longer the drive pulse becomes, which is due to relaxation and dephasing during the driven evolution of the qubit. Also, the maximum readout contrast is limited due to readout errors, as we explain in more detail in the following chapter. From the fit of the Rabi data we obtain the Rabi frequency  $\Omega$ , which we can then use to perform precise single-qubit rotations, as will be explained later. Due to the finite anharmonicity of the qubit, there will always be a leakage to the second excited state  $|2\rangle$  of the qubit which gets the more relevant, the faster we drive the system. This leakage mechanism can be an important source of

errors and very relevant to the experiments that we discuss later.

## 4.6 Dephasing Time Measurement

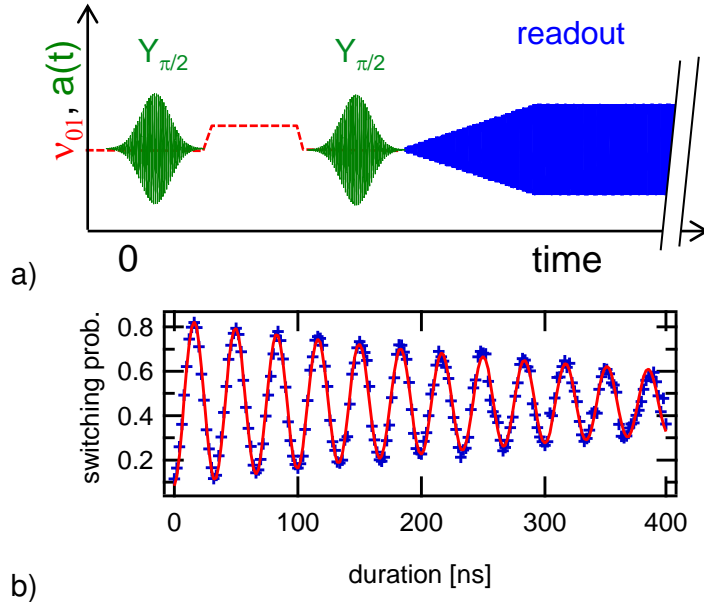
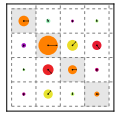


Figure 4.9: Example of a measured qubit Ramsey experiment. Shown is the switching probability of the qubit readout after performing a  $X_{\pi/2}$ -wait- $X_{\pi/2}$  drive sequence at a frequency  $f_{01} - \delta f$ . Fitting the resulting curve with an attenuated sine-wave model allows us to determine the  $f_{01}$  frequency of the Qubit with high accuracy.

After having obtained the transition frequency  $f_{01}$  of the qubit and the Rabi frequency  $\Omega$ , we can characterize the dephasing of the qubit by performing a so-called *Ramsey fringe experiment*. In this kind of experiment, we first perform a  $Y_{\pi/2}$  rotation of the qubit from the state  $|0\rangle$ , obtaining thus a superposed qubit state of the form  $1/\sqrt{2}(|0\rangle + |1\rangle)$ . Then we displace the qubit frequency by an amount  $\Delta f$  by using e.g. a fast magnetic flux pulse and then let the qubit state evolve freely during a certain amount of time  $\Delta t$ . Finally, we apply another  $Y_{\pi/2}$  pulse to the qubit and measure the state of the qubit directly afterwards. The experimental pulse sequence of this experiment is shown in fig. 4.9a. Since the qubit frequency relative to the drive reference frame has been displaced during the free evolution, the qubit will acquire a phase  $\Delta\phi = 2\pi\Delta f\Delta t$ . The final state of the qubit after applying the second  $Y_{\pi/2}$  pulse will therefore become

$$|\phi_f\rangle = \begin{pmatrix} 1 & -1 \\ 1 & 1 \end{pmatrix} \cdot \begin{pmatrix} 1 \\ e^{i\Delta\phi} \end{pmatrix} = \begin{pmatrix} i \sin \Delta\phi/2 \\ -\cos \Delta\phi/2 \end{pmatrix} \quad (4.9)$$

Hence, the resulting state  $|\phi_f\rangle$  will oscillate between the state  $|0\rangle$  and  $|1\rangle$  as a function of the delay with a frequency  $\Delta f/2$ . As before, due to dephasing and relaxation during



the free evolution of the qubit state, the amplitude of these oscillations will decay. If the system dephasing time is limited by qubit relaxation, the decay will follow a Gaussian of the form  $\exp(-\Gamma t^2)$ , otherwise it will also exhibit an exponential decay  $\simeq \exp(-\Gamma t)$ . In the Ramsey sequence, instead of detuning the qubit frequency during the free evolution phase we can also simply detune the qubit drive frequency instead, thereby changing the drive reference frame instead of the real qubit frequency. If this detuning is small in comparison to the Rabi frequency  $\Omega$ , we will still be able to accurately perform the first  $Y_{\pi/2}$  pulse. However, since the drive reference frequency is now slightly detuned from that of the qubit, the state in the drive reference frame will acquire a relative phase  $\Delta f \Delta t$  during the free evolution phase. By fitting the experimental data obtained for such an experiment to a model of the form  $p(|1\rangle) = p_0 + a \cos(\Delta f \Delta t + \phi_0) \exp(-\Gamma_2 t^2/2)$  we can obtain an estimate of  $\Delta f$  and  $\Gamma_2$ , thereby characterizing the effective dephasing time of the qubit. Fig. 4.9b shows an example of measured Ramsey data with a corresponding fit. Furthermore, since we know the frequency detuning of the drive during the free evolution of the qubit we can subtract it from the fitted value  $\Delta f$  and obtain the residual detuning of the qubit frequency from the drive frequency. This allows us to precisely determine the qubit frequency and to correct drive frequency errors with an accuracy of typically 100 kHz.

## 4.7 Relaxation Time Measurement

We can characterize the relaxation time of the qubit by performing a simple experiment where we put the qubit in state  $|1\rangle$  by applying a  $X_\pi$  pulse and let it evolve freely afterwards for a given time before reading out its state, as shown in fig. 4.10a. Due to coupling of the qubit to its environment, relaxation to the ground state can occur during the free evolution. Hence, the longer we wait, the higher the probability that the qubit has relaxed to the ground state. An example of the resulting probability curve obtained through such an experiment is shown in fig. 4.10b. It shows the probability of measuring the qubit in state  $|1\rangle$ , plotted as a function of the delay between the initial state preparation and the measurement of its state. As can be seen, the probability decreases exponentially as a function of time. As before, in the curve the blue markers correspond to experimental data and the red line corresponds to a fit of this data to a model of the form  $p(|1\rangle) = p_0 + p_a \exp(-\Gamma_1 t)$ . From this fit, we can then extract the relaxation rate  $\Gamma_1$  of the qubit at the given working point. In the following chapter we will look more in detail at the relaxation time of both qubits of our processor as a function of their transition frequency and their detuning from the readout resonator.

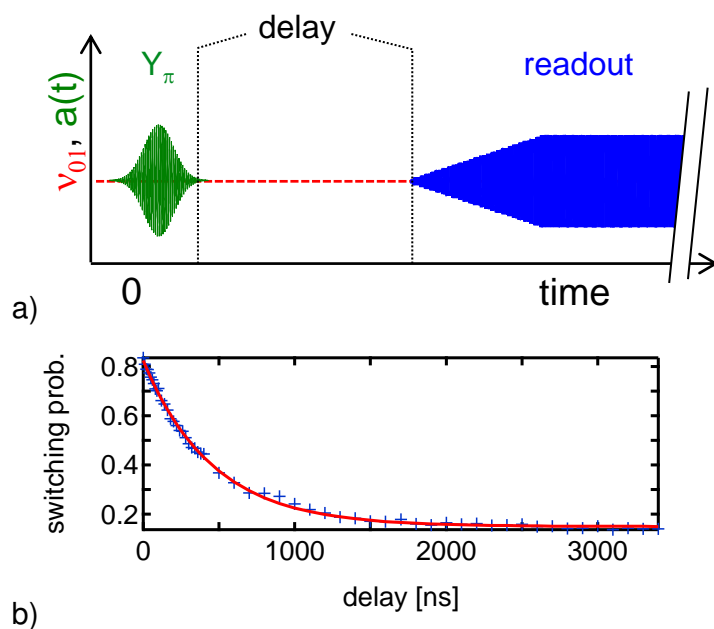
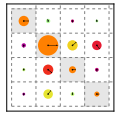


Figure 4.10: Example of a qubit relaxation time measurement. Shown is the probability of measuring the qubit in state  $|1\rangle$  as a function of the delay time between the preparation of the state  $|1\rangle$  and the actual measurement of the qubit state. The decay of this probability follows an exponential law of the form  $p(|1\rangle) \simeq \exp(-\Gamma_1 t)$



# Chapter 5

## Characterizing the Two-Qubit Processor

After having detailed the design of the processor and the measurement techniques employed in this work, we will discuss how we can characterize it to demonstrate the basic functionality that we need to run meaningful quantum algorithms. In particular we show how we can implement a robust two-qubit quantum gate that we will use in the following chapter to run a real-world quantum algorithm on our processor.

We begin the chapter by discussing the measurement of the basic qubit and readout parameters. We will then give a detailed overview of the relevant decoherence times and readout fidelities of our processor at different working points and discuss our strategy for optimizing these parameters during its operation. Afterward we will explain the realization of single-qubit gates together with possible error sources that we need to take into account. We also discuss in detail the generation and characterization of entanglement. Finally, we discuss the implementation of a universal two-qubit gate and its characterization through quantum process tomography.

### 5.1 Qubit & Readout Characterization

The first step in the characterization of the processor consists in obtaining all the relevant qubit and readout parameters. For this, we perform a set of measurements from which we obtain the qubit frequencies, anharmonicities, junction asymmetries, the inter-qubit coupling, the coupling to the microwave drive lines, the coupling of each qubit to its readout and the relaxation and dephasing times of the qubits. Most of these parameters, such as the drive and readout couplings as well as the relaxation and dephasing times are measured for a range of qubit frequencies, which will allow us later to pick an ideal working point for our two-qubit experiments. A detailed account of the measurement

## 5.1. QUBIT & READOUT CHARACTERIZATION

---

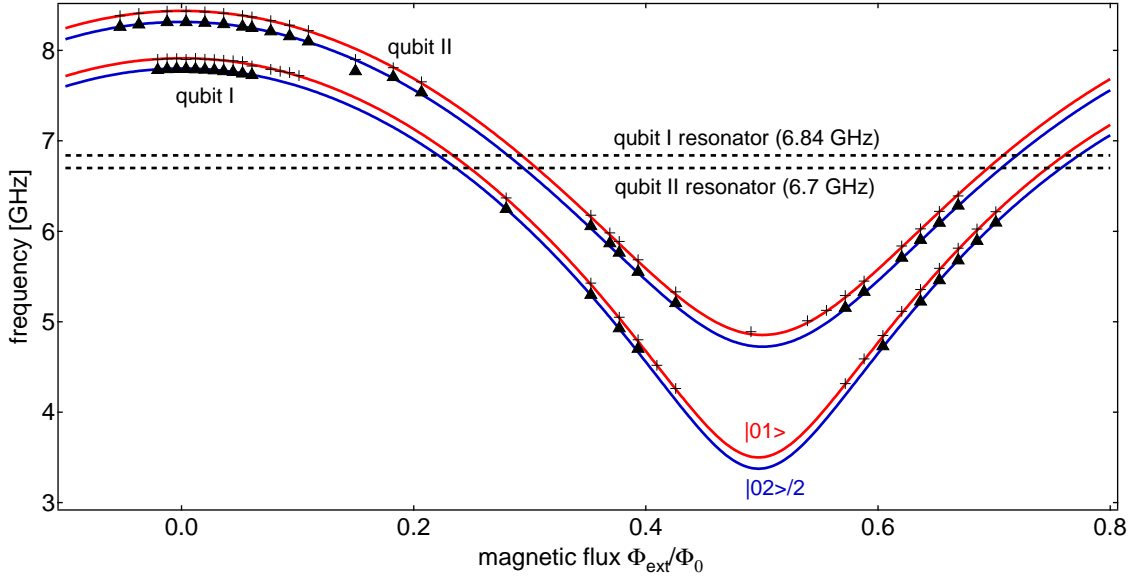


Figure 5.1: Spectroscopy of our two-qubit processor. Shown are the  $|0\rangle \rightarrow |1\rangle$  ( $\omega_{01}$ ) and  $(|0\rangle \rightarrow |2\rangle)/2$  ( $\omega_{02}/2$ ) transition frequencies of the two qubits, together with a fitted analytical model of the qubit parameters. We also show the frequencies of the two readout resonators.

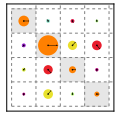
techniques employed here can be found in chapter 4.

### Qubit Frequency, Anharmonicity and Asymmetry

To obtain the Josephson and charging energies as well as the junction asymmetries of the qubits we perform spectroscopic measurements of the single-photon  $|0\rangle \rightarrow |1\rangle$  and the two-photon  $|0\rangle \rightarrow |2\rangle$  qubit transitions at different values of the external magnetic flux  $\Phi_{ext}$ . By fitting the resulting values  $\omega_{01}(\Phi_{ext})$  and  $\omega_{02}(\Phi_{ext})$  to a theoretical model we obtain all relevant qubit parameters. For our processor, these are  $E_J^I/h = 36.2$  GHz,  $E_c^I/h = 0.98$  GHz and  $E_J^{II}/h = 43.1$  GHz,  $E_C^{II}/h = 0.87$  GHz for the Josephson and charging energies of the two qubits, yielding anharmonicities  $\alpha^I \approx 245$  MHz and  $\alpha^{II} \approx 220$  MHz. For the qubit junction asymmetries, we obtain  $d^I = 0.2$ ,  $d^{II} = 0.35$ .

### Readout Parameters

To obtain the resonance frequencies and quality factors of the readout resonators we perform a simple reflectometric measurement of the  $S_{11}$  transmission coefficient of the resonators. The resulting frequencies are  $\nu_R^I = 6.84$  GHz and  $\nu_R^{II} = 6.70$  GHz with quality factors  $Q^I \simeq Q^{II} = 730$ . We measure the Kerr nonlinearity  $K$  of the resonators by following the procedure given in [79, p. 166] and obtain  $K^I/\nu_R^I \simeq K^{II}/\nu_R^{II} = -2.3 \pm 0.5 \times 10^{-5}$ .



## Qubit/Readout Coupling

The coupling of the qubits to the readout resonators can be determined by spectroscopically measuring the avoided level crossing between the two systems. For this, we perform a series of spectroscopic measurements of the resonator while tuning the qubit frequency from a value below the resonator frequency to one above it. The results of these measurements are given in fig. 5.2 and clearly show an avoided level crossing between the two systems. By fitting the obtained data to a theoretical model, we obtain the qubit-resonator coupling coefficients  $g_{01}^I \simeq g_{01}^{II} = 2\pi \cdot 50$  MHz.

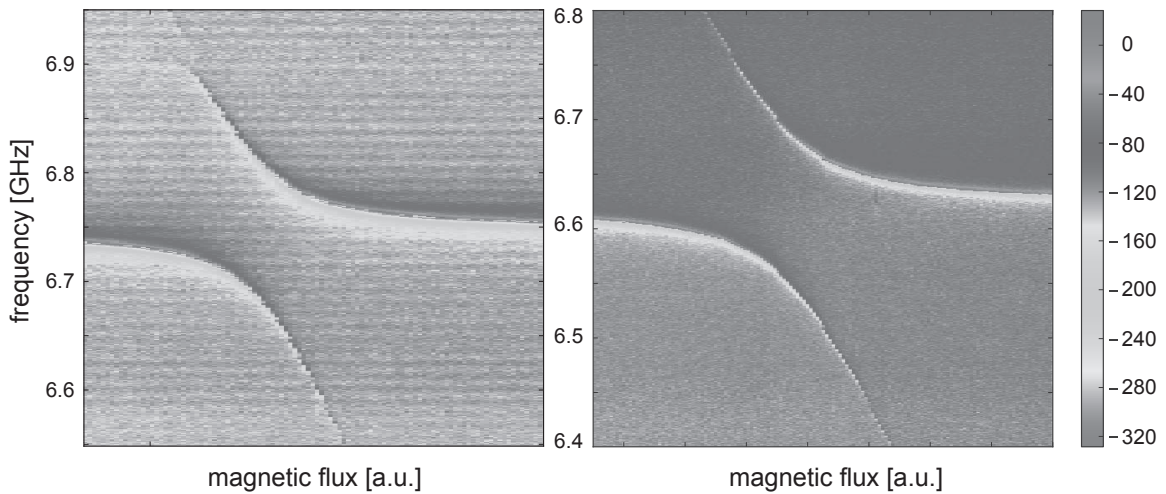


Figure 5.2: Spectroscopic measurement of the avoided level crossing between the two qubits and their corresponding readout resonator, yielding an effective qubit-resonator coupling strength  $2g_{01}/2\pi \approx 50$  MHz.

## Qubit Parameter Survey

In order to determine the optimal working point for our processor we need to characterize the properties of the qubits at many different frequencies. For this, we perform an automated survey where we measure the transition frequencies  $\omega_{01}$  and  $\omega_{02}$ , the readout contrast  $c$  and the relaxation and dephasing times  $T_1$  and  $T_2$  of each qubit at different values of the magnetic flux  $\Phi_{ext}$ . The results of such a parameter survey are summarized in fig 5.3, where we show the relaxation time  $T_1$ , the readout contrast  $c_{01}$  and the Rabi frequency  $f_{Rabi}$  at fixed drive amplitude for the two qubits within a frequency range between 5.2 and 6.5 GHz. As can be seen, the relaxation time of the qubits tends to increase the farther detuned each qubit is from its readout resonator. Not surprisingly, the drive frequency of the qubit also decreases when the qubit-resonator detuning increases, as expected from the Purcell effect, which filters incoming microwave signals that are far-detuned from the resonator frequency. The readout contrast decreases nearly linear

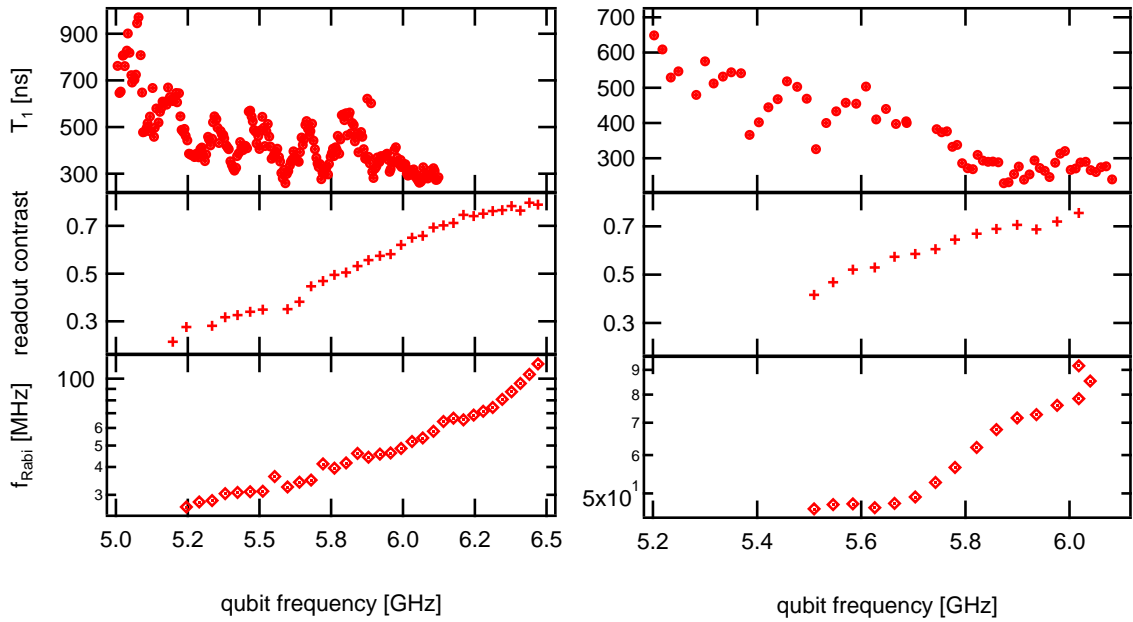
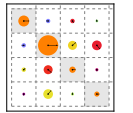


Figure 5.3: A qubit parameter survey showing the relaxation time  $T_1$ , the readout contrast and the Rabi frequency at a fixed drive amplitude for the two qubits over a large range of qubit frequencies.

when increasing the qubit-resonator detuning  $\Delta$ , as expected from the dispersive shift  $\chi \propto 1/\Delta$  given by eq. (2.94).

It is interesting to note the non-monotonous characteristic of the qubit relaxation time  $T_1$  shown in fig. 5.3, which cannot be explained by Purcell-filtering through the readout resonator and hints thus at a different qubit relaxation process present in the system. A possible explanation would be the coupling of the qubit to spurious low-Q resonances in the environment. For example, the coupling of the qubit to volumetric resonance modes of the sample holder or to non-CPW resonance modes of the readout resonator could be possible explanations for the data. Also, the overall dependency of the relaxation time  $T_1$  on the qubit-resonator detuning –ignoring the “fine-structure” present in the system– is not quadratic as would be expected from the Purcell theory but rather linear. Also, by comparing the qubit relaxation time to the Rabi drive frequency reveals that the increase in  $T_1$  is clearly not proportional to the Purcell factor, that determines both the qubit relaxation rate through the readout resonator and the Rabi drive frequency. However, the observed  $T_1$  dependency can be partially explained by taking into account the qubit relaxation through the fast fluxline, which might be too strongly coupled to the qubit, hence inducing additional qubit relaxation beyond the Purcell and intrinsic qubit relaxation rates.



## 5.2 Choice of Processor Working Points

Having characterized all parameters of the qubits as a function of their frequencies  $\omega_{01}^I$  and  $\omega_{01}^{II}$ , we go ahead and choose frequency working points for qubit manipulation and readout. For single-qubit manipulation and parking, we choose the two operating frequencies  $\omega_{01,m}^I/2\pi = 5.247$  GHz and  $\omega_{01,m}^{II}/2\pi = 5.125$  GHz, where we have relaxation times  $T_1^I(\omega_{01,m}^I) \approx 440$  ns and  $T_1^{II}(\omega_{01,m}^{II}) \approx 520$  ns. For qubit readout, we choose  $\omega_{01,r}^I \approx 6.2$  GHz and  $\omega_{01,r}^{II} \approx 6.0$  GHz, where we have single-shot readout contrasts  $c_{01}^I(\omega_{01,r}^I) \approx 75\%$  and  $c_{01}^{II}(\omega_{01,r}^{II}) \approx 73\%$ .

## 5.3 Qubit Readout Characterization

The readout errors of the qubits are fully characterized by the conditional switching probabilities  $p_m(0|0)$  and  $p_m(1|1)$ , where we define  $p_m(x|y)$  as the probability of obtaining a readout value  $x$  after having prepared a qubit state  $|y\rangle$ , where  $x, y \in \{0, 1\}$  for single-qubit readout and  $x, y \in \{00, 01, 10, 11\}$  for two-qubit readout. In addition, a two-qubit readout usually exhibits readout crosstalk errors, which are characterized by the switching probabilities  $p_m(x * |x0) = p_m(x0|x0) + p_m(x1|x0)$ ,  $p_m(x * |x1) = p_m(x0|x1) + p_m(x1|x1)$  as well as  $p_m(*x|0x) = p_m(0x|0x) + p_m(1x|0x)$  and  $p_m(*x|1x) = p_m(0x|1x) + p_m(1x|1x)$ , where  $x \in \{0, 1\}$ . If crosstalk is present,  $p_m(x * |x0) \neq p_m(x * |x1)$  and/or  $p_m(*x|0x) \neq p_m(*x|1x)$ .

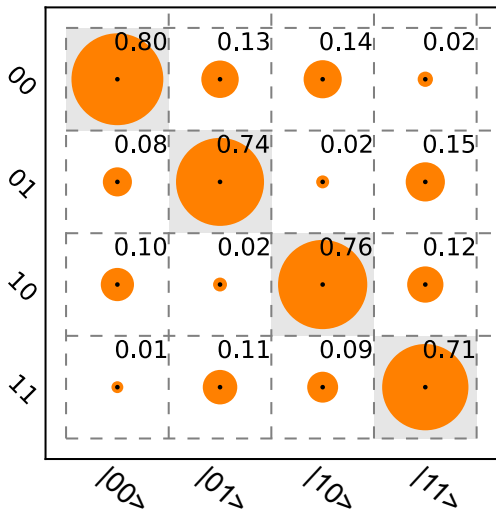


Figure 5.4: The measured readout matrix of our two-qubit processor. Shown are the conditional measurement probabilities  $p_m(x|y)$  where  $x, y \in \{00, 01, 10, 11\}$ . The diagonal elements correspond to the readout fidelities of the four basis states. The single qubit readout fidelities as obtained from the matrix are  $p_m^I(0 * |00) = 0.88$ ,  $p_m^I(1 * |10) = 0.85$ ,  $p_m^{II}(*0|00) = 0.9$  and  $p_m^{II}(*1|01) = 0.85$ , the readout crosstalks are  $p_m(0 * |00) - p_m(0 * |01) = -0.01$ ,  $p_m(1 * |10) - p_m(1 * |11) = -0.02$ ,  $p_m(*0|00) - p_m(*0|10) = 0$  and  $p_m(*1|01) - p_m(*1|11) = -0.01$ .

The single-qubit fidelities  $p_m(0|0)$  and  $p_m(1|1)$  can be simply obtained from an s-curve measurement, as explained in section 4.4. In order to obtain the two-qubit readout errors, we perform an experiment where we measure the full set of conditional probabili-

## 5.4. SINGLE-QUBIT OPERATIONS

---

ties  $p(x|y)$  with  $x, y \in \{00, 01, 10, 11\}$  by initializing the qubit register to each basis state and performing a simultaneous readout of the two qubits. By repeating and averaging the resulting readout outcomes  $i$  for each basis state  $|j\rangle$ , where  $\{i, j\} \in \{00, 01, 10, 11\}$ , we obtain the full set of conditional readout probabilities, which can be plotted as a  $4 \times 4$  readout matrix  $\mathbf{R}$ , as shown in fig. 5.4. From this matrix, all conditional and unconditional readout fidelities as well as the readout crosstalk can be calculated. We can correct a measured set of probabilities  $\mathbf{p}_R = (p_{00}, p_{01}, p_{10}, p_{11})$  for readout errors by simply multiplying it with the inverse of  $\mathbf{R}$ , such that  $\mathbf{p}_R^{corr} = \mathbf{p}_R \cdot \mathbf{R}^{-1}$ . For all experiments discussed in the remainder of this chapter, we will always correct readout errors by this method, unless indicated otherwise.

## 5.4 Single-Qubit Operations

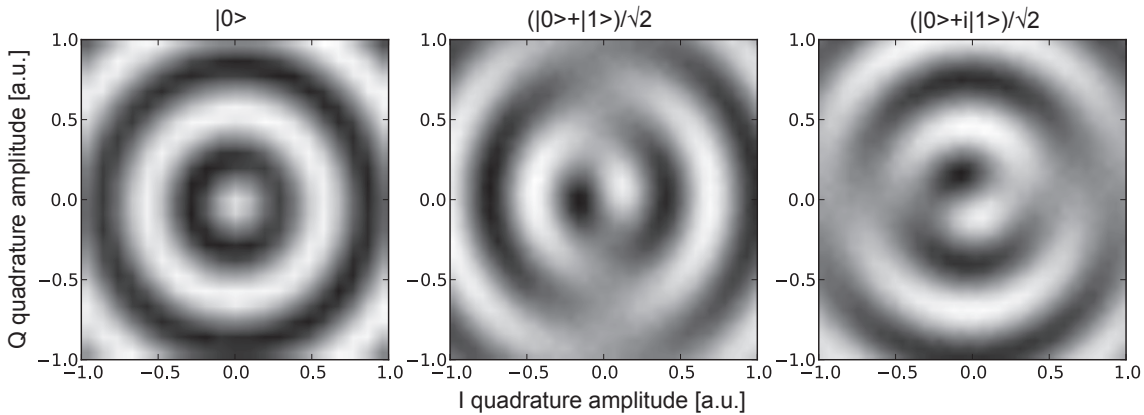
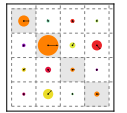


Figure 5.5: Demonstration of single-qubit XY control. The figures show the state probability of a single qubit when preparing it in one of the states  $|1\rangle$ ,  $1/\sqrt{2}(|0\rangle + |1\rangle)$  or  $1/\sqrt{2}(|0\rangle + i|1\rangle)$  and subjecting it to a microwave drive pulse of constant duration with  $a(t) = V_I \cdot \cos \omega_{rf} t + V_Q \cdot \sin \omega_{rf} t$  and of varying amplitudes  $V_I$  and  $V_Q$ .

To perform arbitrary single-qubit operations – as needed e.g. for implementing a quantum algorithm or performing quantum state tomography – we need to implement a universal set of  $X$ ,  $Y$  and  $Z$  qubit gates on our processor. Qubit rotations in the  $XY$ -plane are implemented through microwave drive pulses, where the phase of the drive pulse in reference to an arbitrary reference determines the rotation axis and the amplitude of the drive pulse the Rabi frequency of the gate. To characterize the drive pulses, we perform an experiment where we initialize a single-qubit in the states  $|1\rangle$ ,  $1/\sqrt{2}(|0\rangle + |1\rangle)$  and  $1/\sqrt{2}(|0\rangle + i|1\rangle)$  and subject it afterward to a single microwave pulse of the form  $a(t) = V_I \cdot \cos \omega_{rf} t + V_Q \cdot \sin \omega_{rf} t$ , which we tune by changing the input voltages  $V_I$  and  $V_Q$  to the  $IQ$ -mixer that generates the pulse from a continuous input microwave-tone at frequency  $\omega_{rf}$ . We then measure the qubit state  $|1\rangle$  occupation probability at



different values of  $V_I$ ,  $V_Q$ , obtaining the graph shown in fig. 5.5. The qubit which was prepared in state  $|1\rangle$  shows a perfectly cylinder-symmetric switching probability pattern when subjecting it to an IQ-pulse of a given phase, which is indeed what one would expect for a qubit being prepared in either the  $|0\rangle$  or  $|1\rangle$  state. On the other hand, the switching probability distributions of the qubits prepared in the states  $1/\sqrt{2}(|0\rangle + |1\rangle)$  and  $1/\sqrt{2}(|0\rangle + i|1\rangle)$  are mirror-symmetric, where the switching probability does not vary at all along the drive axis that corresponds to the axis along which the qubit has been prepared. These measurements demonstrate our ability to prepare and drive the qubit along arbitrary axes of the Bloch sphere, which is a necessary prerequisite for implementing a universal set of gates on our processor and for performing quantum state tomography.

## 5.5 Two Qubit Operations

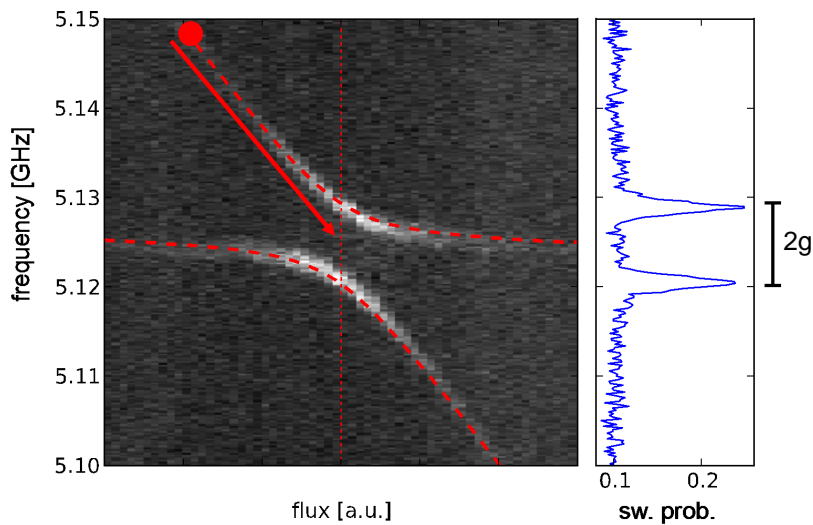


Figure 5.6: a) Spectroscopy measurement of the avoided level crossing between the two qubits of our processor. b) Single spectroscopy of qubit I when in resonance with qubit II. From this spectroscopic measurement, a qubit-qubit coupling strength of  $2g_{qq} = 8.3$  MHz can be deduced.

We use the capacitive coupling between the qubits to implement two-qubit gates and to create entangled states between them. To characterize the qubit-qubit interaction, we first perform a spectroscopic measurement of the qubits. For this, we measure a spectroscopy of qubit I for a range of external fluxes  $\Phi_{ext}^I$ , such that the frequency of qubit I  $\omega_{01}^I$  gets tuned through the frequency of qubit II  $\omega_{01}^{II}$ . Now, if the two qubit frequencies  $\omega_{01}^I$ ,  $\omega_{01}^{II}$  are far detuned such that  $|\omega_{01}^I - \omega_{01}^{II}| \gg 2g_{qq}$ , the eigenstates of the coupled two-qubit Hamiltonian correspond to a very good accuracy to the independent qubit states  $|01\rangle$  and  $|10\rangle$ . Therefore, far from the resonance condition we observe only

one spectroscopic line corresponding to the transition  $|00\rangle \rightarrow |10\rangle$  (since we drive only the first qubit). However, close to resonance, the eigenstates of the two-qubit system approach the two Bell states  $|\Psi_{\pm}\rangle = 1/\sqrt{2}(|10\rangle \pm |01\rangle)$ , which can both be excited by driving qubit I. Hence we observe two spectroscopic lines corresponding to the two transitions  $|00\rangle \rightarrow 1/\sqrt{2}(|01\rangle + |10\rangle)$  and  $|00\rangle \rightarrow 1/\sqrt{2}(|01\rangle - |10\rangle)$ . The frequency width of the gap between these two spectroscopic lines corresponds to the qubit-qubit coupling strength  $2g_{qq}/2\pi$ . Fig 5.6 shows the results of such a spectroscopic measurement, where qubit II was positioned at a  $\omega_{01}^I/2\pi = 5.125$  GHz and the frequency of qubit II was tuned from  $\omega_{01}^{II}/2\pi \in 5.1 - 5.15$  GHz. At resonance, we measure a coupling strength of  $2g_{qq}/2\pi = 8.3$  MHz.

### 5.5.1 Creation of Entanglement

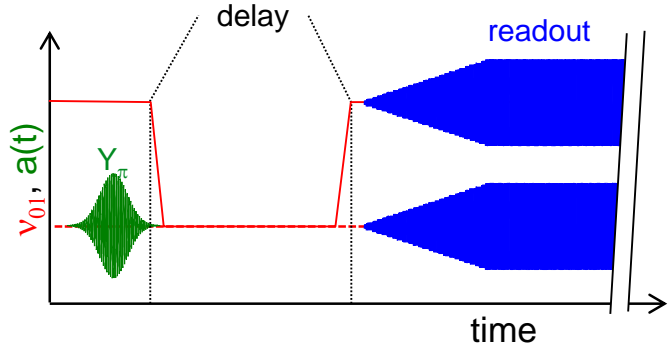


Figure 5.7: Pulse sequence used to create an entangled two-qubit state using a non-adiabatic pulse that brings the qubits in resonance for a well-defined time.

After having characterized the qubit-qubit interaction using a spectroscopic measurement we perform a coherent swapping operation between the qubits. We implement this operation by non-adiabatically changing the resonance frequency of the qubits from an off-resonance condition  $|\omega_{01}^I - \omega_{01}^{II}| \gg g_{qq}$  to an on-resonance condition  $\omega_{01}^I = \omega_{01}^{II}$ . When doing this after preparing the qubits in one of the states  $|01\rangle$  or  $|10\rangle$ , we induce a coherent energy swap between them. We then terminate the interaction after a well-defined time and measure the state of the two-qubit register directly afterward. When the qubits are in resonance, the time evolution operator of their quantum state is given as

$$U(t) = \begin{pmatrix} 1 & 0 & 0 & 0 \\ 0 & \cos(tg_{qq}) & i \sin(tg_{qq}) & 0 \\ 0 & i \sin(tg_{qq}) & \cos(tg_{qq}) & 0 \\ 0 & 0 & 0 & 1 \end{pmatrix}_{\{|00\rangle, |01\rangle, |10\rangle, |11\rangle\}} \quad (5.1)$$

As can be seen, the two basis states  $|01\rangle$  and  $|10\rangle$  indeed oscillate back and forth between each other with frequency  $g_{qq}$ . The states  $|00\rangle$  and  $|11\rangle$  are not affected by the interaction.

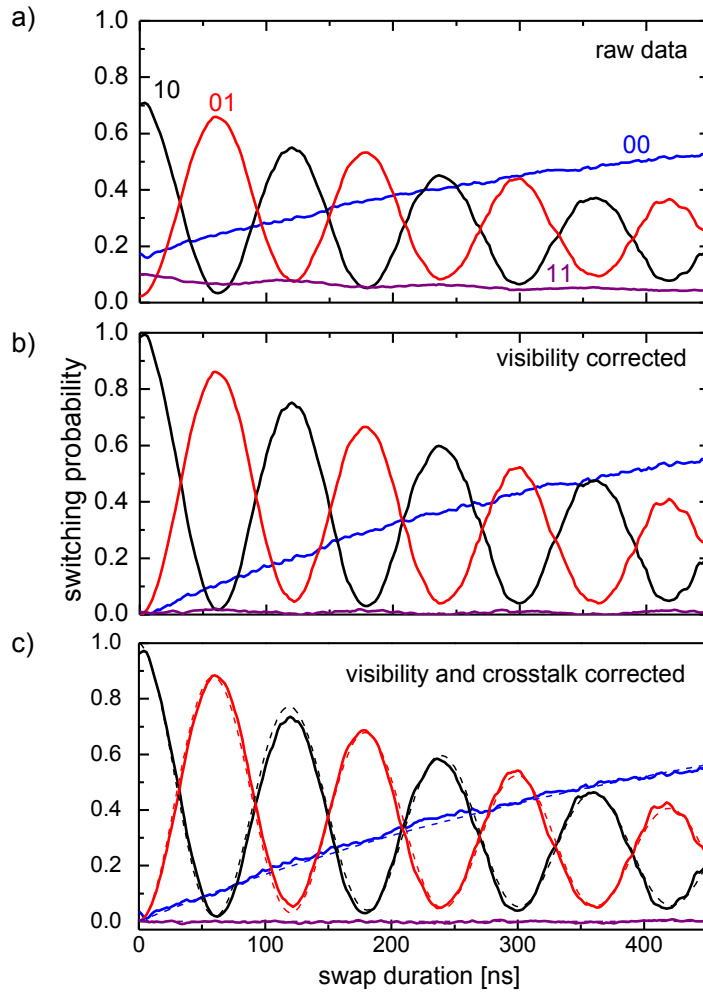
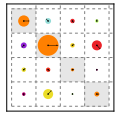


Figure 5.8: State occupation probabilities for the two-qubit register during a coherent energy swap. a) Shows the raw state probabilities corresponding to the states  $|00\rangle$ ,  $|01\rangle$ ,  $|10\rangle$  and  $|11\rangle$ , b) shows the same data corrected for the limited visibility of each qubit readout and c) shows the fully corrected readout data where we account for both visibility and inter-qubit readout crosstalk errors.

Fig. 5.7 summarizes the frequency, drive and measurement pulse sequence that we use for this experiment. When varying the time during which the qubits are in resonance, we can observe the coherent swapping of energy between them. Figure 5.8 presents the results of such a measurement. Shown are the measured qubit state probabilities  $p(|00\rangle)$ ,  $p(|01\rangle)$ ,  $p(|10\rangle)$  and  $p(|11\rangle)$  as a function of the swap duration  $\Delta t$ . Subfigure a) shows the raw, uncorrected readout data, subfigure b) shows the probabilities corrected for limited readout visibility and subfigure c) shown the probabilities corrected for both limited readout visibility and crosstalk, using the readout matrix discussed in section 5.3. The oscillatory behavior between the states  $|01\rangle$  and  $|10\rangle$  is clearly visible in the data.

Also, the frequency of the energy swap  $2g_{qq} = 8.3$  MHz agrees with the value obtained from the spectroscopic measurement. Fig. 5.8c shows, in addition to the measured state occupation probabilities a master equation simulation of the experiment, that the Hamiltonian and Lindblad operators discussed in section 2.5. This simulation takes into account relaxation and dephasing of the qubits. The relaxation rates used in the simulation correspond to the experimentally measured relaxation rates at the operating frequencies of the qubits, whereas the dephasing rates were free fitting parameters. We do not use the measured single-qubit dephasing rates in our simulation since they do not correspond to the effective dephasing rate of the two-qubit system at resonance, which cannot be described within the master equation formalism. The reason for this is that the transition frequency of the two eigenstates  $|\phi_{\pm}\rangle = 1/\sqrt{2}(|01\rangle \pm |10\rangle)$  at resonance  $\omega_{01}^{\pm} = \omega_{01}^{I,II} \pm \sqrt{4g_{qq}^2 + \Delta^2}/2 \approx \omega_{01}^{I,II} \pm g_{qq} + \Delta^2/8g_{qq}$  is insensitive to variations of  $\Delta$  to first order. Hence, the effective dephasing rate of the two-qubit system will be much higher than the single-qubit dephasing rates. To reproduce the experimentally observed dephasing, we therefore used effective dephasing rates  $\Gamma_{\phi}^{I,II} = 2 \mu\text{s}$ . As can be seen, using these rates and the measured relaxation rates as well as coupling parameter  $g_{qq}$ , the simulation agrees well with the experimental data.

### 5.5.2 Quantum State Tomography

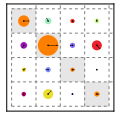
The experiments that we describe in the following sections often require us to determine the density matrix of an experimental two-qubit state. The method that we use for this purpose is called *quantum state tomography* (QST) (see e.g. [75] for an overview of this method). In this section, we therefore explain in detail the procedure that we use to perform QST. Furthermore, we also discuss several sources of errors occurring in standard QST and how we can estimate their effect on our results.

The density matrix of an n-qubit system can be written as

$$\rho = \sum_{v_1, v_2, \dots, v_n} \frac{c_{v_1, v_2, \dots, v_n} \hat{\sigma}_{v_1} \otimes \hat{\sigma}_{v_2} \dots \otimes \hat{\sigma}_{v_n}}{2^n} \quad (5.2)$$

$$c_{v_1, v_2, \dots, v_n} = \text{Tr} \{ \hat{\sigma}_{v_1} \otimes \hat{\sigma}_{v_2} \dots \otimes \hat{\sigma}_{v_n} \rho \} \quad (5.3)$$

where  $v_i \in \{X, Y, Z, I\}$  and  $n$  gives the number of qubits in the system and where the  $c_{v_1, v_2, \dots, v_n}$  are real-valued coefficients that describe the given density matrix. To reconstruct the density matrix of an experimental quantum system, it is thus sufficient to measure the expectation values of these  $n^2 - 1$  coefficients on an ensemble of identically prepared states. For our two qubit system, this means measuring all possible combinations of the operators  $\{I, \hat{\sigma}_x^I, \hat{\sigma}_y^I, \hat{\sigma}_z^I\} \otimes \{I, \hat{\sigma}_x^{II}, \hat{\sigma}_y^{II}, \hat{\sigma}_z^{II}\}$ . However, in our experiments, we can only measure the  $\hat{\sigma}_z$  operator of the qubit, therefore, rather than measuring the



$\hat{\sigma}_x$  and  $\hat{\sigma}_z$  operators directly, we rotate the quantum state of each qubit such that the state vector along the desired measurement axis coincides with the z-axis of the Bloch sphere and then measure  $\hat{\sigma}_z$  instead.

When using this direct method, statistical and systematic measurement errors can produce a set of coefficients  $v_i$  that corresponds to a *non-physical* density matrix, i.e. a density matrix which violates either the positivity  $\langle \psi | \rho | \psi \rangle > 0$  (for all valid states  $|\psi\rangle$ ) or the unity-trace condition  $\text{Tr}(\rho) = 1$ . To alleviate this problem, several techniques can be employed. In the following section we discuss an estimation technique which is able to overcome the problem of non-physical density matrices, the so-called *maximum likelihood estimation*.

### Maximum Likelihood Estimation of Quantum States

Maximum likelihood estimation is a method that numerically or analytically maximizes a likelihood function that is based on a number of measured outcomes and a set of parameters that need to be estimated. The set of parameters that corresponds to the maximum of the probability function can then be interpreted as the one with the highest probability of generating the observed outcomes. When estimating the parameters of a density matrix with this method, the probability function to be maximized is the joint probability of obtaining the measured values  $\{c_{X,X,\dots,X}, c_{Y,X,\dots,X}, \dots, c_{I,I,\dots,I}\}$  for a given density matrix  $\hat{\rho}$ . By numerically or analytically maximizing this joint probability over the set of possible density matrices we obtain the density matrix which is most likely to have produced the set of measurement outcomes that we have observed.

The joint measurement operators  $\hat{\Sigma}_j = \hat{\sigma}_{v_1} \otimes \hat{\sigma}_{v_2} \dots \otimes \hat{\sigma}_{v_n}$  have the eigenvalues  $\pm 1$  and can thus be written as

$$\hat{\sigma}_{v_1} \otimes \hat{\sigma}_{v_2} \dots \otimes \hat{\sigma}_{v_n} = |+_j\rangle\langle+_j| - |-_j\rangle\langle-_j| \quad (5.4)$$

where  $|+_j\rangle$  and  $|-_j\rangle$  are the eigenstates corresponding to the eigenvalues  $\pm 1$  of  $\hat{\Sigma}_j$ . When performing  $l$  measurements of the operator  $\hat{\Sigma}_j$ , the expectation value  $\langle \hat{\Sigma}_j \rangle$  can be estimated as

$$\widehat{\langle \hat{\Sigma}_j \rangle}_\rho = \frac{1}{l} \sum_{i=1}^l m_i(\hat{\Sigma}_j, \rho) \quad (5.5)$$

where  $m_i(\hat{\Sigma}, \rho)$  denotes the outcome of the  $i$ -th measurement of the operator  $\hat{\Sigma}$  on the state described by the density matrix  $\rho$ . Since each outcome  $m_i(\hat{\Sigma}_j, \rho)$  is Bernoulli distributed, the sum  $\widehat{\langle \hat{\Sigma}_j \rangle}_\rho$  of them is binomially distributed with an expectation value  $E(\widehat{\langle \hat{\Sigma}_j \rangle}_\rho) = \langle \hat{\Sigma}_j \rangle_\rho$  and the variance  $\sigma^2(\widehat{\langle \hat{\Sigma}_j \rangle}_\rho) = 1/l \cdot (1 - \langle \hat{\Sigma}_j \rangle_\rho^2)$ . For large sample sizes  $l$ , the binomial distribution can be well approximated by a normal distribution with the same expectation value and variance. The joint probability of obtaining a set of

estimates  $\{s_1, \dots, s_{n^2-1}\}$  for the set of operators  $\{\langle \hat{\Sigma}_1 \rangle_\rho, \dots, \langle \hat{\Sigma}_{n^2-1} \rangle_\rho\}$  for a proposed density matrix  $\rho$  is thus given as

$$P\left(\langle \hat{\Sigma}_1 \rangle_\rho = s_1; \dots; \langle \hat{\Sigma}_{n^2-1} \rangle_\rho = s_{n^2-1}\right) = \prod_{i=1}^{n^2-1} \exp\left(-\frac{l}{2} \frac{(s_i - \langle \hat{\Sigma}_i \rangle_\rho)^2}{1 - \langle \hat{\Sigma}_i \rangle_\rho^2}\right) \quad (5.6)$$

By maximizing this probability (or the logarithm of it) as a function of the parameters of the proposed density matrix  $\rho$ , we obtain the  $\rho$  which has the highest probability of having produced the observed measurement values.

### Including Experimental Tomography Errors

The ML technique also allows us to include further optimization parameters when calculating the joint probability. This is useful for modeling e.g. systematic errors of the measurement or preparation process, which can be described by modifying the operators contained in the probability sum. A common source of errors in our tomography measurements are shifts in the amplitude and phase of the microwave pulses used to drive the qubit. We are obliged to rotate the qubit state when performing state tomography since our measurement apparatus permits us only to measure the  $\hat{\sigma}_z$  operator of each qubit. We can therefore replace the operators  $\hat{\sigma}_x$  and  $\hat{\sigma}_y$  in eq. (5.4) with an effective measurement of  $\hat{\sigma}_z$  preceded by a rotation  $R_{X,Y}$  given as

$$R_X = \exp(-i\hat{\sigma}_y\pi/4) \quad (5.7)$$

$$R_Y = \exp(+i\hat{\sigma}_x\pi/4) \quad (5.8)$$

Within this model, phase and amplitude errors can be modeled by including additional phase factors, yielding

$$R'_X = \exp(-i[+\hat{\sigma}_y \cos \alpha + \hat{\sigma}_x \sin \alpha] [\pi/4 + \gamma]) \quad (5.9)$$

$$R'_Y = \exp(+i[-\hat{\sigma}_y \sin \beta + \hat{\sigma}_x \cos \beta] [\pi/4 + \delta]) \quad (5.10)$$

Here,  $\alpha$  and  $\beta$  represent phase errors whereas  $\gamma$  and  $\delta$  represent amplitude errors in the drive pulses. A detailed discussion of how we fit these parameters to experimental data will be given in section 5.6.5.

#### 5.5.3 Characterizing Two-Qubit States using QST

Using quantum state tomography, we can repeat the swapping experiment described in section 5.5.1 and reconstruct the full experimental density matrix of our system at many different times during the swap sequence by measuring a full Pauli set on an ensemble of

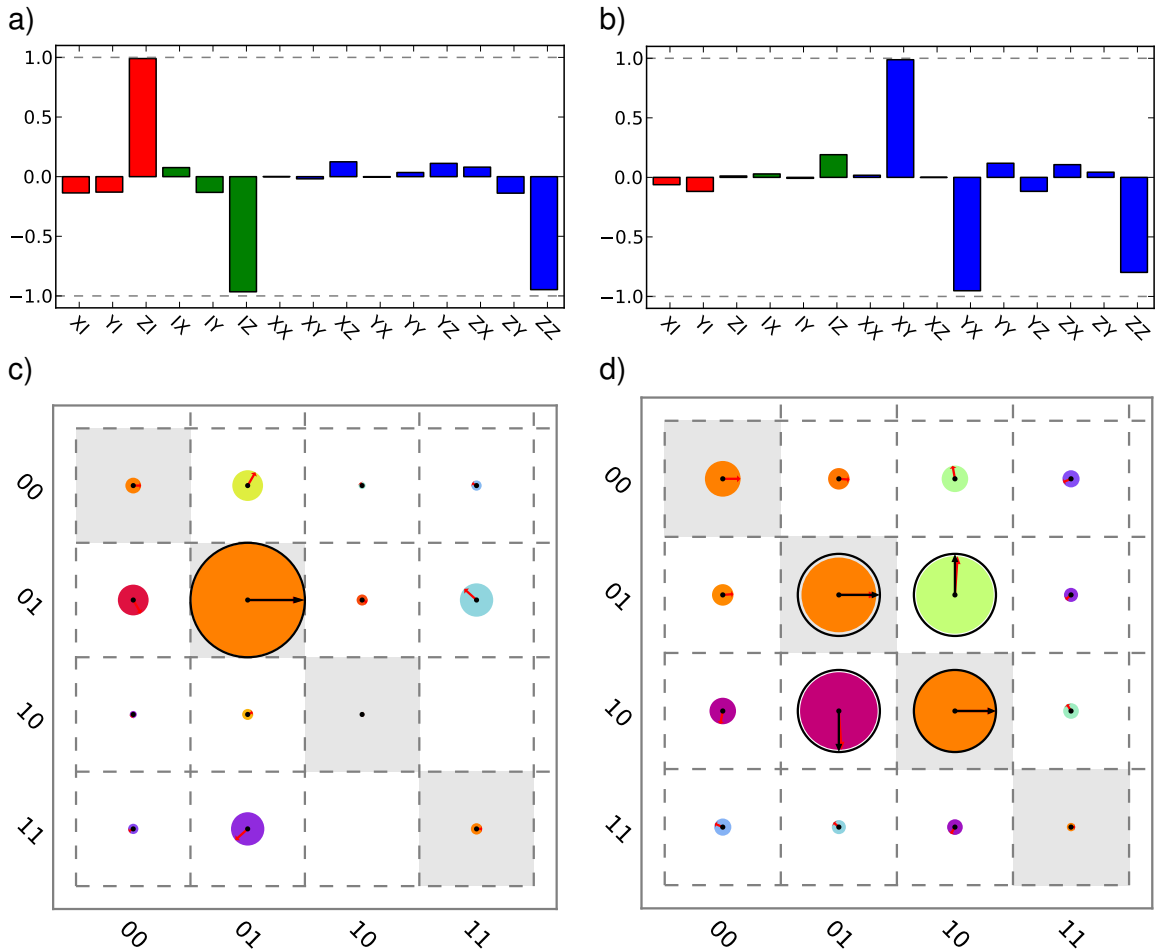
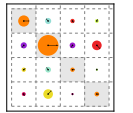


Figure 5.9: a/b) Measured Pauli sets of a prepared  $|01\rangle$  input state and a corresponding output state (b) measured after a swapping time  $t = 31$  ns, showing the measured values of the single-qubit and multi-qubit Pauli operators. c/d) Corresponding density matrices of the input and output states, reconstructed using maximum likelihood estimation. The absolute value  $|\rho_{ij}|$  of each element of the density matrix is represented by the size of each circle, whereas the phase  $\angle \rho_{ij}$  is represented both by the color of the circle and the direction of the arrow. The state fidelities compared to the ideal states  $|\psi^{in}\rangle = |01\rangle$  and  $|\psi^{out}\rangle = 1/\sqrt{2}(|01\rangle + i|10\rangle)$  are  $F_{tr}^{in} = 94\%$  and  $F_{tr}^{out} = 84\%$ , respectively. The density matrices of the ideal states are overlaid in black, for comparison.

identically prepared state. Fig. 5.9 shows an example of two experimentally measured Pauli sets and their associated density matrices, measured at swapping times  $t = 0$  ns and  $t = 31$  ns. As can be seen, the obtained density matrix a) corresponds closely to a pure quantum state  $|01\rangle$  with a fidelity  $F_{tr} = 94\%$ , whereas the density matrix d) corresponds to an entangled two-qubit state  $1/\sqrt{2}(|01\rangle + |10\rangle)$  with fidelity  $F_{tr} = 84\%$ .

Measuring Pauli sets at different times, we can follow the evolution of the quantum state during the course of the swap. Fig. 5.10 shows the result of such an experiment, where we plot the measured values of all Pauli operators as a function of the swapping time between the qubits. The red and green curves correspond to the single-qubit Pauli

## 5.5. TWO QUBIT OPERATIONS

---

operators  $\hat{\sigma}_{X,Y,Z}^I \otimes I$  and  $I \otimes \hat{\sigma}_{X,Y,Z}^{II}$ , the blue curves to the two-qubit Pauli operators  $\hat{\sigma}_{X,Y,Z}^I \otimes \hat{\sigma}_{X,Y,Z}^{II}$ . The dashed line corresponds to a master equation simulation of the swapping experiment, where the qubit coupling, relaxation and dephasing parameters are chosen in accordance with experimental values. As can be seen, the simulation agrees well with the experimental data. Deviation between data and simulation can be seen in the  $\hat{\sigma}_{X,Y}^I \otimes \hat{\sigma}_{X,Y}^{II}$  operators and is caused by an additional phase acquired by the qubits during the swap, which appears due to the fact that we have to shift the frequency of the qubits to bring them in resonance, hence we acquire a dynamical phase in the frame rotating at the uncoupled qubit frequencies. In addition, experimental drift of our measurement equipment may induce an additional phase factor during the measurement, which takes several hours to complete.

In the margins of this thesis book, we show the full set of density matrices at all moments during the swap, as obtained from the measured Pauli sets shown in fig. 5.10. When following the evolution of the quantum state as a function of time (by flipping the pages of the book) the coherent energy swap between the two qubits can be observed, the coherence of the two-qubit state decreasing steadily during the swap due to qubit dephasing and relaxation.

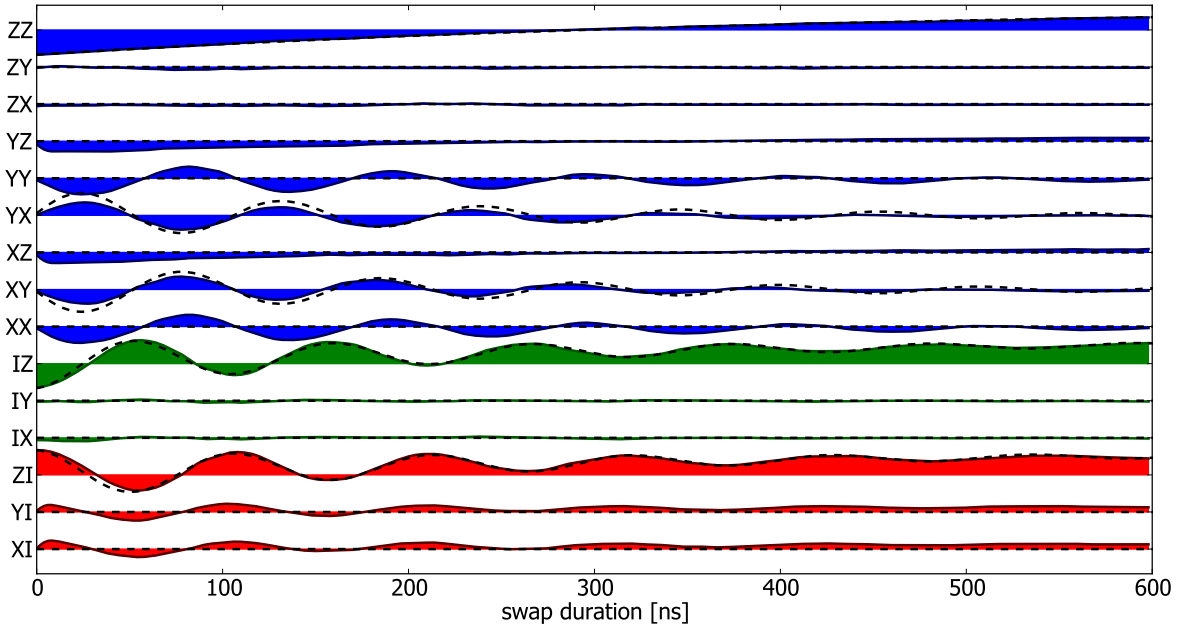
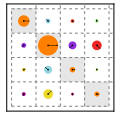


Figure 5.10: Measured Pauli operators  $\hat{\sigma}_i \otimes \hat{\sigma}_j$  with  $i, j \in \{X, Y, Z, I\}$  as a function of the interaction time. Shown are the 6 single-qubit operators as well as the 9 two-qubit correlation operators. The dashed line represents a master-equation simulation of the experiment.



### 5.5.4 Creation of Bell states

We can use the ML method presented above to perform state tomography of entangled Bell states that we create by using the swapping interaction between the qubits. In general, the four Bell states are

$$|\Psi_+\rangle = \frac{1}{\sqrt{2}} (|01\rangle + |10\rangle) \quad (5.11)$$

$$|\Psi_-\rangle = \frac{1}{\sqrt{2}} (|01\rangle - |10\rangle) \quad (5.12)$$

$$|\Phi_+\rangle = \frac{1}{\sqrt{2}} (|00\rangle + |11\rangle) \quad (5.13)$$

$$|\Phi_-\rangle = \frac{1}{\sqrt{2}} (|00\rangle - |11\rangle) \quad (5.14)$$

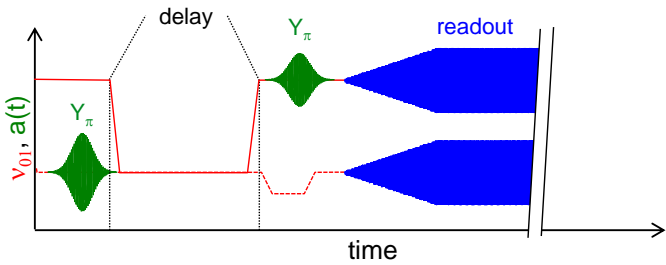


Figure 5.11: Pulse sequence used to experimentally generate entangled Bell states. The sequence consists in exciting one of the qubits to the state  $|1\rangle$ , creating an entangled state using the swapping interaction and correcting the acquired phase of the state. For the  $|\Phi_{\pm}\rangle$  states, we use an additional  $Y(\pi)$  pulse at the end of the sequence.

The experimental protocol that we use for generating a Bell state is shown in fig. 5.11. In essence, we use the swapping interaction between the qubits to create an entangled state and adjust the acquired dynamic phase of that state by a short z-pulse. To create the  $\Phi_+$  and  $\Phi_-$  states we use a  $X(\pi)$  pulse at the end of the sequence in addition. Finally we perform quantum state tomography on the created state to reconstruct its density matrix. In fig. 5.12 we show the reconstructed density matrices of the four created Bell states. The trace fidelity  $\langle \psi | \rho | \psi \rangle$  between the experimentally created and ideal state is shown on top of the density matrix and ranges between 83% and 87%.

### 5.5.5 Violation of the Bell Inequality

After having showed that we can create superposition states of the two qubits using the swapping interaction, we proceed to demonstrate that we have actually created entangled qubit states by performing a so called *Bell test* on our two-qubit system. In this section, we will give an introduction to this test and explain how we implement it on our two-qubit processor.

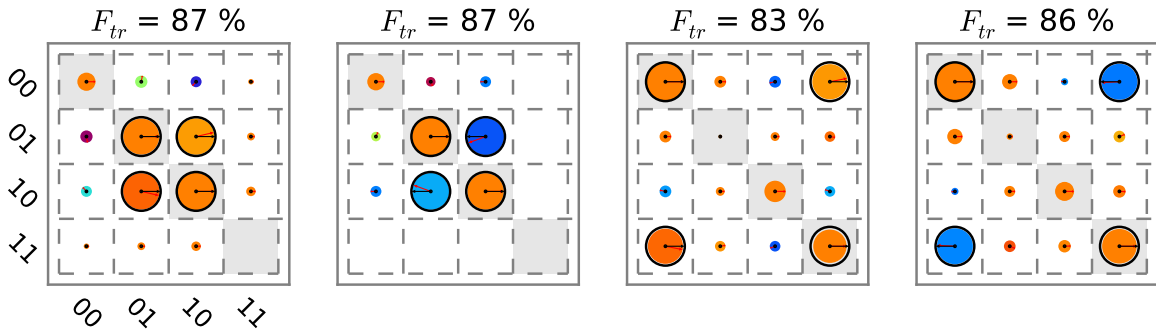


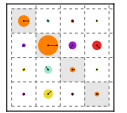
Figure 5.12: Reconstructed density matrices of experimentally created Bell states. Shown are the states  $|\Psi_{\pm}\rangle = 1/\sqrt{2}(|01\rangle \pm |10\rangle)$  and  $|\Phi_{\pm}\rangle = 1/\sqrt{2}(|00\rangle \pm |11\rangle)$ . The trace fidelities of the density matrices,  $F_{tr} = \langle \psi | \rho | \psi \rangle$  range between 83 % and 87 %.

In a famous 1935 paper [35], A. Einstein, B. Podolsky and N. Rosen (EPR) point out that quantum mechanics can be considered “incomplete” if one assumes that a set of simple physical principles holds true. These two principles are *locality* and *realism*, together often referred to as *local realism*. The principle of locality states that an object is influenced directly only by its immediate surroundings, or stated differently, that no interaction between any two objects may propagate faster than the speed of light. The principle of realism states that any physical observable has, at all times, a pre-existing measurement value which exists independent of any actual measurement of the observable. In their paper, Einstein, Podolsky and Rosen showed that within standard quantum mechanics it is possible to write down quantum states that, when performing certain measurements on them, clearly violate at least one of the principles of locality or realism. As an example, take the state

$$|\psi\rangle = \frac{1}{\sqrt{2}} (|\uparrow\downarrow\rangle + |\downarrow\uparrow\rangle) \quad (5.15)$$

which describes a system of two spin 1/2 particles that is in a superposition between the  $|\uparrow\downarrow\rangle$  and  $|\downarrow\uparrow\rangle$  states. Now, when separating the two particles by a large distance and measuring the value of one of the spins –such that by the assumption of locality, no information exchange can take place between the two systems–, the wave function of the system will collapse in either of the two states  $|\uparrow\downarrow\rangle$  or  $|\downarrow\uparrow\rangle$ . Hence, a measurement of one of the particles will instantaneously change the spin state of the other particle, seemingly violating the principle of locality by which no instantaneous information exchange can take place between two distant systems. In their paper, Einstein, Podolsky and Rosen called this effect *spooky action at a distance*.

However, the violation of locality can be resolved by assuming that the state of the quantum system does possess a well-defined value before actually measuring it. This would imply that our description of the quantum-mechanical state as given by eq. (5.15)



is just missing some additional, *hidden variables* that contain the information on the spin of each particle and which are not accessible by us. A hypothetical theory that contains these hidden variables and could thus complete the quantum mechanical description of the particle is usually referred to as a *hidden variable theory*.

In 1964, J. Bell provided a mathematical description of locality and realism and devised an experimental test of the hypothesis formulated by Einstein *et. al.* [8]. Building on his work, J. Clauser, M. Horne, A. Shimony and R. Holt proposed an actual experiment to test the hypotheses of quantum mechanics against hidden-variable or non-local theories as formulated in the Bell and EPR papers [21]. The first successful realization of this proposed experiment was achieved by A. Aspect *et. al.* [3] and confirmed the validity of quantum mechanics, showing that either the assumption of realism or that of locality must be false. In the following decades, several more experiments have been performed to test the Bell hypothesis, trying to close several so-called *loopholes*. Such a loophole is a problem of the experimental setup or design that affects the validity of the experimental findings. Typical loopholes affecting Bell-type experiments are the *detection efficiency* or *fair sampling*, the *communication* or *locality* and the *rotational invariance* loophole. We will discuss the loopholes most relevant to our own experiment in the following paragraph.

To test the Bell inequality with our two-qubit setup, we follow the experimental procedure proposed by Clauser *et. al.* [21]. According to their proposal, we first prepare an entangled two-qubit state of the form

$$|\phi\rangle = \frac{1}{\sqrt{2}} (|01\rangle + e^{-i\varphi} |10\rangle) \quad (5.16)$$

On this quantum state we measure then the expectation value of the operator

$$\text{CHSH} = QS + RS + RT - QT \quad (5.17)$$

where the individual operators Q, R, S, T are given as

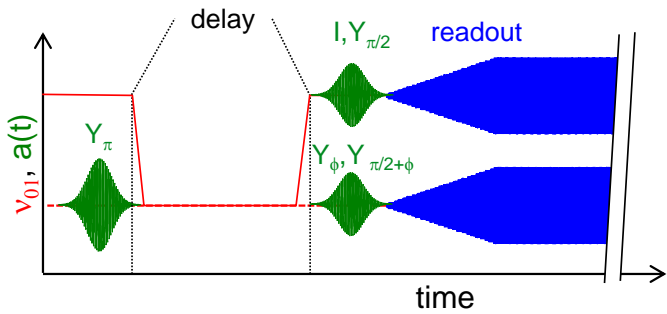
$$\begin{aligned} Q &= \hat{\sigma}_z^1 & S &= \hat{\sigma}_z^2 \cdot \cos \phi + \hat{\sigma}_x^2 \cdot \sin \phi \\ R &= \hat{\sigma}_x^1 & T &= -\hat{\sigma}_z^2 \cdot \sin \phi + \hat{\sigma}_x^2 \cdot \cos \phi \end{aligned} \quad (5.18)$$

Here, the angle  $\phi$  is a parameter that gives the rotation of the measurement basis in respect to the  $z$  axis and should be chosen in accordance to the phase  $\varphi$  of the entangled qubit state to which the operator is applied. To obtain the value of  $\langle \text{CHSH} \rangle$ , we measure  $\langle QS \rangle$ ,  $\langle RS \rangle$ ,  $\langle RT \rangle$  and  $\langle QT \rangle$  on an ensemble of identically prepared quantum states. For a classical state without entanglement, the operator  $\langle \text{CHSH} \rangle$  is bound by

$$|\langle \text{CHSH} \rangle| \leq 2. \quad (5.19)$$

However, for an entangled quantum state, the maximum value of the operator is given as  $2\sqrt{2}$ .

Figure 5.13: Experimental pulse sequence used in the CHSH experiment. It consists in exciting one of the qubits to the state  $|1\rangle$ , bringing it in resonance with the other qubit for a well-defined duration, performing single-qubit rotations to align the qubit state with the desired measurement basis and finally measuring the  $\langle \hat{\sigma}_z^I \cdot \hat{\sigma}_z^{II} \rangle$  operator of the two-qubit register.



The pulse sequence used for generating an entangled two-qubit state and measuring the CHSH operator on it is shown in fig. 5.13. As before, we generate the state by exciting one of the qubits to the state  $|1\rangle$  and bringing it in resonance with the other qubit for a well-defined duration. Afterward, we apply single-qubit rotations to align the qubit state with the axis along which we want to perform the measurement. Finally we measure the  $\langle \hat{\sigma}_z^I \cdot \hat{\sigma}_z^{II} \rangle$  operator of the rotated qubit state. We then repeat this procedure on an ensemble of identically prepared input states for all of the four individual operators of CHSH operator. Figure 5.14 shows the results of such a measurement. As can be seen, the operator  $\langle \text{CHSH} \rangle$  varies sinusoidally as a function of the rotation  $\phi$  of the measurement basis. The maximum and minimum of the raw value of  $\langle \text{CHSH} \rangle$  reaches  $\approx 1.4$ , thereby failing to violate the boundary for non-classical states as given by eq. (5.19). However, when accounting for the readout errors in our experiment, the corrected CHSH data reaches a maximum value  $\approx 2.52$ , thereby violating the classical boundary of the CHSH equation. We can hence violate the Bell inequality with our two-qubit processor, however we are not able to close the detector efficiency loophole. In addition, due to the measurement time required to determine the state of each qubit and the close proximity of the two qubits, we are not able to close the communication or locality loophole either. However, when accepting the general validity of quantum mechanics, the violation of the Bell inequality with the generated two-qubit states can still serve as an entanglement witness and confirm that we are able to generate entangled, non-classical quantum states with our processor.

### Errors

Besides obvious readout errors, the main source of errors in our experiment is drift of the measurement equipment. Most importantly, the phase of the arbitrary waveform generator (AWG), which generates the sideband pulses for driving the qubit, can drift in

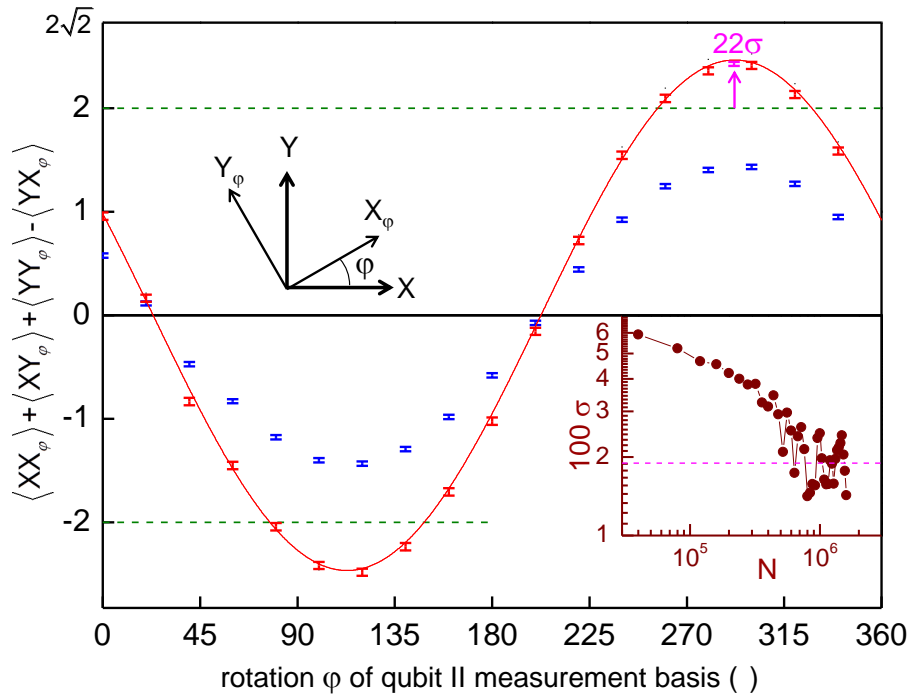
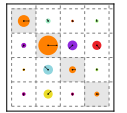


Figure 5.14: Value of the  $\langle \text{CHSH} \rangle$  operator measured for an ensemble of identically prepared Bell states  $1/\sqrt{2}(|01\rangle + e^{-i\varphi}|10\rangle)$ , plotted as a function of the rotation  $\phi$  of the measurement basis. Blue markers correspond to raw measurement data, red markers to data corrected for readout errors. The solid line represents the best fit to the theory. The inset shows the standard deviation  $\sigma$  of the maximum value of the  $\langle \text{CHSH} \rangle$  operator as a function of the sample size. For large sample sizes,  $\sigma$  is limited by experimental drift of the measurement basis.

respect to the phases of the microwave sources, thereby changing the effective phase of the measurement basis of the CHSH operator. Fig. 5.15 illustrates the effect of this drift on the phase of the generated Bell state. Shown is the phase of the state  $|\phi\rangle$  as given by eq. (5.16) extracted from a full CHSH data set as shown in fig. 5.14. When repeatedly measuring  $\varphi$  over a long time period, oscillations with an amplitude of  $\approx 40^\circ$  can be observed. This drift can be explained by a time shift of the AWG of the order of 200 ps, which has indeed been observed independently using a fast oscilloscope.

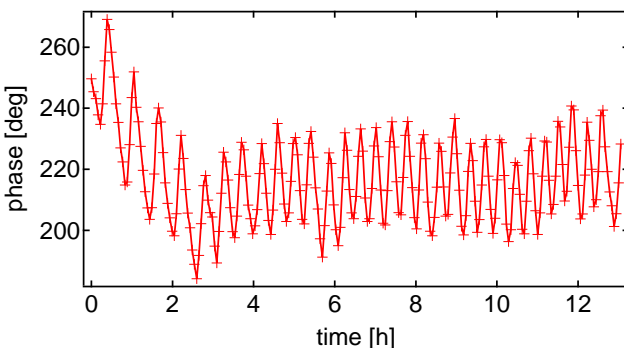


Figure 5.15: Phase  $\varphi$  of an experimentally generated Bell state as a function of time. The phase exhibits oscillatory drift of the order of  $\approx 40^\circ$  being caused by a time offset drift of the AWG.

## 5.6 Realizing a Two-Qubit Gate

We have demonstrated that it is possible to create highly entangled qubit states with our processor by preparing Bell states, performing quantum state tomography and violating the Bell inequality. However, to realize a universal two-qubit quantum processor, it is necessary to implement a so-called *universal two-qubit gate*. Therefore, in the following sections we discuss how to realize and characterize such a gate.

### 5.6.1 Principle

By definition, a universal two-qubit gate together with a set of universal one-qubit gates, allows us to create any possible two-qubit quantum state [4]. In principle, there are (infinitely) many choices for possible universal two-qubit gates. In this work, we are interested mainly in the so-called  $\sqrt{i\text{SWAP}}$  gate, which has the representation

$$U(t) = \begin{pmatrix} 1 & 0 & 0 & 0 \\ 0 & 1/\sqrt{2} & i/\sqrt{2} & 0 \\ 0 & i/\sqrt{2} & 1/\sqrt{2} & 0 \\ 0 & 0 & 0 & 1 \end{pmatrix}_{\{|00\rangle, |01\rangle, |10\rangle, |11\rangle\}} \quad (5.20)$$

We can implement this gate naturally using the swapping interaction as given by eq. (5.1) when letting the qubits evolve in resonance for a time  $t_{\sqrt{i\text{SWAP}}} = 1/8g$ , which, for our experimental value of  $2g = 8.3$  MHz corresponds to  $t_{\sqrt{i\text{SWAP}}} \approx 30$  ns.

### 5.6.2 Experimental Implementation

Figure 5.16 shows the pulse sequence that we use to realize the  $\sqrt{i\text{SWAP}}$  gate with our processor for an exemplary input state. In the case shown, we excite the first qubit to the state  $|1\rangle$ , creating an input state  $|10\rangle$ . We then tune in resonance the two qubits for a time  $t_{\sqrt{i\text{SWAP}}}$ . After tuning the qubits out of resonance again, we apply two single-qubit  $Z$ -gates to compensate the dynamical phases acquired during the swap. Then, we optionally apply single-qubit tomography gates and finally read out the qubit state at the optimal readout working point. Using this technique, we can reconstruct the density matrix of the quantum state after applying the two-qubit gate to it. Similarly, we can perform quantum state tomography on the input state to obtain its density matrix. Reconstructing the input and output density matrices for a range of different input state will then allow us to fully characterize the gate operation, as discussed in the next section.

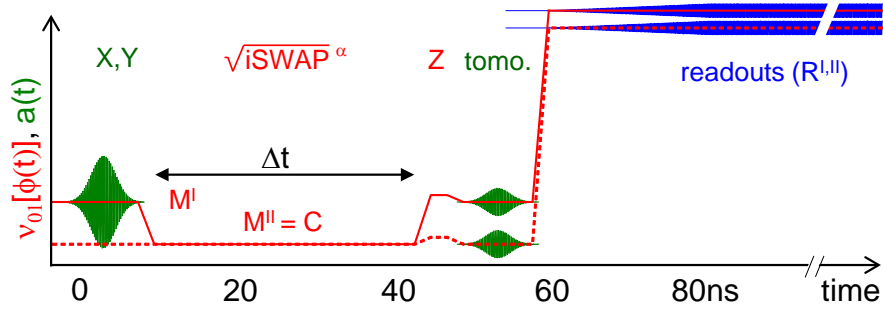
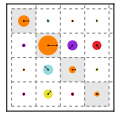


Figure 5.16: Experimental pulse sequence used for implementing the two-qubit  $\sqrt{iSWAP}$  gate. The sequence shown for an exemplary input state  $|10\rangle$  consists in exciting the first qubit to the state  $|1\rangle$ , bringing the qubits in resonance for a time  $t = 1/8g$ , separating them and compensating the acquired dynamical phases by using two single-qubit  $Z$ -pulses. Finally, optional tomographic pulses are applied before reading out the qubit state at the optimal readout frequencies of the qubits.

### 5.6.3 Quantum Process Tomography of the Gate

To characterize the fidelity of our quantum gate, we perform so-called *quantum process tomography* [80]. This procedure allows us to fully characterize an experimental quantum process, such as our implementation of the  $\sqrt{iSWAP}$  gate. The approach that we use in this work is called *standard quantum process tomography* (SQPT). There exist other common methods such as ancilla-assisted quantum process tomography [34, 25, 1], that we will not discuss since they are not relevant to this work.

In the following section we discuss the experimental implementation of standard quantum process tomography on our two-qubit processor.

#### Theoretical Description of a Quantum Process

A quantum process as described in section 2.5 can be described by a set of Kraus operators, as given by eq. (5.21):

$$\mathcal{L}_A(\rho_A) = \sum_i^{N_k} E_i \rho_A E_i^\dagger \quad (5.21)$$

If we express these operators  $E_i$  in a different operator basis  $\tilde{E}_j$  such that  $E_i = \sum_j a_{ij} \tilde{E}_j$  and insert into eq. (??), we obtain

$$\mathcal{E}(\rho) = \sum_i \sum_j a_{ij} \tilde{E}_j \rho \sum_k a_{ik}^* \tilde{E}_k^\dagger \quad (5.22)$$

$$= \sum_{j,k} \tilde{E}_j \rho \tilde{E}_k^\dagger \sum_i a_{ij} a_{ik}^* \quad (5.23)$$

$$= \sum_{j,k} \tilde{E}_j \rho \tilde{E}_k^\dagger \chi_{jk} \quad (5.24)$$

where we defined  $\chi_{jk} = \sum_i a_{ij} a_{ik}^*$ . This is the so-called  $\chi$ -matrix representation of the quantum process. Here, all the information on the process is contained in the matrix  $\chi$ , which controls the action of the now process-independent operators  $\tilde{E}_i$  on the initial density matrix  $\rho$ .

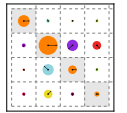
### Implementation

As said before, the goal of QPT is to obtain the coefficients of the  $\chi$ -matrix – or any other complete parametrization of the process – from a set of experimentally measured density matrices  $\{\rho_i\}$  and  $\{\mathcal{E}(\rho_i)\}$ . Standard process tomography [75, 80] can be implemented for our two-qubit gate by using the following procedure:

1. Choose a set of operators  $E_i$  that forms a full basis of  $\mathcal{M} : Q_1 \rightarrow Q_2$ . For n-qubit process tomography we usually choose  $E_{i_1, i_2, \dots, i_n} = \hat{\sigma}_{i_1} \otimes \hat{\sigma}_{i_2} \dots \otimes \hat{\sigma}_{i_n}$ , where  $\hat{\sigma}_i$  are the single-qubit Pauli operators and  $i \in \{I, X, Y, Z\}$ . For a Hilbert space of dimension  $n$ , this yields  $4^n - 1$  operators (excluding the trivial operator  $I^{\otimes n}$ ).
2. Choose  $4^n$  pure quantum states  $|\phi_i\rangle$  such that the basis  $\{|\phi_1\rangle\langle\phi_1|, \dots, |\phi_{4^n}\rangle\langle\phi_{4^n}|\}$  spans the whole space of input density matrices  $\rho$ . Usually, for a n-qubit system we choose  $\phi = \{|0\rangle, |1\rangle, (|0\rangle + |1\rangle)/\sqrt{2}, (|0\rangle + i|1\rangle)/\sqrt{2}\}^{\otimes n}$ , where  $\otimes n$  denotes the n-dimensional Kronecker product of all possible permutations.
3. For each of the  $|\phi_i\rangle$ , determine  $\mathcal{E}(|\phi_i\rangle\langle\phi_i|)$  by quantum state tomography. Usually we also determine  $|\phi_i\rangle\langle\phi_i|$  experimentally since the preparation of this state already entails small preparation errors that should be taken into account when performing quantum process tomography.

After having obtained the  $\rho_i$  and  $\mathcal{E}(\rho_i)$  one obtains the  $\chi$ -matrix by writing  $\mathcal{E}(\rho_i) = \sum_j \lambda_{ij} \tilde{\rho}_j$ , with some arbitrary basis  $\tilde{\rho}_j$  and letting  $\tilde{E}_m \tilde{\rho}_j \tilde{E}_n^\dagger = \sum_k \beta_{jk}^{mn} \tilde{\rho}_k$ . We can then insert into eq. (5.24) and obtain

$$\sum_k \lambda_{ik} \tilde{\rho}_k = \sum_{m,n} \chi_{mn} \sum_k \beta_{ik}^{mn} \tilde{\rho}_k \quad (5.25)$$



This directly yields  $\lambda_{ik} = \sum_{m,n} \beta_{ik}^{mn} \chi_{mn}$ , which, by linear inversion, gives  $\chi$ . Hence, we can fully characterize a quantum process acting on an  $n$ -dimensional Hilbert space by measuring  $2 \cdot 4^n$  experimental density matrices (or  $4^n$  when assuming that no errors occur during the preparation of the input states, which thereby are known).

Similar to quantum state tomography, experimental errors occurring during quantum process tomography can produce a set of process parameters  $\chi$  that are *non-physical* in the sense that the resulting quantum process does not obey the three axioms stated above. We can resolve this problem by rendering the obtained  $\chi$  matrix physical by a standard mathematical procedure. When doing this, we usually choose the physical  $\chi_{ph}$  matrix that has the smallest distance  $d = \|\chi - \chi_{ph}\|$ .

### From the $\chi$ matrix to the Kraus representation

To go back from the  $\chi$ -matrix representation of the quantum process to the Kraus form we write each process-independent operator  $\tilde{E}_i$  as a sum of all the Kraus operators  $E_l$ , such that

$$\tilde{E}_i = \sum_l a_{il} E_l \quad (5.26)$$

Inserting this into eq. (5.24) we obtain

$$\mathcal{E}(\rho) = \sum_{j,k} \chi_{jk} \sum_{l,m} a_{jl} a_{km}^* E_l \rho E_m^\dagger \quad (5.27)$$

$$= \sum_i E_i \rho E_i^\dagger \quad (5.28)$$

We find hence that  $\sum_{j,k} \chi_{jk} a_{jl} a_{km}^* = \delta_l^m$ , or, written in matrix form  $A\chi A^\dagger = I$ . This identity is true for  $A$  being the matrix of eigenvectors of  $\chi$ , multiplied by the square root of the corresponding matrix of eigenvalues. It is thus easy to obtain the Kraus representation of the quantum process by diagonalizing the Hermitian matrix  $\chi$ .

The Kraus operator form of the quantum process is useful since it allows us to easily visualize the different operators acting on the density matrix  $\rho$ . By ordering the Kraus operators in function of their associated eigenvalues we can easily visualize the different unitary and non-unitary processes acting together on the density matrix  $\rho$ .

### Experimental Results: Input/Output Matrices And $\chi$ -Matrix

We perform standard process tomography of our two-qubit gate by following the procedure outlined in the last sections. Figs. 5.18 and 5.18 summarize the experimentally determined input-output density matrices, measured for our two-qubit  $\sqrt{iSWAP}$  quantum gate. We show pairs of corresponding input and output states together, containing

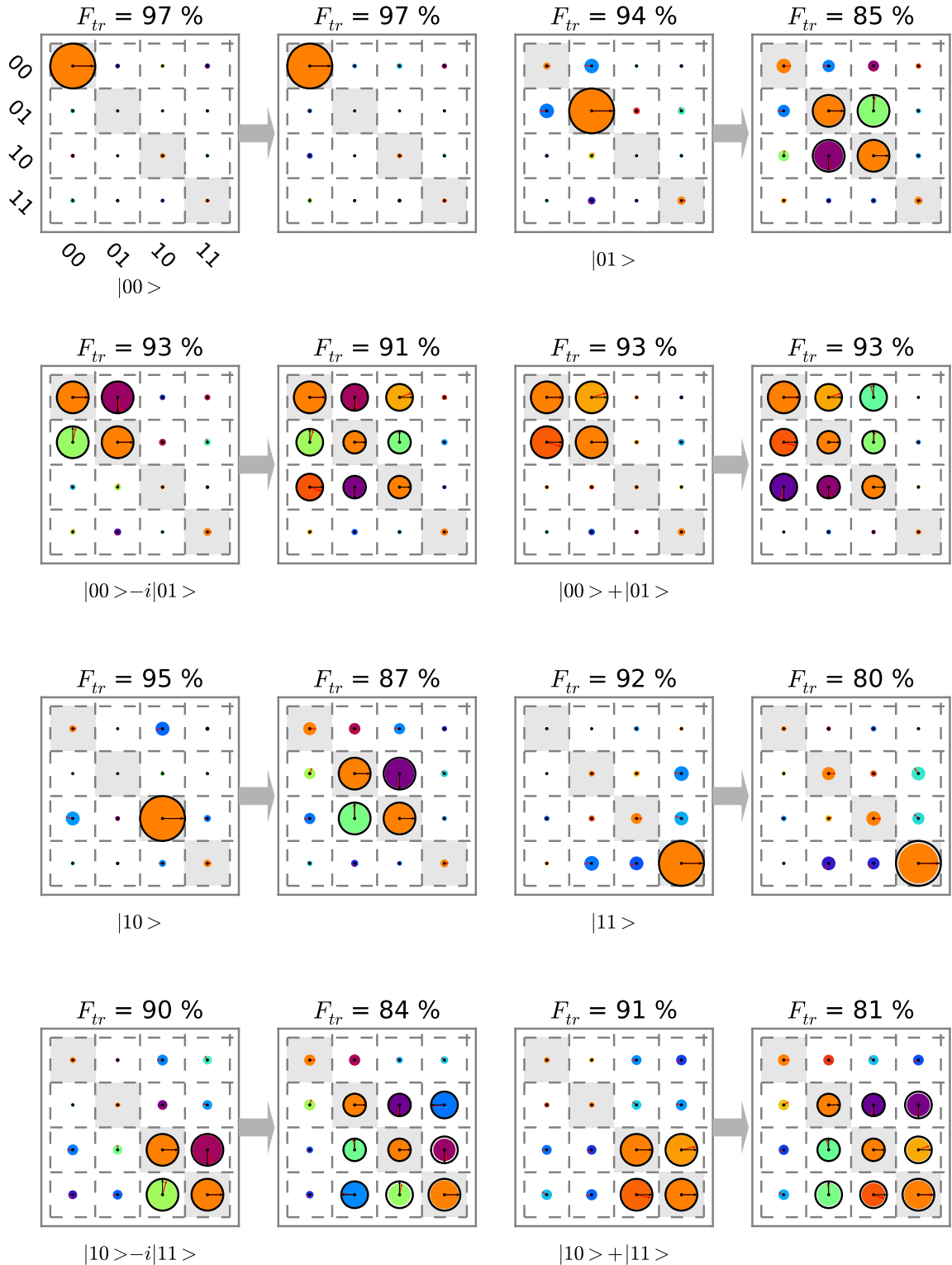


Figure 5.17: The experimental input-output density matrices of the quantum process tomography of the  $\sqrt{i\text{SWAP}}$  gate. Shown are the measured density matrices of 16 different input states and the corresponding output matrices with their state fidelities. The ideal matrices are overlaid in black. (part I/II)

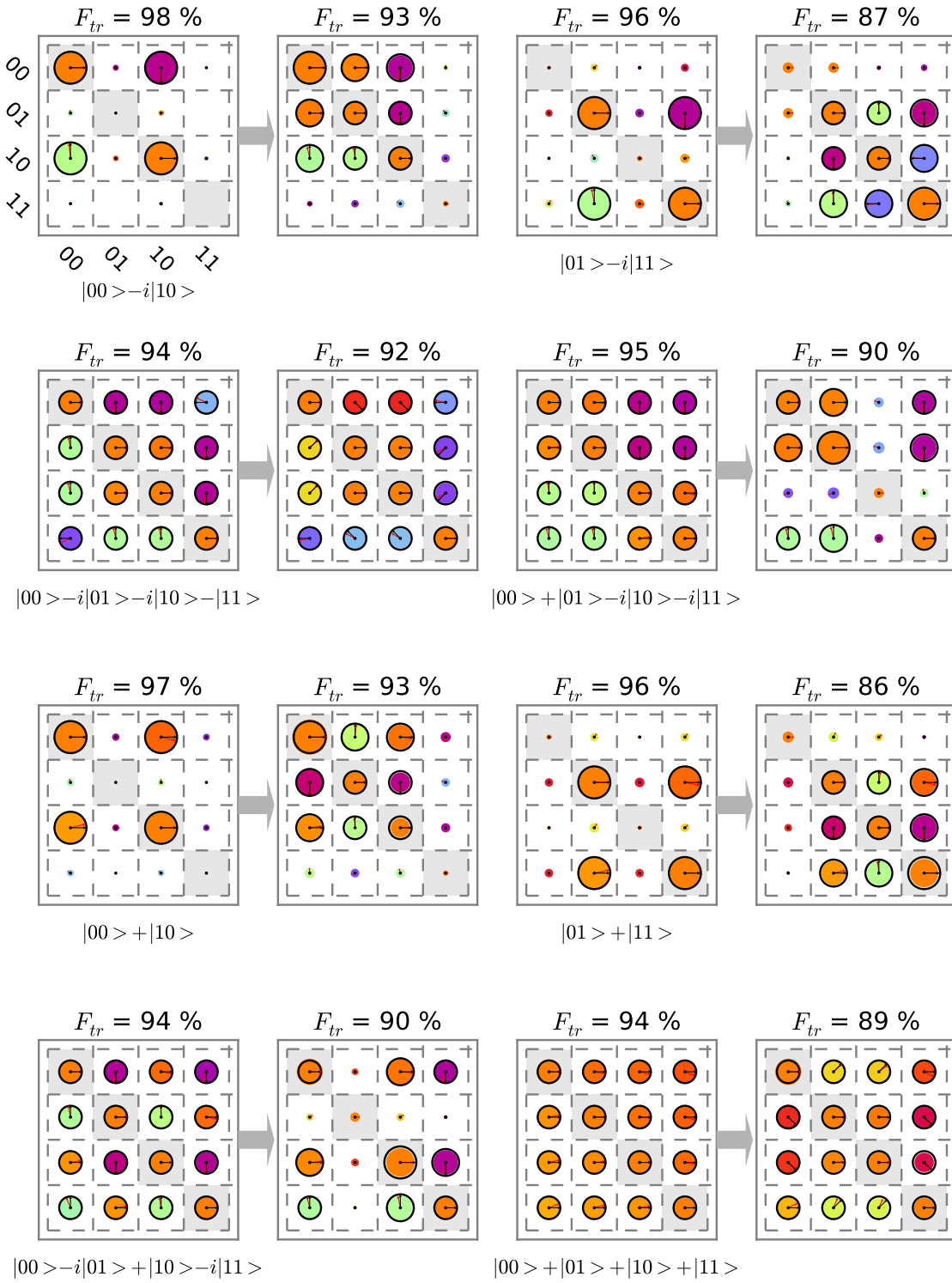
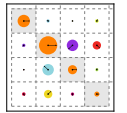


Figure 5.18: The experimental input-output density matrices of the quantum process tomography of the  $\sqrt{i\text{SWAP}}$  gate. Shown are the measured density matrices of 16 different input states and the corresponding output matrices with their state fidelities. The ideal matrices are overlaid in black. (part II/II)

## 5.6. REALIZING A TWO-QUBIT GATE

---

both the reconstructed experimental density matrices as well as the ideal density matrices. The ideal input states are annotated below the corresponding density matrices. Above each matrix we show the trace fidelity between it and the ideal quantum state. A total of 16 input/output pairs has been measured, corresponding to a complete set of states necessary to fully characterize the quantum process of our gate operation.

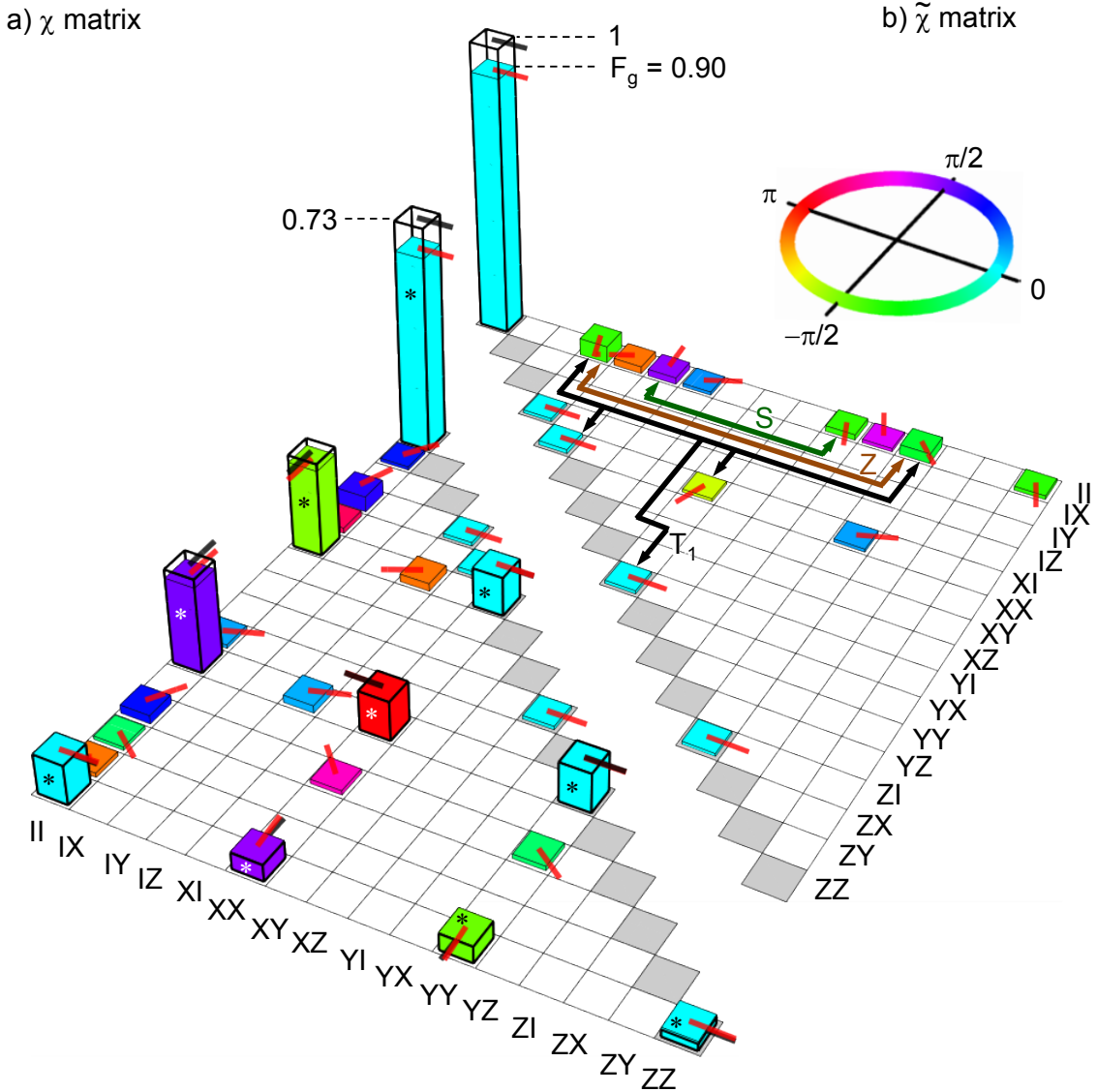
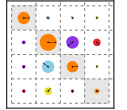


Figure 5.19: The reconstructed  $\chi$  matrix of our implementation of the  $\sqrt{i\text{SWAP}}$  quantum gate. a) shows the lower half of the Hermitian matrix is shown. b) shows the product  $\tilde{\chi} = \chi \cdot \chi_{id}^{-1}$  of the measured  $\chi$  matrix and the ideal process matrix  $\chi_{id}$ . The colored arrows connecting different elements of  $\tilde{\chi}$  indicate unitary and non-unitary error processes to which the corresponding matrix elements can be associated.

From these input/output matrices, we can easily calculate the  $\chi$  matrix of the quantum process by the method described above. The resulting matrix is shown in fig. 5.19. There, we show the experimentally obtained  $\chi$  matrix of our  $\sqrt{i\text{SWAP}}$  gate as well as



the error process defined as  $\tilde{\chi} = \chi \cdot \chi_{id}$ , where  $\chi_{id}$  corresponds to the ideal gate process.  $\chi_{id}$  is as well shown as black outlines overlaid to the measured  $\chi$  matrix. The arrows connecting different parts of the  $\tilde{\chi}$  matrix group several unitary and non-unitary error processes that can be attributed to the individual elements.

### 5.6.4 Gate Fidelity

After having obtained the experimental  $\chi$  matrix, it is trivial to calculate the process fidelity, which is defined as  $F = \text{Tr}\{\chi_{id} \cdot \chi\}$ , where  $\chi_{id}$  corresponds to the ideal quantum process. For our experimental process matrix, it is given as  $F = 0.9$ . The fidelity can be roughly compared to the output state fidelity averaged over the whole set of possible input density matrices.

### 5.6.5 Gate Error Analysis

We treat two classes of errors in our analysis: Unitary and non-unitary gate errors as well as tomography errors. The former are associated to errors in the quantum process itself, whereas the latter are caused by unitary and non-unitary errors during quantum state tomography.

#### Tomographic Errors

Tomographic errors are removed from the process map of our  $\sqrt{iSWAP}$  gate using the following method: The measured Pauli sets corresponding to the sixteen input states are first fitted by a model including errors both in the preparation of the state (index *prep*) and in the tomographic pulses (index *tomo*). The errors included are angular errors  $\varepsilon_{I,II}^{\text{prep}}$  on the nominal  $\pi$  rotations around  $X_{I,II}$ ,  $\eta_{I,II}^{\text{prep,tomo}}$  and  $\delta_{I,II}^{\text{prep,tomo}}$  on the nominal  $\pi/2$  rotations around  $X_{I,II}$  and  $Y_{I,II}$ , a possible departure  $\xi_{I,II}$  from orthogonality of  $(\vec{X}_I, \vec{Y}_I)$  and  $(\vec{X}_{II}, \vec{Y}_{II})$ , and a possible rotation  $\mu_{I,II}$  of the tomographic  $XY$  frame with respect to the preparation one. The rotation operators used for preparing the states and doing their tomography are thus given by

$$\begin{aligned} X_{I,II}^{\text{prep}}(\pi) &= e^{-i(\pi + \varepsilon_{I,II}^{\text{prep}})\hat{\sigma}_x^{I,II}/2}, \\ X_{I,II}^{\text{prep}}(-\pi/2) &= e^{+i(\pi/2 + \eta_{I,II}^{\text{prep}})\hat{\sigma}_x^{I,II}/2}, \\ Y_{I,II}^{\text{prep}}(\pi/2) &= e^{-i(\pi/2 + \delta_{I,II}^{\text{prep}})[\cos(\xi_{I,II})\hat{\sigma}_y^{I,II} - \sin(\xi_{I,II})\hat{\sigma}_x^{I,II}]/2}, \\ X_{I,II}^{\text{tomo}}(\pi/2) &= e^{-i(\pi/2 + \eta_{I,II}^{\text{tomo}})[\sin(\mu_{I,II})\hat{\sigma}_x^{I,II} + \cos(\mu_{I,II})\hat{\sigma}_y^{I,II}]/2}, \\ Y_{I,II}^{\text{tomo}}(-\pi/2) &= e^{+i(\pi/2 + \delta_{I,II}^{\text{tomo}})[\cos(\mu_{I,II} + \xi_{I,II})\hat{\sigma}_y^{I,II} - \sin(\mu_{I,II} + \xi_{I,II})\hat{\sigma}_x^{I,II}]/2}. \end{aligned}$$

The sixteen input states are then  $\{\rho_{\text{in}}^e = U |0\rangle \langle 0| U^\dagger\}$  with

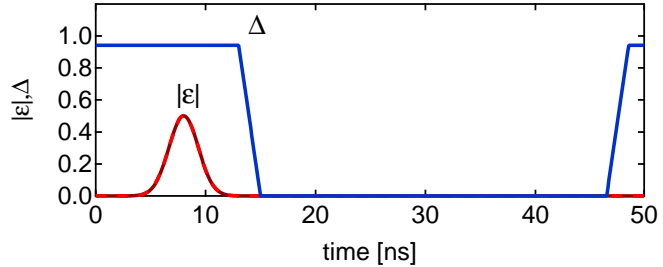
$$\{U\} = \{I_I, X_I^{\text{prep}}(\pi), Y_I^{\text{prep}}(\pi/2), X_I^{\text{prep}}(-\pi/2)\} \otimes \{I_{II}, X_{II}^{\text{prep}}(\pi), Y_{II}^{\text{prep}}(\pi/2), X_{II}^{\text{prep}}(-\pi/2)\}, \quad (5.29)$$

and each input state yields a Pauli set  $\{\langle P_k^e \rangle = \text{Tr}(\rho_{\text{in}}^e P_k^e)\}$  with  $\{P_k^e\} = \{I_I, X_I^e, Y_I^e, Z_I\} \otimes \{I_{II}, X_{II}^e, Y_{II}^e, Z_{II}\}$ ,  $X^e = Y^{\text{tomo}}(-\pi/2)^\dagger \hat{\sigma}_z Y^{\text{tomo}}(-\pi/2)$ , and  $Y^e = X^{\text{tomo}}(\pi/2)^\dagger \hat{\sigma}_z X^{\text{tomo}}(\pi/2)$ . The best fit to the modeled  $\{\langle P_k^e \rangle\}$  set to the measured input Pauli sets yields  $\varepsilon_I^{\text{prep}} = -1^\circ$ ,  $\varepsilon_{II}^{\text{prep}} = -3^\circ$ ,  $\eta_I^{\text{prep}} = 3^\circ$ ,  $\eta_{II}^{\text{prep}} = 4^\circ$ ,  $\delta_I^{\text{prep}} = -6^\circ$ ,  $\delta_{II}^{\text{prep}} = -3^\circ$ ,  $\eta_I^{\text{tomo}} = -6^\circ$ ,  $\eta_{II}^{\text{tomo}} = -4^\circ$ ,  $\lambda_I^{\text{tomo}} = 12^\circ$ ,  $\lambda_{II}^{\text{tomo}} = 5^\circ$ ,  $\xi_I = 1^\circ$ ,  $\xi_{II} = -2^\circ$ , and  $\mu_I = \mu_{II} = -11^\circ$ .

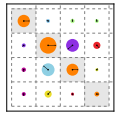
Knowing the tomographic errors and thus  $\{\langle P_k^e \rangle\}$ , we then invert the linear relation  $\{\langle P_k^e \rangle = \text{Tr}(\rho P_k^e)\}$  to find the  $16 \times 16$  matrix  $B$  that links the vector  $\overrightarrow{\langle P_k^e \rangle}$  to the columnized density matrix  $\overrightarrow{\rho}$ , i.e.  $\overrightarrow{\rho} = B \cdot \overrightarrow{\langle P_k^e \rangle}$ . The matrix  $B$  is finally applied to the measured sixteen input and sixteen output Pauli sets to find the sixteen  $(\rho_{\text{in}}, \rho_{\text{out}})_k$  couples to be used for calculating the gate map.

### Unitary and Non-Unitary Gate Errors

Figure 5.20: Drive waveform  $|\epsilon|$  and qubit-qubit detuning  $\Delta_{qq}$  used when simulating the iSWAP gate using a coupled three-level qubit master equation model.



After having eliminated the tomography errors, only gate errors remain. These can be unitary or non-unitary errors occurring during the quantum process. We characterize both of these errors by fitting the experimental  $\chi$  matrix to a master equation model of the quantum process which includes unitary (a frequency offset when performing the swapping interaction and phase errors in the compensating  $Z$  pulses applied after the swap) and non-unitary (qubit relaxation and dephasing during the whole process). Typically, the relaxation and dephasing rates employed in the simulation are chosen in accordance with experimentally measured  $T_1$  and  $T_2$  times (taking into account possible renormalizations of these coefficients). On the other side, the unitary error parameters are used as fitting parameters to maximize the fidelity between the experimentally measured process matrix  $\chi$  and the simulated one  $\chi_{\text{sim}}$ . Using this technique, we can calculate an error budget of the quantum process that quantifies the contributions of individual error sources. For our process, we find a total gate error of 10%, where we can attribute 8% of the errors to relaxation and decoherence during the process and 2% to unitary gate errors. In principle, after having characterized the unitary gate errors occurring during



the process we could, in theory, compensate them in our experiment. However, due to fast drift of the qubit parameters during the experiment we usually do not perform this kind of optimal qubit control to our gate. Under certain circumstances, the effect of non-unitary errors can also be compensated or alleviated by adding or modifying the unitary gate sequence during the quantum process (see e.g. [56]). However, this procedure is in general not applicable to arbitrary quantum processes and is not applicable to this work.

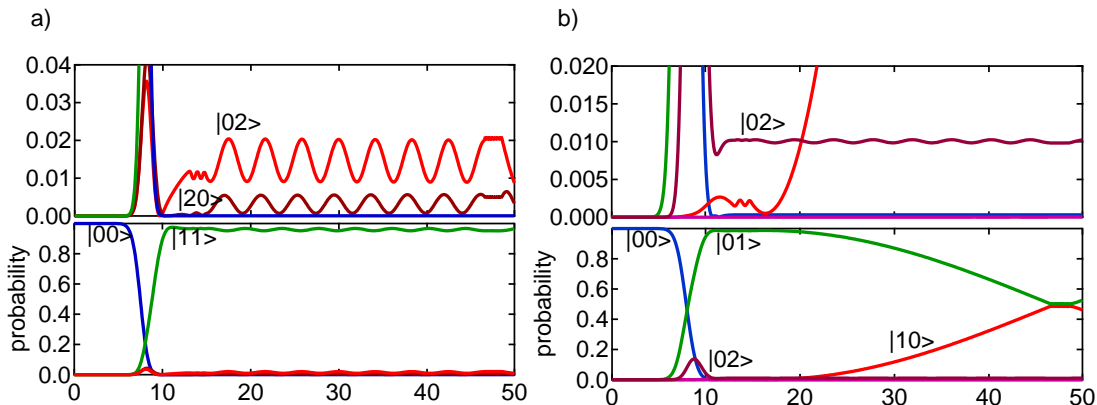


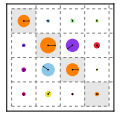
Figure 5.21: Simulated state occupation probabilities for two different input states. a) corresponds to the input state  $|01\rangle$  to the  $\sqrt{i\text{SWAP}}$  gate, b) to the input state  $|11\rangle$ . In both cases, a small excitation of the higher Transmon level  $|2\rangle$  can be observed in the simulation. For the  $|11\rangle$  input state, an oscillation between the states  $|11\rangle$  and  $|02\rangle/|20\rangle$  can be observed, which is an unwanted effect.

Another source of error that we analyze here is the leakage to the higher Transmon level  $|1\rangle$ . This error can occur while driving the qubits or due to the swapping interaction between the  $|11\rangle \leftrightarrow |20\rangle$  and  $|11\rangle \leftrightarrow |02\rangle$ . To quantify the possible error rates associated to this leakage, we perform a master-equation simulation of the  $i\sqrt{\text{SWAP}}$  gate between the two three-level Transmons. The Hamiltonian as well as the Lindblad operators used for this simulation are explained in detail in section . As in our experiment, in the simulation we generate 16 different input states (the same ones as used above for the QPT) using Gaussian drive pulses with a rise time of  $\delta t = 4$  ns while the qubits are detuned by  $\Delta_{qq}/2\pi = 150$  MHz. We then reduce the detuning to  $\Delta_{qQ} = 0$  during  $t_{\text{SWAP}} \approx 31$  ns using a flux pulse with a 2 ns rise time, as shown in fig. 5.20. We calculate then numerically the state fidelity of the output state as compared to an ideal output state that is calculated using the ideal  $i\sqrt{\text{SWAP}}$  operation applied to the simulated input state. By examining the output density matrices we can also give an upper bound for the leakage error into the state  $|2\rangle$ , which is given as  $\approx 1.5\%$ . Figure 5.21 exemplarily shows the simulated state occupation probabilities for the two input states  $|01\rangle$  and  $|11\rangle$ . In both cases, a small excitation of the  $|02\rangle$  and  $|20\rangle$  Transmon states can be observed.

## *5.6. REALIZING A TWO-QUBIT GATE*

---

The  $|11\rangle$  input state, which should not be affected by the SWAP operation, shows a small oscillation due to the coupling to the  $|02\rangle$  state.



# Chapter 6

## Running the Grover Search Algorithm

This chapter describes an experimental implementation of the so-called *Grover search algorithm* with our two-qubit quantum processor. The first section provides a short introduction of the algorithm and motivate the interest in realizing it. The following sections then discuss the details of the experimental realization of the algorithm. We will discuss the results that we obtained and compare the algorithm fidelity and runtime to that of an equivalent, classical algorithm. Finally, we will analyze all relevant unitary and non-unitary error sources relevant to our experiment and provide a quantitative error model of our implementation of the Grover algorithm.

### 6.1 Introduction & Motivation

Search algorithms are of great importance in many domains of mathematics and computer science. One such search problem that often arises and which will be discussed in the following sections can be formulated in simple terms as follows:

**Theorem 6.1.** Assume that we have a search space  $\mathcal{S}$  that consists of a finite number  $N$  of states  $s \in \mathcal{S}$ . The solution to our search problem corresponds to a subset of  $M$  states of the search space  $\mathcal{T} \subset \mathcal{S}$ . We can then define a search function  $\mathcal{C}(s) : \mathcal{S} \rightarrow \{0, 1\}$  that discriminates between states that solve the search problem and states that don't, such that  $\mathcal{C}(s) = 1$  for  $s \in \mathcal{T}$  and  $\mathcal{C}(s) = 0$  otherwise. In accordance with the general convention in the research literature on the Grover search algorithm we will often refer to this search function as the *Oracle function* or (in a quantum-mechanical context) as the *Oracle operator* in the following sections.

Using this definition of the search problem, the goal of a search algorithm is to find all states  $t \in \mathcal{S}$  for which  $\mathcal{C}(t) = 1$ . In the following sections, for the sake of simplicity we assume that the solution set  $\mathcal{T}$  contains only one single state  $t$ . This special case

## 6.1. INTRODUCTION & MOTIVATION

---

can be generalized to cases where more than one solution to the search problem exists (see e.g. [75] for a detailed review of the general-case Grover search algorithm)

The first step in order to solve a search problem of the kind described above using classical or quantum computation is to map the problem to a form suitable for solution by a digital (quantum) computer. For this, we first number and encode the  $N$  input states  $i \in \mathcal{S}$  in binary form as  $i = (b_l^i, \dots, b_0^i)_B$ , where  $l$  is the length of the binary register able to hold all  $N$  input states. With this definition, it is then trivial to find a mathematical representation of  $\mathcal{C}$  that operates on a binary input register.

Using these assumptions and definitions, it can then be shown that the most efficient classical search algorithm for solving the search problem above will use  $\mathcal{O}(N)$  calls of the function  $\mathcal{C}$  to find all solutions  $t$  of the search problem. Assuming that the time to evaluate the function  $\mathcal{C}$  is far superior to the time needed to perform any other operation during the search algorithm, the time needed for calling  $n$ -times the function  $\mathcal{C}$  corresponds approximately to the runtime of the whole search algorithm.

Amazingly, in 1997, Lov Grover found a quantum algorithm that could solve this search problem with only  $\mathcal{O}(\sqrt{N})$  calls to the function  $\mathcal{C}$  [44]. His algorithm achieves this by repeatedly calling a quantum-mechanical implementation of the function  $\mathcal{C}$  starting from a highly superposed qubit register  $\sum_i^N |i\rangle$  and applying a special operator to the output state afterwards. The individual steps of his algorithm are straightforward and are given as follows:

1. Initialize a qubit register to the state  $|\psi\rangle = |0\rangle$  (corresponding to a binary input state  $|0000 \dots 0_B\rangle$ )

2. Apply the generalized Hadamard operation to the qubit register, producing a fully superposed quantum state

$$|\psi\rangle = \frac{1}{\sqrt{N}} \sum_{i=0}^{N-1} |i\rangle$$

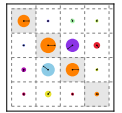
3. Repeat the following sequence  $\mathcal{O}(\sqrt{N})$  times:

- a) Apply the *Oracle operator*  $|i\rangle \rightarrow (-1)^{\mathcal{C}(i)} |i\rangle$  to the state  $|\psi\rangle$

- b) Apply the so-called *diffusion operator*  $|i\rangle \rightarrow -|i\rangle + \frac{2}{N} \sum_{j=0}^{N-1} |j\rangle$  to  $|\psi\rangle$

4. Measure the state of the quantum register in the computational basis  $|i\rangle$ .

For the description above we have enumerated the states of the qubit register from  $|0\rangle$  to  $|N-1\rangle$ . Basically, the Grover algorithm makes use of quantum parallelism to solve the search problem  $\mathcal{O}(\sqrt{N})$  times faster than the most efficient classical algorithm. To understand better the strategy it uses to solve the search problem, the different steps of the algorithm can be rephrased in the following more intuitive way:



- First, the algorithm creates a fully superposed quantum state which contains all possible solutions to the search problem at once. The amplitudes and phases of each individual state are all equal in the beginning.
- Then, it applies the Oracle operator to this superposed state. The effect of the Oracle is to turn the phase of the states  $t$  by an angle  $\pi$  for which  $\mathcal{C}(t) = 1$ . As will be shown later, such an Oracle operator can be implemented in a straightforward way for any classical search function.
- In the next step, it applies a diffusion operator to the quantum state which transfers a fraction of the amplitude from states with zero phase to the states with  $\pi$  phase, increasing thus the amplitude of the latter. In this process, the phases of all states gets also turned back to zero, allowing the algorithm to repeat the sequence above.
- Repeating these two operations increases each time the amplitude of the states that correspond to a solution of the search problem until the amplitudes of all the other states vanish. After that point, the process reverses and the amplitude is transferred back to the original states. It is therefore crucial to stop the repetition sequence given above after the right number of iterations.

By implementing the search function as a quantum operator, the Grover algorithm is able to evaluate it in one single call for all possible input states. This so-called *quantum parallelism* provides the basis for the speed-up of the search in comparison to a classical algorithm. However, being able to encode the result of the search function in the phase of a multi-qubit state does not directly translate to a speed advantage since it is usually very hard to extract this phase information from the quantum state. Indeed, to extract the values of all phases from an  $N$ -qubit state, it would be necessary to perform  $\mathcal{O}(2^N)$  measurements on an ensemble of identically prepared quantum states. However, extracting the state amplitudes from such a state takes only  $\mathcal{O}(N)$  measurements, which in addition can usually be carried out in parallel. It is for this that the Grover algorithm uses an operator that transforms the information encoded in the phases of the qubits to an information encoded in their amplitude. However, since the conversion between phase to amplitude information through the application of an unitary operator is limited by certain physical constraints, the algorithm needs to repeat the encode-and-transfer sequence described above  $\mathcal{O}(\sqrt{N})$  times.

To analyze further the constraints and principles of the algorithm, we will discuss a more detailed derivation of it starting from the Schrödinger equation and we will also explain what limits the efficiency of the phase-to-amplitude conversion in the algorithm.

### 6.1.1 Deriving the Grover Algorithm from Schrödinger's Equation

An interesting derivation of the Grover algorithm starting from Schrödinger's equation has been detailed by Grover himself in a seminal paper [45] and shall be briefly rediscovered here since it sheds light on the basic principles on which the algorithm is based. The derivation begins by considering a quantum system governed by Schrödinger's equation, which can be written as (setting  $\hbar = 1$  for clarity)

$$-i \frac{\partial}{\partial t} \psi(x, t) = \frac{\partial^2}{\partial x^2} \psi(x, t) - V(x) \psi(x, t) \quad (6.1)$$

Here  $\psi(x, t)$  describes the wave-function and  $V$  is a time-independent potential. Let us assume that the potential  $V(x)$  is shaped as in fig. 6.1, i.e. possessing a global minimum of energy. When one initializes the system to a state  $\psi_0(x, t_0)$  and lets it evolve for a given time,  $\psi(x, t)$  will be attracted by the minimum of potential energy and "fall into it" much like a classical particle in such a potential would<sup>1</sup>. We might thus ask if we can encode the solution to a search problem as a point of minimum energy  $x_0$  of a potential  $V(x)$ , take an initial state  $\psi_0(x, t_0)$  and let it evolve into a state that has a high probability around  $x_0$ , thereby solving the search problem. To answer this question, it is first necessary to discretize the wavefunction  $\psi(x, t)$  such that it can represent the search problem stated in the last section, which is defined over a finite number of states. In the most simple case, we can use a regular grid of points  $x_i$  with a spacing  $\Delta x$  for this, as shown in fig. 6.1b. Discretizing the time evolution of eq. 6.1 in steps  $\Delta t$  as well and defining  $\epsilon = \Delta t / \Delta x^2$ , we obtain a new equation of the form

$$-\frac{\psi_i^{t+\Delta t} - \psi_i^t}{\Delta t} = \frac{\psi_{i+1}^t + \psi_{i-1}^t - 2\psi_i^t}{\Delta x^2} - V(x_i) \psi_i^t \quad (6.2)$$

where we have written  $\psi(x_i, t) = \psi_i^t$ . For a circular grid with  $N$  points we can write this equation in matrix form as

$$\vec{\psi}^{t+\Delta t} = S^{\Delta t} \cdot \vec{\psi}^t \quad (6.3)$$

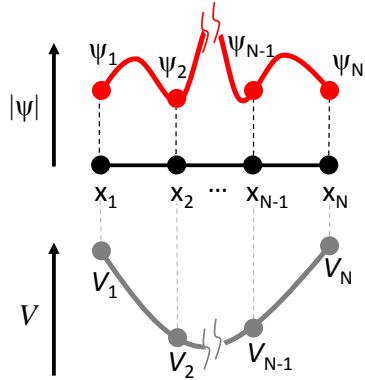
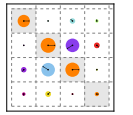


Figure 6.1: A wavefunction  $\psi(x)$  and potential  $V(x)$  defined on a grid of points  $x_1, \dots, x_N$ .

<sup>1</sup>of course, since there is no dissipation, the state will not come to rest at the minimum point of energy but rather oscillate around it conserving its total potential and kinetic energy



with  $S$  being a state transition matrix of the form

$$S^{\Delta t} = \begin{pmatrix} 1 - 2i\epsilon - iV(x_1)\Delta t & i\epsilon & 0 & \dots & i\epsilon \\ i\epsilon & 1 - 2i\epsilon - iV(x_2)\Delta t & i\epsilon & \dots & 0 \\ 0 & i\epsilon & \ddots & & \vdots \\ \vdots & & \ddots & & \vdots \\ i\epsilon & 0 & \dots & i\epsilon & 1 - 2i\epsilon - iV(x_N)\Delta t \end{pmatrix} \quad (6.4)$$

For infinitesimal times  $\Delta t$  we can separate the effect of the potential  $V(x)$  on the wavefunction from the spatial dispersion by writing  $S^{\Delta t} \approx D \cdot R$  with

$$D = \begin{pmatrix} 1 - 2i\epsilon & i\epsilon & 0 & 0 & \dots & i\epsilon \\ i\epsilon & 1 - 2i\epsilon & i\epsilon & 0 & \dots & 0 \\ \dots & \ddots & & & & \vdots \\ i\epsilon & 0 & 0 & \dots & i\epsilon & 1 - 2i\epsilon \end{pmatrix} \quad (6.5)$$

and

$$R = \begin{pmatrix} e^{-iV(x_1)\Delta t} & 0 & \dots & 0 \\ 0 & e^{-iV(x_2)\Delta t} & \dots & 0 \\ 0 & \dots & 0 & e^{-iV(x_N)\Delta t} \end{pmatrix} \quad (6.6)$$

This approximation is correct to  $\mathcal{O}(\epsilon)$  up to an unimportant renormalization factor. We can now repeatedly apply the matrix product  $D \cdot R$  to the wavefunction to obtain its state after a given finite time  $t$  by writing

$$\vec{\psi}^{t_0+t} = \left( \prod_{i=1}^{t/\Delta t} D \cdot R \right) \cdot \vec{\psi}^t \quad (6.7)$$

This technique of splitting up the full evolution operator into a product of two or more non-commuting operators that are applied repeatedly to the wavefunction to obtain its state after a finite time is sometimes referred to as *Trotterification* – in reference to the so-called *Lie-Trotter formula* on which it is based – and is widely used in digital quantum simulation [59, 57].

As can be seen in eq. (6.7), the evolution of the wavefunction at infinitesimal times is governed by two processes: The interaction with the potential  $V$  and a diffusion process that mixes different spatial parts of the wavefunction with each other. The operator  $D$  resembles a Markov diffusion process since each row and column of the matrix sums up to unity, whereas  $R$  changes the phase of each element of the wavefunction in accordance with the local potential seen by it. If we apply  $R$  to a fully superposed initial state of the

form  $\psi_i = 1$  (omitting the normalization factor for clarity) and assume that  $V_i = 0$  for  $i \neq j$  and  $V_j \Delta t = \pi/2$  (the potential thus encoding a search function with  $\mathcal{C}(j) = 1$  and  $\mathcal{C}(i) = 0$  for  $i \neq j$ ), the element  $\psi_j$  will get turned according to  $\psi_j \rightarrow i\psi_j$ , whereas all other elements  $\psi_i$  will remain unchanged. Applying the operator  $D$  to the resulting state will transform  $\psi_j$  according to  $\psi_j \rightarrow \psi_j(i + 2\epsilon(1 + i))$  with a corresponding amplitude  $\sqrt{1 + 4\epsilon + \mathcal{O}(\epsilon^2)}$  and the adjacent states  $\psi_{j\pm 1}$  according to  $\psi_{j\pm 1} \rightarrow \psi_{j\pm 1}(1 - \epsilon(1 + i))$  with an amplitude  $\sqrt{1 - 2\epsilon + \mathcal{O}(\epsilon^2)}$ . Hence there is a transfer of amplitude between the state whose phase has been turned and its neighboring states. If we reset the phases of all the  $\psi_i$  to zero afterwards, we can iterate the application of  $D \cdot R$  until all of the amplitude has been transferred to the element  $\psi_j$  which corresponds to a solution to the search problem. This is, in essence, exactly what the Grover algorithm does, the only difference being that it replaces the matrix  $D$  with an unitary matrix that maximizes the amplitude transfer to the states solving the search problem, thereby speeding up the algorithm. As stated before, the efficiency with which the algorithm can transfer amplitude between different states is limited by physical constraints, in the next section we will therefore discuss exactly what limits this efficiency and which unitary matrix one should choose to maximize it.

### Efficiency of Quantum Searching

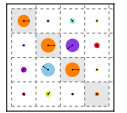
It is interesting to ask which is the maximum amount of amplitude that can be transferred in a single step of the Grover search algorithm and which matrix  $D$  should be chosen to maximize this transfer. To answer this question and derive the ideal diffusion matrix, we will assume first that the matrix  $R$  which encodes the value of the search function  $\mathcal{C}$  in the quantum state of the qubit register can be written in the most general case as

$$R = \sum_{j=0}^{N-1} \exp[i\alpha\mathcal{C}(j)] |j\rangle\langle j| \quad (6.8)$$

Here,  $\alpha$  is a factor which we can choose arbitrarily. So, without loss of generality, we can choose  $\alpha = \pi$ , yielding an Oracle operator of the form

$$R = I - 2 \sum_{j=0}^{N-1} \mathcal{C}(j) |j\rangle\langle j| \quad (6.9)$$

This operator will flip the sign of all states for which  $\mathcal{C}(j) = 1$ . Now, the next step consists in finding a diffusion or state transfer matrix which will maximize the amplitude transfer to states marked by the Oracle operator above and which will also reset the phases of the quantum register to zero afterwards, such that we might apply the Oracle operator to the resulting state again. In the most general case, such a state transfer matrix will



have the form

$$D_c = \begin{pmatrix} b & a & a & \dots & a \\ a & b & a & \dots & a \\ \vdots & \ddots & & & \vdots \\ a & \dots & a & b \end{pmatrix} \quad (6.10)$$

Here, we assume that all non-diagonal elements of the matrix are equal, which is well justified since we have no knowledge of the structure of the search space of the problem and therefore want to treat all basis states equally during the phase-to-amplitude conversion. Furthermore, since both the initial quantum state and the Oracle operator as given by eq. (6.9) contain only real numbers and we demand that the quantum state after applying  $D_c$  may contain only positive real numbers as well it is easy to show that  $a, b$  must be real numbers. Finally, the unitarity of quantum operators demands that  $D_c^\dagger D_c = I$ , which for the matrix above is equivalent to the two conditions

$$1 = b^2 + (N - 1)a^2 \quad (6.11)$$

$$0 = 2ab + (N - 2)a^2 \quad (6.12)$$

Solving these two equations for  $a, b$  yields the trivial solution  $b = \pm 1, a = 0$  and the more interesting one  $b = \pm(1 - 2/N), a = \mp 2/N$ . As can be checked easily, the solution  $b = 1 - 2/N, a = 2/N$  results in a maximum amplitude transfer from states  $|i\rangle$  for which  $\mathcal{C}(i) = 0$  to states  $|j\rangle$  for which  $\mathcal{C}(j) = 1$ . Thus the ideal diffusion matrix to be used in the Grover algorithm is given as

$$D = \begin{pmatrix} -1 + 2/N & 2/N & 2/N & \dots & 2/N \\ 2/N & -1 + 2/N & 2/N & \dots & 2/N \\ \vdots & & \ddots & & \vdots \\ 2/N & 2/N & 2/N & \dots & -1 + 2/N \end{pmatrix} \quad (6.13)$$

This matrix, together with an Oracle operator  $R$  as given by eq. (6.9) will yield the maximum amplitude transfer from states not solving the search problem to states that solve it. Repeating the application of  $D \cdot R$  on an initially fully superposed quantum states for  $\mathcal{O}(\sqrt{N})$  times will transform the input state to a state containing only the solutions of the search problem, thus solving the problem quadratically faster than possible with any classical algorithm.

### 6.1.2 Implementation & Comparability to Classical Algorithms

In the following sections we discuss a two-qubit implementation of the Grover search algorithm that we implemented in this work. To be able to compare the Grover algorithm

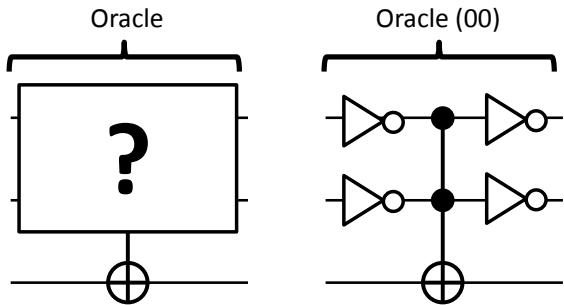


Figure 6.2: a) Two-qubit ancilla-based implementation of the Oracle function  $\mathcal{C}$ . The state of the third bit get flipped if the search function  $\mathcal{C}(i) = 1$  for the given input state  $i$ . b) An example of an ancilla-based search function that returns a true value for the input state 00.

as outlined here to a classical version solving the same search problem, we will now discuss another variant of the algorithm that uses an ancilla qubit to encode the result of the search function. This implementation will make it possible to devise a classical algorithm that can then be compared to the quantum algorithm.

### 6.1.3 Ancilla-based Implementation of the Algorithm

The implementation of the Grover search algorithm as outlined above encodes the value of the search function  $\mathcal{C}$  directly in the phase of the input state supplied to this function. This makes it hard to compare the algorithm to a classical search algorithm which operates on a binary input states and, in general, cannot encode the result of the search function directly in the input state. It is therefore useful to formulate a version of the Grover algorithm where the Oracle function does not directly encode the marked state in the input qubit register but rather uses an ancilla qubit to store the result of calling  $\mathcal{C}$ . Such a representation of the algorithm, although of little practical relevance, is very useful since it allows us to directly compare the quantum algorithm to its classical counterpart implemented using reversible logic gates, thus making it possible to benchmark the quantum algorithm and provide an estimation of the quantum speed-up that can be achieved.

Exemplary implementations of ancilla-based search functions  $\mathcal{C}$  implemented using reversible (quantum) gates are shown in fig. 6.2 for the two-qubit case. There, a two-qubit Toffoli gate in combination with several single-qubit NOT gates (that can be easily implemented as single-qubit  $X_\pi$  rotations) is used to flip the state of an ancilla-qubit conditionally on the input state of the gate. Using a similar approach, any arbitrary classical search function  $\mathcal{C}$  that can be implemented with a set of universal reversible logic gates (e.g. the Toffoli gate and the NOT gate) can be directly mapped to a corresponding quantum operator that works on quantum-mechanical input states and implements the classical search function.

Now, to use the Grover algorithm with such an ancilla-based quantum Oracle, it is necessary to re-encode the result of the Oracle in the qubit input state. Fig. 6.3 shows

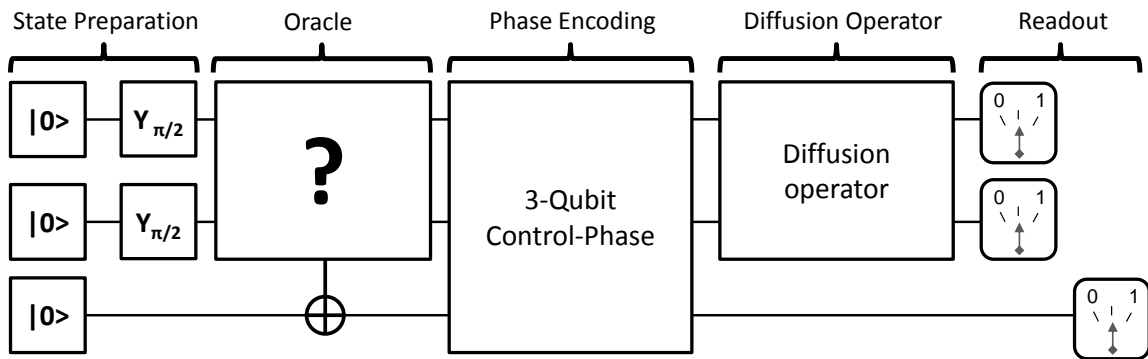
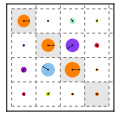


Figure 6.3: A full version of an ancilla-based implementation of the two-qubit Grover search algorithm. The algorithm works on a two-qubit input state and flips the state of a control qubit for one of the four possible input states in accordance to an unknown Oracle function. It then applies a 3-qubit control-phase operation of that maps  $|xy1\rangle \rightarrow -|xy1\rangle$ ,  $|xy0\rangle \rightarrow |xy0\rangle$  to encode the state of the control qubit directly in the two input qubits and then uses a diffusion operator to determine the state which has been marked by the Oracle function.

a version of the two-qubit Grover algorithm that achieves exactly this by using a three-qubit control-not (CNOT) gate  $C$  of the form

$$C = I^{n \otimes n} - 2 \sum_{ij} |ij1\rangle \langle ij1| \quad (6.14)$$

to phase-encode the state of the ancilla qubit in the state of the input qubit register. After the re-encoding of the result, the ancilla qubit is not needed during the remainder of the algorithm and must not be read out before the algorithm terminates.

## 6.2 Comparision to a Classical Algorithm

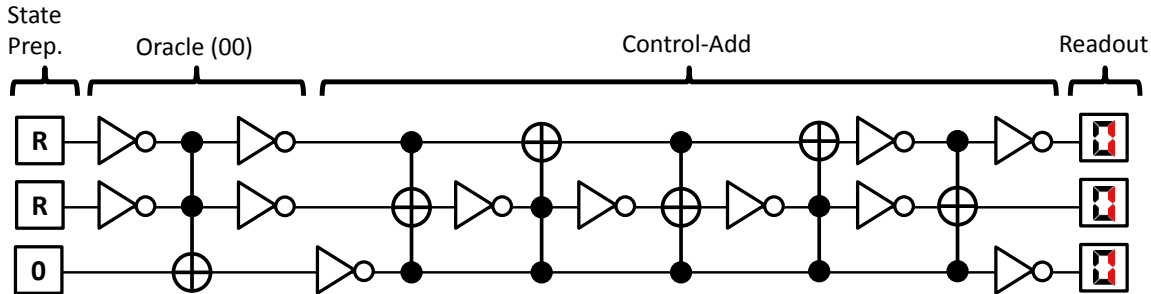


Figure 6.4: Classical reversible implementation of a search algorithm on a two-bit input register. An exemplary Oracle function can be implemented using two single-bit NOT operations and a Toffoli gate. R designates the generation of a random binary value at the beginning of the algorithm. If the Oracle does not yield the correct answer, the test state is incremented. The average success probability of the algorithm is 50 %.

### 6.3. EXPERIMENTAL IMPLEMENTATION

---

In order to quantify the speed-up achieved by a quantum algorithm it is necessary to map the problem it solves to an equivalent problem that can be solved by a classical algorithm. For the Grover algorithm, this is the search problem that we discussed in the first section of this chapter. Using the reversible, ancilla-based implementation of the search function that was introduced in the last section we can directly formulate a classical algorithm that solves the same problem as the Grover algorithm and compare the runtime of the two. Since the two-qubit Grover algorithm evaluates the search function  $\mathcal{C}$  only once it is interesting to ask what would be the success probability of an equivalent classical algorithm that calls  $\mathcal{C}$  once and returns an estimate of the state solving the search problem afterwards. Such an algorithm is shown in fig. 6.4 and it achieves a success probability of 50 % by evaluating once the function  $\mathcal{C}$  for a randomly generated two-bit input value  $r$  and returning  $r$  if it found  $\mathcal{C}(r) = 1$  or  $r + 1 \pmod 4$  otherwise. The 50 % success rate of this algorithm provides a benchmark against which we will measure the speed-up of our implementation of the Grover algorithm.

Alternatively, we can also compare the success probability of the quantum algorithm with either a simple classical “query” algorithm or a “query-and-guess” algorithm, plotting the success probability of either of them as a function of the number of calls to the Oracle function  $\mathcal{C}$ . This makes it possible to compare the performance of the quantum algorithm to the classical ones for an arbitrary number of calls  $n$  to  $\mathcal{C}$ . Such a comparison will be made later in this chapter when reviewing the experimental data obtained for our implementation of the Grover algorithm.

## 6.3 Experimental Implementation

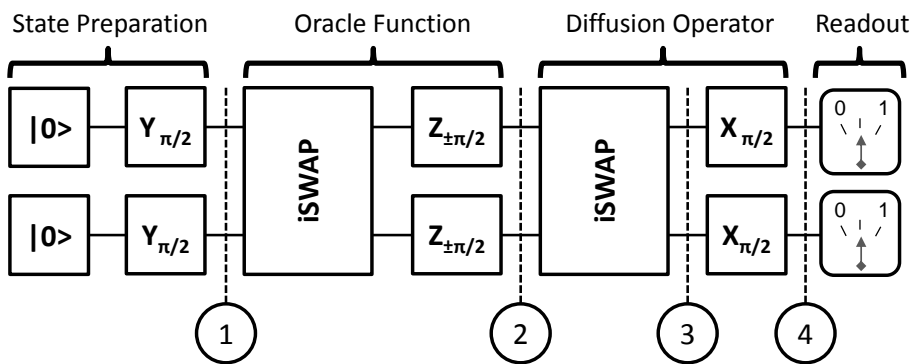
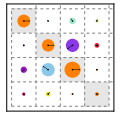


Figure 6.5: Schematic of our implementation of the Grover search algorithm. The algorithm consists in generating a fully superposed input state, applying the Oracle function to it and analyzing the resulting state by applying the Diffusion transform to it and reading out the value of the qubit register afterwards.

We implemented a compiled version of the two-qubit Grover algorithm using our two-



qubit quantum processor. The gate sequence of the algorithm is shown in fig. 6.5 and consists in two *iSWAP* gates and six single-qubit gates applied to an initial state  $|00\rangle$ . Here, the first *iSWAP* gate together with the two single-qubit  $Z_{\pm\pi}$  rotations implements the Oracle function  $f(x)$  as given by eq. (6.9), where the signs of the rotation operations determines the state which is marked by the Oracle. This state can be either  $|00\rangle$  (corresponding to a  $Z_{-\pi/2}^1 \cdot Z_{-\pi/2}^2$  rotation),  $|01\rangle$  ( $Z_{-\pi/2}^1 \cdot Z_{\pi/2}^2$ ),  $|10\rangle$  ( $Z_{\pi/2}^1 \cdot Z_{-\pi/2}^2$ ) or  $|11\rangle$  ( $Z_{\pi/2}^1 \cdot Z_{\pi/2}^2$ ). After the encoding, the second *iSWAP* operation together with the following  $X_{\pi/2}^1 \cdot X_{\pi/2}^2$  single-qubit operations implement the diffusion operator as given by eq. (6.13). The final step of the algorithm consists in reading out the two-qubit register.

### 6.3.1 Pulse Sequence

To implement the gate sequence described above we need to realize a sequence of microwave and flux pulses which realize the individual quantum gates of the sequence. To eliminate possible gate errors, we perform a series of calibration measurements before to tune-up the individual single- and two-qubit gates needed for the algorithm. In addition, we run individual parts of the algorithm successively and perform quantum state tomography to characterize the state of the quantum register after each step of the algorithm and correct the gate operations applied to the qubit in order to maximize the fidelity of the measured states in respect to the ideal ones. Fig. 6.6 shows an experimental pulse sequence for the Grover algorithm with an Oracle operator marking the state  $|00\rangle$ . Shown are the frequencies of the two qubits during the runtime of the algorithm and the microwave drive and readout pulses applied to them.

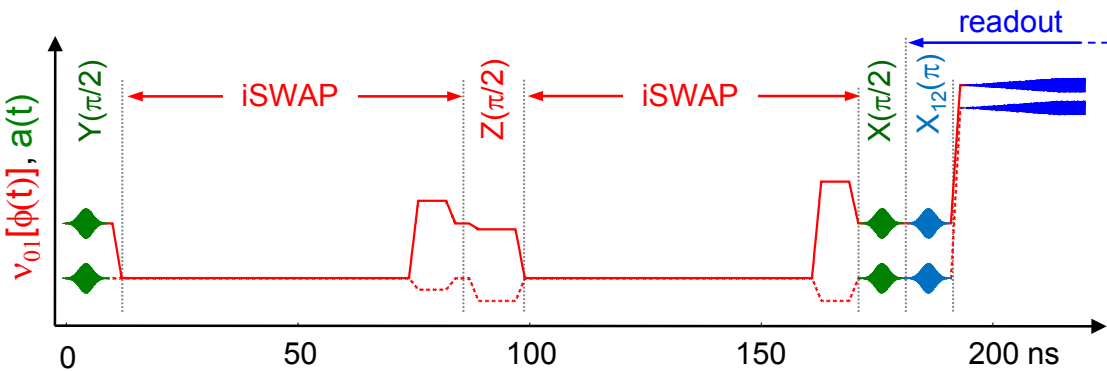


Figure 6.6: The pulse sequence used in realizing Grover's quantum search algorithm. First, a  $Y_{\pi/2}$  pulse is applied to each qubit to produce the fully superposed state  $1/2(|00\rangle + |01\rangle + |10\rangle + |11\rangle)$ . Then, an *iSWAP* gate is applied, followed by a  $Z_{\pm\pi/2}$  gate on each qubit, which corresponds to the application of the oracle function. The resulting state is then analyzed using another *iSWAP* gate and two  $X_{\pi/2}$  gates to extract the state which has been marked by the oracle function. Optionally, a  $Y_{\pi}^{12}$  pulse is used on each qubit to increase the readout fidelity.

## 6.4 Results

Here we discuss the results obtained when running the Grover search algorithm with our two-qubit processor. In the first section we will analyze the quantum state of the qubit register during the algorithm by performing quantum state tomography. In the second section we will present and discuss the single-run results obtained in our experiment.

### 6.4.1 State Tomography of the Quantum Register

Fig. 6.7 shows the experimentally measured density matrices of the two-qubit register when running the Grover search algorithm for the four possible Oracle functions. For each of those four cases, density matrices were measured at the steps 1-4 of the Grover algorithm as indicated in fig. 6.5. The black outlined circles in the density matrices represent the ideal theoretical states and the colored solid circles represent the measured states. The trace fidelities of all states with respect to the ideal states are noted above each density matrix. As can be seen, the fidelity diminishes as a function of the runtime of the algorithm due to dephasing and relaxation of the qubit register, as we will discuss later.

### 6.4.2 Single Run Results

The experimental state tomographies discussed in the last section show that we are able to implement the Grover search algorithm with adequate fidelity using our two-qubit processor. However, the analysis of the two-qubit register by quantum state tomography at the end of the algorithm does not prove that we can achieve real quantum speed-up with our processor. For this, it is necessary to directly read out the state of the qubit register at the end of the algorithm *without* performing any kind of error correction afterwards. By looking at this “raw” outcome data and generating outcome statistics over many single runs of the processor we can then quantify the success rate and the fidelity of the algorithm we implemented. The results of such measurements that we performed for the four possible Oracle functions are shown in fig. 6.8. Besides the single-run probabilities for all four Oracle functions, the diagram shows for comparison the expected outcome probabilities calculated based on the quantum state tomographies discussed above and the readout matrix of the two-qubit processor. As can be seen, the agreement between the measured and calculated probabilities is rather good. The dashed line in the diagrams corresponds to the success probability of a classical single-step “query-and-guess” algorithm as described above, which is bound to 50 % and provides the benchmark against which we measure the quantum speed-up in this system. As can be seen, our implementation of the Grover search algorithm outperforms such a

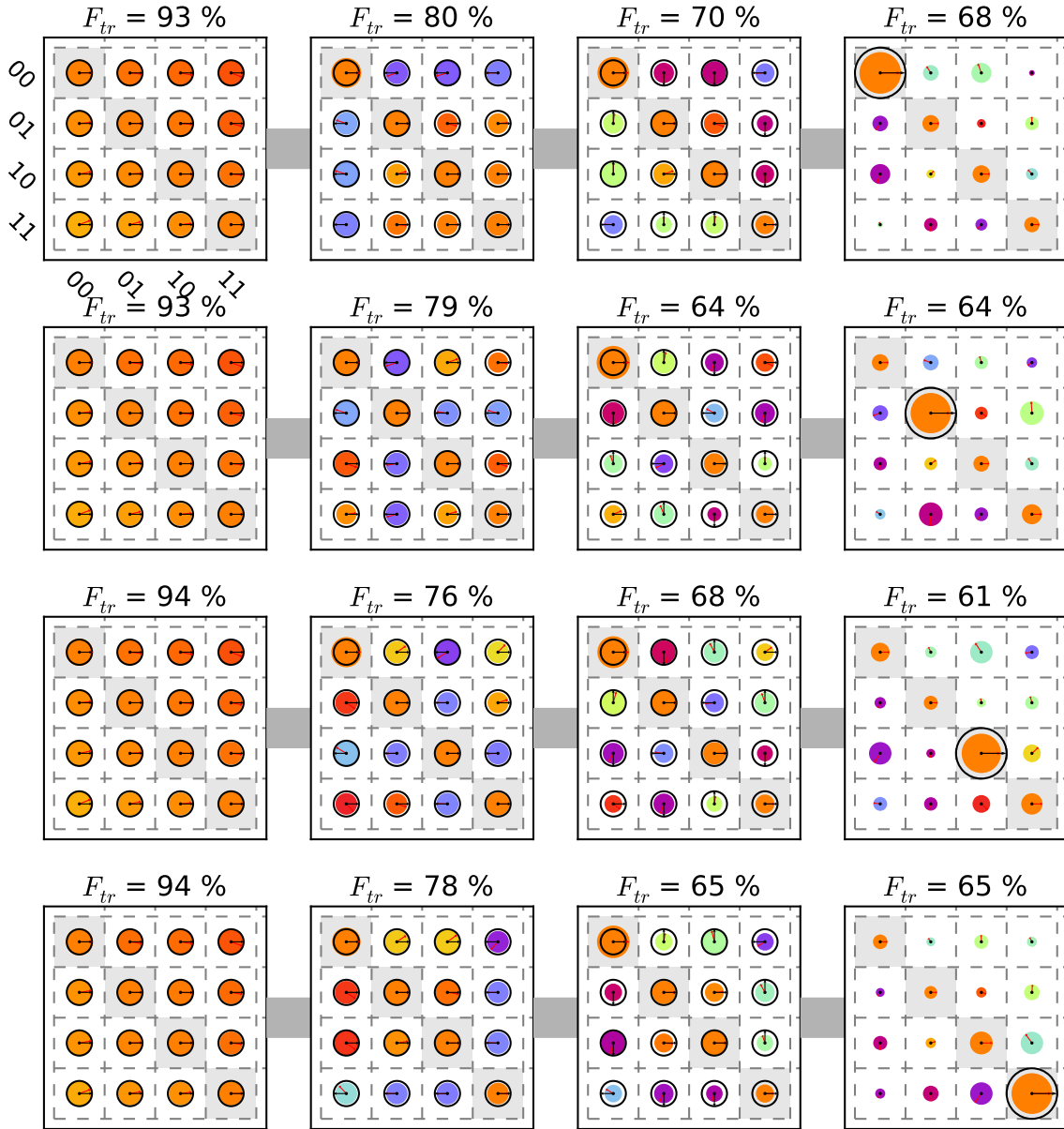
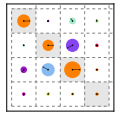


Figure 6.7: Quantum state tomographies at steps 1-4 of the Grover search algorithm, as indicated in fig. 6.6. The density matrices show the experimentally measured states in color and the theoretical states in black. For each state, the trace fidelity  $F_{tr}(\rho_A, \rho_B) = \text{Tr}\{\rho_A \cdot \rho_B\}$  is shown above the density matrix.

classical search algorithm for all four Oracle functions, if only by a small margin.

## 6.5 Algorithm Fidelity

We can define the average fidelity of the algorithm in a single run, which corresponds to the conditional probability of finding the correct state  $|i\rangle$  given a certain Oracle function  $C_i$ . Table 6.1 shows these single-run probabilities along with the so-called *user fidelities*,

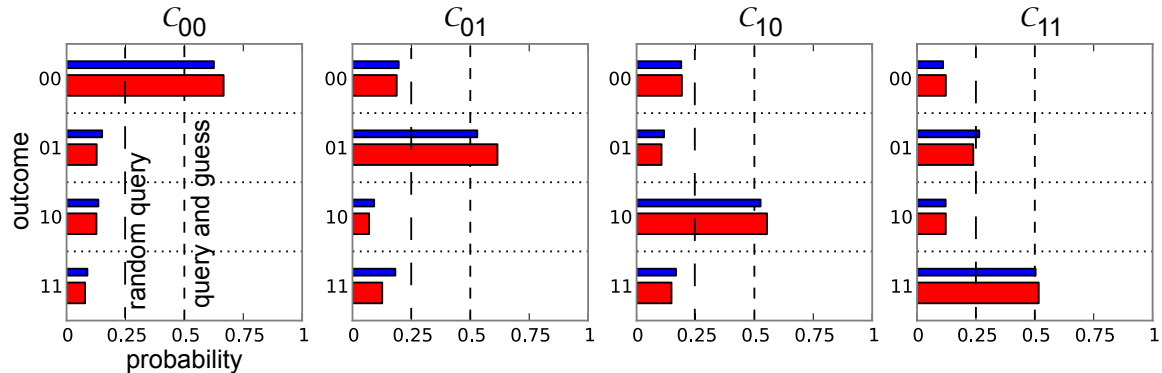


Figure 6.8: The single-run success probabilities of our implementation of the Grover search algorithm. Shown are the averaged probabilities for the four possible Oracle functions. The red bars correspond to measured values, the blue ones to expected probabilities calculated using the reconstructed density matrices after the final step of the algorithm and the measured two-qubit readout matrix. The dashed line indicates the average success probability of a classical query-and-guess algorithm for comparison.

which are given as

$$f_{ab} = p(|ab\rangle |ab) = \frac{p(ab| |ab\rangle)}{\sum_{uv} p(uv| |uv\rangle)} \quad (6.15)$$

, where  $p(ab| |ab\rangle)$  is the conditional probability of obtaining the search result  $ab$  given the Oracle operator  $|ab\rangle$ . The user fidelity is complementary to the average fidelity and correspond to the conditional probability of having found the correct state given a certain measured state, averaged over all possible Oracle functions. For all four Oracles, both the single-run and user fidelities are  $> 50\%$ , hence demonstrating quantum speed-up in comparision with a classical query-and-guess algorithm, as will be discussed below.

$ab/ uv\rangle$	$ 00\rangle$	$ 01\rangle$	$ 10\rangle$	$ 11\rangle$	$\Sigma$	$f_{ab}$
00	0.666	0.192	0.188	0.122	1.168	57.0 %
01	0.127	0.554	0.071	0.122	0.874	63.4 %
10	0.128	0.106	0.615	0.239	1.088	56.5 %
11	0.079	0.148	0.126	0.517	0.870	59.4 %

Table 6.1: Conditional probabilities  $p_{ab/|uv\rangle}$  and user fidelities  $f_{ab}$  for all possible outcomes  $ab$  for our implementation of Grover's algorithm.

## 6.6 Comparison to a Classical Search Algorithm

As discussed above, we can compare the success probability of our implementation of the Grover search algorithm to different classical algorithm in order to quantify the quantum speed-up that we achieve. When repeatedly running the quantum search algorithm

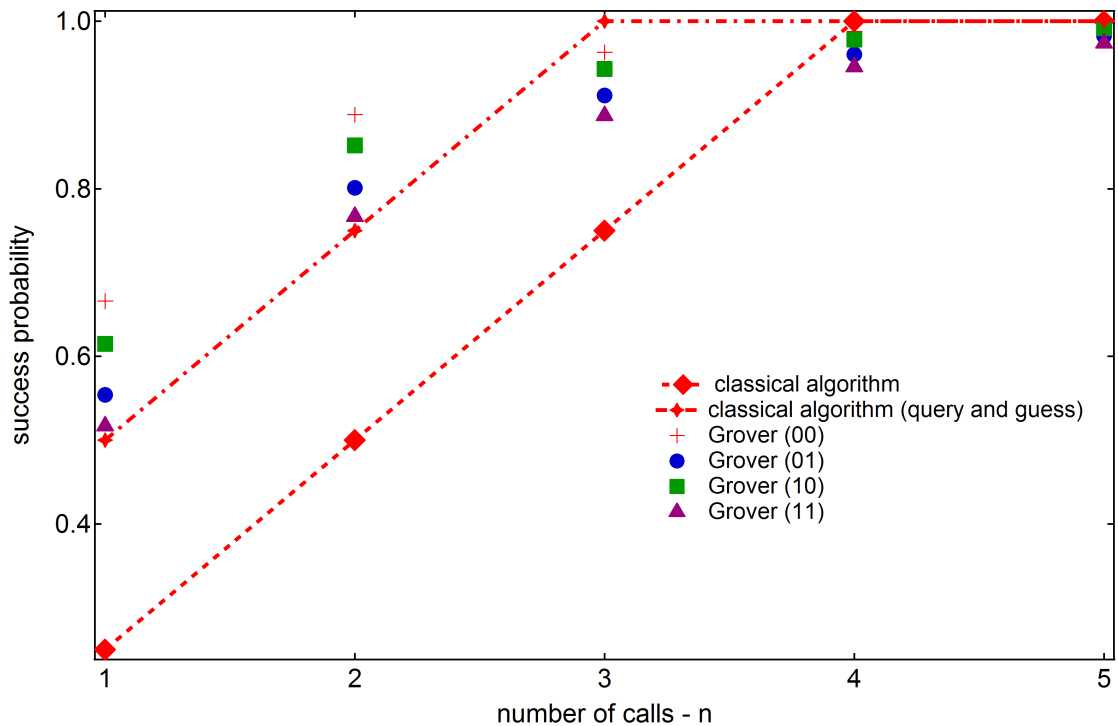
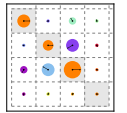


Figure 6.9: Success probability of our implementation of the Grover search algorithm, plotted against the number of single runs of the algorithm  $n$ . For comparison we show the success probabilities of a classical query and a classical query-and-guess search algorithm as a function of  $n$ .

we can define the success probability as the probability of obtaining the right answer to the search problems within  $n$  single runs, which is given as

$$p_s(n) = \sum_{i=1}^n (1 - p_s)^{i-1} p_s \quad (6.16)$$

Here,  $p_s$  is the single-run success probability of the algorithm. We can plot  $p_s(n)$  as a function of the runs of the algorithm and compare it with different classical algorithms. Fig. 6.9 shows such a comparison for our implementation of the Grover search algorithm. For comparison with the quantum algorithm we plot the success probability of a classical query search algorithm and a classical query-and-guess algorithm as a function of Oracle calls  $n$ . The difference between the query and the query-and-guess algorithm is that the former doesn't return a result if it does not find the solution to the search problem after a number of  $n$  calls, whereas the latter takes an "educated guess" at the right state even if it did not obtain it directly by calling the Oracle function  $n$  times. Hence the statistical success probability of the query-and-guess-algorithm is bigger than that of the simple query algorithm.

As can be seen, our implementation of the Grover search algorithm beats the classical query algorithm for  $n < 4$  single runs and the classical query-and-guess algorithm

for  $n < 3$  single runs. However, unlike the classical algorithms it never converges to 100 % success probability due to always-present unitary and non-unitary errors in our system. We will analyze all such different errors relevant to our experiment in the next section.

## 6.7 Error Analysis

There are three kind of errors arising in our implementation of the Grover search algorithm that we will analyze in the following section. These errors are:

1. Deterministic, unitary gate errors
2. Stochastic errors introduced due to qubit decoherence during the runtime of the algorithm
3. Readout errors due to qubit relaxation during readout, insufficient readout sensitivity or retrapping of the readout resonator state during measurement.

We analyze the contributions of all these three error sources for the implementation of the algorithm below.

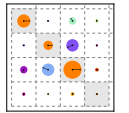
### 6.7.1 Gate Errors & Decoherence

Gate errors are unitary errors that arise due to missshaped or mistuned gate pulses and qubit frequencies. Usually the effect of these errors is combined with stochastic, non-unitary errors arising due to qubit decoherence during the runtime of the algorithm and therefore has to be analyzed together with the latter. Hence, in order to quantify these errors it is necessary to generate an error model of our algorithm that takes into account both unitary and as non-unitary errors. The parameters of such a model can be obtained by numerically fitting it to our experimental results.

#### Modeling Decoherence

**!1!** We could again model decoherence processes in our algorithm by formulating an effective master equation of the two-qubit system that includes relaxation and dephasing processes as we did when analyzing the universal quantum gate that we implemented. For our implementation of the Grover algorithm, however, we chose to rather use a set of discrete decoherence operators that model amplitude (i.e.  $T_1$ ) and phase damping (i.e.  $T_\phi$ ) processes and which we can directly integrate in a more simple, operator-based model of the algorithm. We can then model the decoherence in our algorithm by applying these operators to the calculated quantum states after each individual step of

To Do 1: replace this analytical calculating with a master equation simulation modeling the qubit as a three-level system and capturing all relevant errors



the algorithm. Like this we can generate an error model incorporating the most relevant experimental decoherence processes without the need to numerically integrate an effective master equation, thereby greatly speeding up the process of fitting our experimental data to the formulated error model. In the following paragraphs we introduce the reader to the operators we use to model relaxation and dephasing processes in our error model.

To model qubit relaxation, we can use a pair of single-qubit operators describing amplitude-damaging of the qubit state, which given as [75]

$$E_1^{T_1} = \begin{pmatrix} 1 & 0 \\ 0 & \sqrt{1 - \gamma_{T_1}} \end{pmatrix} \quad E_2^{T_1} = \begin{pmatrix} 0 & \sqrt{\gamma_{T_1}} \\ 0 & 0 \end{pmatrix} \quad (6.17)$$

On the other hand, phase-damaging operators describing qubit dephasing can be written analogously as

$$E_1^{T_{\phi 1}} = \begin{pmatrix} 1 & 0 \\ 0 & \sqrt{1 - \gamma_{\phi}} \end{pmatrix} \quad E_2^{T_{\phi 1}} = \begin{pmatrix} 0 & 0 \\ 0 & \sqrt{\gamma_{\phi}} \end{pmatrix} \quad (6.18)$$

Both operators are applied to a quantum state  $\rho$  according to

$$\rho \rightarrow E_1 \rho E_1^\dagger + E_2 \rho E_2^\dagger \quad (6.19)$$

and yield a trace-preserving, non-unitary evolution of the quantum state of  $\rho$ . The decoherence fraction  $\gamma$  that is used in the operators can be calculated from the corresponding relaxation and dephasing rates as  $\gamma_{T_{1,2}}(t) = 1 - \exp(-t\Gamma_{1,2}^{T_1})$  and  $\gamma_{\phi_{1,2}} = 1 - \exp(-t\Gamma_{1,2}^{T_\phi}/2)$ , where  $t$  is the time during which the state is exposed to the given decoherence process.

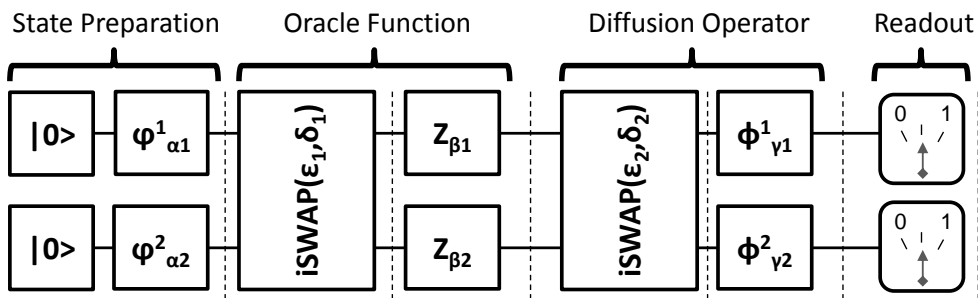


Figure 6.10: The error model we use to analyze the different gate and decoherence errors present when running the Grover search algorithm. The dotted lines indicate the points at which the quantum state has been measured by state tomography.

Using these two operators combined with a set of unitary operators describing the quantum operations performed during the algorithm we formulate a full error model that

## 6.7. ERROR ANALYSIS

---

we use to model our experimental data, as shown in fig. 6.10. This model takes into account the following error sources:

- **Energy relaxation and phase decoherence:** Energy relaxation and dephasing of the qubit is modeled using the processes given in eqs. (6.17) and (6.18), applying these operators with an adapted  $\gamma$  after each unitary operation performed during the algorithm.
- **Single-qubit gate errors:** We model rotation angle and rotation phase errors of our single-qubit  $X_\alpha$  and  $Y_\alpha$  gates by replacing them with operators of the form  $X_\alpha \rightarrow \phi_{\alpha'} = \cos \phi X_{\alpha'} + \sin \phi Y_{\alpha'}$  and  $Y_\alpha \rightarrow \varphi_{\alpha'} = \sin \varphi X_{\alpha'} + \cos \varphi Y_{\alpha'}$ . For  $Z$ -type single-qubit operators we model only rotation angle errors by replacing  $Z_\alpha \rightarrow Z_{\alpha'}$
- **Two-qubit gate errors:** We model both detuning and gate-length errors of our *iSWAP* 2-qubit gates.

For the two-qubit gates, we model the errors present in the *iSWAP* operation by using the representation of the gate

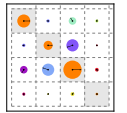
$$i\text{SWAP}(t, \Delta) = \begin{pmatrix} 1 & 0 & 0 & 0 \\ 0 & \cos t g_e - i \frac{\Delta}{g_e} \sin t g_e & i \frac{g}{g_e} \sin t g_e & 0 \\ 0 & i \frac{g}{g_e} \sin t g_e & \cos t g_e + i \frac{\Delta}{g_e} \sin t g_e & 0 \\ 0 & 0 & 0 & 1 \end{pmatrix} \quad (6.20)$$

where  $g_e = \sqrt{g^2 + \Delta^2}$  is the effective swap frequency at a qubit frequency detuning  $f_{01}^1 - f_{01}^2 = 2\Delta$ . Often it is practical to replace  $t$  and  $\Delta$  with  $\beta = t g_e$  and  $\delta = \Delta/g$ . Using this notation of the *iSWAP* gate and the definition of the single-qubit gates as discussed before, the full algorithm with only gate errors can be written as (for right-multiplication)

$$\text{Grover} = \phi_{\gamma_1}^1 \otimes \phi_{\gamma_2}^2 \cdot i\text{SWAP}(\epsilon_2, \delta_2) \cdot Z_{\beta_1} \otimes Z_{\beta_2} \cdot i\text{SWAP}(\epsilon_1, \delta_1) \cdot \varphi_{\alpha_1}^1 \otimes \varphi_{\alpha_2}^2 \quad (6.21)$$

In addition, we add dephasing and relaxation error after each step of the algorithm to model the decoherence during the runtime of the algorithm. Numerical optimization is then used to produce a fit of all the gate errors, which is shown in tab. 6.2. Here, the qubit relaxation and dephasing times were measured independently and are not part of the fit.

The resulting fitted error models obtained for our experimental data are shown in tab. 6.2. As can be seen, the phase and gate-time errors for the first gates are comparatively small and grow bigger during the following steps of the algorithm. Curiously, the phase errors are bigger for the states  $|10\rangle$  and  $|11\rangle$ , as are the gate-length errors for the two *iSWAP* gates used in the algorithm. This fact might be explained by a drift of the



state	$\delta_1$	$\delta_2$	$\alpha_1$	$\alpha_2$	$\varphi_1$	$\varphi_2$	$\epsilon_1$	$\beta_1$	$\beta_2$	$\epsilon_2$	$\gamma_1$	$\gamma_2$	$\phi_1$	$\phi_2$
$ 00\rangle$	0.06	-0.06	-2.5	2.7	6.1	3.1	-7.3	-3.3	-4.1	7.5	29	9.3	0.66	-1.7
$ 01\rangle$	0.04	-0.3	-0.1	0.1	7.9	3.6	-11	-5.9	2.2	-6.9	28	-19	9	2
$ 10\rangle$	0.09	-0.2	-3.1	1.7	1	-2.5	-6.5	-15	-22	-7.5	-15	32	3.6	5.2
$ 11\rangle$	0.16	0.13	-6	3.9	2.2	0.9	-9.5	-20	-15	17	-12	-32	-7	-8.9

Table 6.2: Fitted error parameters for the measured density matrices, modeled according to the error model given in eq. (6.21). All angles are given in deg.

operating point of our microwave setup during the time it took to take the data for the four possible Oracle operators, during which the parameters of individual qubit gates were not recalibrated. Our error model is able to capture most of the observed experimental errors and can reproduce to very good accuracy the observed density matrices. The state fidelities according to eq. ?? between the measured density matrices and those of the fitted error model are all  $> 95\%$ .

### Fidelity of the Oracle and diffusion operators

It is interesting to analyze the individual experimental fidelities of the Oracle and diffusion operators that make up the Grover algorithm achieved in our experiment. For this, we compare the action of the ideal operators  $D'$  and  $R'$  with that of the experimentally implemented versions  $D'_e$  and  $R'_e$ , taking the measured quantum states before applying each of the operators as input. We take then as the fidelity of each operator the average state fidelity of the measured output states as compared to the calculated ones, i.e.

$$F(D'_e) = F(D'\rho_{in}D'^\dagger, D'_e\rho_{in}D_e'^\dagger) \quad (6.22)$$

$$F(R'_e) = F(R'\rho_{in}R'^\dagger, R'_e\rho_{in}R_e'^\dagger) \quad (6.23)$$

where we also make use of the state fidelity according to eq. ?? . By this method, we obtain the following experimental fidelities for the two gate operations:

Operator / State	$ 00\rangle$	$ 01\rangle$	$ 10\rangle$	$ 11\rangle$	Average
$D'$	92.3	93.4	94.3	91.7	92.9
$R'$	94.5	93.6	88.5	87.7	91.1

Table 6.3: Measured fidelities of the quantum Oracle and diffusion operators used in the Grover search algorithm according to eqs. (6.22) and (6.23). All fidelities are given in percent.

As can be seen, on average we are able to implement both the diffusion operator and the quantum Oracle with a fidelity  $> 90\%$ .

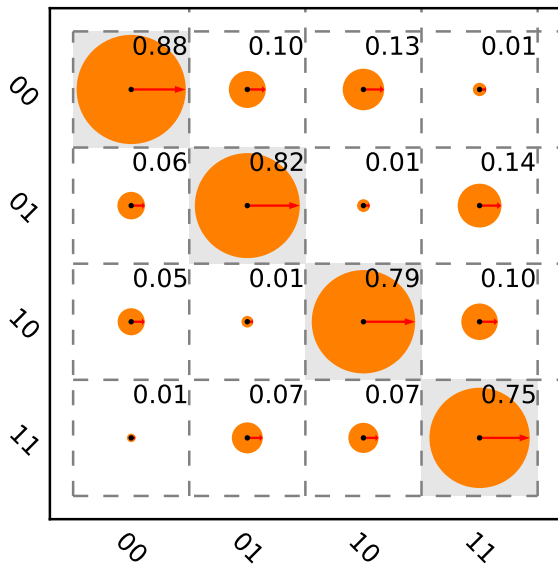


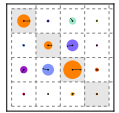
Figure 6.11

### 6.7.2 Readout Errors

Another source of errors affecting the single-run fidelities of the algorithm arises due to the imperfection of our qubit readout. Here, mostly qubit relaxation during the readout process reduces the visibility of individual qubit states and introduces errors when reading out the qubit register in the final step of the algorithm. We can easily quantify those readout errors by using the readout matrix that was introduced in the last chapter. When running the Grover algorithm we use the  $|1\rangle \rightarrow |2\rangle$  shelving method described in the last chapter to increase the readout contrast and thereby the algorithm fidelity. This technique reduces single-qubit readout errors but increases inter-qubit readout crosstalk. The readout matrices measured in our experiment is shown in fig. 6.11. As can be seen, the single-qubit readout fidelities range between 87 - 96 % and the combined two-qubit readout fidelities between 75 - 88 %. Depending on the qubit state we also observe between 3-5 % inter-qubit readout crosstalk in our system.

## 6.8 Conclusions

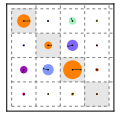
To summarize, we have shown that we can implement the Grover search algorithm with our quantum processor and achieve a single-run fidelity that is sufficient to demonstrate simple probabilistic quantum speed-up as compared to a classical, reversible search algorithm. The error model formulated in this chapter is able to account for most of the observed imperfections and can explain the data we observed. Unfortunately, the coherence times of our qubits does not permit the realization of more complex algorithm with this system, but nevertheless it provides a proof-of-principle of our approach to build a superconducting quantum computer with individual-qubit single shot readout.



In the following chapter, we will discuss the extension of this approach to a system of four qubits and explain different strategies for scaling up such system to an even larger number of qubits.

## *6.8. CONCLUSIONS*

---



# Chapter 7

## Conclusions & Perspective

### 7.1 Designing a Scalable Architecture for Quantum Bits

[40, 64]

#### 7.1.1 Requirements

#### 7.1.2 Qubit-Qubit Coupling

#### 7.1.3 Realizing A Four-Qubit Architecture

#### 7.1.4 Scaling Up

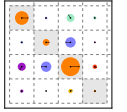
### 7.2 Future Directions in Superconducting QC

#### 7.2.1 3D Circuit Quantum Electrodynamics

#### 7.2.2 Hybrid Quantum Systems

#### 7.2.3 Quantum Error Correction & Feedback





# Appendix A

## Modeling of Multi-Qubit Systems

### A.1 Analytical Approach

#### A.1.1 Multi-Qubit Hamiltonian

#### A.1.2 Energies and Eigenstates

### A.2 Master Equation Approach

$$\hat{H} = \begin{pmatrix} e_0^I + e_0^{II} & & & & & & \\ & e_0^I + e_1^{II} & & & & & \\ & & e_0^I + e_2^{II} & & & & \\ & & & e_1^I + e_0^{II} & & & \\ & & & & e_1^I + e_1^{II} & & \\ & & & & & e_1^I + e_2^{II} & \\ & & & & & & e_2^I + e_0^{II} \\ & & & & & & & e_2^I + e_1^{II} \\ & & & & & & & & e_2^I + e_2^{II} \end{pmatrix} \quad (\text{A.1})$$

Without loss of generality we can assume  $e_0^I = 0$ ,  $e_0^{II} = 0$ . We define  $\omega_{01}^I = e_1^I$ ,  $\omega_{01}^{II} = e_1^{II}$ ,  $\Delta_{01} = \omega_{01}^{II} - \omega_{01}^I$  and  $\alpha^I = e_2^I - 2e_1^I$  and  $\alpha^{II} = e_2^{II} - 2e_1^{II}$ . The interaction

Hamiltonian is given as

$$\hat{H}_i = \begin{pmatrix} 0 & 0 & 0 & g & 0 & 0 & 0 & 0 & 0 \\ 0 & 0 & 0 & 0 & 0 & 0 & 0 & 0 & 0 \\ 0 & 0 & 0 & 0 & \sqrt{2}g & 0 & 0 & 0 & 0 \\ 0 & g & 0 & 0 & 0 & 0 & 0 & 0 & 0 \\ 0 & 0 & \sqrt{2}g & 0 & 0 & 0 & \sqrt{2}g & 0 & 0 \\ 0 & 0 & 0 & 0 & 0 & 0 & 0 & 2g & 0 \\ 0 & 0 & 0 & 0 & \sqrt{2}g & 0 & 0 & 0 & 0 \\ 0 & 0 & 0 & 0 & 0 & 2g & 0 & 0 & 0 \\ 0 & 0 & 0 & 0 & 0 & 0 & 0 & 0 & 0 \end{pmatrix} \quad (\text{A.2})$$

Going to the interaction picture with  $\hat{H}_0 = \hat{H}$  the interaction Hamiltonian  $\hat{H}_i$  becomes

$$\hat{H}_i = \begin{pmatrix} 0 & \dots & & & & & & & \\ 0 & 0 & \dots & & & & & & \\ 0 & 0 & 0 & \dots & & & & & \\ 0 & ge^{-i\Delta t} & 0 & & 0 & \dots & & & \\ 0 & 0 & \sqrt{2}ge^{-i(\Delta-\alpha^{II})t} & 0 & 0 & & \dots & & \\ 0 & 0 & 0 & 0 & 0 & 0 & \dots & & \\ 0 & 0 & 0 & 0 & \sqrt{2}ge^{-i(\Delta+\alpha^I)t} & 0 & 0 & \dots & \\ 0 & 0 & 0 & 0 & 0 & 2ge^{-i(\Delta+\alpha^I-\alpha^{II})t} & 0 & 0 & \dots \\ 0 & 0 & 0 & 0 & 0 & 0 & 0 & 0 & 0 \end{pmatrix} \quad (\text{A.3})$$

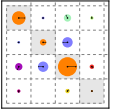
### Relaxation and Dephasing

We can model relaxation and dephasing of the three-level system using a set of 6 Lindblad operators. The relaxation operators are based on the three matrices

$$\sigma_{01}^- = \begin{pmatrix} 0 & 1 & 0 \\ 0 & 0 & 0 \\ 0 & 0 & 0 \end{pmatrix} \quad \sigma_{12}^- = \begin{pmatrix} 0 & 0 & 0 \\ 0 & 0 & 1 \\ 0 & 0 & 0 \end{pmatrix} \quad \sigma_{02}^- = \begin{pmatrix} 0 & 0 & 1 \\ 0 & 0 & 0 \\ 0 & 0 & 0 \end{pmatrix} \quad (\text{A.4})$$

and the dephasing operators on

$$\sigma_{01}^z = \begin{pmatrix} 1 & 0 & 0 \\ 0 & -1 & 0 \\ 0 & 0 & 0 \end{pmatrix} \quad \sigma_{12}^z = \begin{pmatrix} 0 & 0 & 0 \\ 0 & 1 & 0 \\ 0 & 0 & -1 \end{pmatrix} \quad \sigma_{02}^z = \begin{pmatrix} 1 & 0 & 0 \\ 0 & 0 & 0 \\ 0 & 0 & -1 \end{pmatrix} \quad (\text{A.5})$$



Using these matrices, we define a set of three relaxation operators  $L_{01}^r = \sqrt{\Gamma_{10}^r}\sigma_{01}^-$ ,  $L_{12}^r = \sqrt{\Gamma_{12}^r}\sigma_{12}^-$  and  $L_{02}^r = \sqrt{\Gamma_{02}^r}\sigma_{02}^-$  as well as a set of dephasing operators  $L_{01}^\phi = \sqrt{\Gamma_{01}^\phi/2}\sigma_{01}^z$ ,  $L_{12}^\phi = \sqrt{\Gamma_{12}^\phi/2}\sigma_{12}^z$ ,  $L_{02}^\phi = \sqrt{\Gamma_{02}^\phi/2}\sigma_{02}^z$ .

### A.2.1 Direct Integration

We can use the Hamiltonian and the Lindblad operators discussed above to directly integrate the master equation of the two-qubit system, which is given as

$$\frac{d\rho}{dt} = -\frac{i}{\hbar}[H, \rho] + \sum_j [2L_j \rho L_j^\dagger - \{L_j^\dagger L_j, \rho\}] \quad (\text{A.6})$$

Here  $-i/\hbar [H, \rho]$  corresponds to the unitary evolution of the state of the system and the part right to it to the non-unitary part, i.e. relaxation and dephasing. For numerical analysis it is usually convenient to rewrite this equation in the form

$$\frac{d\vec{\rho}}{dt} = \mathcal{L}(t)\vec{\rho}(t) \quad (\text{A.7})$$

where  $\vec{\rho}$  is a column vector containing all elements of  $\rho$  and  $\mathcal{L}$  is the so-called “superoperator” which acts on the vectorized density matrix. For a density matrix with dimension  $N \times N$ , the superoperator has dimensions  $N^2 \times N^2$ , which makes the numerical solution of eq. (A.7) computationally expensive for large  $N$ . An alternative method which avoids this inefficiency is the so-called “quantum monte carlo” method which we will discuss in the next section.

From these matrices, the corresponding two-qubit operator can be obtained as  $L_i^I = L_i \otimes \mathcal{I}$  and  $L_i^{II} = L_i \otimes \mathcal{I}$ .

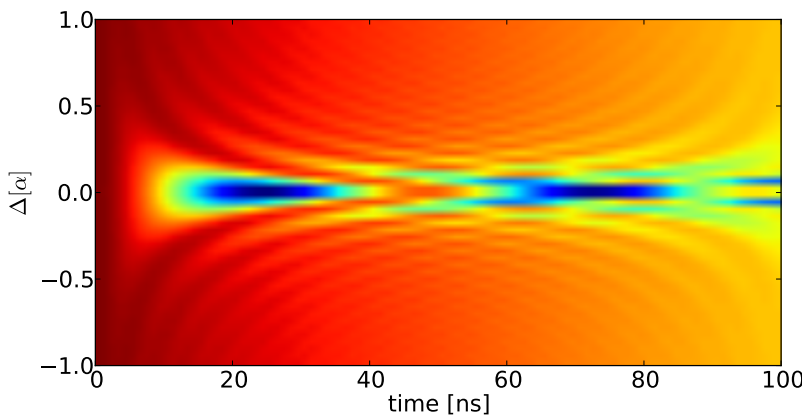


Figure A.1: ...

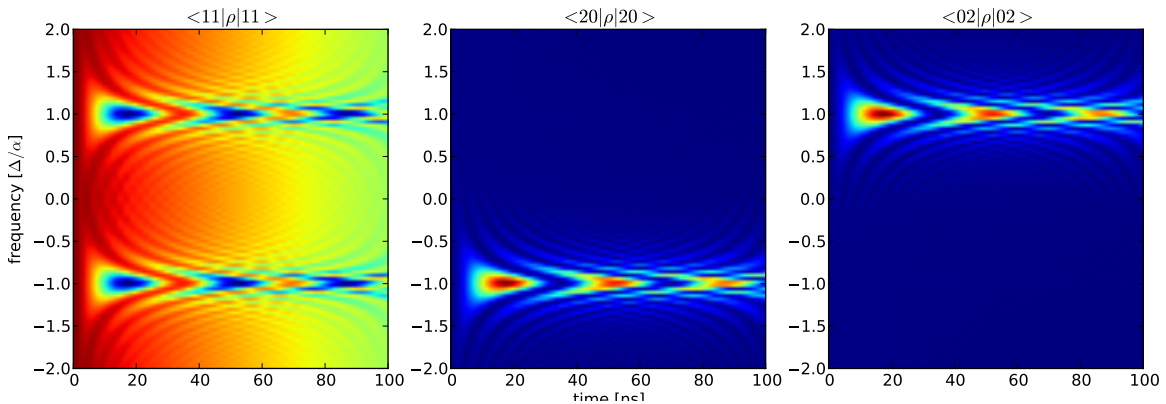


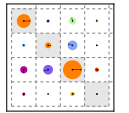
Figure A.2: ...

### A.2.2 Monte Carlo Simulation

### A.2.3 Speeding Up Simulations

```
from helpnet import *

def foo(x,y):
    print "Hello, world. This is quite a long line which
    should be wrapped I guess. The sum x + y = %g" % (x,
    y)
```



## Appendix B

# Data Acquisition & Management

### B.1 Data Acquisition Infrastructure

### B.2 Data Management Requirements

### B.3 PyView

#### B.3.1 Overview

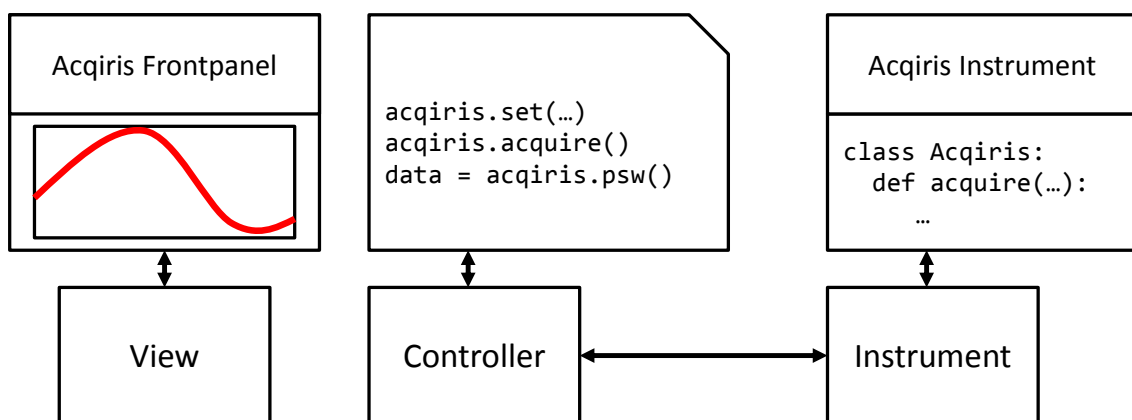


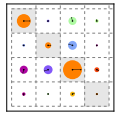
Figure B.1

**B.3.2 Instrument Management**

**B.3.3 Data Acquisition**

**B.3.4 Data Management**

**B.3.5 Data Analysis**



# Appendix C

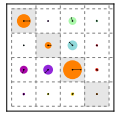
## Design & Fabrication

### C.1 Mask Design

### C.2 Optical Lithography

### C.3 Electron Beam Lithography





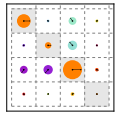
# Bibliography

- [1] J. B. Altepeter, D. Branning, E. Jeffrey, T. C. Wei, P. G. Kwiat, R. T. Thew, J. L. O'Brien, M. A. Nielsen, and A. G. White. Ancilla-assisted quantum process tomography. *Physical Review Letters*, 90(19):193601, May 2003.
- [2] M. Ansmann, H. Wang, R. C. Bialczak, M. Hofheinz, E. Lucero, M. Neeley, A. D. O'Connell, D. Sank, M. Weides, J. Wenner, A. N. Cleland, and J. M. Martinis. Violation of bell's inequality in josephson phase qubits. *Nature*, 461(7263):504–506, 2009.
- [3] A. Aspect, P. Grangier, and G. Roger. Experimental realization of einstein-podolsky-rosen-bohm gedankenexperiment: A new violation of bell's inequalities. *Physical Review Letters*, 49(2):91–94, July 1982.
- [4] A. Barenco, C. H. Bennett, R. Cleve, D. P. DiVincenzo, N. Margolus, P. Shor, T. Sleator, J. A. Smolin, and H. Weinfurter. Elementary gates for quantum computation. *Physical Review A*, 52(5):3457–3467, Nov. 1995.
- [5] R. Barends, N. Vercruyssen, A. Endo, P. J. de Visser, T. Zijlstra, T. M. Klapwijk, P. Diener, S. J. C. Yates, and J. J. A. Baselmans. Minimal resonator loss for circuit quantum electrodynamics. *Applied Physics Letters*, 97(2):023508 –023508–3, July 2010.
- [6] J. T. Barreiro, M. Müller, P. Schindler, D. Nigg, T. Monz, M. Chwalla, M. Hennrich, C. F. Roos, P. Zoller, and R. Blatt. An open-system quantum simulator with trapped ions. *Nature*, 470(7335):486–491, Feb. 2011.
- [7] C. Bauer, R. Freeman, T. Frenkiel, J. Keeler, and A. Shaka. Gaussian pulses. *Journal of Magnetic Resonance (1969)*, 58(3):442–457, July 1984.
- [8] J. Bell. On the einstein podolsky rosen paradox. *Physics*, pages 195–200, 1964.
- [9] P. Bertet, I. Chiorescu, G. Burkard, K. Semba, C. J. P. M. Harmans, D. P. DiVincenzo, and J. E. Mooij. Dephasing of a superconducting qubit induced by photon noise. *Physical Review Letters*, 95(25):257002, Dec. 2005.

## BIBLIOGRAPHY

---

- [10] P. Bertet, I. Chiorescu, C. J. P. M. Harmans, and J. E. Mooij. Dephasing of a flux-qubit coupled to a harmonic oscillator. *arXiv:cond-mat/0507290*, July 2005.
- [11] A. Blais, J. Gambetta, A. Wallraff, D. I. Schuster, S. M. Girvin, M. H. Devoret, and R. J. Schoelkopf. Quantum-information processing with circuit quantum electrodynamics. *Physical Review A*, 75(3):032329, Mar. 2007.
- [12] A. Blais, R.-S. Huang, A. Wallraff, S. M. Girvin, and R. J. Schoelkopf. Cavity quantum electrodynamics for superconducting electrical circuits: An architecture for quantum computation. *Physical Review A*, 69(6):062320, June 2004.
- [13] V. Bouchiat, D. Vion, P. Joyez, D. Esteve, and M. H. Devoret. Quantum coherence with a single cooper pair. *Physica Scripta*, T76(1):165, 1998.
- [14] H.-J. Briegel, T. Calarco, D. Jaksch, J. I. Cirac, and P. Zoller. Quantum computing with neutral atoms. *Journal of Modern Optics*, 47(2-3):415–451, 2000.
- [15] G. Burkard, R. H. Koch, and D. P. DiVincenzo. Multilevel quantum description of decoherence in superconducting qubits. *Physical Review B*, 69(6):064503, Feb. 2004.
- [16] I. Chiorescu, Y. Nakamura, C. J. P. M. Harmans, and J. E. Mooij. Coherent quantum dynamics of a superconducting flux qubit. *Science*, 299(5614):1869 –1871, Mar. 2003.
- [17] J. M. Chow, L. DiCarlo, J. M. Gambetta, F. Motzoi, L. Frunzio, S. M. Girvin, and R. J. Schoelkopf. Optimized driving of superconducting artificial atoms for improved single-qubit gates. *Physical Review A*, 82(4):040305, Oct. 2010.
- [18] J. I. Cirac and P. Zoller. Quantum computations with cold trapped ions. *Physical Review Letters*, 74(20):4091–4094, May 1995.
- [19] J. Clarke. *The SQUID Handbook: Fundamentals and Technology of SQUIDs and SQUID Systems*, volume 1. Wiley-VCH, 2005.
- [20] J. Clarke, A. N. Cleland, M. H. Devoret, D. Esteve, and J. M. Martinis. Quantum mechanics of a macroscopic variable: The phase difference of a josephson junction. *Science*, 239(4843):992–997, Feb. 1988.
- [21] J. F. Clauser, M. A. Horne, A. Shimony, and R. A. Holt. Proposed experiment to test local hidden-variable theories. *Physical Review Letters*, 23(15):880–884, Oct. 1969.

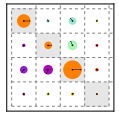


## BIBLIOGRAPHY

---

- [22] E. Collin, G. Ithier, A. Aassime, P. Joyez, D. Vion, and D. Esteve. NMR-like control of a quantum bit superconducting circuit. *Physical Review Letters*, 93(15):157005, Oct. 2004.
- [23] A. Cottet. *Implementation of a quantum bit in a superconducting circuit*. PhD thesis, Université Paris VI, Paris, 2002.
- [24] D. L. Creedon, Y. Reshitnyk, W. Farr, J. M. Martinis, T. L. Duty, and M. E. Tobar. High q-factor sapphire whispering gallery mode microwave resonator at single photon energies and millikelvin temperatures. *Applied Physics Letters*, 98(22):222903–222903–3, June 2011.
- [25] G. M. D’Ariano and P. Lo Presti. Quantum tomography for measuring experimentally the matrix elements of an arbitrary quantum operation. *Physical Review Letters*, 86(19):4195–4198, May 2001.
- [26] C. M. Dawson and M. A. Nielsen. The solovay-kitaev algorithm. *arXiv:quant-ph/0505030*, May 2005.
- [27] D. Deutsch. Quantum theory, the church-turing principle and the universal quantum computer. *Proceedings of the Royal Society of London. A. Mathematical and Physical Sciences*, 400(1818):97 –117, July 1985.
- [28] M. Devoret. Quantum fluctuations in electrical circuits. In *Les Houches Session on Quantum Fluctuations*, volume LXIII, pages 351–386. 1995.
- [29] M. H. Devoret, J. M. Martinis, and J. Clarke. Measurements of macroscopic quantum tunneling out of the zero-voltage state of a current-biased josephson junction. *Physical Review Letters*, 55(18):1908–1911, Oct. 1985.
- [30] L. DiCarlo, J. M. Chow, J. M. Gambetta, L. S. Bishop, B. R. Johnson, D. I. Schuster, J. Majer, A. Blais, L. Frunzio, S. M. Girvin, and R. J. Schoelkopf. Demonstration of two-qubit algorithms with a superconducting quantum processor. *Nature*, 460(7252):240–244, July 2009.
- [31] L. DiCarlo, M. D. Reed, L. Sun, B. R. Johnson, J. M. Chow, J. M. Gambetta, L. Frunzio, S. M. Girvin, M. H. Devoret, and R. J. Schoelkopf. Preparation and measurement of three-qubit entanglement in a superconducting circuit. *Nature*, 467(7315):574–578, 2010.
- [32] D. P. DiVincenzo. The physical implementation of quantum computation. *Fortschritte der Physik*, 48(9-11):771–783, Sept. 2000.

- [33] D. P. DiVincenzo. Fault-tolerant architectures for superconducting qubits. *Physica Scripta*, T137:014020, Dec. 2009.
- [34] W. Dür and J. I. Cirac. Nonlocal operations: Purification, storage, compression, tomography, and probabilistic implementation. *Physical Review A*, 64(1):012317, June 2001.
- [35] A. Einstein, B. Podolsky, and N. Rosen. Can quantum-mechanical description of physical reality be considered complete? *Physical Review*, 47(10):777–780, May 1935.
- [36] E. Farhi, J. Goldstone, S. Gutmann, and M. Sipser. Quantum computation by adiabatic evolution. *arXiv:quant-ph/0001106*, Jan. 2000.
- [37] A. Fedorov, L. Steffen, M. Baur, and A. Wallraff. Implementation of a toffoli gate with superconducting circuits. *arXiv:1108.3966*, Aug. 2011.
- [38] R. Feynman. Simulating physics with computers. *International Journal of Theoretical Physics*, 21(6):467–488, 1982.
- [39] M. H. Freedman, A. Kitaev, and Z. Wang. Simulation of topological field theories by quantum computers. *Communications in Mathematical Physics*, 227(3):587–603, 2002.
- [40] A. Galiautdinov, A. N. Korotkov, and J. M. Martinis. Resonator/zero-qubit architecture for superconducting qubits. *arXiv:1105.3997*, May 2011.
- [41] A. Galiautdinov, A. N. Korotkov, and J. M. Martinis. Resonator–zero-qubit architecture for superconducting qubits. *Physical Review A*, 85(4):042321, Apr. 2012.
- [42] R. Gerritsma, G. Kirchmair, F. Zähringer, E. Solano, R. Blatt, and C. F. Roos. Quantum simulation of the dirac equation. *Nature*, 463(7277):68–71, Jan. 2010.
- [43] L. K. Grover. A fast quantum mechanical algorithm for database search. In *Proceedings of the twenty-eighth annual ACM symposium on Theory of computing*, STOC ’96, page 212–219, New York, NY, USA, 1996. ACM.
- [44] L. K. Grover. Quantum mechanics helps in searching for a needle in a haystack. *Physical Review Letters*, 79(2):325–328, July 1997.
- [45] L. K. Grover. From schrödinger’s equation to the quantum search algorithm. *American Journal of Physics*, 69(7):769–777, 2001.
- [46] S. Haroche and J.-M. Raimond. *Exploring the Quantum: Atoms, Cavities and Photons*. Oxford University Press, 2006.



## BIBLIOGRAPHY

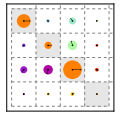
---

- [47] M. Hofheinz, H. Wang, M. Ansmann, R. C. Bialczak, E. Lucero, M. Neeley, A. D. O'Connell, D. Sank, J. Wenner, J. M. Martinis, and A. N. Cleland. Synthesizing arbitrary quantum states in a superconducting resonator. *Nature*, 459(7246):546–549, May 2009.
- [48] B. Johnson. *Controlling Photons in Superconducting Electrical Circuits*. PhD thesis, Yale University, New Haven, 2010.
- [49] J. Jones. NMR quantum computation. *Progress in Nuclear Magnetic Resonance Spectroscopy*, 38(4):325–360, June 2001.
- [50] B. Josephson. Possible new effects in superconductive tunnelling. *Physics Letters*, 1(7):251–253, July 1962.
- [51] M. Khalil, F. Wellstood, and K. Osborn. Loss dependence on geometry and applied power in superconducting coplanar resonators. *IEEE Transactions on Applied Superconductivity*, 21(3):879 –882, June 2011.
- [52] A. Kitaev. Fault-tolerant quantum computation by anyons. *Annals of Physics*, 303(1):2–30, Jan. 2003.
- [53] E. Knill, R. Laflamme, and G. J. Milburn. A scheme for efficient quantum computation with linear optics. *Nature*, 409(6816):46–52, Jan. 2001.
- [54] J. Koch, T. M. Yu, J. Gambetta, A. A. Houck, D. I. Schuster, J. Majer, A. Blais, M. H. Devoret, S. M. Girvin, and R. J. Schoelkopf. Charge-insensitive qubit design derived from the cooper pair box. *Physical Review A*, 76(4):042319, Oct. 2007.
- [55] K. Kraus, A. Böhm, J. D. Dollard, and W. H. Wootters, editors. *States, Effects, and Operations Fundamental Notions of Quantum Theory Lectures in Mathematical Physics at the University of Texas at Austin*. Lecture Notes in Physics. Springer, 1983. DOI: 10.1007/3-540-12732-1.
- [56] G. d. Lange, Z. H. Wang, D. Ristè, V. V. Dobrovitski, and R. Hanson. Universal dynamical decoupling of a single solid-state spin from a spin bath. *Science*, 330(6000):60–63, Jan. 2010.
- [57] B. P. Lanyon, C. Hempel, D. Nigg, M. Müller, R. Gerritsma, F. Zähringer, P. Schindler, J. T. Barreiro, M. Rambach, G. Kirchmair, M. Hennrich, P. Zoller, R. Blatt, and C. F. Roos. Universal digital quantum simulation with trapped ions. *Science*, 334(6052):57–61, July 2011.

## BIBLIOGRAPHY

---

- [58] M. T. Levinsen, R. Y. Chiao, M. J. Feldman, and B. A. Tucker. An inverse ac josephson effect voltage standard. *Applied Physics Letters*, 31(11):776 –778, Dec. 1977.
- [59] S. Lloyd. Universal quantum simulators. *Science*, 273(5278):1073–1078, Aug. 1996.
- [60] D. Loss and D. P. DiVincenzo. Quantum computation with quantum dots. *Physical Review A*, 57(1):120–126, Jan. 1998.
- [61] E. Lucero, J. Kelly, R. C. Bialczak, M. Lenander, M. Mariantoni, M. Neeley, A. D. O’Connell, D. Sank, H. Wang, M. Weides, J. Wenner, T. Yamamoto, A. N. Cleland, and J. M. Martinis. Reduced phase error through optimized control of a superconducting qubit. *Physical Review A*, 82(4):042339, Oct. 2010.
- [62] H. Mabuchi and A. C. Doherty. Cavity quantum electrodynamics: Coherence in context. *Science*, 298(5597):1372–1377, Nov. 2002.
- [63] F. Mallet, F. R. Ong, A. Palacios-Laloy, F. Nguyen, P. Bertet, D. Vion, and D. Esteve. Single-shot qubit readout in circuit quantum electrodynamics. *Nat Phys*, 5(11):791–795, Nov. 2009.
- [64] M. Mariantoni, H. Wang, T. Yamamoto, M. Neeley, R. C. Bialczak, Y. Chen, M. Lenander, E. Lucero, A. D. O’Connell, D. Sank, M. Weides, J. Wenner, Y. Yin, J. Zhao, A. N. Korotkov, A. N. Cleland, and J. M. Martinis. Implementing the quantum von neumann architecture with superconducting circuits. *Science*, 334(6052):61 –65, Oct. 2011.
- [65] J. M. Martinis, K. B. Cooper, R. McDermott, M. Steffen, M. Ansmann, K. D. Osborn, K. Cicak, S. Oh, D. P. Pappas, R. W. Simmonds, and C. C. Yu. Decoherence in josephson qubits from dielectric loss. *Physical Review Letters*, 95(21):210503, Nov. 2005.
- [66] J. M. Martinis, M. H. Devoret, and J. Clarke. Energy-level quantization in the zero-voltage state of a current-biased josephson junction. *Physical Review Letters*, 55(15):1543–1546, Oct. 1985.
- [67] J. M. Martinis, M. H. Devoret, and J. Clarke. Experimental tests for the quantum behavior of a macroscopic degree of freedom: The phase difference across a josephson junction. *Physical Review B*, 35(10):4682–4698, Apr. 1987.
- [68] J. M. Martinis, S. Nam, J. Aumentado, and C. Urbina. Rabi oscillations in a large josephson-junction qubit. *Physical Review Letters*, 89(11):117901, 2002.

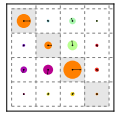


## BIBLIOGRAPHY

---

- [69] A. Megrant, C. Neill, R. Barends, B. Chiaro, Y. Chen, L. Feigl, J. Kelly, E. Lucero, M. Mariantoni, P. J. J. O’Malley, D. Sank, A. Vainsencher, J. Wenner, T. C. White, Y. Yin, J. Zhao, C. J. Palmstrøm, J. M. Martinis, and A. N. Cleland. Planar superconducting resonators with internal quality factors above one million. *Applied Physics Letters*, 100(11):113510–113510–4, Mar. 2012.
- [70] C. Monroe, D. M. Meekhof, B. E. King, W. M. Itano, and D. J. Wineland. Demonstration of a fundamental quantum logic gate. *Physical Review Letters*, 75(25):4714–4717, Dec. 1995.
- [71] J. E. Mooij, T. P. Orlando, L. Levitov, L. Tian, C. H. van der Wal, and S. Lloyd. Josephson persistent-current qubit. *Science*, 285(5430):1036 –1039, 1999.
- [72] F. Motzoi, J. M. Gambetta, P. Rebentrost, and F. K. Wilhelm. Simple pulses for elimination of leakage in weakly nonlinear qubits. *Physical Review Letters*, 103(11):110501, 2009.
- [73] Y. Nakamura, Y. A. Pashkin, and J. S. Tsai. Coherent control of macroscopic quantum states in a single-cooper-pair box. *Nature*, 398(6730):786–788, Apr. 1999.
- [74] F. Nguyen. *Cooper Pair Box Circuits: Two-Qubit Gate, Single-Shot Readout, and Current to Frequency Conversion*. PhD thesis, Université Paris VI, Saclay, 2008.
- [75] M. A. Nielsen and I. L. Chuang. *Quantum Computation and Quantum Information*. Cambridge University Press, 2000.
- [76] S. Osnaghi, P. Bertet, A. Auffeves, P. Maioli, M. Brune, J. M. Raimond, and S. Haroche. Coherent control of an atomic collision in a cavity. *Physical Review Letters*, 87(3):037902, June 2001.
- [77] L. Ozyuzer, A. E. Koshelev, C. Kurter, N. Gopalsami, Q. Li, M. Tachiki, K. Kadouki, T. Yamamoto, H. Minami, H. Yamaguchi, T. Tachiki, K. E. Gray, W.-K. Kwok, and U. Welp. Emission of coherent THz radiation from superconductors. *Science*, 318(5854):1291–1293, Nov. 2007.
- [78] H. Paik, D. I. Schuster, L. S. Bishop, G. Kirchmair, G. Catelani, A. P. Sears, B. R. Johnson, M. J. Reagor, L. Frunzio, L. I. Glazman, S. M. Girvin, M. H. Devoret, and R. J. Schoelkopf. Observation of high coherence in josephson junction qubits measured in a three-dimensional circuit QED architecture. *Physical Review Letters*, 107(24):240501, Dec. 2011.

- [79] A. Palacios-Laloy. *Superconducting Qubit in a Resonator: Test of the Leggett-Garg Inequality and Single-Shot Readout*. PhD thesis, Commissariat à l'Energie Atomique, Saclay, 2010.
- [80] J. F. Poyatos, J. I. Cirac, and P. Zoller. Complete characterization of a quantum process: The two-bit quantum gate. *Physical Review Letters*, 78(2):390–393, Jan. 1997.
- [81] D. M. Pozar. *Microwave Engineering*. Wiley, 4 edition, Nov. 2011.
- [82] E. Purcell. Spontaneous emission probabilities at radio frequencies. In *Physical Review*, volume 69, page 681, 1946.
- [83] R. Raussendorf and H. J. Briegel. A one-way quantum computer. *Physical Review Letters*, 86(22):5188–5191, May 2001.
- [84] M. D. Reed, L. DiCarlo, S. E. Nigg, L. Sun, L. Frunzio, S. M. Girvin, and R. J. Schoelkopf. Realization of three-qubit quantum error correction with superconducting circuits. *arXiv:1109.4948*, Sept. 2011.
- [85] C. Rigetti, S. Poletto, J. M. Gambetta, B. L. T. Plourde, J. M. Chow, A. D. Corcoles, J. A. Smolin, S. T. Merkel, J. R. Rozen, G. A. Keefe, M. B. Rothwell, M. B. Ketchen, and M. Steffen. Superconducting qubit in waveguide cavity with coherence time approaching 0.1ms. *arXiv:1202.5533*, Feb. 2012.
- [86] D. I. Schuster. *Circuit Quantum Electrodynamics*. PhD thesis, Yale University, New Haven, 2007.
- [87] N. Shenvi, J. Kempe, and K. B. Whaley. Quantum random-walk search algorithm. *Physical Review A*, 67(5):052307, May 2003.
- [88] P. Shor. Algorithms for quantum computation: discrete logarithms and factoring. In *Foundations of Computer Science, 1994 Proceedings., 35th Annual Symposium on*, pages 124 –134, Nov. 1994.
- [89] P. W. Shor. Polynomial-time algorithms for prime factorization and discrete logarithms on a quantum computer. *arXiv:quant-ph/9508027*, Aug. 1995. SIAM J.Sci.Statist.Comput. 26 (1997) 1484.
- [90] I. Siddiqi, R. Vijay, M. Metcalfe, E. Boaknin, L. Frunzio, R. J. Schoelkopf, and M. H. Devoret. Dispersive measurements of superconducting qubit coherence with a fast latching readout. *Physical Review B*, 73(5):054510, Feb. 2006.



- [91] I. Siddiqi, R. Vijay, F. Pierre, C. M. Wilson, M. Metcalfe, C. Rigetti, L. Frunzio, and M. H. Devoret. RF-Driven josephson bifurcation amplifier for quantum measurement. *Physical Review Letters*, 93(20):207002, Nov. 2004.
- [92] R. W. Simmonds, K. M. Lang, D. A. Hite, S. Nam, D. P. Pappas, and J. M. Martinis. Decoherence in josephson phase qubits from junction resonators. *Physical Review Letters*, 93(7):077003, Aug. 2004.
- [93] J. Simon, W. S. Bakr, R. Ma, M. E. Tai, P. M. Preiss, and M. Greiner. Quantum simulation of antiferromagnetic spin chains in an optical lattice. *Nature*, 472(7343):307–312, Apr. 2011.
- [94] S. J. Srinivasan, A. J. Hoffman, J. M. Gambetta, and A. A. Houck. Tunable coupling in circuit quantum electrodynamics using a superconducting charge qubit with a v-shaped energy level diagram. *Physical Review Letters*, 106(8):083601, Feb. 2011.
- [95] D. J. Van Harlingen, T. L. Robertson, B. L. T. Plourde, P. A. Reichardt, T. A. Crane, and J. Clarke. Decoherence in josephson-junction qubits due to critical-current fluctuations. *Physical Review B*, 70(6):064517, Aug. 2004.
- [96] L. M. K. Vandersypen, M. Steffen, G. Breyta, C. S. Yannoni, M. H. Sherwood, and I. L. Chuang. Experimental realization of shor’s quantum factoring algorithm using nuclear magnetic resonance. *Nature*, 414(6866):883–887, Dec. 2001.
- [97] R. Vijay, M. H. Devoret, and I. Siddiqi. Invited review article: The josephson bifurcation amplifier. *Review of Scientific Instruments*, 80(11):111101–111101–17, Nov. 2009.
- [98] R. Vijay, C. Macklin, D. H. Slichter, S. J. Weber, K. W. Murch, R. Naik, A. N. Korotkov, and I. Siddiqi. Quantum feedback control of a superconducting qubit: Persistent rabi oscillations. *arXiv:1205.5591*, May 2012.
- [99] D. Vion, A. Aassime, A. Cottet, P. Joyez, H. Pothier, C. Urbina, D. Esteve, and M. H. Devoret. Manipulating the quantum state of an electrical circuit. *Science*, 296(5569):886 –889, May 2002.
- [100] A. Wallraff, D. I. Schuster, A. Blais, L. Frunzio, R.-S. Huang, J. Majer, S. Kumar, S. M. Girvin, and R. J. Schoelkopf. Strong coupling of a single photon to a superconducting qubit using circuit quantum electrodynamics. *Nature*, 431(7005):162–167, 2004.
- [101] H. Walther, B. T. H. Varcoe, B.-G. Englert, and T. Becker. Cavity quantum electrodynamics. *Reports on Progress in Physics*, 69(5):1325–1382, May 2006.

## BIBLIOGRAPHY

---

- [102] H. Wang, M. Hofheinz, J. Wenner, M. Ansmann, R. C. Bialczak, M. Lenander, E. Lucero, M. Neeley, A. D. OConnell, D. Sank, M. Weides, A. N. Cleland, and J. M. Martinis. Improving the coherence time of superconducting coplanar resonators. *Applied Physics Letters*, 95(23):233508 –233508–3, Dec. 2009.
- [103] T. Yamamoto, M. Neeley, E. Lucero, R. C. Bialczak, J. Kelly, M. Lenander, M. Mariantoni, A. D. O’Connell, D. Sank, H. Wang, M. Weides, J. Wenner, Y. Yin, A. N. Cleland, and J. M. Martinis. Quantum process tomography of two-qubit controlled-z and controlled-NOT gates using superconducting phase qubits. *Physical Review B*, 82(18):184515, Nov. 2010.
- [104] B. Yurke and J. S. Denker. Quantum network theory. *Physical Review A*, 29(3):1419–1437, Mar. 1984.
- [105] S.-B. Zheng. One-step synthesis of multiatom greenberger-horne-zeilinger states. *Physical Review Letters*, 87(23):230404, Nov. 2001.
- [106] S.-B. Zheng and G.-C. Guo. Efficient scheme for two-atom entanglement and quantum information processing in cavity QED. *Physical Review Letters*, 85(11):2392–2395, Sept. 2000.

## Characterization of a Two-Transmon Processor with Individual Single-Shot Qubit Readout

A. Dewes,<sup>1</sup> F. R. Ong,<sup>1</sup> V. Schmitt,<sup>1</sup> R. Lauro,<sup>1</sup> N. Boulant,<sup>2</sup> P. Bertet,<sup>1</sup> D. Vion,<sup>1</sup> and D. Esteve<sup>1</sup>

<sup>1</sup>*Quantronics group, Service de Physique de l'État Condensé (CNRS URA 2464), IRAMIS, DSM, CEA-Saclay, 91191 Gif-sur-Yvette, France*

<sup>2</sup>*LRMN, Neurospin, I2BM, DSV, 91191CEA-Saclay, 91191 Gif-sur-Yvette, France*

(Received 26 September 2011; published 2 February 2012)

We report the characterization of a two-qubit processor implemented with two capacitively coupled tunable superconducting qubits of the transmon type, each qubit having its own nondestructive single-shot readout. The fixed capacitive coupling yields the  $\sqrt{iSWAP}$  two-qubit gate for a suitable interaction time. We reconstruct by state tomography the coherent dynamics of the two-bit register as a function of the interaction time, observe a violation of the Bell inequality by 22 standard deviations after correcting readout errors, and measure by quantum process tomography a gate fidelity of 90%.

DOI: [10.1103/PhysRevLett.108.057002](https://doi.org/10.1103/PhysRevLett.108.057002)

PACS numbers: 85.25.Cp, 03.67.Lx, 74.78.Na

Quantum-information processing is one of the most appealing ideas for exploiting the resources of quantum physics and performing tasks beyond the reach of classical machines [1]. Ideally, a quantum processor consists of an ensemble of highly coherent two-level systems, the qubits, that can be efficiently reset, that can follow any unitary evolution needed by an algorithm using a universal set of single- and two-qubit gates, and that can be readout projectively. In the domain of electrical quantum circuits [2], important progress [3–7] has been achieved recently with the operation of elementary quantum processors based on different superconducting qubits. Those based on transmon qubits [3,4,8,9] are well protected against decoherence but embed all the qubits in a single resonator used both for coupling them and for joint readout. Consequently, individual readout of the qubits is not possible and the results of a calculation, as the Grover search algorithm demonstrated on two qubits [3], cannot be obtained by running the algorithm only once. Furthermore, the overhead for getting a result from such a processor without single-shot readout but with a larger number of qubits overcomes the speed-up gain expected for any useful algorithm. The situation is different for processors based on phase qubits [5,6,10], where the qubits are more sensitive to decoherence but can be read individually with high fidelity, although destructively. This significant departure from the wished scheme can be circumvented, when needed, since a destructive readout can be transformed into a nondestructive one at the cost of adding one ancilla qubit and one extra two-qubit gate for each qubit to be read projectively. Moreover, energy release during a destructive readout can result in a sizable cross talk between the readout outcomes, which can also be solved at the expense of a more complex architecture [10,11].

In this work, we operate a new architecture that comes closer to the ideal quantum processor design than the above-mentioned ones. Our circuit is based on frequency tunable transmons that are capacitively coupled. Although

the coupling is fixed, the interaction is effective only when the qubits are on resonance, which yields the  $\sqrt{iSWAP}$  universal gate for an adequate coupling duration. Each qubit is equipped with its own nondestructive single-shot readout [12,13] and the two qubits can be read with low cross talk. In order to characterize the circuit operation, we reconstruct the time evolution of the two-qubit register density matrix during the resonant and coherent exchange of a single quantum of excitation between the qubits by quantum state tomography. Then, we prepare a Bell state with concurrence 0.85, measure the Clauser-Horne-Shimony-Holt (CHSH) entanglement witness, and find a violation of the corresponding Bell inequality by 22 standard deviations. We then characterize the  $\sqrt{iSWAP}$  universal gate operation by determining its process map with quantum process tomography [1]. We find a gate fidelity of 90% due to qubit decoherence and systematic unitary errors.

The circuit implemented is schematized in Fig. 1(a): the coupled qubits with their respective control and readout subcircuits are fabricated on a Si chip [see Supplemental Material (SM), Sec. I [14]]. The chip is cooled down to 20 mK in a dilution refrigerator and connected to room-temperature sources and measurement devices by attenuated and filtered control lines and by two measurement lines equipped with cryogenic amplifiers. Each transmon  $j = \text{I}, \text{II}$  is a capacitively shunted SQUID characterized by its Coulomb energy  $E_C^j$  for a Cooper pair, the asymmetry  $d_j$  between its two Josephson junctions, and its total effective Josephson energy  $E_J^j(\phi_j) = E_J^j |\cos(x_j)| \sqrt{1 + d_j^2 \tan^2(x_j)}$ , with  $x_j = \pi\phi_j/\phi_0$ ,  $\phi_0$  the flux quantum, and  $\phi_j$  the magnetic flux through the SQUIDs induced by two local current lines with a 0.5 GHz bandwidth. The transition frequencies  $\nu_j \approx \sqrt{2E_C^j E_J^j}/h$  between the two lowest energy states  $|0\rangle_j$  and  $|1\rangle_j$  can thus be tuned by  $\phi_j$ . The qubits are coupled by a capacitor with nominal value  $C_c \approx 0.13$  fF and form a register with the Hamiltonian (see Sec. II of the SM [14])

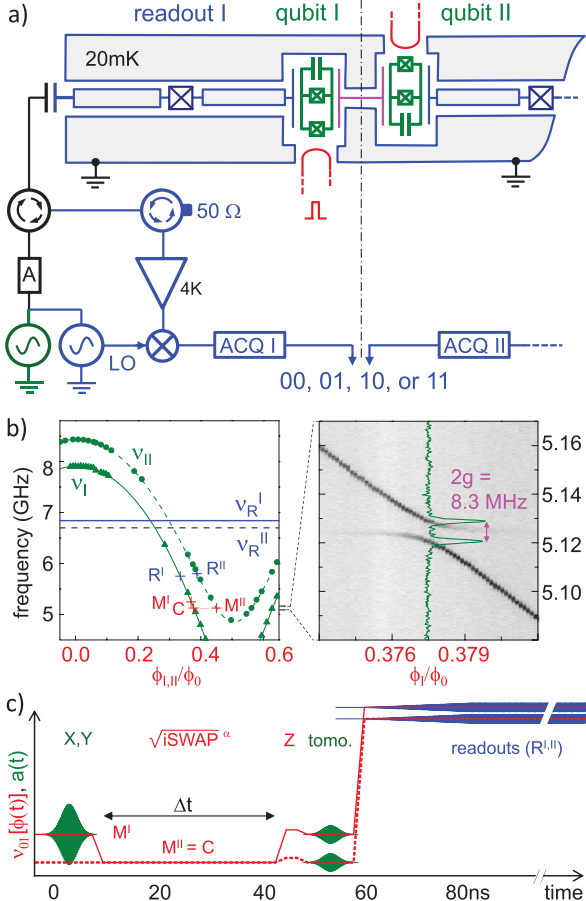


FIG. 1 (color). (a) Circuit schematics of the experiment showing the qubits I and II in green, their readout devices in grayed blue, and the homodyne detection circuits with their digitizer (ACQ) in blue. (b) Left-hand panel: Spectroscopy of the sample showing the resonator frequencies  $\nu_R^I = 6.84$  GHz and  $\nu_R^{II} = 6.70$  GHz (horizontal lines), and the measured (disks, triangles) and fitted (lines) qubit frequencies  $\nu_{I,II}$  as a function of their flux bias  $\phi_{I,II}$  when the other qubit is far detuned. Right-hand panel: Spectroscopic anticrossing of the two qubits revealed by the 2D plot of  $p_{01} + p_{10}$  as a function of the probe frequency and of  $\phi_1$ , at  $\nu_{II} = 5.124$  GHz. (c) Typical pulse sequence including  $X$  or  $Y$  rotations, a  $\sqrt{iSWAP}^\alpha$  gate,  $Z$  rotations, and tomographic and readout pulses. Microwave pulses  $a(t)$  for qubit (green) and for readout (blue) are drawn on top of the  $\nu_{I,II}(\phi)$  dc pulses (red lines).

$H = h(-\nu_I \sigma_z^I - \nu_{II} \sigma_z^{II} + 2g \sigma_y^I \sigma_y^{II})/2$ . Here  $h$  is the Planck constant,  $\sigma_{x,y,z}$  are the Pauli operators,  $2g = \sqrt{E_C^I E_C^{II} \nu_{II}}/E_{C_c} \ll \nu_{I,II}$  is the coupling frequency, and  $E_{C_c}$  the Coulomb energy of a Cooper pair on the coupling capacitor. The two-qubit gate is defined in the uncoupled basis  $\{|uv\rangle\} \equiv \{|0\rangle_I, |1\rangle_I\} \otimes \{|0\rangle_{II}, |1\rangle_{II}\}$ , at a working point  $M_{I,II}$  where the qubits are sufficiently detuned ( $\nu_{II} - \nu_I \gg 2g$ ) to be negligibly coupled. Bringing them on resonance at a frequency  $\nu$  in a time much shorter than  $1/2g$  but much

longer than  $1/\nu$ , and keeping them on resonance during a time  $\Delta t$ , one implements an operation  $\Theta_I \Theta_{II} \sqrt{iSWAP}^{(8g\Delta t)}$ , which is the product of the

$$\sqrt{iSWAP} = \begin{pmatrix} 1 & 0 & 0 & 0 \\ 0 & 1/\sqrt{2} & -i/\sqrt{2} & 0 \\ 0 & -i/\sqrt{2} & 1/\sqrt{2} & 0 \\ 0 & 0 & 0 & 1 \end{pmatrix}$$

gate to an adjustable power and of two single qubit phase gates  $\Theta_j = \exp(i\theta_j \sigma_z^j/2)$  accounting for the dynamical phases  $\theta_j = \int 2\pi(\nu - \nu_j)dt$  accumulated during the coupling. The exact  $\sqrt{iSWAP}$  gate can thus be obtained by choosing  $\Delta t = 1/8g$  and by applying a compensation rotation  $\Theta_j^{-1}$  to each qubit afterward.

For readout, each qubit is capacitively coupled to its own  $\lambda/2$  coplanar waveguide resonator with frequency  $\nu_R^j$  and quality factor  $Q_j \approx 700$ . The frequency  $\nu_R^j$  is shifted by  $\pm\chi$  depending on the measured qubit state, with  $\chi \approx g_0^2/(\nu_R^j - \nu_j)$  and  $g_0$  the qubit-resonator coupling frequency. Each resonator is made nonlinear with a Josephson junction and is operated as a Josephson bifurcation amplifier, as explained in detail in [13]: ideally, it switches from a low to a high amplitude oscillating state when qubit state  $|1\rangle$  is measured. Consequently, the homodyne measurement [see Fig. 1(a)] of two microwave pulses simultaneously applied to and reflected from the two resonators yields a two-bit outcome  $uv$  that maps with a high fidelity the state  $|uv\rangle$  on which the register is projected; the probabilities  $p_{uv}$  of the four possible outcomes are determined by repeating the same experimental sequence a few  $10^4$  times. Single qubit rotations  $u(\theta)$  by an angle  $\theta$  around an axis  $\vec{u}$  of the XY plane of the Bloch sphere are obtained by applying Gaussian microwave pulses directly through the readout resonators, with frequencies  $\nu_j$ , phases  $\varphi_j = (\vec{X}, \vec{u})$ , and calibrated areas  $A_j \propto \theta$ ; a sufficiently high power is used to compensate for the filtering effect of each resonator, which depends on the detuning  $\nu_j - \nu_R^j$ . Rotations around Z are obtained by changing temporarily  $\nu_{I,II}$  with dc pulses on the current lines.

The sample is first characterized by spectroscopy [see Fig. 1(b)], and a fit of the transmon model to the data yields the sample parameters (see Sec. III of the SM [14]). The working points where the qubits are manipulated ( $M^{I,II}$ ), resonantly coupled ( $C$ ), and readout ( $R^{I,II}$ ) are chosen to yield sufficiently long relaxation times  $\sim 0.5 \mu\text{s}$  [15] during gates, negligible residual coupling during single qubit rotations and readout, and best possible fidelities at readout. Figure 1(b) shows these points as well as the spectroscopic anticrossing of the two qubits at point C, where  $2g = 8.3$  MHz in agreement with the design value of  $C_c$ . Then, readout errors are characterized at  $R^{I,II}$  (see Sec. IV of the SM [14]): In a first approximation, the errors are independent for the two readouts and are of about 10% and 20% when reading  $|0\rangle$  and  $|1\rangle$ , respectively. This limited

fidelity results for a large part from energy relaxation of the qubits at readout. In addition, we observe a small readout cross talk, i.e., a variation of up to 2% in the probability of an outcome of readout  $j$  depending on the state of the other qubit. All these effects are calibrated by measuring the four  $p_{uv}$  probabilities for each of the four  $|uv\rangle$  states, which allows us to calculate a  $4 \times 4$  readout matrix  $\mathcal{R}$  linking the  $p_{uv}$ 's to the  $|uv\rangle$  populations.

Repeating the pulse sequence shown in Fig. 1(c) at  $M^I = 5.247$  GHz,  $M^{II} = C = 5.125$  GHz,  $R^I = 5.80$  GHz,  $R^{II} = 5.75$  GHz, and applying the readout corrections  $\mathcal{R}$ , we observe the coherent exchange of a single excitation initially stored in qubit  $I$ . We show in Fig. 2 the time evolution of the measured  $|uv\rangle$  populations, in fair agreement with a prediction obtained by integration of a

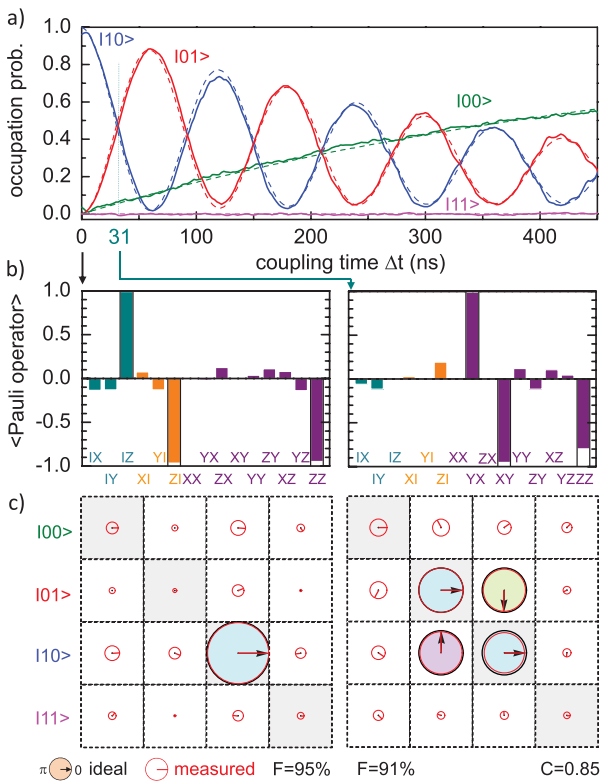


FIG. 2 (color). Coherent swapping of a single excitation between the qubits. (a) Experimental (solid lines) and fitted (dashed lines) occupation probabilities of the four computational states  $|00\rangle \dots |11\rangle$  as a function of the coupling duration. No Z or tomographic pulses are applied here. (b),(c) State tomography of the initial state (left) and of the state produced by the  $\sqrt{iSWAP}$  gate (right). (b) Ideal (empty bars) and experimental (color filling) expected values of the 15 Pauli operators  $IX, \dots, ZZ$ . (c) Corresponding ideal (color-filled black circles with black arrow) and experimental (red circle and arrow) density matrices, as well as fidelity  $F$  and concurrence  $C$ . Each complex matrix element is represented by a circle with an area proportional to its modulus (diameter equals cell size for unit modulus) and by an arrow giving its argument. See Sec. VI of the SM [14] for a real and imaginary part representation of the matrices.

simple time independent Liouville master equation of the system, involving the independently measured relaxation times  $T_1^I = 0.44 \mu\text{s}$  and  $T_1^{II} = 0.52 \mu\text{s}$ , and two independent effective pure dephasing times  $T_\varphi^I = T_\varphi^{II} = 2.0 \mu\text{s}$  as fitting parameters. Tomographic reconstruction of the register density matrix  $\rho$  is obtained by measuring the expectation values of the 15 two-qubit Pauli operators  $\{P_k\} = \{I, X, Y, Z\}_I \otimes \{I, X, Y, Z\}_{II} - \{II\}$ , the  $X_j$  and  $Y_j$  measurements being obtained using tomographic pulses  $\vec{Y}_j$  ( $-90^\circ$ ) or  $\vec{X}_j$  ( $90^\circ$ ) just before readout. The  $\rho$  matrix is calculated from the Pauli set by global minimization of the Hilbert-Schmidt distance between the possibly non-physical  $\rho$  and all physical (i.e., positive-semidefinite)  $\rho$ 's. This can be done at regular intervals of the coupling time to produce a movie of  $\rho(\Delta t)$  (see the Supplemental Material [14]) showing the swapping of the  $|10\rangle$  and  $|01\rangle$  populations at frequency  $2g$ , the corresponding oscillation of the coherences, as well as the relaxation towards  $|00\rangle$ . Figure 2 shows  $\langle\langle P_k \rangle\rangle$  and  $\rho$  only at  $\Delta t = 0$  ns and after a  $\sqrt{iSWAP}$  obtained at  $\Delta t = 31$  ns with  $\Theta_j^{-1}$  rotations of  $\theta_I \simeq -65^\circ$  and  $\theta_{II} \simeq +60^\circ$ . The fidelity  $F = \langle\psi_{id}|\rho|\psi_{id}\rangle$  of  $\rho$  with the ideal density matrices  $|\psi_{id}\rangle\langle\psi_{id}|$  is 95% and 91%, respectively, and is limited by errors on the preparation pulse, statistical noise, and relaxation.

To quantify in a different way our ability to entangle the two qubits, we prepare a Bell state  $|10\rangle + e^{i\psi}|01\rangle$  (with  $\psi = \theta_{II} - \theta_I$ ) using the pulse sequence of Fig. 1(c) with  $\Delta t = 31$  ns and no  $\Theta_j^{-1}$  rotations, and measure the CHSH

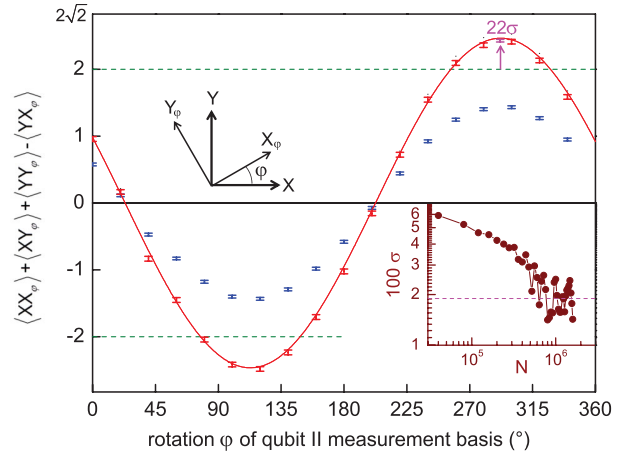


FIG. 3 (color). Test of the CHSH-Bell inequality on a  $|10\rangle + e^{i\psi}|01\rangle$  state by measuring the qubits along  $X^I$  or  $Y^I$  and  $X_\varphi^{II}$  or  $Y_\varphi^{II}$  (see top-left inset), respectively. Blue (red) error bars are the experimental CHSH entanglement witness determined from the raw (readout-error corrected) measurements as a function of the angle  $\varphi$  between the measuring basis, whereas solid line is a fit using  $\psi$  as the only fitting parameter. Height of error bars is  $\pm 1$  standard deviation  $\sigma(N)$  (see bottom-right inset), with  $N$  the number of sequences per point. Note that averaging beyond  $N = 10^6$  does not improve the violation because of a slow drift of  $\varphi$ .

entanglement witness  $\langle XX_\varphi \rangle + \langle XY_\varphi \rangle + \langle YY_\varphi \rangle - \langle YX_\varphi \rangle$  as a function of the angle  $\varphi$  between the orthogonal measurement bases of qubits I and II. Figure 3 compares the results obtained with and without correcting the readout errors with what is theoretically expected from the decoherence parameters indicated previously: unlike in [11] and because of a readout contrast limited to 70%–75%, the witness does not exceed the classical bound of 2 without correcting the readout errors. After correction, it reaches 2.43, in good agreement with the theoretical prediction (see also [16]), and exceeds the classical bound by up to 22 standard deviations when averaged over  $10^6$  sequences.

In a last experiment, we characterize the imperfections of our  $\sqrt{iSWAP}$  gate by quantum process tomography [1]. We build a completely positive map  $\rho_{\text{out}} = \mathcal{E}(\rho_{\text{in}}) = \sum_{m,n} \chi_{mn} P'_m \rho_{\text{in}} P'_n^\dagger$  characterized by a  $16 \times 16$  matrix  $\chi$  expressed here in the modified Pauli operator basis  $\{P'_k\} = \{I, X, Y' = iY, Z\}^{\otimes 2}$ , for which all matrices are real. For that purpose, we apply the gate (using pulse sequences similar to that of Fig. 1(c), with  $\Delta t = 31$  ns and  $\Theta_j^{-1}$  rotations) to the 16 input states  $\{|0\rangle, |1\rangle, |0\rangle + |1\rangle, |0\rangle + i|1\rangle\}^{\otimes 2}$  and characterize both the input and output states by quantum state tomography. By operating as described previously, we would obtain apparent input and output density matrices including errors made in the state tomography itself, which we do not want to include in the gate map. Instead, we fit the 16 experimental input Pauli sets by a model (see Sec. V of the SM [14]) including amplitude and phase errors for the  $X$  and  $Y$  preparation and tomographic pulses, in order to determine which operator set  $\{P'_k\}$  is actually measured. The input and output matrices  $\rho_{\text{in,out}}$  corrected from the tomographic errors only are calculated by inverting the linear relation  $\langle P'_k \rangle = \text{Tr}(\rho P'_k)$  and by applying it to the experimental Pauli sets. We then calculate from the  $\{\rho_{\text{in,out}}\}$  set an Hermitian  $\chi$  matrix that is not necessarily physical due to statistical errors, and which we render physical by taking the nearest Hermitian positive matrix. This final  $\chi$  matrix is shown and compared to the ideal matrix  $\chi_{\text{id}}$  in Fig. 4, which yields a gate fidelity  $F_g = \text{Tr}(\chi \chi_{\text{id}}) = 0.9$  [17] for a single run of the gate. To better understand the imperfections, we also show the map  $\tilde{\chi}$  of the actual process preceded by the inverse ideal process [18]. The first diagonal element of  $\tilde{\chi}$  is equal to  $F_g$  by construction. Then, main visible errors arise from unitary operations and reduce fidelity by 1%–2% (a fit yields a too long coupling time inducing a  $95^\circ$  swap instead of  $90^\circ$  and  $\theta_{\text{I,II}}$  rotations too small by  $3.5^\circ$  and  $7^\circ$ , respectively). On the other hand the known relaxation and dephasing times reduce fidelity by 8% but is barely visible in  $\tilde{\chi}$  due to a spread over many matrix elements with modulus of the order of or below the 1%–2% noise level.

In conclusion, we have demonstrated a high fidelity  $\sqrt{iSWAP}$  gate in a two Josephson qubit circuit with individual nondestructive single-shot readouts, observed a

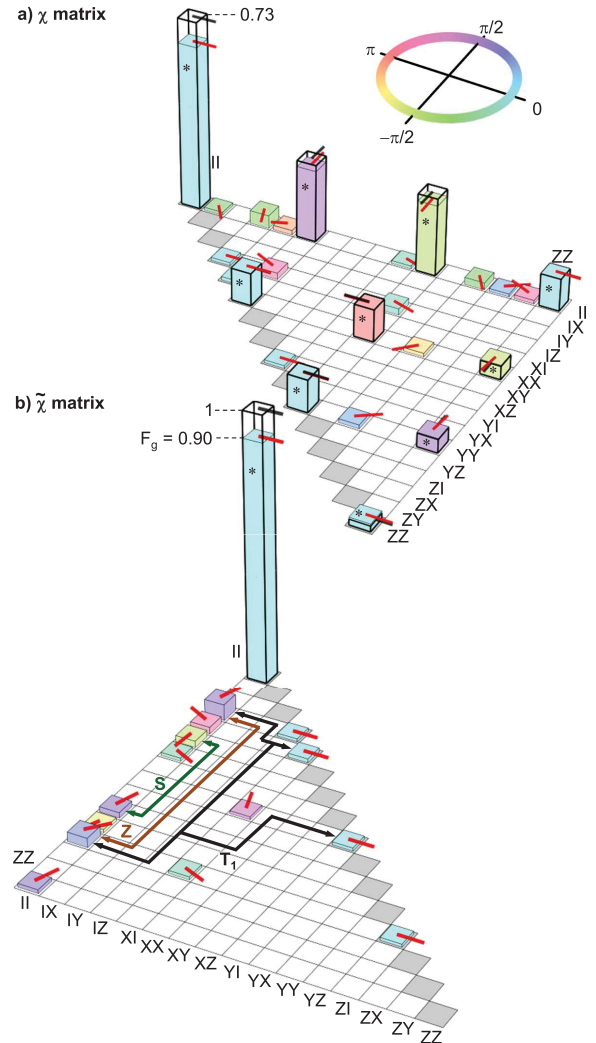


FIG. 4 (color). Map of the implemented  $\sqrt{iSWAP}$  gate yielding a fidelity  $F_g = 90\%$ . Superposition of the ideal (empty thick bars) and experimental (color-filled bars) upper part of the Hermitian process matrix  $\chi$  (a) and lower part of the Hermitian error matrix  $\tilde{\chi}$  (b), in the two-qubit Pauli operators basis  $\{II, \dots, ZZ\}$ . Expected elements are marked with a star, and elements below 1% are not shown. Each complex matrix element is represented by a bar with height proportional to its modulus and by an arrow at the top of the bar (as well as a filling color for the experiment—see top inset) giving its argument. See also Sec. VI of the SM [14] for a real and imaginary part representation of these matrices and for additional information. Labeled arrows indicate the main visible contributions to errors, i.e., a too long swapping time (S), too small rotations  $\theta_{\text{I,II}}$  (Z), and relaxation ( $T_1$ )—see text.

violation of the CHSH-Bell inequality, and followed the register's dynamics by tomography. Although quantum coherence and readout fidelity are still limited in this circuit, they are sufficient to test in the near future simple quantum algorithms and get their result in a single run, which would demonstrate the concept of quantum speed-up.

We gratefully acknowledge discussions with J. Martinis and his co-workers, with M. Devoret, D. DiVicenzo, A. Korotkov, P. Milman, and within the Quantronics group, technical support from P. Orfila, P. Senat, and J. C. Tack, as well as financial support from the European research contracts MIDAS and SOLID, from ANR Masquelspec and C’Nano, and from the German Ministry of Education and Research.

- 
- [1] M. A. Nielsen and I. L. Chuang, *Quantum Computation and Quantum Information* (Cambridge University Press, Cambridge, England, 2000).
  - [2] J. Clarke and F. Wilhelm, *Nature (London)* **453**, 1031 (2008).
  - [3] L. DiCarlo *et al.*, *Nature (London)* **460**, 240 (2009).
  - [4] L. DiCarlo *et al.*, *Nature (London)* **467**, 574 (2010).
  - [5] T. Yamamoto *et al.*, *Phys. Rev. B* **82**, 184515 (2010).
  - [6] R. C. Bialczak *et al.*, *Nature Phys.* **6**, 409 (2010).
  - [7] J. M. Chow *et al.*, *Phys. Rev. Lett.* **107**, 080502 (2011).
  - [8] J. Koch *et al.*, *Phys. Rev. A* **76**, 042319 (2007).
  - [9] J. A. Schreier *et al.*, *Phys. Rev. B* **77**, 180502(R) (2008).

- [10] M. Mariantoni *et al.*, *Science* **334**, 61 (2011).
- [11] M. Ansmann *et al.*, *Nature (London)* **461**, 504 (2009).
- [12] I. Siddiqi *et al.*, *Phys. Rev. Lett.* **93**, 207002 (2004).
- [13] F. Mallet *et al.*, *Nature Phys.* **5**, 791 (2009).
- [14] See Supplemental Material at <http://link.aps.org/supplemental/10.1103/PhysRevLett.108.057002> for additional information about the sample preparation and experimental setup, the two-qubit Hamiltonian, the sample parameters, the readout characterization, the removal of errors on tomographic pulses, as well as for different representations of the matrices shown in Figs. 2 and 4.
- [15] The relaxation times  $T_1 \sim 0.5 \mu\text{s}$  are twice as low as in Ref. [13], which is likely due to a lack of control of the electromagnetic impedance as seen from the qubit in the present and more complicated circuit and/or to the large asymmetry  $d$  of the transmons that opens a new relaxation channel.
- [16] J. M. Chow *et al.*, *Phys. Rev. A* **81**, 062325 (2010).
- [17] Note that  $F_g$  is also equal to Shumacher’s fidelity  $\text{Tr}[S_{\text{id}}^\dagger S]/\text{Tr}[S_{\text{id}}^\dagger S_{\text{id}}]$  with  $S$  ( $S_{\text{id}}$ ) the super operator of the actual (ideal unitary) process and that fidelities  $F$  for the 16 output states range between 80% and 99.5%.
- [18] A. G. Kofman and A. N. Korotkov, *Phys. Rev. A* **80**, 042103 (2009); private communication.

# Supplementary Information for Characterization of a two-transmon processor with individual single-shot qubit readout

A. Dewes<sup>1</sup>, F. R. Ong<sup>1</sup>, V. Schmitt<sup>1</sup>, R. Lauro<sup>1</sup>, N. Boulant<sup>2</sup>, P. Bertet<sup>1</sup>, D. Vion<sup>1</sup>, and D. Esteve<sup>1</sup>

<sup>1</sup>*Quantronics group, Service de Physique de l'État Condensé (CNRS URA 2464),*

*IRAMIS, DSM, CEA-Saclay, 91191 Gif-sur-Yvette, France and*

<sup>2</sup>*I2BM, Neurospin, LRMN, 91191 CEA-Saclay, 91191 Gif-sur-Yvette, France*

(Dated: December 8, 2011)

## I. SAMPLE PREPARATION AND EXPERIMENTAL SETUP

- Sample fabrication: the sample is fabricated on a silicon chip oxidized over 50 nm. A 150 nm thick niobium layer is first deposited by magnetron sputtering and then dry-etched in a  $SF_6$  plasma to pattern the readout resonators, the current lines for frequency tuning, and their ports. Finally, the transmon qubit, the coupling capacitance and the Josephson junctions of the resonators are fabricated by double-angle evaporation of aluminum through a shadow mask patterned by e-beam lithography. The first layer of aluminum is oxidized in a  $Ar - O_2$  mixture to form the oxide barrier of the junctions. The chip is glued with wax on a printed circuit board (PCB) and wire bonded to it. The PCB is then screwed in a copper box anchored to the cold plate of a dilution refrigerator.
- Qubit microwave pulses: The qubit drive pulses are generated by two phase-locked microwave generators whose continuous wave outputs are fed to a pair of I/Q-mixers. The two IF inputs of each of these mixers are provided by a 4-Channel 1 GS/s arbitrary waveform generator (AWG Tektronix AWG5014). Single-sideband mixing in the frequency range of 50 – 300 MHz is used to generate multi-tone drive pulses and to obtain a high ON/OFF ratio ( $> 50$  dB) of the signal at the output of the mixers. Phase and amplitude errors of the mixers are corrected by measuring the signals at the output and applying sideband and carrier frequency dependent corrections in amplitude and offset to the IF input channels.
- Flux Pulses: The flux control pulses are generated by a second AWG and sent to the chip through a transmission line, equipped with 40 dB of attenuation distributed over different temperature stages and a pair of 1 GHz absorptive low-pass filters at 4 K. The input signal of each flux line is fed back to room temperature through an identical transmission line and is then measured to compensate the non-ideal frequency response of the line.
- Readout Pulses: The pulses for the Josephson bifurcation amplifier (JBA) readouts are generated by mixing the continuous signals of a pair of microwave generators with IF pulses provided by a 1 GS/s arbitrary function generator. Each readout pulse consists of a measurement part with a rise time of 30 ns and a hold time of 100 ns, followed by a  $2\ \mu s$  long latching part at 90 % of the pulse height.
- Drive and Measurement Lines: The drive and readout microwave signals of each qubit are combined and sent to the sample through a pair of transmission lines that are attenuated by 70 dB over different temperature stages and filtered at 4 K and 300 mK. A microwave circulator at 20 mK separates the input signals going to the chip from the reflected signals coming from the chip. The latter are amplified by 36 dB at 4 K by two cryogenic HEMT amplifiers (CIT Cryo 1) with noise temperature 5 K. The reflected readout pulses get further amplified at room temperature and are then demodulated with the continuous signals of the readout microwave sources. The IQ quadratures of the demodulated signals are sampled at 1 GS/s by a 4-channel Data Acquisition system (Acqiris DC282).

## II. TWO-QUBIT HAMILTONIAN

The Hamiltonian of a Cooper pair box  $j$  [s2, s1] with total Coulomb energy  $E_C^j$  (for a Cooper pair), with total Josephson energy  $E_J^j(\phi_j)$ , with island charge  $N_j$  (in Cooper pair units) and conjugated phase variable  $\delta_j$ , biased by a gate charge  $N_{g,j}$ , is  $H_j = E_C^j \left( \widehat{N}_j - N_{g,j} \right)^2 - E_J^j(\phi_j) \cos \left[ \widehat{\delta}_j - \delta_{j,0}(\phi_j) \right]$  with  $\tan(\delta_{j,0}) = d_j \tan(\pi \phi_j / \phi_0)$ . In the limit  $E_J^j \gg E_C^j$  [8] that corresponds to the transmon qubit and when restricting the Hilbert space to the two lowest eigenstates  $\{|0\rangle_j, |1\rangle_j\}$ , the  $N_{g,j}$  parameters become irrelevant, and one has  $\langle 0 | \widehat{N}_j | 0 \rangle \simeq \langle 1 | \widehat{N}_j | 1 \rangle \simeq 0$ ,  $\langle 0 | \widehat{N}_j | 0 \rangle = 2^{-3/4} i \left( E_J^j / E_C^j \right)^{1/4}$ , and  $H_j = -h\nu_j \sigma_z^j / 2$  with  $\nu_j \simeq \sqrt{2E_C^j E_J^j(\phi_j) / h}$ . When coupling two such transmon qubits by

a capacitance  $C_c$  much smaller than each total island capacitance, the total Hamiltonian is  $H = H_1 + H_2 + H_{\text{int}}$  with  $H_{\text{int}} = 2E_C^{\text{I}}E_C^{\text{II}}/E_{Cc}\widehat{N}_1\widehat{N}_2$  and  $E_{Cc}$  the Coulomb energy of a Cooper pair on the coupling capacitor. Using the matrix elements above leads to  $H_{\text{int}} = hg\sigma_y^{\text{I}}\sigma_y^{\text{II}}$  with  $g = \sqrt{E_C^{\text{I}}E_C^{\text{II}}\nu_I\nu_{\text{II}}/(2E_{Cc})}$ . This symmetric and purely transverse coupling term  $\sigma_y^{\text{I}}\sigma_y^{\text{II}}$  (exchange term) is not surprising since each charge on a transmon island varying at the frequency of the other qubit plays the role of a resonant gate drive for this second qubit, and makes it rotate around an equatorial axis of its Bloch sphere. The precise YY nature (rather than XX for instance) is on the other hand meaningless and is a matter of initial convention for the global phases of the  $|0\rangle$  and  $|1\rangle$  states.

### III. SAMPLE PARAMETERS

The sample is first characterized by spectroscopy (see Fig. 1.b of main text). The incident power used is high enough to observe the resonator frequency  $\nu_R$ , the qubit line  $\nu_{01}$ , and the two-photon transition at frequency  $\nu_{02}/2$  between the ground and second excited states of each transmon (data not shown). A fit of the transmon model to the data yields the sample parameters  $E_J^{\text{I}}/h = 36.2$  GHz,  $E_C^{\text{I}}/h = 0.98$  GHz,  $d_I = 0.2$ ,  $E_J^{\text{II}}/h = 43.1$  GHz,  $E_C^{\text{II}}/h = 0.87$  GHz,  $d_{\text{II}} = 0.35$ ,  $\nu_R^{\text{I}} = 6.84$  GHz, and  $\nu_R^{\text{II}} = 6.70$  GHz. The qubit-readout anti crossing at  $\nu = \nu_R$  yields the qubit-readout couplings  $g_0^{\text{I}} \simeq g_0^{\text{II}} \simeq 50$  MHz. Independent measurements of the resonator dynamics (data not shown) yield quality factors  $Q_{\text{I}} = Q_{\text{II}} = 730$  and Kerr non linearities [s3],[13]  $K_{\text{I}}/\nu_R^{\text{I}} \simeq K_{\text{II}}/\nu_R^{\text{II}} \simeq -2.3 \pm 0.5 \times 10^{-5}$ .

### IV. READOUT CHARACTERIZATION

Errors in our readout scheme are discussed in detail in [13] for a single qubit. First, incorrect mapping  $|0\rangle \rightarrow 1$  or  $|1\rangle \rightarrow 0$  of the projected state of the qubit to the dynamical state of the resonator can occur, due to the stochastic nature of the switching between the two dynamical states. As shown in Fig. IV.1, the probability  $p$  to obtain the outcome 1 varies continuously from 0 to 1 over a certain range of drive power  $P_d$  applied to the readout. When the shift in power between the two  $p_{|0\rangle,|1\rangle}(P_d)$  curves is not much larger than this range, the two curves overlap and errors are significant even at the optimal drive power where the difference in  $p$  is maximum. Second, even in the case of non overlapping  $p_{|0\rangle,|1\rangle}(P_d)$  curves, the qubit initially projected in state  $|1\rangle$  can relax down to  $|0\rangle$  before the end of the measurement, yielding an outcome 0 instead of 1. The probability of these two types of errors vary in opposite directions as a function of the frequency detuning  $\Delta = \nu_R - \nu > 0$  between the resonator and the qubit, so that a compromise has to be found for  $\Delta$ . Besides, the contrast  $c = \text{Max}(p_{|1\rangle} - p_{|0\rangle})$  can be increased [13] by shelving state  $|1\rangle$  into state  $|2\rangle$  with a microwave  $\pi$  pulse at frequency  $\nu_{12}$  just before the readout resonator pulse. The smallest errors  $e_0^{\text{I},\text{II}}$  and  $e_1^{\text{I},\text{II}}$  when reading  $|0\rangle$  and  $|1\rangle$  are found for  $\Delta_{\text{I}} = 440$  MHz and  $\Delta_{\text{II}} = 575$  MHz and are shown by arrows in the top panels of Fig. IV.1:  $e_0^{\text{I}} = 5\%$  and  $e_1^{\text{I}} = 13\%$  (contrast  $c_{\text{I}} = 1 - e_0^{\text{I}} - e_1^{\text{I}} = 82\%$ ), and  $e_0^{\text{II}} = 5.5\%$  and  $e_1^{\text{II}} = 12\%$  ( $c_{\text{II}} = 82\%$ ). When using the  $|1\rangle \rightarrow |2\rangle$  shelving before readout,  $e_0^{\text{I}} = 2.5\%$  and  $e_2^{\text{I}} = 9.5\%$  (contrast  $c_{\text{I}} = 1 - e_0^{\text{I}} - e_2^{\text{I}} = 88\%$ ), and  $e_0^{\text{II}} = 3\%$  and  $e_2^{\text{II}} = 8\%$  ( $c_{\text{II}} = 89\%$ ). These best results are very close to those obtained in [12], but are unfortunately not relevant to this work.

Indeed, when the two qubits are measured simultaneously, one has also to take into account a possible readout crosstalk, i.e. an influence of the projected state of each qubit on the outcome of the readout of the other qubit. We do observe such an effect and have to minimize it by increasing  $\Delta_{\text{I,II}}$  up to  $\sim 1$  GHz (where the dispersive shift  $\chi \simeq 2.5$  MHz is still large enough), and by not using the shelving technique. An immediate consequence shown in Fig. IV.1(b) is a reduction of the  $c_{\text{I,II}}$  contrasts. The errors when reading  $|0\rangle$  and  $|1\rangle$  are now  $e_0^{\text{I}} = 19\%$  and  $e_1^{\text{I}} = 7\%$  (contrast  $c_{\text{I}} = 74\%$ ) and  $e_0^{\text{II}} = 19\%$  and  $e_1^{\text{II}} = 12\%$  (contrast  $c_{\text{II}} = 69\%$ ). Then to characterize the errors due to crosstalk, we measure the  $4 \times 4$  readout matrix  $\mathcal{R}$  linking the probabilities  $p_{uv}$  of the four possible  $uv$  outcomes to the population of the four  $|uv\rangle$  states. As shown in Fig. IV.1(c-d), we then rewrite  $\mathcal{R} = \mathcal{C}_{\text{CT}} \cdot (\mathcal{C}_{\text{I}} \otimes \mathcal{C}_{\text{II}})$  as the product of a  $4 \times 4$  pure crosstalk matrix  $\mathcal{C}_{\text{CT}}$  with the tensorial product of the two  $2 \times 2$  single qubit readout matrices

$$\mathcal{C}_{\text{I,II}} = \begin{pmatrix} 1 - e_0^{\text{I},\text{II}} & e_1^{\text{I},\text{II}} \\ e_0^{\text{I},\text{II}} & 1 - e_1^{\text{I},\text{II}} \end{pmatrix}.$$

In the worst case, the readout crosstalk is 2.1%. We also illustrate on the figure the impact of the readout errors on our swapping experiment by comparing the bare readout outcomes  $uv$ , the outcomes corrected from the independent readout errors only, and the  $|uv\rangle$  population calculated with the full correction including crosstalk.

We now explain briefly the cause of the readout crosstalk in our processor. Unlike what was observed for other qubit readout schemes using switching detectors [5], the crosstalk we observe is not directly due to an electromagnetic perturbation induced by the switching of one detector that would help or prevent the switching of the other one.

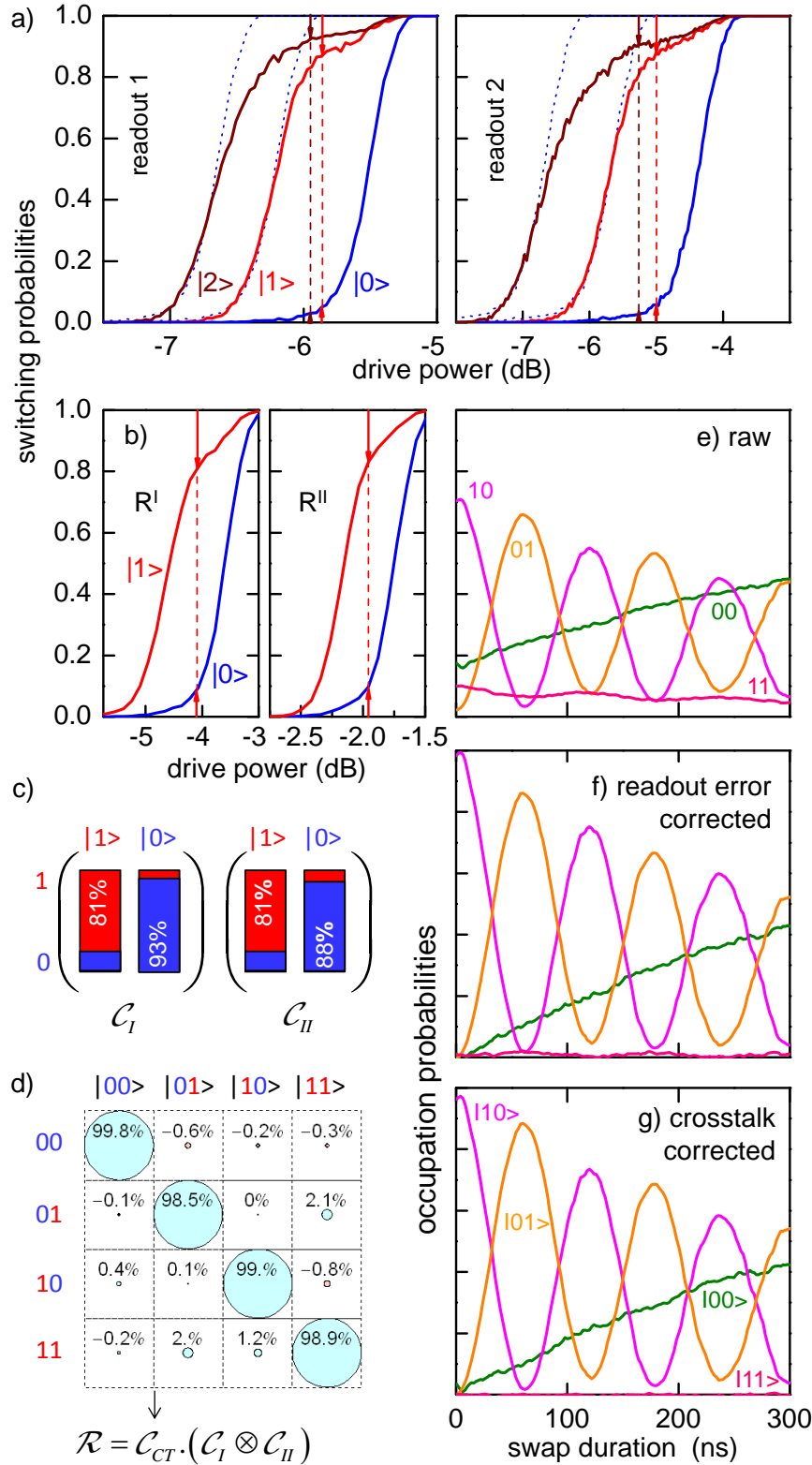


Figure IV.1: Readout imperfections and their correction. (a) Switching probabilities of the readouts as a function of their driving power, with the qubit prepared in state  $|0\rangle$  (blue),  $|1\rangle$  (red), or  $|2\rangle$  (brown), at the optimal readout points. The arrows and dashed segments indicate the readout errors and contrast, at the power where the latter is maximum. (b) Same as (a) but at readout points  $R^{I,II}$  used in this work. (c-d) Single readout matrices  $\mathcal{C}_{I,II}$  and pure readout crosstalk matrix  $\mathcal{C}_{CT}$  characterizing the simultaneous readout of the two qubits. (e-g) bare readout outcomes  $uv$ , outcomes corrected from the independent readout errors only, and  $|uv\rangle$  population calculated with the full correction including crosstalk for the swapping experiment of Fig. 2.

Indeed, when both qubits frequencies  $\nu_{I,II}$  are moved far below  $\nu_R^{I,II}$ , the readout crosstalk disappears: the switching of a detector has no measurable effect on the switching of the other one. The crosstalk is actually due to the rather strong ac-Stark shift  $\sim 2(n_H - n_L)g_0^2/(R - \nu_R) \sim 500$  MHz of the qubit frequency when a readout resonator switches from its low to high amplitude dynamical state with  $n_L \sim 10$  and  $n_H \sim 10^2$  photons, respectively. The small residual effective coupling between the qubits at readout can then slightly shift the frequency of the other resonator, yielding a change of its switching probability by a few percent. Note that coupling the two qubits by a resonator rather than by a fixed capacitor would solve this problem.

## V. REMOVING ERRORS ON TOMOGRAPHIC PULSES BEFORE CALCULATING THE GATE PROCESS MAP

Tomographic errors are removed from the process map of our  $\sqrt{iSWAP}$  gate using the following method. The measured Pauli sets corresponding to the sixteen input states are first fitted by a model including errors both in the preparation of the state (index *prep*) and in the tomographic pulses (index *tomo*). The errors included are angular errors  $\varepsilon_{I,II}^{\text{prep}}$  on the nominal  $\pi$  rotations around  $X_{I,II}$ ,  $\eta_{I,II}^{\text{prep,tomo}}$  and  $\delta_{I,II}^{\text{prep,tomo}}$  on the nominal  $\pi/2$  rotations around  $X_{I,II}$  and  $Y_{I,II}$ , a possible departure  $\xi_{I,II}$  from orthogonality of  $(\vec{X}_I, \vec{Y}_I)$  and  $(\vec{X}_{II}, \vec{Y}_{II})$ , and a possible rotation  $\mu_{I,II}$  of the tomographic  $XY$  frame with respect to the preparation one. The rotation operators used for preparing the states and for doing their tomography are thus given by

$$\begin{aligned} X_{I,II}^{\text{prep}}(\pi) &= e^{-i(\pi + \varepsilon_{I,II}^{\text{prep}})\sigma_x^{I,II}/2}, \\ X_{I,II}^{\text{prep}}(-\pi/2) &= e^{+i(\pi/2 + \eta_{I,II}^{\text{prep}})\sigma_x^{I,II}/2}, \\ Y_{I,II}^{\text{prep}}(\pi/2) &= e^{-i(\pi/2 + \delta_{I,II}^{\text{prep}})[\cos(\xi_{I,II})\sigma_y^{I,II} - \sin(\xi_{I,II})\sigma_x^{I,II}]/2}, \\ X_{I,II}^{\text{tomo}}(\pi/2) &= e^{-i(\pi/2 + \eta_{I,II}^{\text{tomo}})[\sin(\mu_{I,II})\sigma_x^{I,II} + \cos(\mu_{I,II})\sigma_y^{I,II}]/2}, \\ Y_{I,II}^{\text{tomo}}(-\pi/2) &= e^{+i(\pi/2 + \delta_{I,II}^{\text{tomo}})[\cos(\mu_{I,II} + \xi_{I,II})\sigma_y^{I,II} - \sin(\mu_{I,II} + \xi_{I,II})\sigma_x^{I,II}]/2}. \end{aligned}$$

The sixteen input states are then  $\{\rho_{\text{in}}^e = U|0\rangle\langle 0|U^\dagger\}$  with  $\{U\} = \{I_I, X_I^{\text{prep}}(\pi), Y_I^{\text{prep}}(\pi/2), X_I^{\text{prep}}(-\pi/2)\} \otimes \{I_{II}, X_{II}^{\text{prep}}(\pi), Y_{II}^{\text{prep}}(\pi/2), X_{II}^{\text{prep}}(-\pi/2)\}$ , and each input state yields a Pauli set  $\{\langle P_k^e \rangle = \text{Tr}(\rho_{\text{in}}^e P_k^e)\}$  with  $\{P_k^e\} = \{I_I, X_I^e, Y_I^e, Z_I\} \otimes \{I_{II}, X_{II}^e, Y_{II}^e, Z_{II}\}$ ,  $X^e = Y^{\text{tomo}}(-\pi/2)^\dagger \sigma_z Y^{\text{tomo}}(-\pi/2)$ , and  $Y^e = X^{\text{tomo}}(\pi/2)^\dagger \sigma_z X^{\text{tomo}}(\pi/2)$ . Figure V.1 shows the best fit of the modeled  $\{\langle P_k^e \rangle\}$  set to the measured input Pauli sets, yielding  $\varepsilon_I^{\text{prep}} = -1^\circ$ ,  $\varepsilon_{II}^{\text{prep}} = -3^\circ$ ,  $\eta_I^{\text{prep}} = 3^\circ$ ,  $\eta_{II}^{\text{prep}} = 4^\circ$ ,  $\delta_I^{\text{prep}} = -6^\circ$ ,  $\delta_{II}^{\text{prep}} = -3^\circ$ ,  $\eta_I^{\text{tomo}} = -6^\circ$ ,  $\eta_{II}^{\text{tomo}} = -4^\circ$ ,  $\lambda_I^{\text{tomo}} = 12^\circ$ ,  $\lambda_{II}^{\text{tomo}} = 5^\circ$ ,  $\xi_I = 1^\circ$ ,  $\xi_{II} = -2^\circ$ , and  $\mu_I = \mu_{II} = -11^\circ$ .

Knowing the tomographic errors and thus  $\{\langle P_k^e \rangle\}$ , we then invert the linear relation  $\{\langle P_k^e \rangle = \text{Tr}(\rho P_k^e)\}$  to find the  $16 \times 16$  matrix  $B$  that links the vector  $\overrightarrow{\langle P_k^e \rangle}$  to the columnized density matrix  $\overrightarrow{\rho}$ , i.e.  $\overrightarrow{\rho} = B \cdot \overrightarrow{\langle P_k^e \rangle}$ . The matrix  $B$  is finally applied to the measured sixteen input and sixteen output Pauli sets to find the sixteen  $(\rho_{\text{in}}, \rho_{\text{out}})_k$  couples to be used for calculating the gate map.

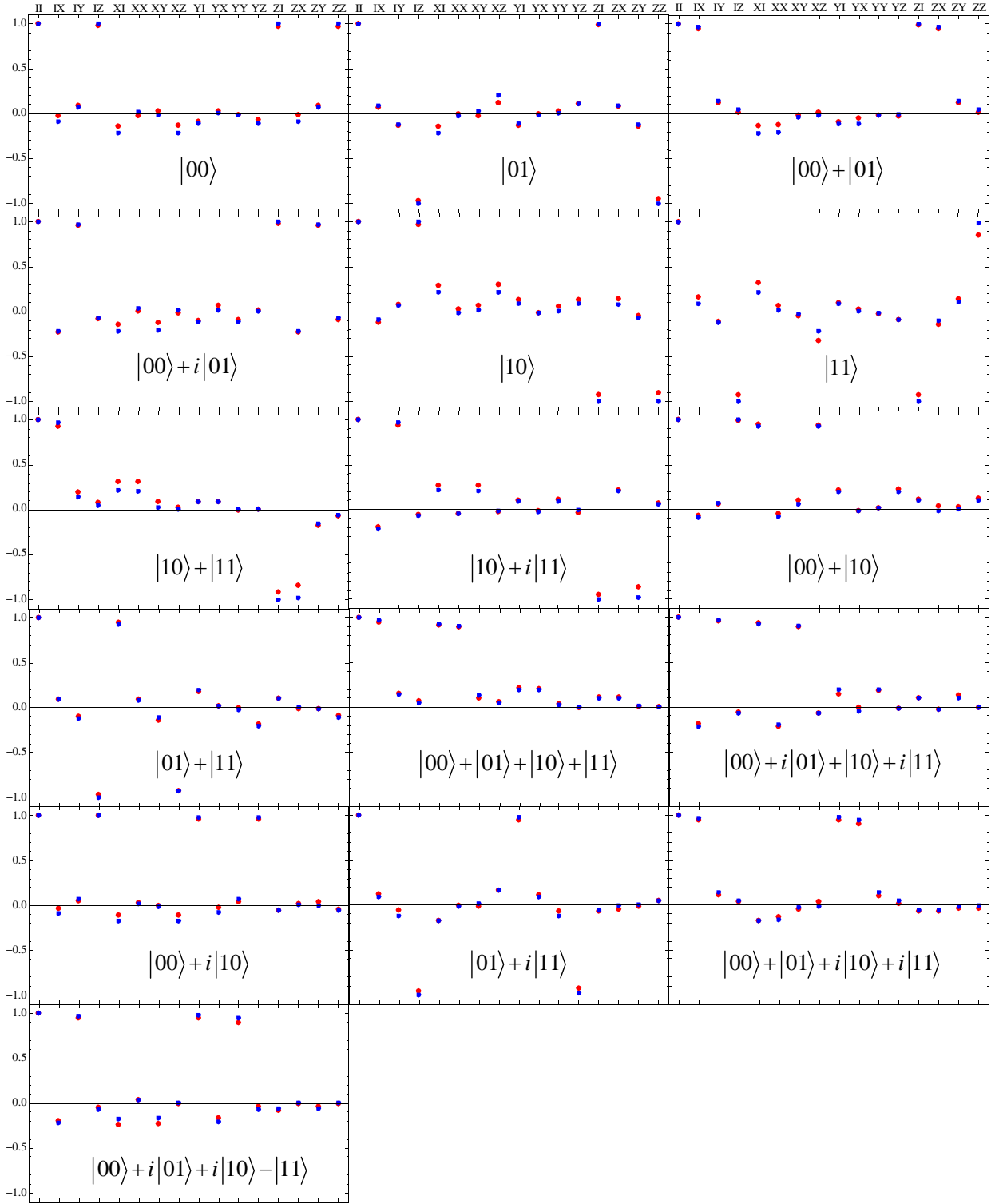


Figure V.1: Fitting of the pulse errors at state preparation and tomography. Measured (red) and fitted (blue - see text) Pauli sets  $\langle P_k^e \rangle$  for the sixteen targeted input states  $\{|0\rangle, |1\rangle, |0\rangle + |1\rangle, |0\rangle + i|1\rangle\}^{\otimes 2}$ . The  $\{II, IX, IY, IZ, XI, \dots\}$  operators indicated in abscissa are the targeted operators and not those actually measured (due to tomographic errors).

## VI. REAL AND IMAGINARY PART REPRESENTATION OF THE MATRICES OF MAIN FIGURES 2 AND 4.

The  $\rho$ ,  $\chi$  and  $\tilde{\chi}$  matrices of figures 2 and 4 of the main text are represented in an unconventional way that allows to encode both the modulus and the argument of each matrix element in the same matrix cell. Figures VI.1 to VI.3 show the same matrices using the more conventional real and imaginary part representation.

In addition, we show in Fig. VI.4 the contributions of relaxation, of inaccurate swapping time and of inaccurate rotations  $\theta_{I,II}$  to the error matrix  $\tilde{\chi}$ . Contribution of relaxation is directly calculated from the independently measured values of the relaxation time  $T_1$ , whereas the two other contributions result from a fit to the whole experimental  $\tilde{\chi}$  matrix.

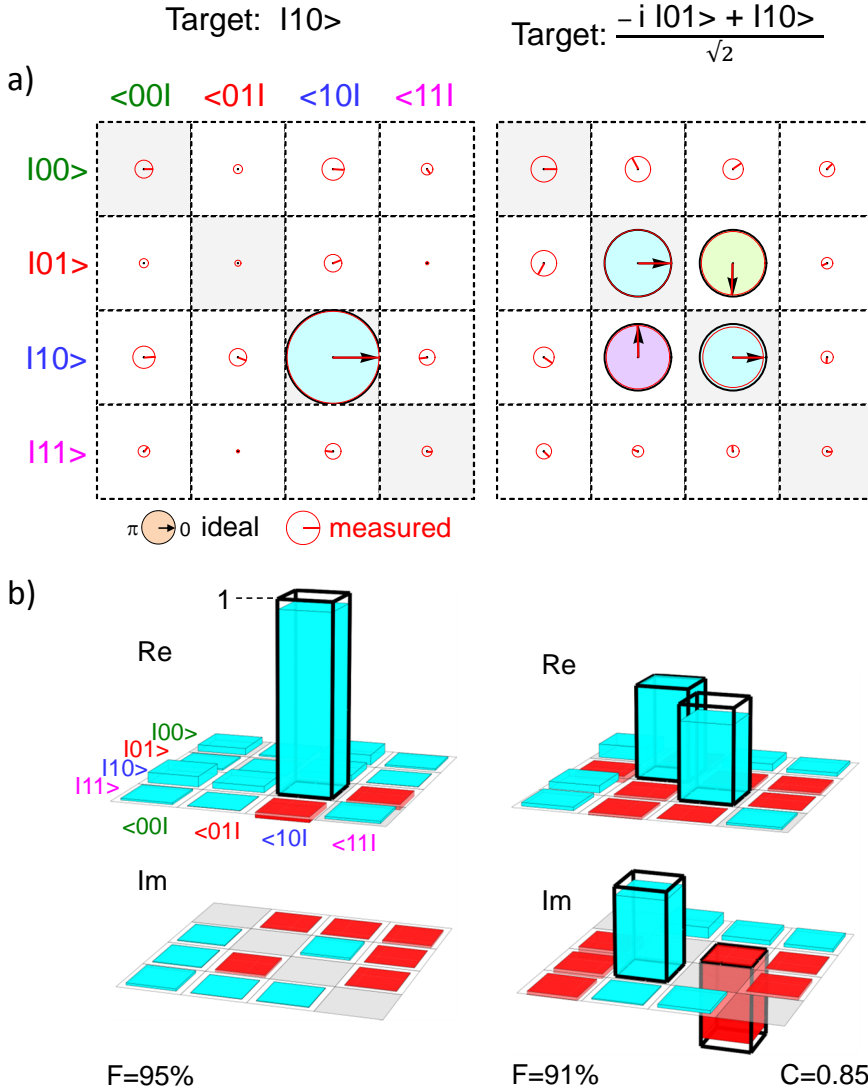


Figure VI.1: Same ideal and experimental density matrices as in Fig. 2, before and after one operation of the  $\sqrt{iSWAP}$  gate. (a) Color-filled black circles with black arrow is the ideal matrix whereas red circles and arrows is the experimental one. Each complex matrix element is represented by a circle with an area proportional to its modulus (diameter = cell size for unit modulus) and by an arrow giving its argument (usual trigonometric convention). (b) Real (top) and imaginary (bottom) parts of the same matrices, with positive and negative numbers being encoded along the vertical direction. The ideal matrix is represented by thick black empty bars, whereas experimental data are shown as blue-filled (positive) or red-filled (negative) thin bars.

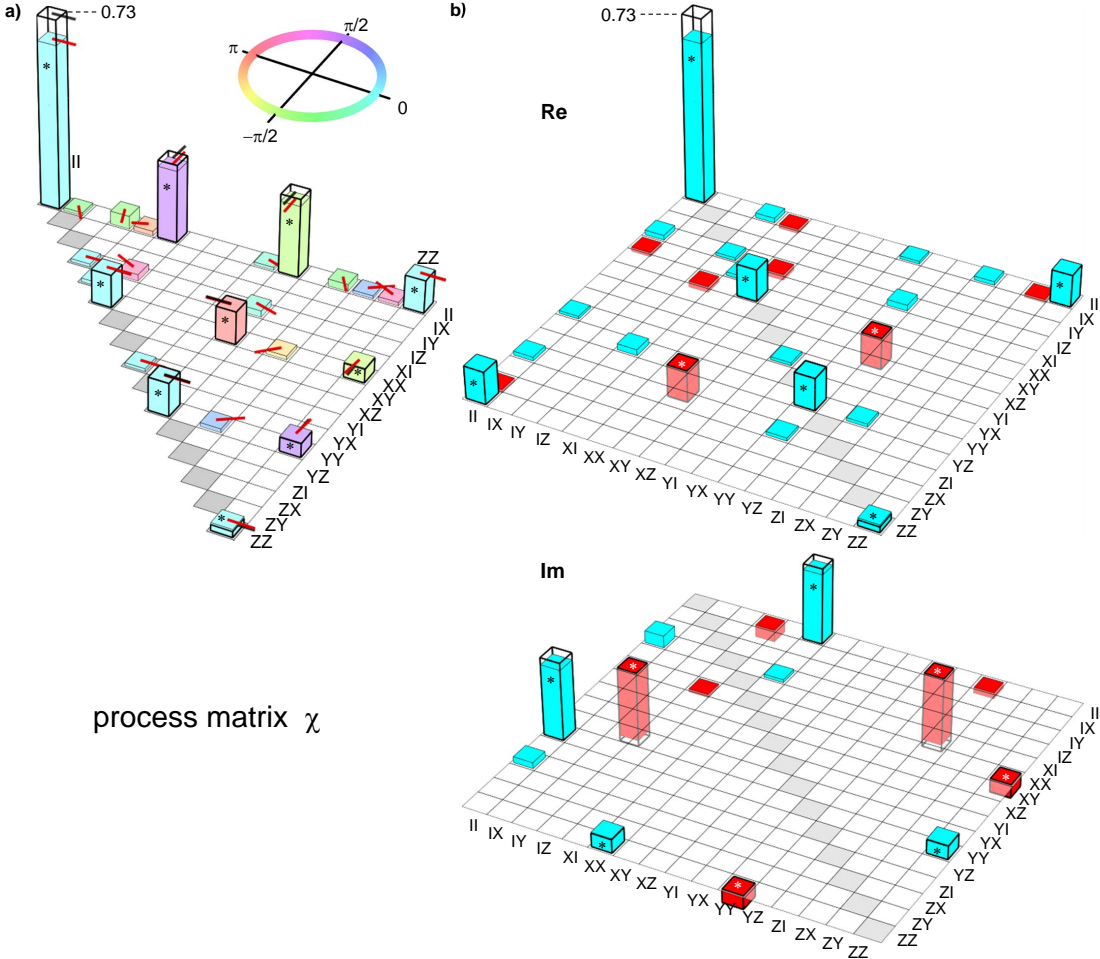


Figure VI.2: Same ideal and experimental process matrix  $\chi$  as in Fig. 4(a). Expected elements are marked with a star and elements below 1% are not shown. (a) Each complex matrix element is represented by a bar with height proportional to its modulus and by an arrow at the top of the bar (as well as a filling color for the experiment - see top inset) giving its argument. (b) Real (top) and imaginary (bottom) parts of the same matrix, with positive and negative numbers being encoded along the vertical direction. The ideal matrix is represented by thick black empty bars, whereas experimental data are shown as blue-filled (positive) or red-filled (negative) thin bars.

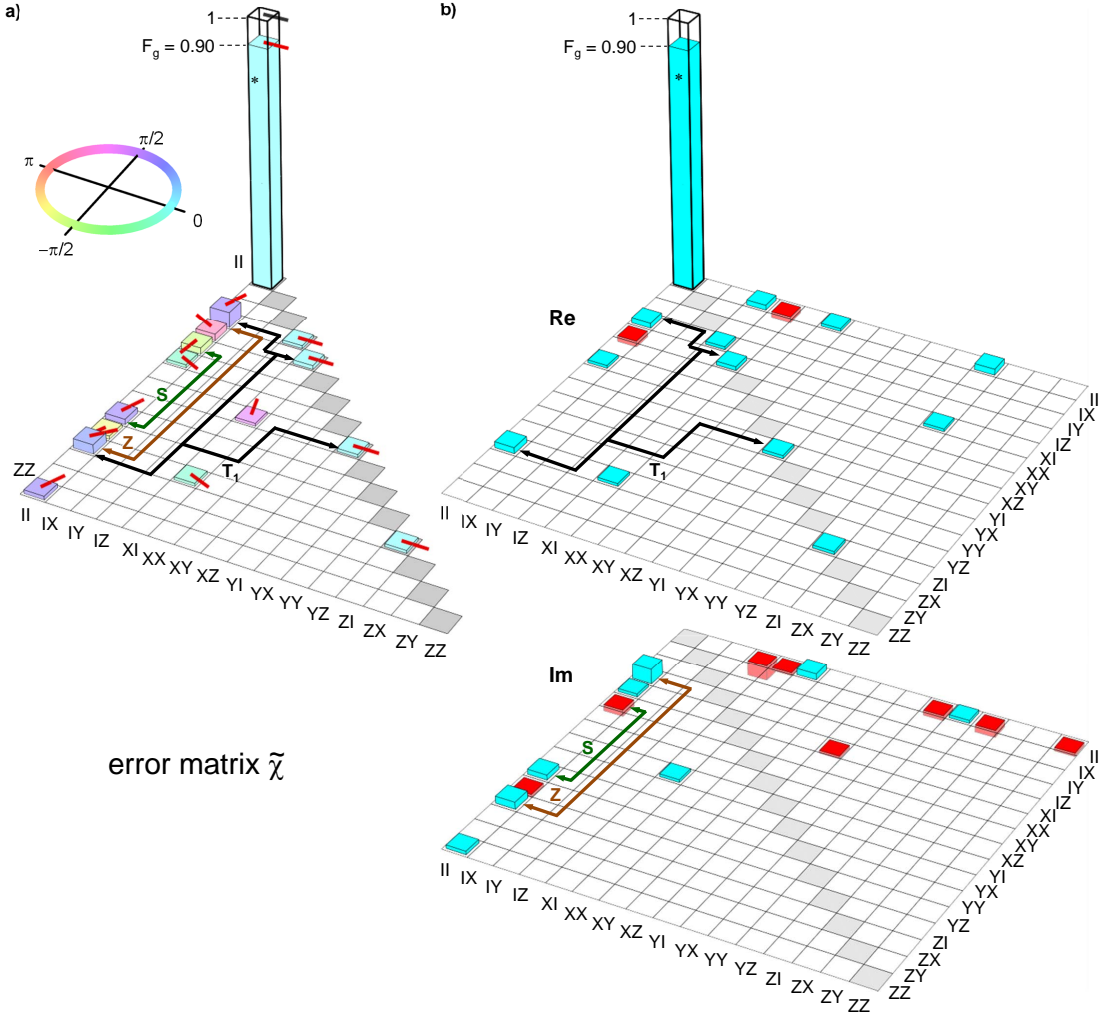


Figure VI.3: Same ideal and experimental error matrix  $\tilde{\chi}$  as in Fig. 4(b). The  $III$  matrix element is the only expected one; elements with modulus below 1% are not shown. (a) Each complex matrix element is represented by a bar with height proportional to its modulus and by an arrow at the top of the bar (as well as a filling color for the experiment - see left inset) giving its argument. (b) Real (top) and imaginary (bottom) parts of the same matrix, with positive and negative numbers being encoded along the vertical direction. The ideal matrix is represented by thick black empty bars, whereas experimental data are shown as blue-filled (positive) or red-filled (negative) thin bars. Labeled arrows indicate the main visible contributions to errors, i.e. a too long swapping time (S), too small rotations  $\theta_{I,II}$  (Z), and relaxation ( $T_1$ ).

[s1] D. Vion *et al.*, Science 296, 886 (2002).

[s2] A. Cottet, Ph.D. thesis, Universite Paris VI, 2002.

[s3] F. R. Ong *et al.*, Phys. Rev. Lett. 106, 167002 (2011).

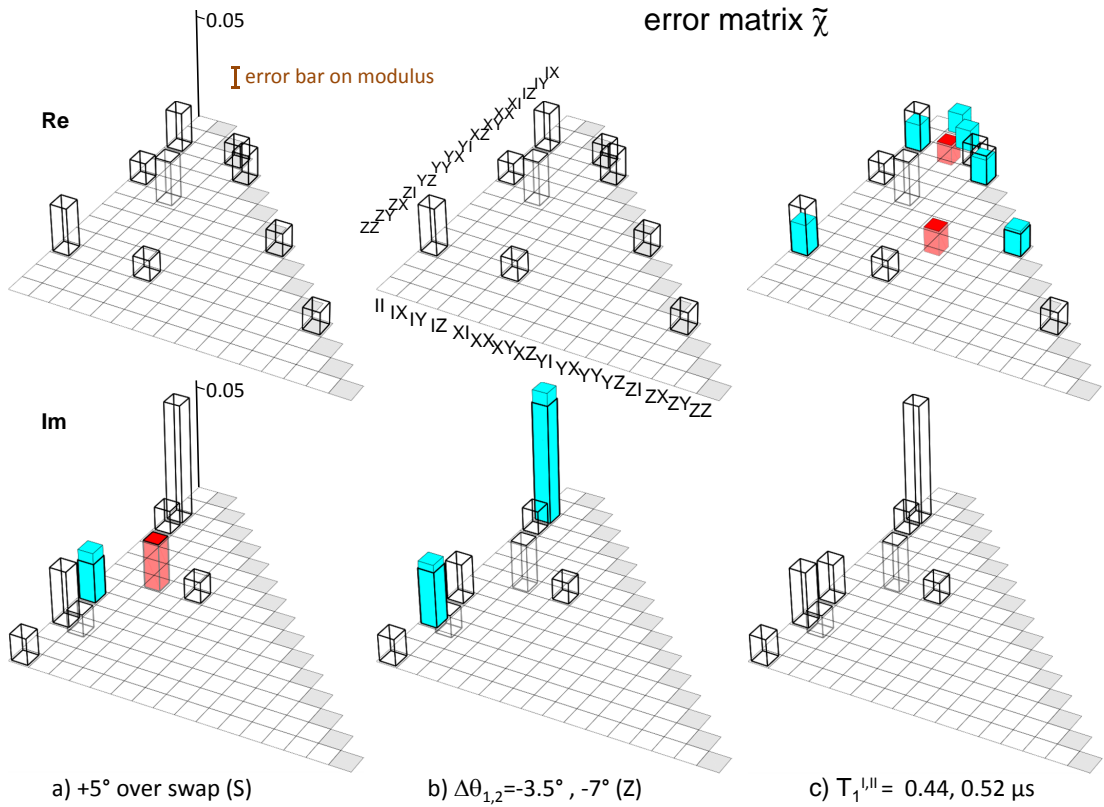


Figure VI.4: Experimental (empty bars) and calculated (color-filled thin bars)  $\tilde{\chi}$  matrix for the three error contributions S, Z, and  $T_1$  mentioned in the text and indicated in Figs. 4(b) and VI.3. Note that the vertical scale is expanded by a factor 10 with respect to other figures, and that matrix element  $IIII$  as well as elements with modulus below the statistical error of 1% (see error bar) are not shown. Contribution  $T_1$  is directly calculated from the independently measured values of the relaxation time  $T_1$ , whereas contributions S and Z result from a fit to the whole experimental  $\tilde{\chi}$  matrix (including the many small elements below 1%).



## Quantum speeding-up of computation demonstrated in a superconducting two-qubit processor

Andreas Dewes,<sup>1</sup> Romain Lauro,<sup>1</sup> Florian R. Ong,<sup>1</sup> Vivien Schmitt,<sup>1</sup> Perola Milman,<sup>2,3</sup> Patrice Bertet,<sup>1</sup> Denis Vion,<sup>1</sup> and Daniel Esteve<sup>1</sup>

<sup>1</sup>Service de Physique de l'Etat Condensé/IRAMIS/DSM (CNRS URA 2464), CEA Saclay, 91191 Gif-sur-Yvette, France

<sup>2</sup>Laboratoire Matériaux et Phénomènes Quantiques, Université Paris Diderot, 10 rue Alice Domon et Léonie Duquet, 75205 Paris, France

<sup>3</sup>Université Paris-Sud 11, Institut de Sciences Moléculaires d'Orsay (CNRS), 91405 Orsay, France

(Received 20 October 2011; revised manuscript received 31 January 2012; published 5 April 2012)

We operate a superconducting quantum processor consisting of two tunable transmon qubits coupled by a swapping interaction, and equipped with nondestructive single-shot readout of the two qubits. With this processor, we run the Grover search algorithm among four objects and find that the correct answer is retrieved after a single run with a success probability between 0.52 and 0.67, which is significantly larger than the 0.25 achieved with a classical algorithm. This constitutes a proof of concept for the quantum speed-up of electrical quantum processors.

DOI: [10.1103/PhysRevB.85.140503](https://doi.org/10.1103/PhysRevB.85.140503)

PACS number(s): 85.25.Cp, 03.67.Lx, 74.78.Na

The proposition of quantum algorithms<sup>1–3</sup> that perform useful computational tasks more efficiently than classical algorithms has motivated the realization of physical systems<sup>4</sup> able to implement them and to demonstrate quantum speed-up. The versatility and the potential scalability of electrical circuits make them very appealing for implementing a quantum processor built as sketched in Fig. 1. Ideally, a quantum processor consists of a scalable set of quantum bits that can be efficiently reset, that can follow any unitary evolution needed by an algorithm using a universal set of single- and two-qubit gates, and that can be read projectively.<sup>5</sup> The nonunitary projective readout operations can be performed at various stages of an algorithm, and in any case at the end in order to get the final outcome. Quantum processors based on superconducting qubits have already been operated, but they fail to meet the above criteria in different aspects. With the transmon qubit<sup>6,7</sup> derived from the Cooper pair box,<sup>8</sup> simple quantum algorithms, namely, the Deutsch-Jozsa algorithm,<sup>9</sup> the Grover search algorithm,<sup>1</sup> and a three-qubit quantum error correction code, were demonstrated in two- and three-qubit processors with the coupling between the qubits mediated by a cavity also used for readout.<sup>10,11</sup> In this circuit, the qubits are not read independently, but the value of a single collective variable is determined from the cavity transmission measured over a large number of repeated sequences. By applying suitable qubit rotations prior to this measurement, the density matrix of the two-qubit register was inferred at different steps of the algorithm, and it was found to be in good agreement with the predicted one. Demonstrating quantum speed-up is, however, more demanding than measuring a collective qubit variable since it requests to obtain an outcome after a single run, i.e., to perform the single-shot readout of the qubit register. Up to now, single-shot readout in superconducting processors has been achieved only for phase qubits.<sup>12,13</sup> In a multiphase-qubit processor equipped with single-shot but destructive readout of each qubit, the Deutsch-Jozsa algorithm<sup>9</sup> was demonstrated in Ref. 12 with a success probability of order 0.7 in a single run, to be compared to 0.5 for a classical algorithm. Very recently a similar processor ran a compiled version of Shor's algorithm,<sup>2</sup> yielding prime factors of 15 with a 48% success rate.<sup>14</sup>

Since the Deutsch-Jozsa classification algorithm is not directly related to any practical situation, demonstrating quantum speed-up for more useful algorithms in an electrical processor designed along the blueprint of Fig. 1 is an important goal.<sup>14</sup> In this Rapid Communication, we report the operation of a two-transmon-qubit processor<sup>15</sup> that comes closer to the ideal scheme than those previously mentioned, and the single-shot run of the Grover search algorithm among four objects. Since, in this case, the algorithm ideally yields the answer after one algorithm step, its success probability after a single run provides a simple benchmark. We find that our processor yields the correct answer at each run, with a success probability that ranges between 0.52 and 0.67, whereas a single-step classical algorithm using a random query would yield the correct answer with probability 0.25.

The sample and the setup used for this experiment are the very same as those described and characterized in detail in Ref. 15. The sample fabrication and parameters are summarized in Secs. I and II of the Supplemental Material,<sup>16</sup> whereas the scheme of our processor and its mode of operation are recalled in Fig. 2: Two tunable transmon qubits coupled by a fixed capacitor are embedded in two identical control and readout subcircuits. The Hamiltonian of the two qubits {I,II} is  $H/h = (-\nu_I \sigma_z^I - \nu_{II} \sigma_z^{II} + 2g\sigma_y^I \sigma_y^{II})/2$ , where  $\sigma_{x,y,z}$  are the Pauli operators,  $\nu_{I,II}$  are the qubit frequencies controlled by the flux applied to each transmon superconducting quantum interference device (SQUID) loop with fast (0.5-GHz bandwidth) local current lines, and  $g = 4.6$  MHz  $\ll \nu_{I,II}$  is the coupling frequency controlled by the coupling capacitance (see Sec. II of the Supplemental Material and Ref. 17). The achieved frequency control allows us to place the two transmons on resonance during times precise enough for performing the universal two-qubit gate  $\sqrt{i}\text{SWAP}$  (Ref. 15) and the exchange gate  $i\text{SWAP}$  used in this work. The qubit frequencies are tuned to different values for single-qubit manipulation, two-qubit gate operation, and readout (see Sec. III of the Supplemental Material<sup>16</sup>). The readout is independently and simultaneously performed for each qubit using the single-shot method of Ref. 18. It is based on the dynamical transition of a nonlinear resonator<sup>19,20</sup> that maps the quantum state of each transmon to the bifurcated or nonbifurcated state of its resonator, which

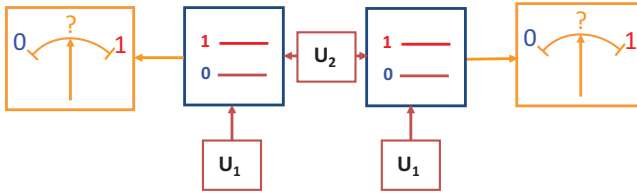


FIG. 1. (Color online) Schematic blueprint of a quantum processor based on quantum gates, represented here in the two-qubit case relevant for our experiment. A quantum processor consists of a qubit register that can perform any unitary evolution needed by an algorithm under the effect of a universal set of quantum gates (single-qubit gate  $U_1$ , two-qubit gate  $U_2$ ). Ideally, all the qubits may be read projectively, and may be reset.

yields a binary outcome for each qubit. This readout method is potentially nondestructive, but its nondestructive character is presently limited by relaxation during the readout pulse. In order to further improve the readout fidelity, we resort to a shelving method that exploits the second excited state of the transmon. For this purpose, a microwave pulse that induces a transition from state  $|1\rangle$  toward the second excited state  $|2\rangle$  of the transmon is applied just before the readout pulse, as demonstrated in Ref. 18 (this variant does not alter the nondestructive aspect of the readout method since an extra pulse bringing state  $|2\rangle$  back to state  $|1\rangle$  could be applied after readout). Although the readout contrast achieved with this shelving method and with optimized microwave pulses reaches 0.88 and 0.89 for the two qubits, respectively, the values achieved at working points suitable for processor operation are lower and equal to 0.84 and 0.83. The sources of readout errors are discussed in Sec. IV of the Supplemental Material<sup>16</sup> and include a small readout crosstalk contribution. The overall readout fidelity is thus characterized by a  $4 \times 4$  matrix  $\mathcal{R}$ , giving the readout outcome probabilities for each of the input states of the two-qubit register.

In order to characterize the evolution of this register during the algorithm, we determine its density matrix by state tomography. For this purpose, we measure the expectation values of the extended Pauli set of operators  $\{\sigma_x I, \dots, \sigma_z \sigma_z\}$  by applying the suitable rotations just before readout and by averaging typically  $10^4$  times. Note that the readout errors are corrected by inverting the readout matrix  $\mathcal{R}$  when determining the expectation value of the Pauli set, and thus do not contribute to tomography errors, as explained in Ref. 15. The density matrix  $\rho$  is then taken as the acceptable positive-semidefinite matrix that, according to the Hilbert-Schmidt distance, is the closest to the possibly nonphysical one derived from the measurement set. In order to characterize the fidelity of the algorithm at all steps, we use the state fidelity  $F = \langle \psi | \rho | \psi \rangle$ , with  $|\psi\rangle$  the ideal quantum state at the step considered;  $F$  is in this case the probability for the qubit register to be in state  $|\psi\rangle$ .

The Grover search algorithm<sup>1</sup> consists of retrieving a particular basis state in a Hilbert space of size  $N$  using a function able to discriminate it from the other ones. This function is used to build an oracle operator that tags the searched state. Starting from the superposition  $|\phi\rangle$  of all register states, a unitary sequence that incorporates the oracle operator is repeated about  $\sqrt{N}$  times, and eventually yields the

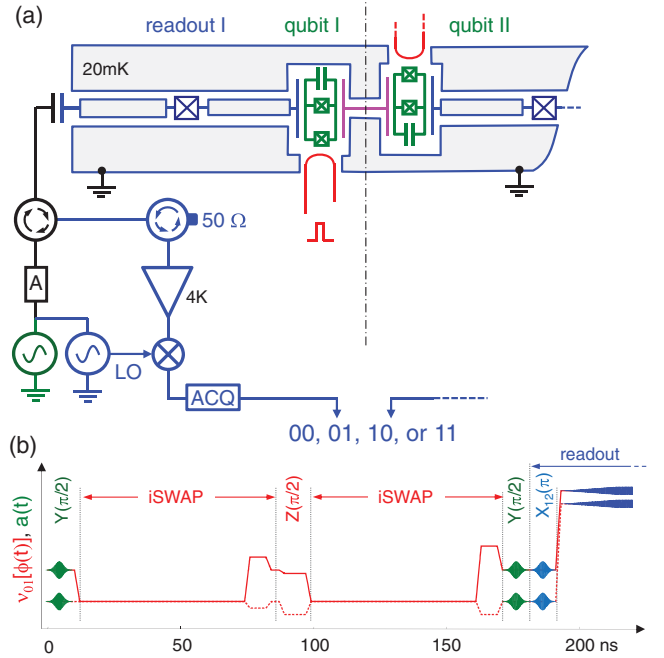


FIG. 2. (Color online) Electrical scheme of the two-qubit circuit operated and typical sequence during processor operation. (a) Two capacitively coupled transmon qubits have tunable frequencies controlled by the flux induced in their SQUID loop by a local current line. The coupling capacitance (center) yields a swapping evolution between the qubits when on resonance. Each transmon is embedded in a nonlinear resonator used for single-shot readout. Each reflected readout pulse is routed to a cryogenic amplifier through circulators, homodyned at room temperature, and acquired digitally, which yields a two-bit outcome. (b) Typical operation of the processor showing the resonant microwave pulses  $\alpha(t)$  applied to the qubits and to the readouts, on top of the dc pulses (polylines) that vary the transition frequencies of qubit I (solid) and II (dashed). With the qubits tuned at a first working point for single-qubit gates, resonant pulses are applied for performing  $X$  and  $Y$  rotations, as well as small flux pulses for  $Z$  rotations; qubits are then moved to the interaction point for two-qubit gate operations. Such sequences can be combined as needed by the algorithm. Qubits are then moved to their initial working points for applying tomography pulses as well as a  $|1\rangle \rightarrow |2\rangle$  pulse  $X_{12}(\pi)$  to increase the fidelity of the forthcoming readout. Finally, they are moved to better readout points and read.

searched state with a high probability. The implementation of Grover's algorithm in a two-qubit Hilbert space often proceeds in a simpler way<sup>21–26</sup> since the result is obtained with certainty after a single algorithm step. The algorithm then consists of an encoding sequence depending on the searched state, followed by a universal decoding sequence that retrieves it. Grover's algorithm thus provides a simple benchmark for two-qubit processors. Its implementation with our quantum processor is shown in Fig. 3(a). First, the superposed state  $|\phi\rangle$  is obtained by applying  $\pi/2$  rotations around the  $Y$  axis for the two qubits. The oracle operator  $O_{uv}$  tagging the two-qubit state  $|uv\rangle \equiv |u\rangle_I \otimes |v\rangle_{II}$  to be searched is then applied to state  $|\phi\rangle$ . Each  $O_{uv}$  consists of an iSWAP gate followed by a  $Z(\pm\pi/2)$  rotation on each qubit, with the four possible sign combinations  $(-, -)$ ,  $(+, -)$ ,  $(-, +)$ , and  $(+, +)$  corresponding to  $uv = 00, 01, 10$ , and  $11$ , respectively. In the algorithm we

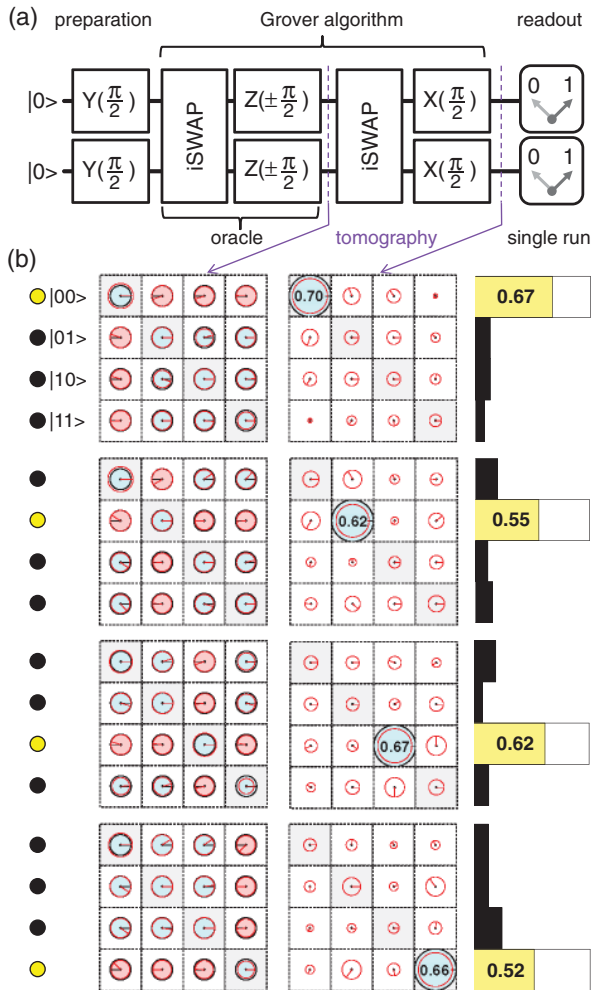


FIG. 3. (Color online) (a) Experimental sequence used for implementing the Grover search algorithm on four objects. First,  $Y(\pi/2)$  rotations are applied to produce the superposition  $|\phi\rangle = (1/2)\sum_{u,v} |uv\rangle$  of all basis states; then one of the four possible oracles (corresponding to the four sign combinations of the  $Z$  rotations) is applied. The tagged state is then decoded in all cases using an  $iSWAP$  operation followed by  $X(\pi/2)$  rotations. (b) State tomography at two steps of the algorithm ( $\rho$  matrices) and success probability after a single run (histograms). The bright dots on the left-hand side mark the basis state tagged by each oracle operator used. The amplitude of each matrix element is represented by a disk [black for the ideal density matrix, red (gray) for the measured one] and its phase by an arrow (as well as a filling color for the ideal matrix). After applying the oracle, the information on the tagged state is encoded in the phase of six particular elements of  $\rho$ . After decoding, the tagged state should be the only matrix element present in  $\rho$ . The fidelity  $F_{final}$  actually obtained is indicated in this element. The probability distribution of the single-run readout outcomes is shown on the right-hand side (bright box for the correct answer, solid dark boxes for the wrong ones).

use, the encoding is a phase encoding as in Ref. 10. When applied to  $|\phi\rangle$ , each oracle operator inverts the sign of the component corresponding to the state it tags, respectively, to the other ones. The density matrix, after applying the oracle,

ideally takes a simple form: The amplitude of all coefficients is  $1/4$ , and the phase of an element  $\rho_{rs}$  is  $\varphi_{rs} = \pi(\delta_{rt} + \delta_{st})$ , where  $t$  corresponds to the state tagged by the oracle operator. The state tomography performed after applying the oracle, shown in Fig. 3(b), is in good agreement with this prediction. More quantitatively, we find that after having applied the oracle operator, the intermediate fidelity is  $F_{int} = 0.87, 0.80, 0.84$ , and  $0.82$ , respectively. The last part of the algorithm consists in transforming the obtained state in the searched state irrespectively of it, or equivalently to transform the phase information distributed over the elements of the density matrix in a weight information with the whole weight on the searched state. This operation is readily performed by applying an  $iSWAP$  gate followed by  $X(\pi/2)$  rotations for both qubits. We find that the fidelity of the density matrix at the end of the algorithm is  $F_{final} = 0.70, 0.62, 0.67$ , and  $0.66$ , respectively. We explain both  $F_{int}$  and  $F_{final}$  by gate errors at a  $2\%$  level, by errors in the tomography pulses at a  $2\%$  level, as well as by decoherence during the whole experimental sequence [at the coupling point, relaxation times are  $T_1^I \simeq 450$  ns and  $T_1^{II} \simeq 500$  ns, and the effective dephasing times  $T_\varphi^I \simeq T_\varphi^{II} \simeq 2$   $\mu$ s (Ref. 15)].

We now consider the success probability obtained after a single run (with no tomography pulses), which probes the quantum speed-up actually achieved by the processor. We find (see Fig. 3) that our processor does yield the correct answer with a success probability  $P_S = 0.67, 0.55, 0.62$ , and  $0.52$  for the four basis states, which is smaller than the density matrix fidelity  $F_{final}$ . One notices that the difference between  $F_{final}$  and  $P_S$ , mostly due to readout errors, slightly depends on the searched state: The larger the energy of the searched state, the larger is the difference. This dependence is well explained by the effect of relaxation during the readout pulse, which is the main error source at readout, the second one being readout crosstalk. One also notices that the outcome errors are distributed over all the wrong answers. To summarize, the errors of our implementation of Grover's algorithm originate both from small unitary errors accumulated during the algorithm, and from decoherence during the whole sequence, in particular, during the final readout.

We finally discuss the significance of the obtained results in terms of quantum information processing. The achieved success probability is smaller than the theoretically achievable value 1, but nevertheless it is sizably larger than the value of 0.25 obtained by running once the classical algorithm that consists in making a random trial. From the point of view of a user who has to find out which unknown oracle has been given to him, the fidelity of the algorithm outcome is  $f_{ab} = 0.57, 0.63, 0.57$ , and  $0.59$  for the 00, 01, 10, and 11 outcomes, respectively, as explained in Sec. V of the Supplemental Material.<sup>16</sup> Despite the presence of errors, this result demonstrates the quantum speed-up for Grover's algorithm when searching in a Hilbert space with a small size  $N = 4$ .

In conclusion, we have demonstrated the operation of the Grover search algorithm in a superconducting two-qubit processor with a single-shot nondestructive readout. This result indicates that the quantum speed-up expected from quantum algorithms is within reach of superconducting quantum bit processors. Demonstrating the  $\sqrt{N}$  speed-up for Grover's algorithm in larger Hilbert spaces requires a qubit architecture

more scalable than the present one, which presently is a major challenge in the field.

We gratefully acknowledge discussions with M. Devoret, D. DiVicenzo, L. DiCarlo, and within the Quantronics

group, technical support from P. Orfila, P. Senat, and J. C. Tack, as well as financial support from the European research contract SOLID, from ANR Masquelspec and C'Nano, and from the German Ministry of Education and Research.

- <sup>1</sup>L. K. Grover, in *Proceedings of the 28th Annual ACM Symposium on the Theory of Computing*, edited by G. L. Miller (ACM, New York, 1996), p. 212; *Am. J. Phys.* **69**, 769 (2001).
- <sup>2</sup>P. W. Shor, *Proceedings of the 35th Annual Symposium on Foundations of Computer Science* (IEEE, Los Alamitos, CA, 1994); *SIAM J. Comput.* **26**, 1484 (1997).
- <sup>3</sup>M. A. Nielsen and I. L. Chuang, *Quantum Computation and Quantum Information* (Cambridge University Press, Cambridge, UK, 2000).
- <sup>4</sup>T. D. Ladd, F. Jelezko, R. Laflamme, Y. Nakamura, C. Monroe, and J. L. O'Brien, *Nature (London)* **464**, 45 (2010).
- <sup>5</sup>D. P. DiVincenzo, *Fortschr. Phys.* **48**, 771 (2000).
- <sup>6</sup>J. Koch, T. M. Yu, J. Gambetta, A. A. Houck, D. I. Schuster, J. Majer, A. Blais, M. H. Devoret, S. M. Girvin, and R. J. Schoelkopf, *Phys. Rev. A* **76**, 042319 (2007).
- <sup>7</sup>J. A. Schreier, A. A. Houck, J. Koch, D. I. Schuster, B. R. Johnson, J. M. Chow, J. M. Gambetta, J. Majer, L. Frunzio, M. H. Devoret, S. M. Girvin, and R. J. Schoelkopf, *Phys. Rev. B* **77**, 180502 (2008).
- <sup>8</sup>Y. Nakamura, Yu. A. Pashkin, and J. S. Tsai, *Nature (London)* **398**, 786 (1999).
- <sup>9</sup>D. Deutsch and R. Jozsa, *Proc. R. Soc. London A* **439**, 553 (1992).
- <sup>10</sup>L. DiCarlo, J. M. Chow, J. M. Gambetta, L. S. Bishop, B. R. Johnson, D. I. Schuster, J. Majer, A. Blais, L. Frunzio, S. M. Girvin, and R. J. Schoelkopf, *Nature (London)* **460**, 240 (2009).
- <sup>11</sup>M. D. Reed, L. DiCarlo, S. E. Nigg, L. Sun, L. Frunzio, S. M. Girvin, and R. J. Schoelkopf, *Nature (London)* **482**, 382 (2012).
- <sup>12</sup>T. Yamamoto, M. Neeley, E. Lucero, R. C. Bialczak, J. Kelly, M. Lenander, M. Mariantoni, A. D. O'Connell, D. Sank, H. Wang, M. Weides, J. Wenner, Y. Yin, A. N. Cleland, and J. M. Martinis, *Phys. Rev. B* **82**, 184515 (2010).
- <sup>13</sup>M. Mariantoni, H. Wang, T. Yamamoto, M. Neeley, R. C. Bialczak, Y. Chen, M. Lenander, E. Lucero, A. D. O'Connell, D. Sank, M. Weides, J. Wenner, Y. Yin, J. Zhao, A. N. Korotkov, A. N. Cleland, and J. M. Martinis, *Science* **334**, 6052 (2011).
- <sup>14</sup>E. Lucero, R. Barends, Y. Chen, J. Kelly, M. Mariantoni, A. Megrant, P. O'Malley, D. Sank, A. Vainsencher, J. Wenner, T. White, Y. Yin, A. N. Cleland, and J. M. Martinis, e-print [arXiv:1202.5707](http://arxiv.org/abs/1202.5707).
- <sup>15</sup>A. Dewes, F. R. Ong, V. Schmitt, R. Lauro, N. Boulant, P. Bertet, D. Vion, and D. Esteve, *Phys. Rev. Lett.* **108**, 057002 (2012).
- <sup>16</sup>See Supplemental Material at <http://link.aps.org/supplemental/10.1103/PhysRevB.85.140503> for technical information about the sample preparation (I), sample parameters (II), and experimental setup (III), and for the detailed analysis of readout errors (IV) and algorithm fidelity (V).
- <sup>17</sup>F. R. Ong, M. Boissonneault, F. Mallet, A. Palacios-Laloy, A. Dewes, A. C. Doherty, A. Blais, P. Bertet, D. Vion, and D. Esteve, *Phys. Rev. Lett.* **106**, 167002 (2011).
- <sup>18</sup>F. Mallet, Florian R. Ong, A. Palacios-Laloy, F. Nguyen, P. Bertet, D. Vion, and D. Esteve, *Nat. Phys.* **5**, 791 (2009).
- <sup>19</sup>I. Siddiqi, R. Vijay, F. Pierre, C. M. Wilson, M. Metcalfe, C. Rigetti, L. Frunzio, and M. H. Devoret, *Phys. Rev. Lett.* **93**, 207002 (2004).
- <sup>20</sup>M. B. Metcalfe, E. Boaknin, V. Manucharyan, R. Vijay, I. Siddiqi, C. Rigetti, L. Frunzio, R. J. Schoelkopf, and M. H. Devoret, *Phys. Rev. B* **76**, 174516 (2007).
- <sup>21</sup>J. A. Jones, M. Mosca, and R. H. Hansen, *Nature (London)* **393**, 344 (1998).
- <sup>22</sup>I. L. Chuang, N. Gershenfeld, and M. Kubinec, *Phys. Rev. Lett.* **80**, 3408 (1998).
- <sup>23</sup>K. A. Brickman, P. C. Haljan, P. J. Lee, M. Acton, L. Deslauriers, and C. Monroe, *Phys. Rev. A* **72**, 050306 (2005).
- <sup>24</sup>N. Bhattacharya, H. B. van Linden van den Heuvell, and R. J. C. Spreeuw, *Phys. Rev. Lett.* **88**, 137901 (2002).
- <sup>25</sup>P. Walther, K. J. Resch, T. Rudolph, E. Schenck, H. Weinfurter, V. Vedral, M. Aspelmeyer, and A. Zeilinger, *Nature (London)* **434**, 169 (2005).
- <sup>26</sup>J. Ahn, T. C. Weinacht, and P. H. Bucksbaum, *Science* **287**, 463 (2000).

## Supplemental material

### Demonstrating quantum speed-up in a superconducting two-qubit processor

A. Dewes<sup>1</sup>, R. Lauro<sup>1</sup>, F.R. Ong<sup>1</sup>, V. Schmitt<sup>1</sup>,  
P. Milman<sup>2</sup>, P. Bertet<sup>1</sup>, D. Vion<sup>1</sup>, and D. Esteve<sup>1</sup>

<sup>1</sup>*Service de Physique de l'Etat Condensé/IRAMIS/DSM (CNRS URA 2464),*

*CEA Saclay, F-91191 Gif-sur-Yvette, France and*

<sup>2</sup>*Laboratoire Matériaux et Phénomènes Quantiques,*

*Université Paris Diderot, Bâtiment Condorcet, 10,*

*rue Alice Domon et Léonie Duquet, F75205 Paris, France*

## I. SAMPLE PREPARATION

The sample is fabricated on a silicon chip oxidized over 50 nm. A 150 nm thick niobium layer is first deposited by magnetron sputtering and then dry-etched in a  $SF_6$  plasma to pattern the readout resonators, the current lines for frequency tuning, and their ports. Finally, the transmon qubit, the coupling capacitance and the Josephson junctions of the resonators are fabricated by double-angle evaporation of aluminum through a shadow mask patterned by e-beam lithography. The first layer of aluminum is oxidized in a  $Ar - O_2$  mixture to form the oxide barrier of the junctions. The chip is glued with wax on a printed circuit board (PCB) and wire bonded to it. The PCB is then screwed in a copper box anchored to the cold plate of a dilution refrigerator.

## II. SAMPLE PARAMETERS

The sample is first characterized by spectroscopy [15]. The incident power used is high enough to observe the resonator frequency  $\nu_R$ , the qubit line  $\nu_{01}$ , and the two-photon transition at frequency  $\nu_{02}/2$  between the ground and second excited states of each transmon. A fit of the transmon model to the data yields the sample parameters, i.e. total Josephson energies of the transmons in zero magnetic field  $E_J^I/h = 36.2$  GHz and  $E_J^{II}/h = 43.1$  GHz, total charging energies  $E_C^I/h = 0.98$  GHz and  $E_C^{II}/h = 0.87$  GHz, assymmetries between the two junctions of a transmon  $d_I = 0.2$  and  $d_{II} = 0.35$ . The measured resonance frequencies of the readout resonators are  $\nu_R^I = 6.84$  GHz, and  $\nu_R^{II} = 6.70$  GHz. The qubit-readout anti-crossing at  $\nu = \nu_R$  yields the qubit-readout couplings  $g_0^I \simeq g_0^{II} \simeq (2\pi) 50$  MHz. Independent measurements of the resonator dynamics yield quality factors  $Q_I = Q_{II} = 730$  and Kerr non linearities [15,17]  $K_I/\nu_R^I \simeq K_{II}/\nu_R^{II} \simeq -2.3 \pm 0.5 \times 10^{-5}$ .

## III. EXPERIMENTAL SETUP

- Qubit resonant microwave pulses: The qubit drive pulses are generated by two phase-locked microwave generators feeding a pair of I/Q-mixers. The IF inputs are provided by a 4-Channel1 GS/s arbitrary waveform generator (AWG Tektronix AWG5014). Single-sideband mixing in the frequency range of 50-300 MHz is used to generate

multi-tone drive pulses and to obtain a high ON/OFF ratio ( $> 50$  dB). Phase and amplitude errors are corrected by applying suitable sideband and carrier frequency dependent corrections to the amplitude and offset of the IF signals.

- Qubit frequency control: Flux control pulses are generated by a second AWG and sent to the chip through a transmission line equipped with 40 dB total attenuation and a pair of 1 GHz dissipative low-pass filters at 4 K. The input signal of each flux line is returned to room temperature through an identical transmission line and measured, which allows to compensate the non-ideal frequency response of the line.
- Readout pulses: The driving pulses for the Josephson bifurcation amplifier (JBA) readouts are generated by mixing the continuous signals of a pair of microwave generators with IF pulses provided by a 1 GS/s arbitrary waveform generator (AWG Tektronix AWG5014). Each readout pulse consists of a measurement part with a rise time of 30 ns and a hold time of 100 ns, followed by a  $2 \mu\text{s}$  long latching part at 90 % of the pulse height.
- Drive and measurement lines: The drive and readout microwave signals of each qubit are combined and sent to the sample through a pair of transmission lines with total attenuation 70 dB and filtered at 4 K and 300 mK. A microwave circulator at 20 mK protects the chip from the amplifier noise. The signals are amplified by 36 dB at 4 K by two cryogenic HEMT amplifiers (CIT Cryo 1) with noise temperature 5 K. The reflected readout pulses are amplified and demodulated at room temperature. The IQ quadratures of the demodulated signals are sampled at 1 GS/s by a 4-channel data acquisition system (Acqiris DC282).

#### IV. READOUT ERRORS

Errors in our readout scheme are discussed in detail in Ref. [15] for a single qubit. First, incorrect mapping  $|0\rangle \rightarrow 1$  or  $|1\rangle \rightarrow 0$  of the projected state of the qubit to the dynamical state of the resonator can occur, due to the stochastic nature of the switching between the two dynamical states. As shown in Fig. 4.1, the probability  $p$  to obtain the outcome 1 varies continuously from 0 to 1 over a certain range of drive power  $P_d$  applied to the readout. When the shift in power between the two  $p_{|0\rangle,|1\rangle}(P_d)$  curves is not much larger than

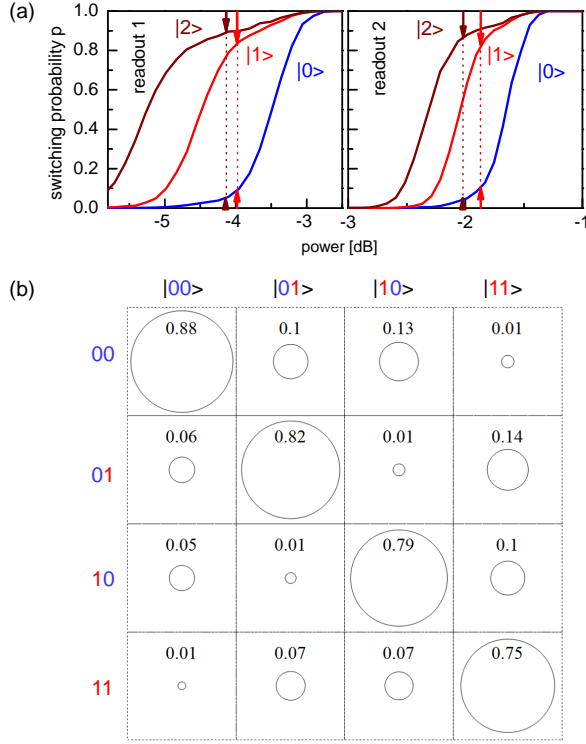


Figure IV.1:

(a) Switching probability  $p$  of each readout as a function of its peak driving power, when its qubit is prepared in state  $|0\rangle$  (blue),  $|1\rangle$  (red), or  $|2\rangle$  (brown), with the other qubit being far detuned. The arrows indicate the readout errors where the contrast is optimal with (brown) and without (red)  $|1\rangle \rightarrow |2\rangle$  shelving. (b) Readout matrix  $\mathcal{R}$  giving the probabilities of the four  $ab$  outcomes, for the four computational input states  $|uv\rangle$ , when using  $|1\rangle \rightarrow |2\rangle$  shelving. Each matrix elements is represented by a circle of area proportional to its value (a unit circle would touch the cell borders).

this range, the two curves overlap and errors are significant even at the optimal drive power where the difference in  $p$  is maximum. Second, even in the case of non overlapping  $p_{|0\rangle,|1\rangle}(P_d)$  curves, the qubit initially projected in state  $|1\rangle$  can relax down to  $|0\rangle$  before the end of the measurement, yielding an outcome 0 instead of 1. The probability of these two types of errors vary in opposite directions as a function of the frequency detuning  $\Delta = \nu_R - \nu > 0$  between the resonator and the qubit, so that a compromise has to be found for  $\Delta$ . As explained in the main text, we use a shelving method to the second excited state in order to improve the readout contrast  $c = \text{Max} (p_{|1\rangle} - p_{|0\rangle})$ , with a microwave  $\pi$  pulse at frequency

$\nu_{12}$  bringing state  $|1\rangle$  into state  $|2\rangle$  just before the readout pulse. The smallest errors  $e_0^{\text{I},\text{II}}$  and  $e_1^{\text{I},\text{II}}$  when reading  $|0\rangle$  and  $|1\rangle$  are found for  $\Delta_{\text{I}} = 440$  MHz and  $\Delta_{\text{II}} = 575$  MHz:  $e_0^{\text{I}} = 5\%$  and  $e_1^{\text{I}} = 13\%$  (contrast  $c_{\text{I}} = 1 - e_0^{\text{I}} - e_1^{\text{I}} = 82\%$ ), and  $e_0^{\text{II}} = 5.5\%$  and  $e_1^{\text{II}} = 12\%$  ( $c_{\text{II}} = 82\%$ ). When using the  $|1\rangle \rightarrow |2\rangle$  shelving before readout,  $e_0^{\text{I}} = 2.5\%$  and  $e_2^{\text{I}} = 9.5\%$  (contrast  $c_{\text{I}} = 1 - e_0^{\text{I}} - e_2^{\text{I}} = 88\%$ ), and  $e_0^{\text{II}} = 3\%$  and  $e_2^{\text{II}} = 8\%$  ( $c_{\text{II}} = 89\%$ ). These best results are very close to those obtained in Ref. [15] of main text, but cannot however be exploited for simultaneous readout of the two qubits.

Indeed, when the two qubits are measured simultaneously, we find an influence of the projected state of each qubit on the outcome of the readout of the other one. In order to minimize this spurious effect, we increase the detuning  $\Delta_{\text{I,II}}$  up to  $\sim 1$  GHz with respect to previous optimal values. An immediate consequence shown in Fig. S4.1(a) is a reduction of the  $c_{\text{I,II}}$  contrasts. The errors when reading  $|0\rangle$  and  $|1\rangle$  are then  $e_0^{\text{I}} = 10\%$  and  $e_1^{\text{I}} = 16\%$  (contrast  $c_{\text{I}} = 74\%$ ) and  $e_0^{\text{II}} = 12\%$  and  $e_1^{\text{II}} = 15\%$  (contrast  $c_{\text{II}} = 73\%$ ). When shelving the qubit in state  $|2\rangle$ , the errors are  $e_0^{\text{I}} = 5\%$ ,  $e_2^{\text{I}} = 11\%$  (contrast  $c_{\text{I}} = 84\%$ ),  $e_0^{\text{II}} = 5\%$ ,  $e_2^{\text{II}} = 12\%$  (contrast  $c_{\text{I}} = 83\%$ ). The readout errors are captured in the  $4 \times 4$  readout matrix  $\mathcal{R}$  shown in Fig. S4.1(c), that gives the probabilities  $p_{uv}$  of the four possible outcomes for the different input states using the  $|1\rangle \rightarrow |2\rangle$  shelving technique. This matrix  $\mathcal{R}$  is used to correct the readout errors only when doing state tomography, and not when running the algorithm once. The cause of the readout crosstalk in our processor is discussed in Ref. [15].

## V. ALGORITHM FIDELITY

From the point of view of a user that would search which unknown oracle has been given to him, the fidelity  $f_{ab}$  of the algorithm for each possible outcome  $ab$  is  $f_{ab} = p_{ab/O_{ab}} / (p_{ab/O_{00}} + p_{ab/O_{01}} + p_{ab/O_{10}} + p_{ab/O_{11}})$  with  $p_{ab/O_{uv}}$  the probability of obtaining outcome  $ab$  knowing that  $O_{uv}$  has been used. These probabilities are shown in table V.1, yielding  $f_{00,01,10,11} = 0.57, 0.63, 0.57$ , and  $0.59$ .

$ab/O_{uv}$	$O_{00}$	$O_{01}$	$O_{10}$	$O_{11}$	$\sum$	$f_{ab}$
00	0.666	0.192	0.188	0.122	1.168	57.0 %
01	0.127	0.554	0.071	0.122	0.874	63.4 %
10	0.128	0.106	0.615	0.239	1.088	56.5 %
11	0.079	0.148	0.126	0.517	0.870	59.4 %

Table V.1: Conditional probabilities  $p_{ab/O_{uv}}$  and statistical fidelities  $f_{ab}$  for all possible outcomes  $ab$ , measured for our version of Grover's algorithm.